



UNIVERSITY OF
TEXAS
ARLINGTON

TECHNICAL REPORT 0-7068-1

IDENTIFY AND ANALYZE INUNDATED BRIDGE
SUPERSTRUCTURES IN HIGH VELOCITY FLOOD EVENTS

Habib Ahmari, Ph.D., P.E.
Michelle Hummel, Ph.D.
Shih-Ho (Simon) Chao, Ph.D., P.E.
Shah Md Imran Kabir
Fahad Pervaiz
Bhupendra Raj Acharya
Maxfield Dean, M.Sc.
Qazi Ashique Mowla

Submitted: September 2021
Published: December 2021
Project: 0-7068

The University of Texas at Arlington
in cooperation with the Texas Department of Transportation and Federal Highway Administration

TECHNICAL REPORT DOCUMENTATION PAGE

1. Report No. FHWA/TX-21/0-7068-1	2. Government Accession No.	3. Recipient's Catalog No.	
4. Title and Subtitle Identify and Analyze Inundated Bridge Superstructures in High Velocity Flood Events: Final Report		5. Report Date September 2021 Published December 2021	
		6. Performing Organization Code UTA	
7. Author(s) Habib Ahmari, Ph.D., P.E. https://orcid.org/0000-0002-8803-842X Michelle Hummel, Ph.D. https://orcid.org/0000-0002-5524-2547 Shih-Ho (Simon) Chao, Ph.D., P.E. https://orcid.org/0000-0003-2679-7364 Shah Md Imran Kabir, Fahad Pervaiz, Bhupendra Raj Acharya, Maxfield Dean M.Sc., Qazi Ashique Mowla		8. Performing Organization Report No. 0-7608-1	
9. Performing Organization Name and Address The University of Texas at Arlington Department of Civil Engineering P.O. Box 19308 Arlington, TX 76019		10. Work Unit No.	
		11. Contract or Grant No. 0-7608	
12. Sponsoring Agency Name and Address Texas Department of Transportation Research and Technology Implementation Division 125 E. 11th Street Austin, TX 78701		13. Type of Report and Period Covered Technical Report November 2020 - October 2021	
		14. Sponsoring Agency Code	
15. Supplementary Notes Project performed in cooperation with the Texas Department of Transportation and the Federal Highway Administration.			
16. Abstract Flood events are reported as the most frequent cause of bridge failure in the United States. Current design guidelines and standards specify the use of 100-year flood for analyzing the overtopping of bridges. Still, many bridge failures in the U.S. occur during floods with return periods smaller than 100 years. These guidelines only address hydrodynamic forces on substructures and do not provide any information on estimating flood force on superstructures. Also, the effectiveness of structural countermeasures, recommended by several state departments of transportation, to prevent hydraulic failure of bridges is unknown. In this project, the magnitude of potential hydraulic parameters at bridges in riverine and coastal areas in Texas was determined. The parameters were used in physical and numerical modeling of bridge structures to assess the efficacy of using countermeasures, particularly shear keys and earwalls, to reduce the risk of bridge failure during flood events. A series of small-scale laboratory experiments and computational fluid dynamics (CFD) modeling were conducted to examine the hydrodynamic forces on typical TxDOT bridge decks. The effects of a range of parameters, including bridge geometry and orientation, flow velocity and depth, and the presence of debris, on hydrodynamic forces on bridges were tested under steady flow and wave loading conditions. Full-scale CFD modeling was also performed to calculate the magnitude of hydrodynamic forces on typical TxDOT bridges. Finite element models for single-span TxDOT bridges with typical I-girders, box beams, and slab beams were developed. Results from the CFD analyses were used to conduct a structural analysis of each bridge geometry to determine whether current shear key details are adequate, or if modified details are warranted. It was found from this study that the drag force can be much greater than the capacity of the shear key or earwall especially for the cases with a Froude number of 0.9. Debris also considerably increases the drag forces. For the cases where the interface shear strength is not sufficient, several approaches are recommended to increase the interface shear capacity: (1) increase the size and/or quantity of the interface shear reinforcement, (2) increase the quantity of the shear keys, and (3) increase the length of the bent cap hence the length of the earwall.			
17. Key Words Hydrodynamic Forces, Bridge Failure, Physical Modeling, Computational Fluid Dynamics, Bridge, Flood Countermeasures, Shear Keys, Shear-Friction		18. Distribution Statement No restrictions. This document is available to the public through the National Technical Information Service, Alexandria, Virginia 22312, https://www.ntis.gov/ .	
19. Security Classif. (of this report) Unclassified	20. Security Classif. (of this page) Unclassified	21. No. of Pages 213	22. Price



Identify and Analyze Inundated Bridge Superstructures in High Velocity Flood Events

Technical Report 0-7068-1

Prepared for:

Texas Department of Transportation
P.O. Box 5080, Austin, Texas 78763

Project Manager
Martin Dassi

Prepared by:

Habib Ahmari, Ph.D., P.E.
Michelle Hummel, Ph.D.
Shih-Ho (Simon) Chao, Ph.D., P.E.
Shah Md Imran Kabir
Fahad Pervaiz
Bhupendra Raj Acharya
Maxfield Dean, M.Sc.
Qazi Ashique Mowla

The University of Texas at Arlington, Arlington, Texas, USA

October 2021

Published December 2021

DISCLAIMER

The contents of this report reflect the views of the authors, who are responsible for the facts and the accuracy of the data presented herein. The contents do not necessarily reflect the official view or policies of the Federal Highway Administration (FHWA) or the Texas Department of Transportation (TxDOT). While every effort has been made to ensure the accuracy of information provided in this report, this material is not intended to be a substitute for the actual codes and specifications for the design of bridge superstructures.

This report does not constitute a standard, specification, or regulation; and is not intended for constructing, bidding, or permit purposes.

The United States Government and the State of Texas do not endorse products or manufacturers. Trade or manufacturers' names appear herein solely because they are considered essential to the object of this report.

ACKNOWLEDGEMENT

This project was supported by TxDOT as part of Project 0-7068, “Identify and Analyze Inundated Bridge Superstructures in High Velocity Flood Events”. The authors are grateful for the support and guidance provided by Mr. Martin Dassi, Project Manager of Research and Technology Implementation. The authors are also thankful for the technical guidance provided by the TxDOT staff, Michael Hyzak, Rose Marie Klee, Abderrahmane Maamar Tayeb, Ryan Eaves, and Charlie Reed. Their assistance was central to the successful completion of this research project.

TABLE OF CONTENTS

EXECUTIVE SUMMARY	x
1 INTRODUCTION	1
1.1 Background and Problem Statement	1
1.2 Objectives and Scope	1
1.3 Research Plan	2
1.4 Report Outline	4
2 LITERATURE REVIEW OF BRIDGES HYDRODYNAMIC FORCES AND STRUCTURAL COUNTERMEASURES	5
2.1 Introduction	5
2.2 History of Bridge Failure and Causes in the United States	5
2.2.1 History of Bridge Failures in the United States	5
2.2.2 Causes of Bridge Failure.....	7
2.3 Flood Forces.....	8
2.3.1 Definitions of Flood Forces and Flow Parameters.....	8
2.3.2 Bridge Design Standard for Calculating Flood Forces	9
2.4 Experimental and Numerical Modeling of Inundated Bridges	10
2.5 Design Charts for Hydrodynamic Forces	15
2.5.1 Drag Coefficient	15
2.5.2 Lift Coefficient	16
2.5.3 Moment Coefficient.....	16
2.6 Structural Design and Countermeasures to Hydrodynamic Loading	17
2.7 DOT's Design Standards and Countermeasures to Hydrodynamic Forces	19
2.7.1 TxDOT's Design Standards and Countermeasures.....	19
2.7.2 Design Standard and Countermeasures of Other DOTs.....	20
2.8 Climate Change Impact on Hydraulic Structures	23
3 FLOW CHARACTERIZATION AT TEXAS RIVERINE AND COASTAL BRIDGES	25
3.1 Introduction	25
3.2 Background on Design Guidelines and Modeling Approaches	25
3.2.1 Design Guidelines and Modeling Approaches in Riverine Areas.....	25
3.2.2 Design Guidelines and Modeling Approaches in Coastal Areas	27
3.3 Riverine Flow Parameter Identification	29
3.3.1 Hydrologic and Hydraulic Models.....	29
3.3.2 As-Built Drawings	33
3.3.3 Flow Parameters	34
3.4 Coastal Parameter Identification	41
3.4.1 Coastal Water Level and Wave Models.....	41
3.4.2 Storm Surge and Wave Parameters.....	45
3.5 Summary	47
4 PHYSICAL MODELING OF RIVER CROSSING BRIDGES	49
4.1 Introduction	49
4.2 Physical Modeling Approach and Plan	50
4.3 Bridge and Debris Models.....	50
4.3.1 Bridge Superstructure and Substructure	50
4.3.2 Debris.....	51
4.4 Flow and Wave Parameters.....	52
4.4.1 Flow Parameters	52
4.4.2 Wave Parameters	53
4.5 Experimental Setup and Procedure	54
4.5.1 Experimental Setup.....	54
4.5.2 Experiments Procedure.....	55
Superstructure Experiments	55
Debris Experiments.....	56
Superstructure and Substructure Experiments	56

Superstructure and Substructure Experiments (no-contact scenario).....	56
Wave Experiments	57
4.6 Results	57
4.6.1 Superstructures with no Debris	57
4.6.2 Bridges with Skewed Decks	58
4.6.3 Bridges with Debris Loading	59
4.6.4 Bridges with Substructures	59
4.6.5 Effect of Proximity Ratio (Pr).....	59
4.6.6 Bridges with Wave Loading	59
4.6.7 Superstructure and Substructure (contact scenarios)	60
4.7 Summary	66
5 COMPUTATIONAL FLUID DYNAMICS MODELING OF RIVER CROSSING BRIDGES	68
5.1 Introduction	68
5.2 Background	68
5.3 Governing CFD Equations	69
5.3.1 Navier Stokes Equations	69
5.3.2 Reynolds-Averaged Navier-Stokes (RANS) Equations.....	70
5.3.3 Turbulence Models	71
5.3.4 Volume of Fluid Model	72
5.3.5 Wave Theories	73
5.4 CFD Modeling Scenarios	74
5.4.1 Bridge Models	76
5.4.2 Debris.....	76
5.4.3 Flow Parameters	76
5.4.4 Wave Parameters	77
5.5 Model Setup	77
5.5.1 Overview of the Numerical Flume.....	79
5.5.2 Meshing	80
5.5.3 Boundary Conditions and Solution Methods	81
5.5.4 Sensitivity Analysis	82
5.5.5 Validation of Model Against Previous Studies.....	86
5.5.6 Validation of Model against Physical Modeling Performed at UTA.....	88
5.6 Results and Discussion.....	91
5.6.1 Test Series A.....	91
5.6.2 Test Series B.....	100
5.6.3 Test Series C.....	102
5.6.4 Test Series D.....	102
5.6.5 Test Series E: Full-Scale Modeling	105
5.6.6 Contour plots	107
6 STRUCTURAL MODELING AND ANALYSIS OF RIVER CROSSING BRIDGES.....	108
6.1 Introduction	108
6.2 Interface Shear Resistance.....	111
6.3 Finite Element Modeling.....	112
6.4 Material Properties	113
6.5 Contact Properties	114
6.6 Calculations of Interface Area of Shear Keys/Earwalls and Corresponding Area of Interface Reinforcement	115
6.6.1 Length of Shear Key for 24-ft Roadway Bridge (TxDOT Detail BIG-24).....	115
6.6.2 Length of Shear Key for 44-ft Roadway Bridge (TxDOT Detail BIG-44).....	116
6.6.3 Length of Shear Key for 44-ft Roadway and 15-degree Skew Bridge (TxDOT Detail BIG-44-15) ..	117
6.6.4 Length of Shear Key for 44-ft Roadway and 30-degree Skew Bridge (TxDOT Detail BIG-44-30) ..	118
6.6.5 Length of Shear Key for 44-ft Roadway and 45-degree Skew Bridge (TxDOT Detail BIG-44-45) ..	118
6.6.6 Length of Earwall for Slab Beam Bridge (TxDOT Detail BPSP-24).....	119
6.6.7 Length of Earwall for Box Beam Bridge (TxDOT Detail BBB-24).....	119
6.7 Interface Shear Strengths of Shear Key and Earwall.....	121
6.7.1 Shear Key Resistance for 24-ft Roadway (TX28 Thru TX54 Girders)	121

6.7.2	Shear Key Resistance for 44-ft Roadway (TX28 Thru TX54 Girders)	122
6.7.3	Shear Key Resistance for 44' Roadway, 15° Skew (TX28 Thru TX54 Girders)	123
6.7.4	Shear Key Resistance for 44' Roadway, 30° Skew (TX28 Thru TX54 Girders)	124
6.7.5	Shear Key Resistance for 44' Roadway, 45° Skew (TX28 Thru TX54 Girders)	125
6.7.6	Earwall Resistance for 24' Roadway Box Beam Bridge (30' Thru 95' Spans).....	126
6.7.7	Earwall Resistance for 24' Roadway Slab Beam Bridge (TX SB12 or SB15).....	127
6.7.8	Summary of Shear Keys/Earwalls Resistance	128
6.8	Force Transfer on Shear Key and Earwall.....	129
6.9	Analysis Results	130
6.9.1	Summary of Full-scale Bridge Model Results for TX28 I-girder Bridge	130
6.9.2	Summary of Full-scale Bridge Model Results for TX54 I-girder Bridge	133
6.9.3	Summary of the Full-scale Bridge Model Results for TX54 I-girder Bridge with Debris and 10-ft Wave	135
6.9.4	Summary of Full-scale Bridge Model Results for Box Beam Bridge.....	137
6.9.5	Summary of Full-scale Bridge Model Results for Slab Beam Bridge	138
6.10	Recommended Modifications of Shear Key/Earwall	139
6.10.1	Examples of Recommended Modifications to Shear Key on Bent Cap for TX28 I-girder Bridges	139
6.10.2	Examples of Recommended Modifications to Shear Key on Bent Cap for TX54 I-girder Bridges ..	142
6.10.3	Examples of Recommended Modifications to Earwall on Bent Cap for Box Beam Bridges	143
6.10.4	Examples of Recommended Modifications to Earwall on Bent Cap for Slab Beam Bridges.....	145
6.11	Limitations of the Study	147
7	CONCLUSIONS AND RECOMMENDATIONS	148
	<u>REFERENCES</u>	151
	<u>APPENDIX A</u>	155
	<u>APPENDIX B</u>	162
	<u>APPENDIX C</u>	170
	<u>APPENDIX D</u>	172
	<u>APPENDIX E</u>	180

LIST OF TABLES

Table 2.1 Examples of bridges damaged by flood events in the U.S. between 1987 and 2018.....	6
Table 2.2 Most common causes of the collapse of different types of bridges (Deng et al., 2016)	7
Table 2.3 Bridge design standard for calculating flood forces	11
Table 2.4 Examples of experimental and numerical studies of flood forces on bridges performed in the past 40 years	12
Table 2.5 DOT's design flood and freeboard (vertical clearances) for bridge design.....	21
Table 2.6 DOT's countermeasure to hydrodynamic and seismic forces	22
Table 3.1 Levels of coastal flood analysis requirements for bridges in coastal areas (TxDOT, 2019).....	29
Table 3.2 Summary of data sources and modeling methods for the City of Austin and HCFCD HEC-HMS and HEC-RAS models (FEMA, 2019a and 2020).....	32
Table 3.3 Watersheds in Travis County and the number of bridges modeled along the main stem (COA, 2019)	33
Table 3.4 Watersheds in Harris County and the number of bridges modeled along the main stem (HCFCD, 2020).....	33
Table 3.5 Summary of flow parameters and bridge impacts for 10% AEP and 2% AEP flood events in Travis County watersheds	35
Table 3.6 Summary of flow parameters and bridge impacts for 1% AEP and 0.2% AEP flood events in Travis County watersheds	36
Table 3.7 Summary of flow parameters and bridge impacts for 10% AEP and 2% AEP flood events in Harris County watersheds	37
Table 3.8 Summary of flow parameters and bridge impacts for 1% AEP and 0.2% AEP flood events in Harris County watersheds	38
Table 3.9 Summary of water depth above bridge low chord values extracted from as-built drawings	39
Table 3.10 Summary of channel velocity values extracted from as-built drawings	40
Table 4.1 Minimum and maximum wave experiment parameters.....	54
Table 4.2 Summary of fitted equation parameters for Tx28, TX54, SB15, BB28, and all deck types	66
Table 5.1 Water depth classification in a wave environment	74
Table 5.2 Summary of experimental conditions for Test Series A to D (scaled models)	75
Table 5.3 Summary of experimental conditions for Test Series E (full-scale models).....	75
Table 5.4 Effect of different upstream flume lengths on hydrodynamic forces.....	83
Table 5.5 Drag and lift coefficient values for 0.15" and 0.24" mesh size	84
Table 5.6 Effect of channel bottom roughness on hydrodynamic forces.....	85
Table 5.7 Effect of turbulence models on drag and lift coefficients	85
Table 5.8 Full-scale modeling results for $Fr = 0.9$ and $h^*=2.5$ ($h^*=0.75$ for wave modeling).....	105
Table 5.9 Full-scale modeling results for $Fr = 0.5$ and $h^*=2.5$ ($h^*=0.75$ for wave modeling).....	106
Table 5.10 Full-scale modeling results for $Fr = 0.34$ and $h^*=2.5$ ($h^*=0.75$ for wave modeling).....	106
Table 6.1 Contact Properties.....	114
Table 6.2 Summary of area of shear keys/earwalls and area of reinforcement used	120
Table 6.3 Summary of shear keys/earwalls resistance.....	128
Table 6.4 Summary of full-scale bridge model results for TX28 I-girder bridge and capacity comparison.....	133
Table 6.5 Summary of full-scale bridge model results for TX54 I-girder bridge and capacity comparison.....	135
Table 6.6 Summary of the full-scale bridge model results for TX54 I-girder bridge with debris and wave	137
Table 6.7 Summary of the full-scale bridge model results for box beam bridge	138
Table 6.8 Summary of the full-scale bridge model results for slab beam bridge.....	139
Table A. 1 The Project Value of Research (VoR)	155
Table C. 1 Identification of flow parameters from TxDOT As-built Drawings	170
Table D.1 Summary of experimental conditions for test Series A to F	172
Table D.2 Bridge Dimensions (Bridge Model 1: TX-28).....	173
Table D.3 Bridge Dimensions (Bridge Model 2: TX-54).....	173
Table D.4 Bridge Dimensions (Bridge Model 3: SB-15 Slab Beam)	173
Table D.5 Bridge Dimensions (Bridge Model 4: BB-28 Box Beam)	173

LIST OF FIGURES

Figure 2.1 Number of bridge failures in the U.S. from 1989 to 2012 (1989-2000 data from Wardhana and Hadipriono, 2003; and 2000-2012 data from Taricska, 2014).....	6
Figure 2.2 Number of failed Bridges and causes of failure from 1980-2012 (Lee et al., 2013)	7
Figure 2.3 Schematic of forces and overturning moment applied on stream-crossing bridges.....	8
Figure 2.4 Schematic diagram of a fully submerged bridge deck.....	9
Figure 2.5 Drag coefficient vs inundation ratio for: (a) six-girder bridge and (b) three-girder bridge (Kerenyi et al., 2009).....	15
Figure 2.6 Drag coefficient vs flow parameters: (a) drag coefficient for a bridge superstructure with debris (Parola et al., 2000) and (b) drag coefficient vs proximity ratio (Standard Australia, 2000).....	16
Figure 2.7 Lift coefficient vs inundation ratio for: (a) a six-girder bridge and (b) three girder bridges (Kerenyi et al., 2009).....	16
Figure 2.8 Moment coefficient vs inundation ratio for: (a) six-girder bridge and (b) three girder bridges (Kerenyi et al., 2009).....	17
Figure 2.9 Countermeasures for bridges under storm surges: (a) schematic of the superstructure installed with fairing and (b) bridge physical model with fairing (Zhang et al., 2012)	17
Figure 2.10 Railway bridge adjacent to the I-10 twin span bridge between New Orleans and Slidell (Chen et al., 2005)	18
Figure 2.11 Retrofitting options for coastal bridges recommended by AASHTO guidelines: (a) air vents in the bridge deck and (b) air vents in the bridge diaphragm (Bozorgnia, 2012)	18
Figure 2.12 Schematic of deck fairing countermeasure (Oudenbroek et al., 2018).....	19
Figure 2.13 Schematic of the TxDOT countermeasures: (a) shear key and (b) earwall	20
Figure 3.1 Factors that contribute to coastal water levels (TxDOT, 2019).....	28
Figure 3.2 Watersheds in Travis County with available hydrologic and hydraulic models for flow parameter identification.....	30
Figure 3.3 Watersheds in Harris County with available hydrologic and hydraulic models for flow parameter identification.....	31
Figure 3.4 Coastal counties of Texas.....	42
Figure 3.5 SLOSH model domains for the 32 operational storm surge basins (NOAA, 2020).....	43
Figure 4.1 Schematic of the bridge substructure and superstructure	51
Figure 4.2 Schematic of the debris model: (a) flat plate debris and (b) wedge debris.....	52
Figure 4.3 Wave experiment schematic (Model 2: TX54-26' wide deck).....	53
Figure 4.4 Bridge position with reference to the still water surface elevation during wave experiments (Model 2: TX54-26')	54
Figure 4.5 Photo of the: (a) experimental flume and (b) mounting frame, load and torque cells, and support plates	55
Figure 4.6 Design charts for drag, lift, and moment coefficient versus inundation ratio for superstructure I-girder TX28	61
Figure 4.7 Design charts for drag, lift, and moment coefficient versus inundation ratio for superstructure I-girder TX54	61
Figure 4.8 Design charts for drag, lift, and moment coefficient versus inundation ratio for superstructure Slab Beam SB15	62
Figure 4.9 Design charts for drag, lift, and moment coefficient versus inundation ratio for superstructure Box Beam BB28.....	62
Figure 4.10 Design charts for drag, lift, and moment coefficient versus inundation ratio for all deck types	63
Figure 4.11 Effects of deck skewness on drag, lift, and moment coefficients.....	63
Figure 4.12 Effect of debris on drag, lift, and moment coefficients	64
Figure 4.13 Effects of substructures on drag, lift, and moment coefficients	64
Figure 4.14 Dependency of drag coefficient, lift, and moment coefficient on proximity ratio (Model 1: TX-28 with 26' deck)	64
Figure 4.15 Comparison of vertical and horizontal wave and flood forces	65
Figure 5.1 Fraction function for the blue phase in the VOF	72
Figure 5.2 Schematic diagram of the steps of ANSYS Fluent CFD model set.....	78
Figure 5.3 Geometry of scaled numerical flume	79
Figure 5.4 Geometry of full-scale numerical flume.....	79

Figure 5.5 Mesh distribution around the scaled bridge.....	80
Figure 5.6 Mesh distribution around the full-scaled bridge.....	81
Figure 5.7 Boundary conditions of numerical simulations	81
Figure 5.8 Mesh distribution around the bridge a) 0.15" b) 0.24".....	84
Figure 5.9 Dimensions of three girder bridge deck	86
Figure 5.10 Railing of three-girder bridge deck	86
Figure 5.11 Comparison of drag, lift, and moment coefficients for FHWA 3-girder bridge.....	87
Figure 5.12 Comparison of drag, lift, and moment coefficients for bridge model (TX28 with 26' deck).....	89
Figure 5.13 Comparison of Drag, lift, and moment coefficients for bridge model TX-28 with 46' deck (15° skewed deck).....	90
Figure 5.14 Comparison of vertical and horizontal forces under wave conditions for bridge model (TX-54 with 26' deck).....	91
Figure 5.15 Drag, lift, and moment coefficients for bridge model (TX28-26' deck).....	93
Figure 5.16 Drag, lift, and moment coefficients for bridge model (TX28-46' deck).....	94
Figure 5.17 Drag, lift, and moment coefficients for bridge model (TX54-26' deck).....	96
Figure 5.18 Drag, lift, and moment coefficients for bridge model (TX54-46' deck).....	97
Figure 5.19 Drag, lift, and moment coefficients for bridge model (Slab Beam-26' deck).....	98
Figure 5.20 Drag, lift, and moment coefficients for bridge model (Box Beam-26' deck).....	99
Figure 5.21 Effects of deck skewness on drag, lift, and moment coefficients for bridge model (TX28-46' deck)....	101
Figure 5.22 Effect of debris on drag, lift, and moment coefficients for bridge model (TX28-46' deck).....	103
Figure 5.23 Effect of wave height on horizontal and vertical forces for bridge model (TX54-26' deck).....	104
Figure 6.1 Shear key on bridge bent cap	108
Figure 6.2 TxDOT shear key (plan view).....	109
Figure 6.3 TxDOT shear key (elevation view).....	109
Figure 6.4 Earwall on bridge	110
Figure 6.5 TxDOT earwall plan.....	110
Figure 6.6 TxDOT earwall elevation.....	111
Figure 6.7 Shear friction mechanism (Waweru et al., 2018).....	112
Figure 6.8 Finite element (FE) model of a bridge	113
Figure 6.9 Elements of I-girder bridge	114
Figure 6.10 Elements of box beam bridge.....	114
Figure 6.11 (a) Shear key and other elements (b) Interface shear reinforcement in shear key.....	115
Figure 6.12 Bent cap for 24-ft roadway I-girder bridge	116
Figure 6.13 Bent cap for 44-ft roadway I-girder bridge	117
Figure 6.14 Bent cap for 44-ft roadway 15-degree skew I-girder bridge	117
Figure 6.15 Bent cap for 44-ft roadway 30-degree skew I-girder bridge	118
Figure 6.16 Bent cap for 44-ft roadway 45-degree skew I-girder bridge	119
Figure 6.17 Bent cap for slab beam bridge.....	119
Figure 6.18 Bent cap for box beam bridge	120
Figure 6.19 Force transfer in shear key	129
Figure 6.20 Lateral force transfer in I-girder bridge.....	130
Figure 6.21 Lateral force transfer in box beam bridge	130
Figure 6.22 24-ft roadway TX28 I-girder bridge.....	131
Figure 6.23 44-ft roadway TX28 I-girder bridge.....	131
Figure 6.24 15-degree skew, 44-ft roadway TX28 I-girder bridge.....	132
Figure 6.25 30-degree skew, 44-ft roadway TX28 I-girder bridge.....	132
Figure 6.26 45-degree skew, 44-ft roadway TX28 I-girder bridge.....	132
Figure 6.27 24-ft roadway TX54 I-girder bridge.....	134
Figure 6.28 44-ft roadway TX54 I-girder bridge.....	134
Figure 6.29 I-girder bridge with flat plate debris (section).....	136
Figure 6.30 I-girder bridge with flat plate debris (elevation)	136
Figure 6.31 I-girder bridge with wedge shape debris (section)	136
Figure 6.32 I-girder bridge with wedge shape debris (elevation).....	136
Figure 6.33 TxDOT 24-ft roadway box beam bridge	137
Figure 6.34 TxDOT 24-ft roadway slab beam bridge.....	138
Figure 6.35 Two shear keys in bent cap	140

Figure 6.36 Existing shear key details (plan).....	140
Figure 6.37 Existing shear key details (3D view).....	141
Figure 6.38 Modified shear key details (plan).....	141
Figure 6.39 Modified shear key details (3D view).....	141
Figure 6.40 Bridge having 4 shear keys.....	142
Figure 6.41 Bridge having 3 shear keys.....	143
Figure 6.42 Existing earwall for box beam bridge.....	144
Figure 6.43 Proposed earwall for box beam bridge (plan).....	144
Figure 6.44 Proposed earwall for box beam bridge (elevation).....	144
Figure 6.45 Existing earwall for slab beam bridge.....	145
Figure 6.46 Modified earwall for slab beam bridge (plan).....	146
Figure 6.47 Modified earwall for slab beam bridge (elevation).....	146
Figure 6.48 Modified earwall for slab beam bridge (plan).....	147
Figure 6.49 Modified earwall for slab beam bridge (elevation).....	147
Figure A.1 Value of Identify and Analyze Inundated Bridge Superstructures in High Velocity Flood Events.....	158
Figure D.1 Bridge Model 1: a) 26' deck with four TX-28 girders, b) 46' deck with six TX-28 girders.....	174
Figure D.2 Bridge Model 2: a) 26' deck with four TX-54 girders, b) 46' deck with six TX-54 girders.....	174
Figure D.3 Bridge Model 3: a) 26' deck with four 5SB-15 slab beams, b) 46' deck with six 5SB-15 and four 4SB-15 slab beams.....	175
Figure D.4 Bridge Model 4: a) 26' deck with four 5BB-28 box beams, b) 46' deck with six 5BB-28 and four 4BB-28 box beams.....	175
Figure D.5 T221 Bridge railing model.....	175
Figure D.6 Test Series A: Bridge Models: (a) 26-ft deck TX-28, (b) 46-ft deck TX-28, (c) 26-ft deck TX-54, (d) 46-ft deck TX-54, (e) 26-ft deck SB-15, (f) 46-ft deck SB-15, (g) 26-ft deck BB-28, (h) 46-ft deck BB-28.....	176
Figure D.7 Test Series B: Bridge Model 1 with skew deck; (a) 15-deg skew deck side view (b) 15-deg skew deck top view, (c) 30-deg skew deck side view, (d) 30-deg skew deck side view, (e) 45-deg skew deck side view, (f) 45-deg skew deck top view.....	177
Figure D.8 Test Series C: Bridge Model 2 with derbies; (a) with flat plate debris, (b) with wedge debris.....	178
Figure D.9 Test Series D: Bridge Models 1 to 4 with substructures; (a) Bridge Model 1 (TX-28), (b) Bridge Model 2 (TX-54), (c) Bridge Model 3 (SB-15), (d) Bridge Model 4 (BB-28).....	178
Figure D.10 Test series E: (a) bearing pad installation and (b) substructure test configuration.....	179
Figure D.11 Test Series F: Bridge Models 2 under wave loading; (a) TX54-26' deck, (b) TX54-46' deck.....	179
Figure E.1 Bridge Model TX28-26' wide Deck ($h^* = 2.5$, $Fr = 0.34$).....	180
Figure E.2 Bridge Model TX28-46' wide Deck ($h^* = 2.5$, $Fr = 0.34$).....	181
Figure E.3 Bridge Model TX54-26' wide Deck ($h^* = 2.5$, $Fr = 0.34$).....	182
Figure E.4 Bridge Model TX54-46' wide Deck ($h^* = 2.5$, $Fr = 0.34$).....	183
Figure E.5 Bridge Model Slab Beam-26' wide Deck ($h^* = 2.5$, $Fr = 0.34$).....	184
Figure E.6 Bridge Model Box Beam-26' wide Deck ($h^* = 2.5$, $Fr = 0.34$).....	185
Figure E.7 Bridge Model TX54-46' wide Deck with Flat Plate Debris ($h^* = 1$, $Fr = 0.34$).....	186
Figure E.8 Wave height = 1" Bridge Model TX54-26' wide Deck ($h^* = 0.26$).....	187
Figure E.9 Wave height = 2" Bridge Model TX54-26' wide Deck ($h^* = 0.26$).....	187
Figure E.10 Wave height = 1" Bridge Model TX54-46' wide Deck ($h^* = 0.26$).....	188
Figure E.11 Wave height = 2" Bridge Model TX54-46' wide Deck ($h^* = 0.26$).....	188
Figure E.12 Bridge Model TX28-26' wide Deck ($h^* = 2.5$, $Fr = 0.9$).....	189
Figure E.13 Bridge Model TX28-46' wide Deck ($h^* = 2.5$, $Fr = 0.9$).....	190
Figure E.14 Bridge Model TX54-26' wide Deck ($h^* = 2.5$, $Fr = 0.9$).....	191
Figure E.15 Bridge Model TX54-46' wide Deck ($h^* = 2.5$, $Fr = 0.9$).....	192
Figure E.16 Bridge Model Slab Beam-26' wide Deck ($h^* = 2.5$, $Fr = 0.9$).....	193
Figure E.17 Bridge Model Box Beam-26' wide Deck ($h^* = 2.5$, $Fr = 0.9$).....	194
Figure E.18 Bridge Model TX54-46' wide Deck with Flat Plate Debris ($h^* = 2.5$, $Fr = 0.9$).....	195
Figure E.19 Bridge Model TX54-46' wide Deck with Wedge Shape Debris ($h^* = 2.5$, $Fr = 0.9$).....	196
Figure E.20 Contour Plots of Air Volume Fraction for Waves modeling.....	197

EXECUTIVE SUMMARY

Bridges are designed to withstand flood and debris loads; however, it is reported that 53% of bridge failures in the U.S. are caused by hydraulic events, including floods, scour, and debris. Even though stream-crossing bridges are designed to pass the design flood while maintaining a minimum freeboard, flood events are reported as the most frequent cause of bridge failure in the U.S. and around the world. Most bridges in Texas are built to withstand 25- or 50-year floods, while interstate highways are designed to withstand 100-year floods. No specific design guideline is available for bridges that only pass floods with return periods smaller than 100 years in areas with significant flow velocity and debris. The Texas Department of Transportation Bridge Design Manual – LRFD (TxDOT 2020) requires shear keys in bridges crossing rivers and streams, based on a freeboard 100-year flood level. Even though bridge design guidelines and standards specify the use of the 100-year flood for analyzing the overtopping of modern interstate bridges receiving federal funding, many bridge failures in the United States occur during floods with return periods smaller than 100 years. The effectiveness of structural countermeasures, such as shear keys, to hydraulic failure of bridges is unknown. The primary objectives of the projects were to 1) to identify Texas bridges that have the potential to become inundated during high velocity flow events, and use this information to characterize the velocity and flood levels to design scale flume tests; 2) conduct scale experimental tests and numerical modeling to determine flood force effects on superstructures and substructures, using typical TxDOT bridge details (TxGirder, Box Beam, and Slab Beam superstructures); 3) perform structural analyses to determine whether shear key details are adequate, or whether additional countermeasures are warranted. Hydrodynamic forces on typical TxDOT bridges under flood, surge and debris loadings were determined. The effectiveness of current TxDOT countermeasures was assessed, and several approaches were recommended if the capacity of the measure was not sufficient to ensure the bridge stability and prevent failure due to hydraulic events.

A comprehensive literature search was conducted on bridge design standards, guidelines, policies, and research studies on hydrodynamic loads from floods and storm surges. The search covers different state and federal administrations and government agencies, such as state DOTs. International practices such as the bridge design standards in Australia, Europe, Japan, and India are also covered in this review. The literature search on physical and numerical modeling of hydrodynamic forces on bridges was performed. A substantial number of physical, numerical, and analytical models and survey reports were reviewed; however, only well-documented articles that include detailed information on the subject were documented. Where available, respective technical manuals and data that were used in the creation of the models were reviewed. Research papers that present real-world examples, compare model performances, or discuss the models' capabilities or weaknesses were also explored.

A review was conducted to determine the magnitude of potential hydraulic parameters at bridges in riverine and coastal areas in Texas. Existing data sets, as-built drawings, and model outputs were assessed to extract riverine flow characteristics, including water surface elevations, flow regimes, and velocities, and coastal hydrodynamic factors, including stillwater elevations and wave heights, in the vicinity of bridges. The riverine bridges considered in the analysis were primarily located in Travis and Harris Counties, where detailed, publicly available hydraulic models have been developed for many watersheds. These two counties were selected because they represent highly developed, flood-prone regions and have very different topographic characteristics, which allows for an assessment of the potential variations in flow regimes across the state. Bridges in all 16 coastal counties in Texas were considered in the assessment of hydrodynamic forces. The highest flow velocities were observed for bridges in Travis County, which generally has higher topographic gradients. At coastal bridge locations, wave heights of up to 20.0 feet and stillwater depths of 62.6 feet are possible. The highest total water depths and wave heights were observed in Calhoun and Galveston Counties. For Category 5 hurricanes, almost 250 bridges are exposed to storm surges greater than 18 feet above the ground. Across all hurricane categories, Harris County has the highest number of exposed bridges. The hydraulic and hydrodynamic parameters from this review were used in physical and numerical modeling of bridge structures to assess the efficacy of using countermeasures, particularly shear keys, to reduce the risk of bridge failure during flood events.

Experiments on 1:50 scale models of four bridge deck types were performed. More than 500 tests were performed in a laboratory flume to evaluate the general response of the drag, lift and moment coefficients to bridge geometry (deck type, deck width, skewness), flow condition (inundation ratio, Froude number), flow blockage by debris and substructures, and wave loading. Design charts and equations are developed for each bridge deck type. The results of all bridge deck types were combined to develop universal design charts and equations for all bridge deck geometries.

A series of computational fluid dynamics (CFD) modeling was conducted to examine the hydrodynamic forces on typical TxDOT bridge decks. More than 1,000 numerical simulations were performed to thoroughly examine the effects of a range of parameters, including bridge geometry and orientation, flow velocity and depth, and the presence of debris, on hydrodynamic forces on bridges under steady flow and wave loading conditions. Scaled modeling was conducted for comparison with previous studies and the physical testing mentioned above. Full-scale modeling was also performed to calculate the magnitude of hydrodynamic forces on typical TxDOT bridges for use in structural analysis.

Finite element (FE) models for single-span TxDOT bridges with typical I-girders, box beams, and slab beams were developed using ANSYS. Results from the CFD analyses were used to conduct a structural analysis of each bridge geometry to determine whether current shear key details are adequate, or if modified details are warranted. Specifically, the drag force obtained from CFD analysis was compared with the interface shear strength of the shear key or earwall, which was estimated according to the shear-friction equations in 2020 AASHTO LRFD Specifications. It was

found from this study that the drag force can be much greater than the capacity of the shear key or earwall especially for the cases with a Froude number of 0.9. Debris also considerably increases the drag forces. For the cases where the interface shear strength is not sufficient, several approaches are recommended to increase the interface shear capacity: (1) increase the size and/or quantity of the interface shear reinforcement, (2) increase the quantity of the shear keys, and (3) increase the length of the bent cap hence the length of the earwall.

1 INTRODUCTION

1.1 Background and Problem Statement

Bridges are designed to withstand flood and debris loads; however, it is reported that hydraulic events, including floods, scour, debris, and drifts, cause 53% of bridge failures in the United States (Wardhana and Hadipriono, 2003). When a bridge fails, it loses total or partial serviceability, causing fatalities, delays in emergency transportation and evacuation efforts, and economic losses. During the 2015 Memorial Day floods, the RM 165 two-lane bridge over the Blanco River, Texas, was completely washed out, and another bridge was significantly damaged. In 2018, the FM 2900 bridge over the Llano River in Kingsland, Texas, collapsed due to historic rainfall and flooding. During high flow events, bridges may become fully or partially submerged, and the flood exerts significant hydrodynamic forces on the bridge superstructure, resulting in shearing and overturning the bridge deck, which may cause bridge failure.

The AASHTO Load and Resistance Factor Design (LRFD) Bridge Design Specifications (AASHTO 2020) define forces exerted by flood and waves on bridges; however, it only addresses forces on substructures. Besides, AASHTO and other traditional methods of calculating hydrodynamic forces on bridges do not accurately estimate the flood loading, including drag and lift forces. These methods incorporate constant coefficients for drag and lift forces, while results from physical and numerical modeling of hydrodynamic forces on river-crossing bridges indicate the dependency of these coefficients on the depth of inundation, flow velocity, degree of flow blockage with debris, etc. (Jempson, 2000; Malavasi and Guadagnini, 2003; FHWA, 2009; Oudenbroek et al., 2018). The effects of hydrodynamic forces on the stability of inundated bridges were studied by the Federal Highway Administration (FHWA, 2009). This report provides guidance on predicting these forces and force coefficients on bridge deck in riverine conditions.

Most bridges in Texas are built to withstand 25- or 50-year floods, while interstate highways are designed to withstand 100-year floods. The Texas Department of Transportation Bridge Design Manual – LRFD (TxDOT 2020) requires shear keys in bridges crossing rivers and streams, based on a freeboard 100-year flood level. Even though bridge design guidelines and standards specify the use of the 100-year flood for analyzing the overtopping of modern interstate bridges receiving federal funding, many bridge failures in the United States occur during floods with return periods smaller than 100 years. No specific design guideline is available for bridges that only pass floods with return periods smaller than 100 years in areas with significant flow velocity and debris. The effectiveness of structural countermeasures, such as shear keys, to hydraulic failure of bridges is unknown.

1.2 Objectives and Scope

The objectives of this study were as follows.

- Identify bridges that have the potential to become inundated during high-velocity flow events and use this information to characterize the velocity and flood levels to design scale flume tests.
- Conduct scale flume tests to determine flood force effects on superstructures and substructures, using typical TxDOT bridge details.
- Perform structural analyses to determine if shear key details are adequate or whether additional countermeasures are warranted.

This study mainly focused on bridge superstructures with TxGirder, Box Beam, and Slab Beam. However, experimental studies on a scale model of a full bridge structure were also performed. The scale model consisted of the bridge deck system, railing, piers, bent cap, and bearing.

1.3 Research Plan

The following five major tasks were performed to accomplish the objectives of this research study.

Task 1: Project Management

This task included documenting findings from this project, submitting monthly progress reports, attending project progress meetings as scheduled by TxDOT, and determining the project's Value of Research (VoR). The benefits of reducing the risk of bridge failures due to hydraulic events by implementing recommended countermeasures by this research are presented in Appendix A. These benefits are quantified for both future and existing bridges. The areas that the state and TxDOT benefit from the results of this study are discussed in this appendix. The benefit areas include level of knowledge, system reliability, increased service life, traffic and congestion reduction, reduced construction, operation and maintenance cost, and infrastructure condition.

Task 2: Review Design Standards, Policies, Guidelines, and Research Studies on Hydrodynamic Forces on Bridges and Structural Countermeasures

The research team performed a comprehensive review of previous studies related to the physical and numerical modeling of hydrodynamic forces of bridges due to flood and storm surges. The TxDOT's and 47 States Department of Transportation's (DOTs) design standards and measures to counteract flood loading and restrain the lateral movement of superstructures are also reviewed. The result of this review is summarized in Chapter 2.

Task 3: Identifying Bridges with Potential Inundation in High Velocity Flow Events

The hydraulic and hydrodynamic parameters of 908 stream-crossing bridges in Texas were collected from various sources. These parameters included flow and stream information, such as design flood magnitude and frequency, flow velocity, submergence ratio, deck clearance, and storm surge parameters (for bridges vulnerable to coastal storms). The bridges considered in the analysis were primarily located in Travis County and Harris County, Texas, where detailed, publicly available hydraulic models have been developed for many watersheds. This information was used in designing physical and numerical models of bridge structures. A summary of findings in this task is presented in Chapter 3.

Task 4: Conduct Scale Modeling to Determine Hydrodynamic Forces on Bridges Using Typical TxDOT Bridge Details

Physical model studies of typical TxDOT bridge details were performed in a laboratory flume to provide information on the effects of flood forces on superstructures and substructures. The physical model study included evaluating forces on the TxGirder, Box Beam, and Slab Beam superstructures without and with substructures. The performance of 1:50 scale bridge models with different deck system shapes was examined under different flow conditions, deck orientation, and debris accumulation. Selected bridge structures were also tested under wave action. The effects of waves on vertical and horizontal forces were assessed under different wave conditions. The experiments evaluated the general response of the drag, lift and moment coefficients to bridge geometry (deck type, deck width, skewness), flow condition (inundation ratio, Froude number), flow blockage by debris and substructures, and wave loading. Design charts and equations are developed for each bridge deck type. The results of all bridge deck types were combined to develop universal design charts and equations for all bridge deck geometries. The results provide calibration data for the computational fluid dynamic (CFD) models undertaken for the project in Task 5. The results of physical modeling are discussed in Chapter 4.

Task 5: Perform Structural Analysis to Assess the Performance of Flood Force Countermeasures

This task included two activities: 1) computational fluid dynamics (CFD) modeling and 2) finite element (FE) modeling and structural analysis. The CFD modeling was conducted to examine the hydrodynamic forces on typical TxDOT bridge decks. More than 1,000 numerical simulations were performed to thoroughly examine the effects of a range of parameters, including bridge geometry and orientation, flow velocity and depth, and the presence of debris, on hydrodynamic forces on bridges under steady flow and wave loading conditions. Scaled modeling was conducted for comparison with previous studies and physical testing conducted in Task 4. Full-scale modeling was also performed to calculate the magnitude of hydrodynamic forces on typical TxDOT bridges for use in structural analysis. The CFD modeling results are presented in Chapter 5.

The FE models of single-span TxDOT bridges with typical I-girders, box beams, and slab beams were developed using ANSYS. The developed models were used for CFD analysis to find the drag force on shear keys/earwalls for different flow conditions. The CFD analyses were then used to conduct a structural analysis of each bridge geometry to determine whether current shear key details are adequate, or if modified details are warranted. The drag force obtained from the CFD analysis was compared with the interface shear strength of the shear key or earwall, which was estimated according to the shear-friction equations in 2020 AASHTO LRFD Specifications. It was found that the drag force can be much greater than the capacity of the shear key or earwall, especially for flood scenarios with a Froude number of 0.9. Debris accumulation also considerably increases the drag force. For the cases where the interface shear strength is not sufficient, several approaches are recommended to increase the interface shear capacity. The results from the structural analysis and recommended countermeasure are described in Chapter 6.

1.4 Report Outline

Chapter 1 provides an introduction to the research project. Chapter 2 documents the literature review. Chapter 3 summarizes the magnitude of potential hydraulic and hydrodynamic forces on bridges in riverine and coastal areas in Texas. The information obtained from physical modeling is presented in Chapter 4. Chapters 5 and 6 present the results of computational fluid dynamics modeling and summarize the results of subsequent FE modeling and structural analysis, respectively. Chapter 7 outlines the summary of the project, along with conclusions, and provides design recommendations for bridges subject to hydrodynamic loading during flood events. Additional details of this study are documented in Appendices A to E.

2 LITERATURE REVIEW OF BRIDGES HYDRODYNAMIC FORCES AND STRUCTURAL COUNTERMEASURES

2.1 Introduction

Bridge design and construction significantly impact the economy of highway design, safety of transportation, and the stream flow regime and environment. Bridges are designed to withstand flood and debris loads; however, it is reported that 53% of bridge failures in the United States are caused by hydraulic events, including floods, scour, debris, drifts, etc. (Wardhana and Hadipriono, 2003). During high flow events, bridges may become fully or partially submerged, and flood exerts significant hydrodynamic forces on bridges, resulting in shearing and overturning the bridge deck, which may cause bridge failure. The effects of hydrodynamic forces on the stability of inundated bridges were studied by the Federal Highway Administration (Kerenyi et al., 2009), and they provided guidance on predicting these forces on bridge superstructures in riverine conditions. The Texas Department of Transportation (TxDOT) issued a design policy for mitigating flood forces that requires shear keys in bridges crossing rivers and streams, based on a freeboard 100-year flood level (TxDOT, 2020). Even though the guidelines specify the use of the 100-year flood for analyzing the overtopping of modern interstate bridges receiving federal funding (Kerenyi et al., 2009), more than 65% of bridge failures in the United States occur during floods with return periods smaller than 100 years. Most bridges in Texas are built to withstand 25- or 50-year floods, while interstate highways are designed to withstand 100-year floods. Since the design guidelines developed by the FHWA (2009) do not apply to bridges that only pass 25-year and 50-year floods in areas with significant stream velocity and debris, accurate estimates of the hydrodynamic forces on such stream crossings appear imperative. The main objective of this research project is to develop bridge design standards for hydrodynamic forces and provisions for connections between bridge superstructures and substructures, and to resist flood loading and storm surges. The current literature review was conducted to assist with developing these design standards.

2.2 History of Bridge Failure and Causes in the United States

2.2.1 History of Bridge Failures in the United States

Stream-crossing bridges are crucial elements of road infrastructures. Natural hazards, such as flood water, are responsible for damages to bridges. Over the past 40 years, numerous bridges have been damaged by flooding and other factors in the U.S. and worldwide (Lee et al., 2013). Wardhana and Hadipriono (2003) conducted an investigation on bridge failures in the U.S. and found that 503 bridges of various types failed between 1989 and 2000. Taricska (2014) reported a total of 329 bridge failures in the U.S. from 2000 to 2012. Figure 2.1 presents the number of bridge failures between 1989 and 2012.

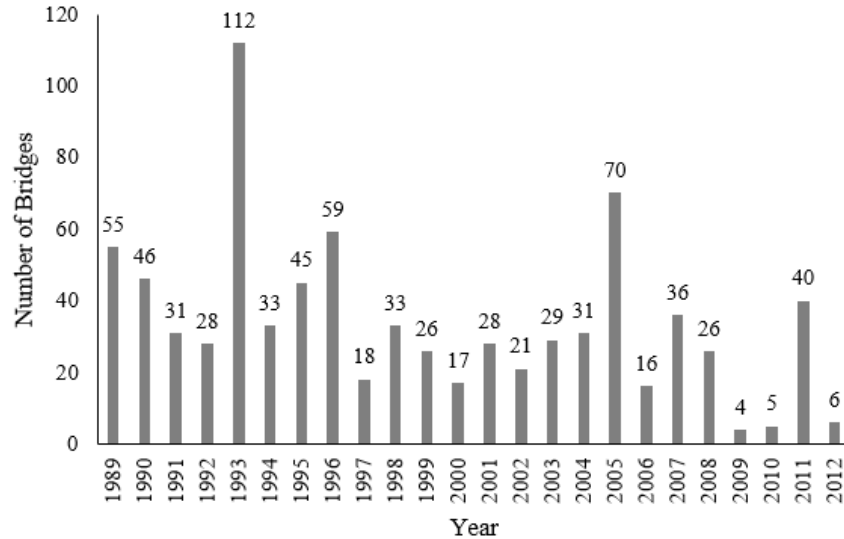


Figure 2.1 Number of bridge failures in the U.S. from 1989 to 2012 (1989-2000 data from Wardhana and Hadipriono, 2003; and 2000-2012 data from Taricska, 2014)

As illustrated in Figure 2.1, the highest number of bridge failures between 1989 and 2012 was recorded in 1993 and was attributed to the occurrence of a major flood in the Midwest (Wardhana and Hadipriono, 2003). The second highest number of bridge failures was in 2005. A study performed by the Hurricane Research Division (HRD) of the Atlantic Oceanographic and Meteorological Laboratory indicated that in 2005, the number of storms and hurricanes events was the highest recorded from 1900 to 2018, which might have contributed to the highest number of bridge failures (Landsea, 2016). Earthquakes and floods were attributed to a high number of bridge failures in 1989 and 1996, respectively (Wardhana and Hadipriono, 2003). A list of major bridge failures in the U.S. between 1987 and 2018 is presented in Table 2.1.

Table 2.1 Examples of bridges damaged by flood events in the U.S. between 1987 and 2018

Bridge Name	Causes of Damage	Year	Reference
Schohaire Creek Bridge, New York	Snowmelt combined with heavy rainfall	1987	Storey et al., 2003
Hatchie Bridge, Tennessee	Moving streambank and scour below the footing	1989	Zevenbergen et al., 2012
Harrison Road Bridge, Ohio	Debris accumulation	1989	Diehl, 1997
Walnut Street Bridge, Pennsylvania	Scour due to flooding	1996	Lee and Sternberg, 2008
I-10 Twin Span Bridge, Louisiana	Storm surges	2005	Chen et al., 2005
I-88 Bridge, New York	Heavy rainfall	2006	Meegoda et al., 2009
RM 165 bridge and Fisher Store Road Bridge, Texas	Flash flood	2015	Fechter, 2015
FM 2900 Bridge, Texas	Catastrophic flooding	2018	Byrne, 2019

2.2.2 Causes of Bridge Failure

Bridges are becoming more prone to failure due to the increased frequency of flood events, and the resultant hydrodynamic loadings generated from flood forces on structures (Cook et al., 2015). Lee et al. (2013) investigated the causes of bridge failure during the time frame of 1980-2012, and their findings were similar to those of Wardhana and Hadipriono (2003) and Taricska (2014). Floods and scour were reported as the cause of 47% of bridge failures, and collisions and overloads were the cause of 15% and 13% of bridge failures, respectively (Figure 2.2).

Different types of bridges are vulnerable and sensitive to different causes of failure (Table 2.2). The structural stability of bridge superstructures depends on the bridge type. The design details and age of a bridge also play important roles in a bridge's failure.

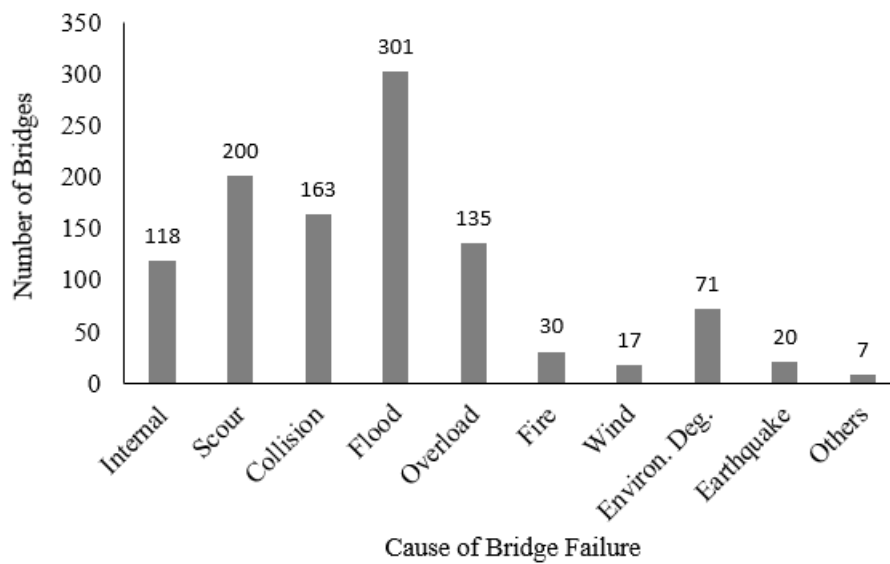


Figure 2.2 Number of failed Bridges and causes of failure from 1980-2012 (Lee et al., 2013)

Table 2.2 Most common causes of the collapse of different types of bridges (Deng et al., 2016)

Types of Bridge	Most Vulnerable Causes
Beam bridge	Flood, scour, earthquake, collision, overloading
Masonry arch bridge	Flood, scour, overloading, earthquake
Steel arch bridge	Overloading, wind
Steel truss bridge	Overloading, fatigue
Flexible long-span bridge	Wind

2.3 Flood Forces

2.3.1 Definitions of Flood Forces and Flow Parameters

An accurate estimation of hydrodynamic forces on a bridge superstructure is vital to assessing its vulnerability to flooding. Stream-crossing bridges experience hydrostatic, buoyant, and hydrodynamic forces. Hydrostatic force (F_h) is caused by the difference in the water levels of upstream and downstream sides of an inundated bridge; buoyant force (F_B) is equal to the weight of water displaced by submerged bridge elements. Hydrodynamic forces include drag force (F_D), which is created by the pressure of the flowing water in the flow direction, and lift force (F_L) which is produced by the pressure of the flowing water in the normal direction of the flow. Bridges may also experience overturning moments (M_{cg}) that are created by uneven forces applied on a bridge, as schematically shown in Figure 2.3. Equations 2.1 to 2.5 are used to calculate the forces and overturning moments.

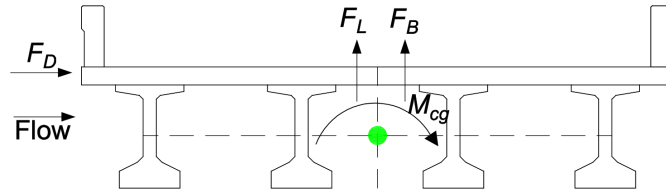


Figure 2.3 Schematic of forces and overturning moment applied on stream-crossing bridges

$$F_R = \frac{1}{2} \rho_w g h A \quad (\text{hydrostatic force}) \quad (2.1)$$

$$F_B = \rho_w g \Psi \quad (\text{buoyant force}) \quad (2.2)$$

$$F_D = \frac{1}{2} \rho_w C_D A_D V^2 \quad (\text{drag force}) \quad (2.3)$$

$$F_L = \frac{1}{2} \rho_w C_L A_L V^2 \quad (\text{lift force}) \quad (2.4)$$

$$M_{cg} = \frac{1}{2} \rho_w C_M L W^2 V^2 \quad (\text{overturning moment}) \quad (2.5)$$

In these equations, ρ_w is water density, g is gravitational acceleration, h is the depth of the water, A is the projected area of the submerged portion of the bridge, A_D is the projected area of the submerged object upon which drag force is exerted and normal to the flow, A_L is the projected area of the submerged object on which the lift force acts and parallel to the flow, Ψ is the volume of bridge elements submerged, and V is the depth-averaged approach flow velocity. L and W are the bridge length and width, respectively. C_D , C_L , and C_M are drag force, lift force, and moment coefficients.

The coefficients of hydrodynamic forces and overturning moments are essential information for designing bridges under flood forces. They are usually parameterized as a function of inundation

ratio (h^*), proximity ratio (Pr), and Froude number (Fr). A schematic representation of these parameters is illustrated in Figure 2.4.

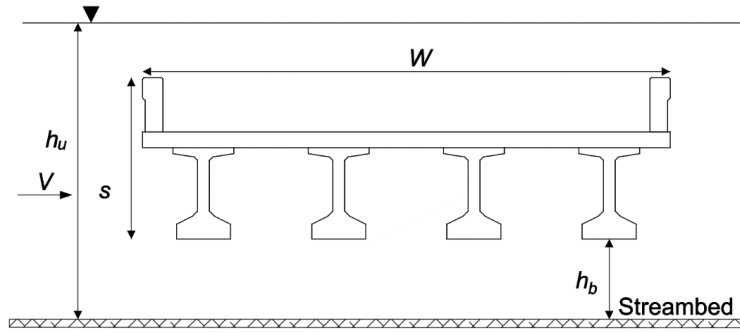


Figure 2.4 Schematic diagram of a fully submerged bridge deck

The inundation ratio (h^*) is defined as the water depth measured from the low chord of a bridge girder ($h_u - h_b$) to the height of a bridge superstructure (s) and is expressed as

$$h^* = \frac{h_u - h_b}{s} \quad (2.6)$$

The proximity ratio (Pr) is defined as the ratio of the distance of a bridge low chord from the channel bottom (h_b) to the height of a bridge superstructure (s) and is expressed as

$$Pr = \frac{h_b}{s} \quad (2.7)$$

In Equations 2.6 and 2.7, s is the superstructure height, h_b is the distance from the streambed to the low chord of girders, and h_u is the upstream flow depth.

The blockage ratio B_r is defined as

$$B_r = \frac{A_b}{A_b + A_c} \quad (2.8)$$

where A_b is the flow area blocked by debris in the contracted bridge section, and A_c is the unobstructed cross-sectional area in the contracted bridge section.

The Froude number (Fr) is defined as the ratio of the inertia force and gravity force and is expressed as

$$Fr = \frac{V}{\sqrt{gh_u}} \quad (2.9)$$

2.3.2 Bridge Design Standard for Calculating Flood Forces

The bridge design standards of different countries were reviewed, and a summary of the major standards used for calculating hydrodynamic loads on bridge superstructures is presented in Table 2.3. In general, every design standard considers the same types of forces on bridges that result from water. It should be noted that only the relevant parts of each standard are presented here.

The U.S. Federal Highway Administration (Kerenyi et al., 2009) specifies drag, lift, and moment coefficients for bridge decks of various shapes. The coefficients vary as a function of bridge decks' relative submergence. The Australian Bridge Design Standard AS 5100 (2004) specifies lift coefficient for bridge deck as a function of relative submergence, whereas the drag coefficient is dependent on relative submergence and proximity ratio. The Eurocode (EN 1991-1-6, 2005) identifies the horizontal force exerted by the flow on a deck or pier by a drag equation, with the constant drag coefficient dependent on the cross-sectional shape (1.44 for rectangular and 0.7 for circular). The Japanese Bridge Design Standard (JRA-2002) considers the calculation of hydrodynamic pressure force, drag force, and hydrostatic pressure. The Indian Bridge Design Standard (IRC-2016) considers only the calculation of horizontal force and buoyancy due to water current.

2.4 Experimental and Numerical Modeling of Inundated Bridges

Numerous authors have investigated the hydrodynamic forces that are exerted on partially or fully submerged bridges. Because of the complex behavior of hydrodynamic forces, they are studied by constructing physical models in the laboratory and performing numerical simulations. The studies that have been conducted in the past 40 years are grouped into experimental and numerical models and listed in Table 2.4.

Table 2.3 Bridge design standard for calculating flood forces

Standard	Hydrostatic Pressure (P_h)	Hydrodynamic Pressure (P)	Lateral Hydrodynamic Pressure (p)	Buoyant Force (F_B)	Drag Force (F_D)	Lift Force (F_L)	Debris Impact (F_{deb})	Note
American Bridge Standard (AASHTO, 2017)	wh	$\frac{C_D V^2}{1000}$	$\frac{C_L V^2}{1000}$	$\sum p_y$	$\frac{C_D V^2}{1000} A$	-	$\frac{0.5wV^2}{2g}$	V : water velocity (ft/s), P_h : pressure of flowing water (ksf), C_D : drag coefficient, p: lateral pressure (ksf), C_L : lateral drag coefficient, A: projected surface area, w: specific weight of water (kcf), h : water depth, p_y : vertical static pressure.
Australian Bridge Standard (AS5100.2-2004)	-	-	-	-	$0.5C_d V^2 A_d$	$0.5C_L V^2 A_L$	$0.5C_d V^2 A_{deb}$	V : mean velocity of the water (m/s), A_d : wetted area of the superstructure (m ²), C_L : lift coefficient, C_m : moment coefficient, A_L : projected area normal to flow direction, C_d : drag coefficient, and A_{deb} : projected area of the debris mat (m ²).
Eurocode (EN 1991-1-6, 2005)	-	-	-	-	$\frac{1}{2} k \rho_{wa} h b v_w^2$	-	$k_{deb} A_{deb} v_{wa}^2$	v_{wa} : Mean speed of the water (m/s), ρ_{wa} : density of water, (kg/m ³), h : water depth, b : object width, k : shape factor, k_{deb} : debris density parameter (kg/m ²), and A_{deb} : area of obstruction presented by debris (m ²).
Indian Bridge Design Standard (IRC: 6-2016)	-	$52KV^2$	-	-	-	-	-	V : velocity of the current at the point where the pressure is calculated, and K : constant for piers shapes,
Japanese Bridge Standard (JRA - 2002)	-	-	-	-	$\frac{1}{2} \rho_w C_d v_w^2 A_s$	$\frac{1}{2} \rho_w C_L v_w^2 A_t$	-	v_w : flow velocity (m/s), A_s : projected area of the deck subjected to drag force (m ²), A_t : projected area of a deck subjected to lift force, C_d : drag coefficient, and ρ_w : density of water.

Table 2.4 Examples of experimental and numerical studies of flood forces on bridges performed in the past 40 years

Author(s)	Type of study	Study Objectives	Focus Parameters	Findings
Roberts et al. (1983)	Experimental	To estimate drag and uplift forces exerted on bridge deck subjected to overtopping during flood	Submergence ratio, Froude number	Results indicated that the coefficient of drag values used in the Australian and Indian codes prior to this study might have been low. An approach was identified to provide designers with more realistic data for optimizing low level bridge crossings.
Naudascher et al. (1983)	Experimental	To theoretically and experimentally determine hydrodynamic forces acting on a bridge and force coefficients	Geometric parameters, Froude number, flow angle	It was found that the peak loading on a submerged bridge occurs due to wave motion between girders induced by flow instability and vortex formation.
Jempson (2000)	Experimental	To assess the effect of Froude number, degree of submergence, and proximity ratio on hydrodynamic forces and moments.	Froude number (Fr), degree of submergence (S_R), effect of debris, proximity of the superstructure (P_r), and moments	Drag, lift and moment coefficients were found to be dependent on Fr , P_r , and S_R , and under some conditions, an inter-dependence existed between the coefficients.
Malavasi & Guadagnini (2003)	Experimental	To estimate hydrodynamic loading on partially or fully submerged bridges	Froude number and inundation ratio	Results indicated that the presence of the free surface and bottom boundary caused drag and lift forces different from what would be expected from an identical geometry in an unbounded flow situation.
Malavasi et al. (2008)	Numerical	To investigate the proximity effects of a solid wall on the wake flow of a rectangular cylinder	Aspect ratio, proximity ratio	Model results indicated that the drag and lift coefficients increased as the gap ratio (distance between the cylinder bottom face and the bottom wall) decreased.
Kerenyi et al. (2009)	Experimental and Numerical	To calculate hydrodynamic forces under different flow conditions, inundation ratio, and bridge types	Inundation ratio (h^*), Froude number	The results indicated that lift and moment coefficients increased overall and reached their critical values in partially-inundated to completely-inundated zone ($h^*=1$), though drag coefficient was reduced in this zone. The

Fr and bridge deck types also influenced the force and moment coefficient values.

Patil et al. (2009)	Numerical	To compare and validate the drag and lift coefficients with experimental data	Froude number, submergence ratio	The results indicated that the transient VOF (Volume of Fluid) free-surface simulations were much more unstable than usual steady-state single phase simulations, and simulation results also strongly depended on the turbulence models used.
Guo et al. (2010)	Numerical and Experimental	To establish a validated computational practice to address research needs in bridge hydraulics	Velocity, pressure and shear stress distribution	The results of this study provide a tool for designing new and retrofitting existing bridges so that they are able to withstand the forces and moments that may result from partial or complete inundation.
Arsalan et al. (2013)	Numerical and Experimental	To study the flow field around a partially submerged rectangular cylinder	Submergence ratio, Reynolds number	The findings indicated that the flow separation and reattachment underneath the cylinder and the vortex formation in the wake area were highly related to the submergence ratio and the turbulence intensity in the approaching flow.
Chu et al. (2016)	Numerical	To investigate the effect of a submerged rectangular cylinder on the hydrodynamics of free surface flow	Reynolds number, Froude number, and blockage ratio	The results indicate that the drag and lift coefficient is dependent on the deck's Froude number and blockage ratio of the bridge deck, rather than the Reynolds number.
Oudenbroek (2018)	Experimental	To determine design values for hydrodynamic loading on bridge superstructures	Relative submergence, proximity ratios, debris	Results indicated that the resistance against the horizontal movement of a bridge deck increases as Fr increases. Fr also increases the overall magnitude of the drag and negative lift forces. It was also shown that standalone piers always have strong resistance against overturning with no debris force. However, with the presence of debris force, the pier breaks down and can cause overturn of the deck over a pier.

Nasim et al., (2019)	Numerical	To investigate the flood effect on bridge piers using the finite volume method	Pressure distribution, velocity variation	Results indicate that the shape of the pier cross-section has a significant effect on the fluid pressure exerted on bridge piers under flooding. The results also indicate that the AS5100 (Standards Australia, 2004) method is not conservative for estimating pressure distribution on circular piers.
Dráb et al. (2019)	Experimental	To determine drag, lift, and moment coefficients.	Bridge deck shape	The results confirmed that the deck shape has a significant influence on the drag coefficients. The results also showed that the lowest values of the drag coefficients were obtained by the bridge deck shape with chamfered edges.
Thai (2019)	Numerical	To numerically investigate turbulent flow with high Reynolds number over fully submerged bridge deck with various length-to-thickness ratio	Blockage ratio, submergence ratio, aspect ratio	Effect of the aspect ratio on the flow behavior and drag coefficient was investigated. The results indicated that as the aspect ratio of bridge deck decreases, the water level decreases more abruptly downstream.

2.5 Design Charts for Hydrodynamic Forces

The following section discusses the design charts and tables for hydrodynamic force coefficients developed in previous studies. The coefficients include drag, lift, and overturning moment.

2.5.1 Drag Coefficient

The drag coefficient is a function of the shape of the bridge pier or deck, and the skew of their axis versus the flow direction. The AASHTO-LRFD Bridge Design Specifications (AASHTO, 2017) recommend drag coefficient values between 0.7 and 1.4 for piers with different shapes; however, the drag force on bridge decks is not discussed in the document. A study was performed by FHWA to provide guidance on evaluating the stream forces acting on inundated bridge superstructures (Kerenyi et al., 2009). In this study, drag coefficients for a three-girder, six-girder, and streamlined bridge decks were estimated from physical experiments and numerical modeling. This study showed that the drag coefficient significantly changes with the degree of inundation, especially when the bridge is transitioning from being partially inundated to completely inundated (Figure 2.5).

The effect of debris on drag force was studied using physical modeling by the National Cooperative Highway Research Program (NCHRP, 2000). A series of envelope curves and tables are provided for assessing the drag coefficient for debris on piers and superstructures as a function of the amount of blockage caused by debris and Froude number in the contracted section of the bridge (Figure 2.6a). The Australian Bridge Design Standards AS5100 (Standards Australia, 2004) also provide graphs of drag coefficients for bridge piers and superstructures with proximity ratios between 1.5 to 10 (Figure 2.6b). This figure indicates that drag coefficients decrease as the velocity and proximity ratio increases.

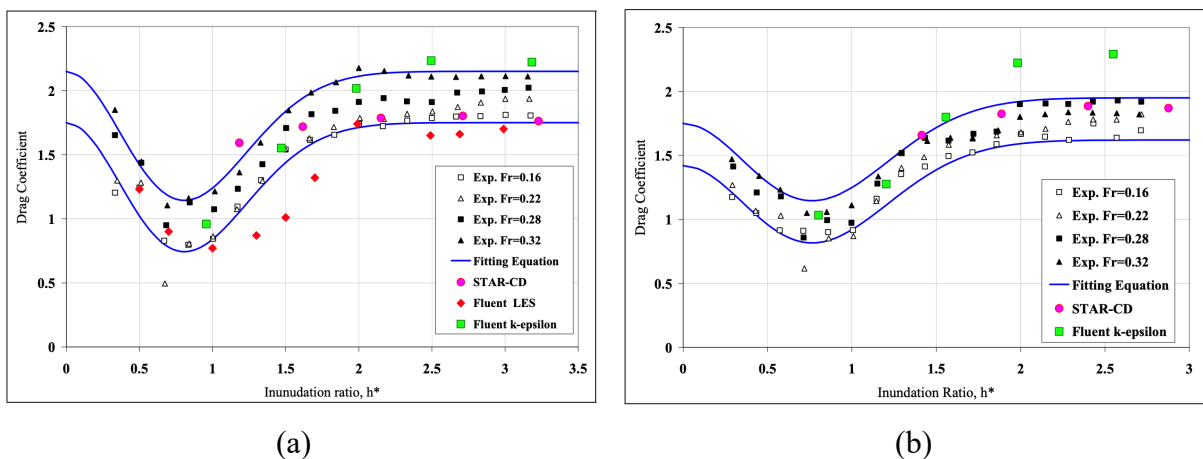
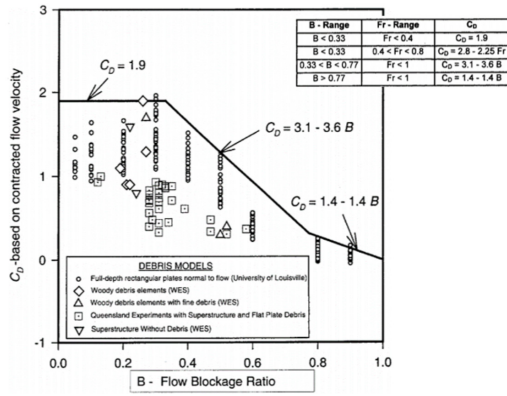
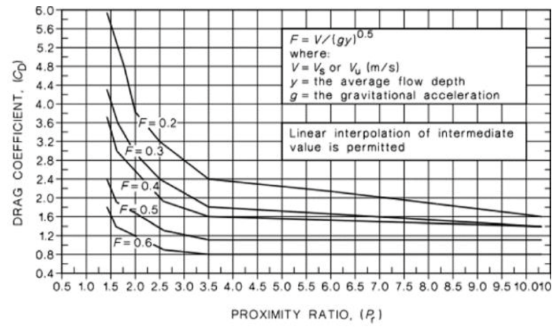


Figure 2.5 Drag coefficient vs inundation ratio for: (a) six-girder bridge and (b) three-girder bridge (Kerenyi et al., 2009)



(a)

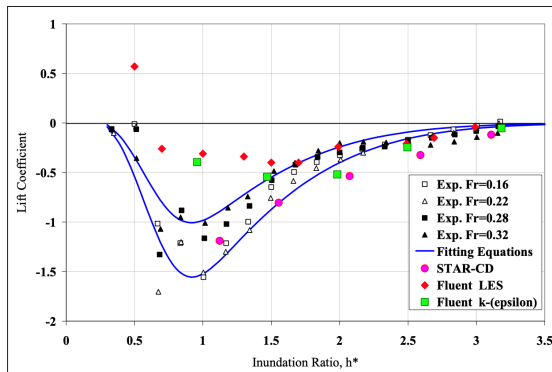


(b)

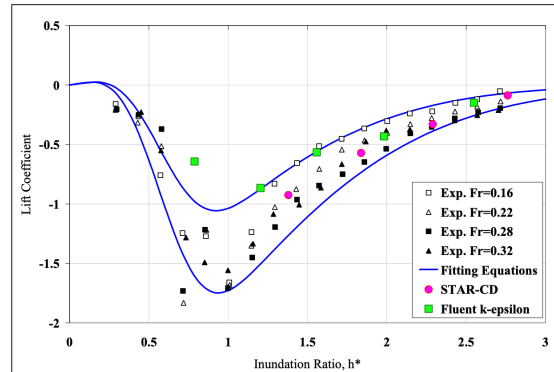
Figure 2.6 Drag coefficient vs flow parameters: (a) drag coefficient for a bridge superstructure with debris (Parola et al., 2000) and (b) drag coefficient vs proximity ratio (Standard Australia, 2000)

2.5.2 Lift Coefficient

The lift force and lift coefficient are not addressed in the AASHTO-LRFD Bridge Design Specifications (AASHTO, 2017). The FHWA study provides design values for the lift coefficient for three types of bridge decks that are mentioned above (Kerenyi et al., 2009). Figure 2.7 shows how the lift coefficient changes with the inundation ratio and Froude number for a six-girder and three-girder bridge deck.



(a)



(b)

Figure 2.7 Lift coefficient vs inundation ratio for: (a) a six-girder bridge and (b) three girder bridges (Kerenyi et al., 2009)

2.5.3 Moment Coefficient

The AASHTO LRFD Bridge Design Standards do not address the overturning moment or moment coefficients due to flood force on the river crossing bridges. However, the study performed by FHWA (Kerenyi et al., 2009) established a relationship between the moment coefficient and the inundation ratio, where inundation ration (h^*) is dependent on the Froude number (Fr). Figure 2.8 shows that the peak moment coefficient occurred when the bridge was roughly halfway inundated. At a higher Fr , the moment coefficient decreased. Additionally, in the 1.5 – 2.0 range for h^* , the

moment coefficient became negative and then stabilized for the $Fr = 0.28$ and $Fr = 0.32$, which meant the bridge would rotate in the clockwise direction.

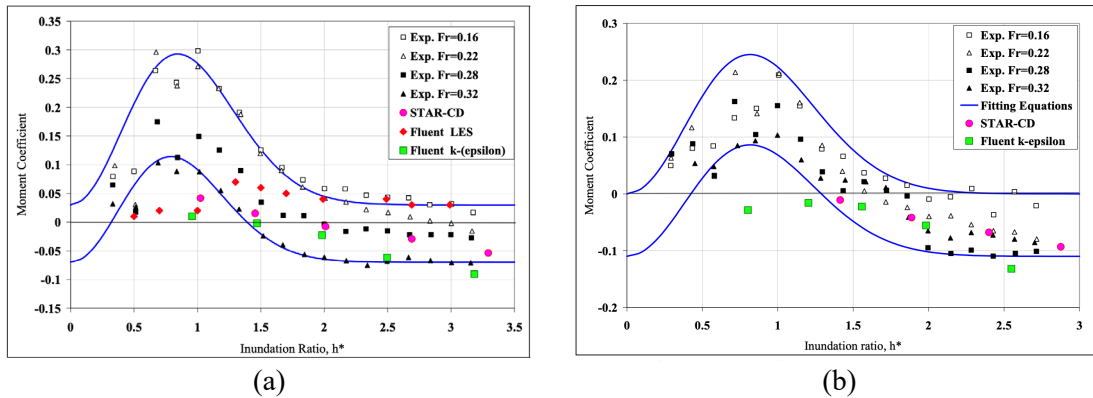


Figure 2.8 Moment coefficient vs inundation ratio for: (a) six-girder bridge and (b) three girder bridges (Kerenyi et al., 2009)

2.6 Structural Design and Countermeasures to Hydrodynamic Loading

There are very few studies and design standards on methods and countermeasures that can be utilized by designers to ensure adequate bridge performance under hydrodynamic loading. The following section discusses the countermeasure techniques adopted by several studies.

The strategies of maintaining bridge stability against storm surges are discussed in AASHTO (2017) and include force mitigation and force accommodation. The force mitigation measures include increasing vertical clearance, preferably over 11.8 in (0.3 m) above the 100-year event wave crest line; using open or sacrificial parapets; venting air-trapping cells; using diaphragms with large openings; using continuous spans; and using solid or voided slab bridges to reduce buoyancy forces.

Zhang et al. (2012) used physical models to investigate the effects of installing a fairing on the upstream side of bridge superstructures to increase the stability of bridges vulnerable to storm surges (Figure 2.9). Results from this study showed the effectiveness of these countermeasures in reducing the risk of bridge failure due to hydrodynamic forces.

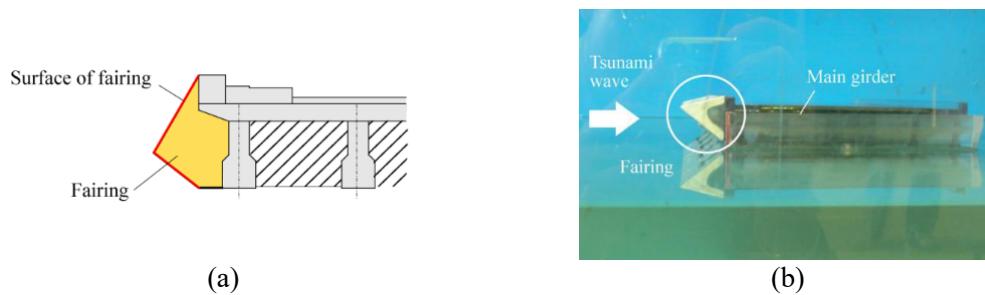


Figure 2.9 Countermeasures for bridges under storm surges: (a) schematic of the superstructure installed with fairing and (b) bridge physical model with fairing (Zhang et al., 2012)

Chen et al. (2005) showed the effectiveness of shear keys on the I-10 twin bridge in New Orleans, Louisiana during Hurricane Katrina. As shown in Figure 2.10, the railway bridge consists of solid slabs and supporting piers that make it difficult to trap air beneath the slabs to reduce the effective gravity loads. Therefore, the bridge spans were unlikely to float during the hurricane. Due to the presence of shear keys at both ends of the cap beams, there was no evidence of dislocation of the bridge segment.



Figure 2.10 Railway bridge adjacent to the I-10 twin span bridge between New Orleans and Slidell (Chen et al., 2005)

Bozorgnia (2012) evaluated two retrofitting options for reducing hydrodynamic forces applied on bridge superstructures due to entrapped air between bridge girders and diaphragm. These options include a 2-in (5-cm) air vent in the bridge deck, and an air vent in the bridge diaphragms (Figure 2.11). It was observed that water filled up the cavities between the bridge girders and diaphragm of a retrofitted bridge more than it did for an un-retrofitted bridge, significantly reducing the buoyant forces applied to the bridge superstructure. These retrofitting options for reducing hydrodynamic forces applied to bridge superstructures are effective and inexpensive.

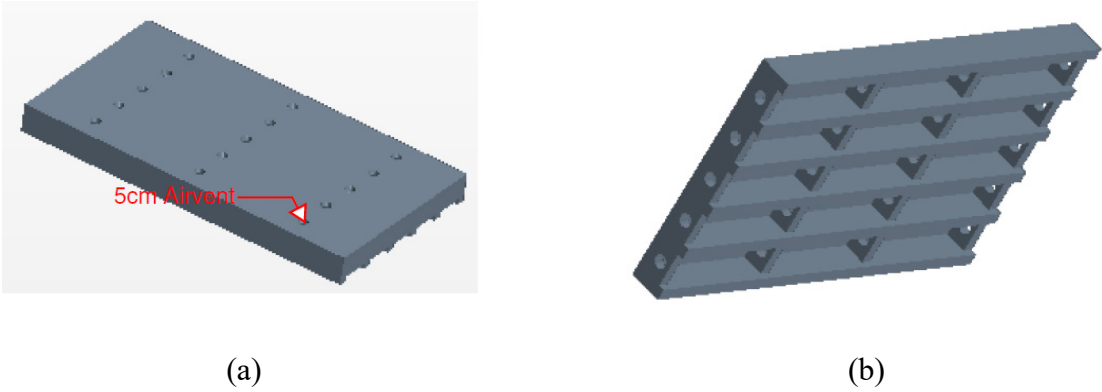


Figure 2.11 Retrofitting options for coastal bridges recommended by AASHTO guidelines: (a) air vents in the bridge deck and (b) air vents in the bridge diaphragm (Bozorgnia, 2012)

Oudenbroek et al. (2018) studied the effects of installing fairing on bridges under flood loading, using CFD modeling (Figure 2.12). They stated that the failures of both deck and piers could be prevented by strengthening the pier-deck connections or by streamlining the bridge deck. It means that one effective countermeasure to hydrodynamic failure of both deck and piers is a robust connection between these units. In their study, the effectiveness of the end caps on the leading and trailing edges of the deck was investigated as a countermeasure to deck failure. The researchers found that the end caps reduced the deck drag coefficient by shifting the deck away from a blunt body flow regime to a more streamlined regime, and further played a practical role by functioning as bicycle or pedestrian lanes atop the deck. Six types of end caps were considered in the study to increase the stability of the bridge deck (Figure 2.12). Attaching six different shapes of wings under different inundation ratios and Froude numbers indicated that a rational shape of the wings could significantly alter the flow pattern around the deck and postpone occurrence of failure during conditions of really high-water levels ($h^* > 2.5$) and high flood velocity with $Fr > 2.5$. The researchers also found that T-girder decks are more stable than box girder decks because the T-girders are less blunt and experience less buoyancy.

All the countermeasures discussed above could be effective for reducing the hydrodynamic force induced by floods. However, the mitigation of flood forces is strongly dependent on the geometry of the fairing, and a fairing with unsuitable geometry might enlarge the flood force adversely (Zhang et al., 2012).

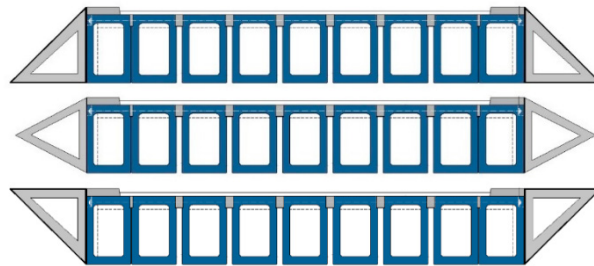


Figure 2.12 Schematic of deck fairing countermeasure (Oudenbroek et al., 2018)

2.7 DOT’s Design Standards and Countermeasures to Hydrodynamic Forces

2.7.1 TxDOT’s Design Standards and Countermeasures

To counteract flood loading and restrain the lateral movement of superstructures, the TxDOT Bridge Design Manual-LRFD (TxDOT Bridge Design Manual, 2020) requires incorporating shear keys or earwalls on abutments and bent caps of I-girder, U-beam, and spread box beam (X-beams) bridges that cross water features and meet any of the following criteria: (1) river and stream crossings if the distance between the bottom of the beam and the 100-year high water level is less than 4 feet, (2) tide-influenced bridges.

The shear key is placed on the upstream side of a bridge between the outside girder and the next adjacent girder (TxDOT Bridge Design Manual, 2020). Figure 2.13a schematically shows the TxDOT I-girder shear key (IGSK) on an interior bent with no skew. In the case of slab beam and box beam bridges, lateral restraint is provided by earwalls on the bent cap as shown in Figure 2.13b. The details of shear key and earwalls design are discussed in Chapter 6.

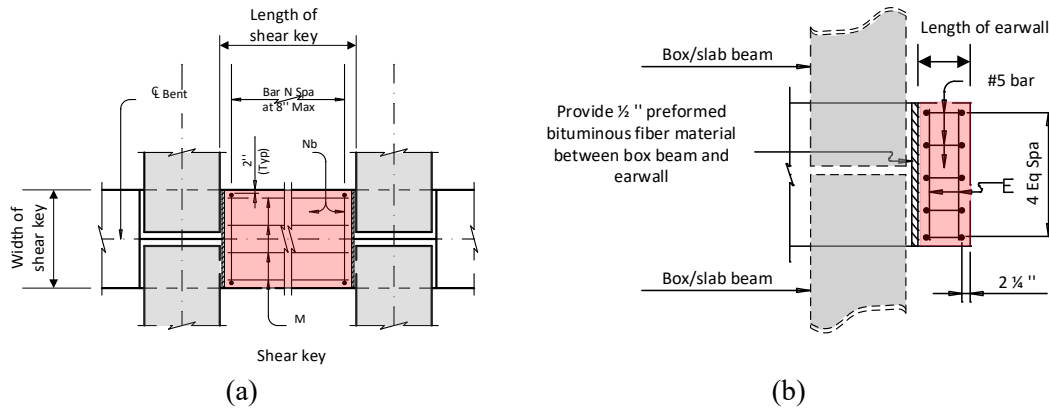


Figure 2.13 Schematic of the TxDOT countermeasures: (a) shear key and (b) earwall

2.7.2 Design Standard and Countermeasures of Other DOTs

The objective of this section was to review all U.S. Department of Transportation’s (DOTs) design standards and countermeasures to hydrodynamic forces. The literature search focused on the design flood, freeboard (vertical clearances), and countermeasures to hydrodynamic forces. Appendix B presents detailed information on each of the DOT’s current bridge design standards, policies, and guidelines. The findings on flood return periods and freeboard are summarized in Table 2.5. This table shows that most of the states adopted a design flood with a return period of 50 to 500 years, although Iowa, New Hampshire, Rhode Island, Virginia, and Wisconsin design some bridges for less frequent floods (2 to 25 years). The literature search on freeboard indicated that most of the states use 1 ft minimum vertical clearance. Colorado, Louisiana, New Mexico, Utah, and Wyoming use a minimum freeboard of 2 ft, Mississippi uses 3 ft, and Wyoming uses 7 ft.

Table 2.6 presents different countermeasures proposed by DOTs to resist hydrodynamic forces, seismic loads, scour, and debris loads. The shear key is widely used to provide resistance against seismic and lateral forces (i.e., sliding, water pressure, and deck movement). The most suggested countermeasure for scour is to design the bridge foundation to withstand scour for the design flood of 100 years and check flood of 500 years. Seven DOTs recommend using riprap on the streambed near bridge piers and abutments. Adequate waterway openings and concrete floors with a cutoff wall are suggested by the Alaska and Arizona DOTs, respectively, to mitigate scour risk. Debris deflector walls and debris protectors are used by the Colorado and Wisconsin DOTs, respectively, to reduce debris loads.

Table 2.5 DOT's design flood and freeboard (vertical clearances) for bridge design

State	Flood Return Period (year)								Freeboard (ft)	
	2	5	10	25	50	100	200	500	Min	Max
Alabama					x	x	x	x	1	
Alaska						x	x		1	
Arizona					x			x	1	
Arkansas										
California					x	x	x	x	1	
Colorado						x			2	4
Connecticut					x	x	x	x	1	
Delaware						x			1	4
Florida						x			1	
Georgia					x	x	x	x	1	
Idaho					x	x	x	x	1	
Illinois					x			x	1	
Indiana					x					
Iowa	x	x	x	x	x	x	x	x	1	
Kansas										
Kentucky										
Louisiana						x			2	
Maine					x	x	x	x	1	
Massachusetts						x			1	
Michigan					x	x		x	1	
Minnesota								x	1	3
Mississippi					x	x	x	x	1	
Missouri					x	x	x	x	1	
Montana					x		x	x	1	
Nebraska					x	x	x	x		
Nevada					x	x	x	x		
New Hampshire	x	x	x	x	x	x	x	x	1	
New Jersey					x			x	1	
New Mexico					x	x		x	2	
New York					x	x		x		
North Carolina										
North Dakota					x	x	x	x	1	
Ohio								x	1	
Oklahoma					x	x	x	x	1	
Oregon				x	x	x			1	
Pennsylvania						x	x	x	1	
Rhode Island	x		x	x		x		x	1	
South Carolina				x	x	x			1	
South Dakota								x	1	
Tennessee					x			x	1	
Texas				x	x	x				
Utah					x	x	x	x	2	
Vermont					x	x	x	x	1	
Virginia	x	x	x	x	x	x		x	1	
Washington						x		x	1	
West Virginia						x		x	1	
Wisconsin	x	x	x			x			1	
Wyoming						x			2	7

Table 2.6 DOTs countermeasure to hydrodynamic and seismic forces

State	Countermeasures			
	Scour Risk	Seismic Force	Lateral Force	Debris Load
Alabama	-	-	-	-
Alaska	Adequate waterway opening	Shear key	-	-
Arizona	Concrete floor with cut-off walls	Shear key	-	-
Arkansas	-	-	-	-
California	-	Shear key	-	-
Colorado	-	-	Shear Key	Debris deflector walls
Connecticut	Riprap	-	-	-
Delaware	Riprap	-	--	-
Florida	-	-	-	-
Georgia	Foundation design	-	-	-
Hawaii	-	-	-	-
Idaho	-	-	-	-
Illinois	-	-	Shear key	-
Indiana	Riprap	-	Shear key	-
Iowa	-	-	-	-
Kansas	-	-	-	-
Kentucky	-	-	-	-
Louisiana	-	-	-	-
Maine	-	Shear key	-	-
Maryland	-	-	-	-
Massachusetts	-	-	Shear key	-
Michigan	-	-	-	-
Minnesota	-	-	-	-
Mississippi	-	-	-	-
Missouri	-	-	-	-
Montana	-	-	Shear key	-
Nebraska	Foundation design	-	-	-
Nevada	-	Shear key	-	-
New Hampshire	Foundation design	-	Shear key	-
New Jersey	Foundation design	Shear key	-	-
New Mexico	Foundation design	-	Shear key	-
New York	Foundation design	-	-	-
North Carolina	-	-	--	-
North Dakota	Riprap	-	-	-
Ohio	-	-	-	-
Oklahoma	-	-	-	-
Oregon	-	-	-	-
Pennsylvania	Riprap	-	-	-
Rhode Island	Foundation design	-	-	-
South Carolina	-	-	Shear key	-
South Dakota	Foundation design	-	-	-
Tennessee	-	-	-	-
Texas	-	-	Shear key	-
Utah	-	-	Shear key	-
Vermont	Foundation design	-	-	-
Virginia	Riprap	-	-	-
Washington	Riprap	-	Shear key	-
West Virginia	-	-	Shear key	-
Wisconsin	-	-	-	Debris protector
Wyoming	-	-	-	-

2.8 Climate Change Impact on Hydraulic Structures

In most cases, bridges are designed to withstand floods with certain return periods (e.g., 100 or 500 years). However, climate change has the potential to influence the precipitation patterns and storm frequencies, resulting in an increased frequency of storms in many locations. The DOT Center of Climate Change and Environmental Forecasting predicted that weather patterns would change as global temperatures increase (Guo et al., 2010).

Several studies discussed the critical and devastating impacts of climate change on natural ecosystems and human society (Thai, 2019; Doney et al., 2011; IPCC, 2013). A report by the U.S. Climate Change Science Program (CCSP) (2008) provided evidence of changes in weather and climate extremes such as temperature; precipitation, which includes droughts and heavy precipitation; tropical storms and cyclones; winter storms, etc. According to the IPCC AR5 (Intergovernmental Panel on Climate Change - 5th Assessment Report) (2013), the global mean temperature has increased by 0.78°C, and the sea level has risen by 7.5 inches during the past century, both of which clearly indicate climate change. This report also indicates that the rate of global mean sea-level rise during the 21st century will exceed the rate observed during the period of 1971-2010 for all representative concentration pathway (RCP) scenarios, due to increases in ocean temperatures and the loss of mass from glaciers and ice sheets. The IPCC AR5 reported a “likely range” of 17.72 to 32.28-in (0.45 to 0.82-m) for sea level projections for the 21st century (average from period of 2081 to 2100) and of 20.5 to 38.6-in (0.52 to 0.98-m) by 2100, with a rate during the period of 2081-2100 of 0.31-0.63 in/yr (8-16 mm/yr) (Church et al., 2013). This significant increase in the rise of water levels will increase extreme weather events such as storms, floods, etc.

When considering the impacts of climate change, it is important to study its effect on the transportation infrastructure, and agencies like the United States Department of Transportation (USDOT) and the Federal Highway Administration (FHWA) have conducted several such studies. Like other infrastructures, river-crossing bridges will suffer the consequences of climate change, and the design that is currently used for them may not be sufficient because previous design standards did not contemplate the climate change influence, especially in terms of precipitation intensity (Akhtar et al., 2018). Several studies have been performed to understand the effects of climate change on the transportation infrastructure. The following section discusses a summary of relevant studies.

The Iowa DOT conducted a climate change impact study on the vulnerability of bridges to an increase in peak stream flow resulting from increased precipitation, which has been predicted by 19 climate models. They analyzed six bridges in Iowa and suggested possible adaptation strategies (Takle et al., 2015).

The Connecticut DOT performed a system-level vulnerability assessment of bridges and culverts that experienced inland flooding from rainfall events. They examined 52 structures for current precipitation data and analyzed their sufficiency in design for hydraulic stability. The results indicated that 65% of the structures satisfied design criteria (Hogan et al., 2014).

The Minnesota DOT investigated the resiliency of bridges and culverts against flash flooding scenarios predicted for climate change. The river-crossing structures were investigated for three risk levels: low, medium, and high, represented by RCPs of 4.5, 6.0, and 8.5, respectively. The study also analyzed adaptation options, using the economic analysis COAST tool (Coastal Adaptation to Sea level rise Tool) (Almodovar-rosario et al., 2014).

According to Akhtar et al. (2018), climate change-induced flow increments will increase the overtopping potential for bridges during flood events. For example, the US-59 bridge will be overtopped at a 90-year flood event instead of 119-year flood event, and the SH-36 bridge will be overtopped at an 87-year flood event instead of a 127-year flood event. They also found that scour conditions will worsen under the increased precipitation scenario. For example, the US-59 bridge is identified as a scour-critical bridge on the National Bridge Inventory (NBI) record, and the allowable scour depth for this bridge should exceed that of 55-year flood events under existing climate conditions. However, it is estimated that based on the future climate data, the bridge will exceed the allowable scour depth for 43-year flood events.

Several studies have been conducted to research the impacts of climate change on hydraulic structures, and they all indicated that climate change increases flood frequency by changing precipitation patterns and imparts adverse effects on hydraulic structures.

3 FLOW CHARACTERIZATION AT TEXAS RIVERINE AND COASTAL BRIDGES

3.1 Introduction

This chapter presents the results of Task 3 of Project 0-7068. Task 3 is titled: *Identifying Bridges with Potential Inundation in High Velocity Flow Events*. The main goal of this task was to review existing studies and datasets characterizing the flood potential at bridges in Texas and extract information about riverine and coastal flood parameters to inform physical and numerical modeling of hydrodynamic forces on bridges (Tasks 4 and 5).

This chapter is structured as follows. Section 3.1 provides an introduction to this task. Section 3.2 provides an overview of design guidelines and modeling approaches for bridges subject to riverine or coastal flooding. Section 3.3 summarizes the results of the riverine flow parameter identification. Section 3.4 identifies the coastal flood parameters for bridges in coastal counties. Section 3.5 concludes the summary of findings of Task 3.

3.2 Background on Design Guidelines and Modeling Approaches

The design of bridges must account for the potential for inundation due to extreme flood events. For bridges subject to riverine flooding, hydrologic and hydraulic modeling provides information about water surface elevations and velocities in river channels and floodplains. In coastal areas, circulation and wave models provide further insight into potential storm surge and wave loading. Detailed information about modeling approaches for designing bridges in riverine and coastal areas are outlined in TxDOT's Hydraulic Design Manual (TxDOT, 2019). The following section provides a brief summary of hydraulic design guidelines for Texas bridges and recommended approaches for modeling riverine and coastal flood hazards.

3.2.1 Design Guidelines and Modeling Approaches in Riverine Areas

Hydrologic and hydraulic analyses are required for designing all new bridges over waterways, as well as for any bridge widening, bridge replacement, or roadway profile modification projects that may adversely affect the floodplain, even if no structural modifications are necessary (TxDOT, 2019). These analyses provide a basis for ensuring that the bridge is built to withstand the design flood forces and to assess the impact that the bridge structure will have on the local flow regime along the channel. Specific hydrologic and hydraulic data needs, analysis approaches, and modeling software are described in more detail below.

Hydrologic Modeling

Hydrologic modeling approaches account for processes in a watershed that convert precipitation to runoff and that convey water through the system. This modeling allows for estimation of the discharge associated with a design storm event at points of interest in the watershed. Such

information is critical for designing bridges that span waterways. Typical hydrologic analysis approaches account for the following processes:

1. *Rainfall*: The precipitation depth, duration, and frequency associated with the design storm provide the meteorological input to the model.
2. *Rainfall losses*: Losses include interception of rainfall by vegetation before reaching the ground, ponding on the ground, and infiltration into the soil, which all reduce the amount of rainfall that is converted to runoff.
3. *Sub-basin response*: The watershed is divided into sub-basins with defined parameters (e.g., land cover, topography). The response of each sub-basin to the rainfall time series, or hyetograph, is represented by an outflow hydrograph showing the discharge from the outlet point over time.
4. *Routing*: Routing methods describe how the hydrograph changes as it moves downstream. The two features of interest are the lag time, or time required for the flood wave to reach a downstream location, and the attenuation, or change in the shape of the hydrograph due to storage along the reach.
5. *Storage*: Storage in the channel or floodplain, or in other storage features such as reservoirs, is modeled to account for impacts on the flood wave attenuation and outflow hydrographs.

The primary outputs of interest include discharge hydrographs and/or peak flows at specific points of interest in the watershed. These outputs are incorporated into hydraulic models to determine water surface elevations and velocities associated with the design storm (FEMA, 2019c).

HEC-HMS

The HEC-HMS software program developed by the U.S. Army Corps of Engineers (UASCE) is frequently used for hydrologic modeling to inform FEMA flood risk analysis and mapping (USACE, 2016a). HEC-HMS is also used in reconnaissance, feasibility, and design-level studies for assessing proposed bridge design alternatives. HEC-HMS includes all features required for detailed hydrologic analysis of bridge projects, including simulation of precipitation, interception, infiltration, runoff, channel routing, and storage and their cumulative influence on discharge hydrographs and peak flows.

Hydraulic Modeling

Hydraulic modeling approaches are used to compute velocities and water surface elevations in channels. This information is needed to evaluate the effects of constructing bridges and hydraulic structures within the floodplain to ensure that these structures are designed to withstand flood events. Hydraulic modeling is also used to map floodplain inundation for federal flood insurance programs and to evaluate the effects of new development projects that encroach on the floodplain (FEMA, 2016b).

Typical hydraulic analysis approaches consist of the following components:

1. *Geometric properties*: Detailed topographic and bathymetric data characterizing the channel and floodplain is necessary. Information about the channel bed material, vegetation, and ground cover is used to determine appropriate roughness coefficients to account for frictional losses.
2. *Structures*: An inventory of existing and/or proposed structures, including culverts, bridges, and weirs, and their geometric properties is needed. For bridges, relevant design properties include the deck width, deck elevation, low chord elevation, skewness, number and length of spans, and number, diameter, and spacing of piers.
3. *Flow regime*: Knowledge of the flow regime and contraction or expansion behavior around existing structures is required.
4. *Boundary conditions*: Boundary conditions provide starting hydraulic parameters for model simulations. Depending on the flow regime and whether the simulation is steady-state or time-dependent, boundary conditions are required at one or both ends of a reach. Inflows from a hydrologic model can be used to set the boundary conditions in the hydraulic simulation.
5. *Calibration and validation*: The model can be calibrated and validated through comparisons with historical gauge data, watermarks, and imagery taken during past flood events.

HEC-RAS

The HEC-RAS software program developed by USACE is used for one- and two-dimensional hydraulic modeling in river channels and is commonly used in conjunction with HEC-HMS for FEMA flood mapping assessments (USACE, 2016b). The steady flow component of the HEC-RAS simulation engine is capable of modeling subcritical, supercritical, and mixed flow regimes. The software includes the capability to model flow contractions upstream of bridges; friction, turbulence, and drag losses under bridges; and flow expansions downstream of bridges. Model outputs include water surface elevation, velocity, and floodwater inundation area.

3.2.2 Design Guidelines and Modeling Approaches in Coastal Areas

When designing bridges in coastal areas, the highly dynamic and energetic nature of marine processes and storm events must be considered. Figure 3.1 summarizes the processes that contribute to coastal hydrodynamics and may influence coastal bridge design. Stillwater levels include the effects of tides, storm surge, and sea-level rise (FEMA, 2016a). Wave setup and runup can further elevate water levels along the coast and generate wave-induced currents that influence local scouring and sediment transport (FEMA, 2015 & 2018). A complete assessment of coastal water level effects on infrastructure must incorporate all of these processes.

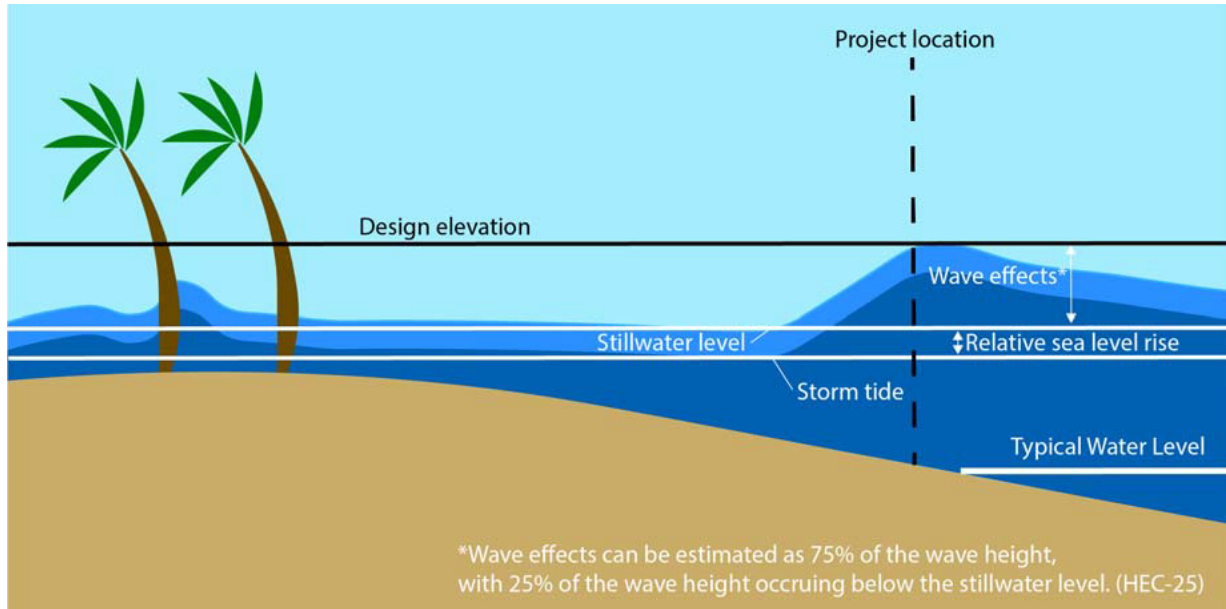


Figure 3.1 Factors that contribute to coastal water levels (TxDOT, 2019)

Coastal hydraulic analysis is required for projects located in TxDOT’s designated Coastal Risk Area. The Coastal Risk Area encompasses FEMA’s AE hazard zones, which are subject to inundation during the 1% annual exceedance probability (AEP) storm event, and VE hazards zones, which are subject to both inundation and storm-induced velocity wave action during the 1% AEP event. The Coastal Risk Area extends along the Gulf of Mexico coastline and spans five of TxDOT’s districts, including Beaumont, Houston, Yoakum, Corpus Christi, and Pharr. Projects located outside of this zone that may still be subject to coastal inundation or wave action, especially during tropical storm events or as a result of future sea-level rise and subsidence, should also account for the influence of coastal processes and hazards.

The extent of hydraulic analysis required by TxDOT for coastal bridge design varies depending on the project’s level of investment and potential vulnerability. TxDOT outlines three levels of analysis for coastal processes, which are summarized in Table 3.1. Level 1 analyses are used for bridges with low investment by TxDOT and low vulnerability to coastal processes. Existing data can be employed to assess potential risks. Level 2 analyses characterize projects with moderate to high levels of investment by TxDOT and moderate to high vulnerability to coastal processes. Assessment of existing data sources is combined with common modeling approaches to assess more complex risks. Level 3 analyses are used for projects with high investment by TxDOT and high vulnerability to coastal processes. These projects may also serve critical functions during storms events, such as providing primary evacuation routes. Due to the high level of vulnerability and the severe implications of failure, detailed data acquisition and modeling approaches are required for proper design. Table 3.1 also summarizes recommended data sources and modeling approaches for each analysis level.

Table 3.1 Levels of coastal flood analysis requirements for bridges in coastal areas (TxDOT, 2019)

Analysis Level	1	2	3
TxDOT investment	low	moderate to high	high
Vulnerability	low	moderate to high	high
Stillwater level data sources and modeling methods	<ul style="list-style-type: none"> · NOAA Tides and Currents · USACE water level analyses · NOAA hurricane tracks · NOAA SLOSH outputs · NOAA/TGLO SLR projections 	<ul style="list-style-type: none"> · NOAA Tides and Currents · USACE water level analyses · NOAA hurricane tracks · NOAA SLOSH outputs · NOAA/TGLO SLR projections 	<ul style="list-style-type: none"> · NOAA Tides and Currents · USACE water level analyses · NOAA hurricane tracks · NOAA SLOSH outputs · NOAA/TGLO SLR projections · 2D/3D hydrodynamic models
Wave data sources and modeling methods	<ul style="list-style-type: none"> · FEMA FISs · NOAA Tides and Currents · NOAA NDBC 	<ul style="list-style-type: none"> · FEMA FISs · NOAA Tides and Currents · NOAA NDBC · 1D wave models 	<ul style="list-style-type: none"> · FEMA FISs · NOAA Tides and Currents · NOAA NDBC · Site-specific wave models

Key:

- FEMA = Federal Emergency Management Agency
- FIS = Flood Insurance Study
- NDBC = National Data Buoy Center
- NOAA = National Oceanic and Atmospheric Administration
- SLOSH = Sea, Lake and Overland Surges from Hurricanes
- SLR = sea-level rise
- TGLO = Texas General Land Office
- USACE = United States Army Corps of Engineers

3.3 Riverine Flow Parameter Identification

This section presents the results of the analysis of riverine flow parameters in the vicinity of bridges in Texas. Existing hydrologic and hydraulic models developed as part of FEMA’s FISs in Travis and Harris Counties and TxDOT as-built bridge drawings were examined to obtain the results presented here.

3.3.1 Hydrologic and Hydraulic Models

Hydrologic and hydraulic models were obtained from the City of Austin and Harris County Flood Control District (HCFCD) (COA, 2019; HCFCD, 2020). The models cover most of the major watersheds in Travis County (Figure 3.2) and Harris County (Figure 3.3) areas. Travis County is located in the so-called flash flood alley of central Texas, where intense rainfall, low infiltration rates, and steep topography combine to cause rapidly moving, extreme events (Sharif et al., 2010). Harris County’s position along the Texas coast makes it vulnerable to both riverine and coastal flooding driven by intense, short-duration thunderstorms, slower-moving frontal systems, and

tropical storms. Low topography, poorly-draining soils, and extensive network of bayous and streams elevate the risk of flooding for residents and critical infrastructure systems in Harris County (FEMA 2019a).

The City of Austin and HCFCD maintain HEC-HMS hydrologic models and HEC-RAS hydraulic models developed as part of FEMA FISs to delineate floodplains and to set flood insurance rates and requirements (COA, 2020; HCFCD, 2009). Peak discharge outputs from the HEC-HMS models serve as input into the HEC-RAS models, which are used to compute water surface elevations and flow velocities. The data sources and methods used in the models are summarized in Table 3.2.

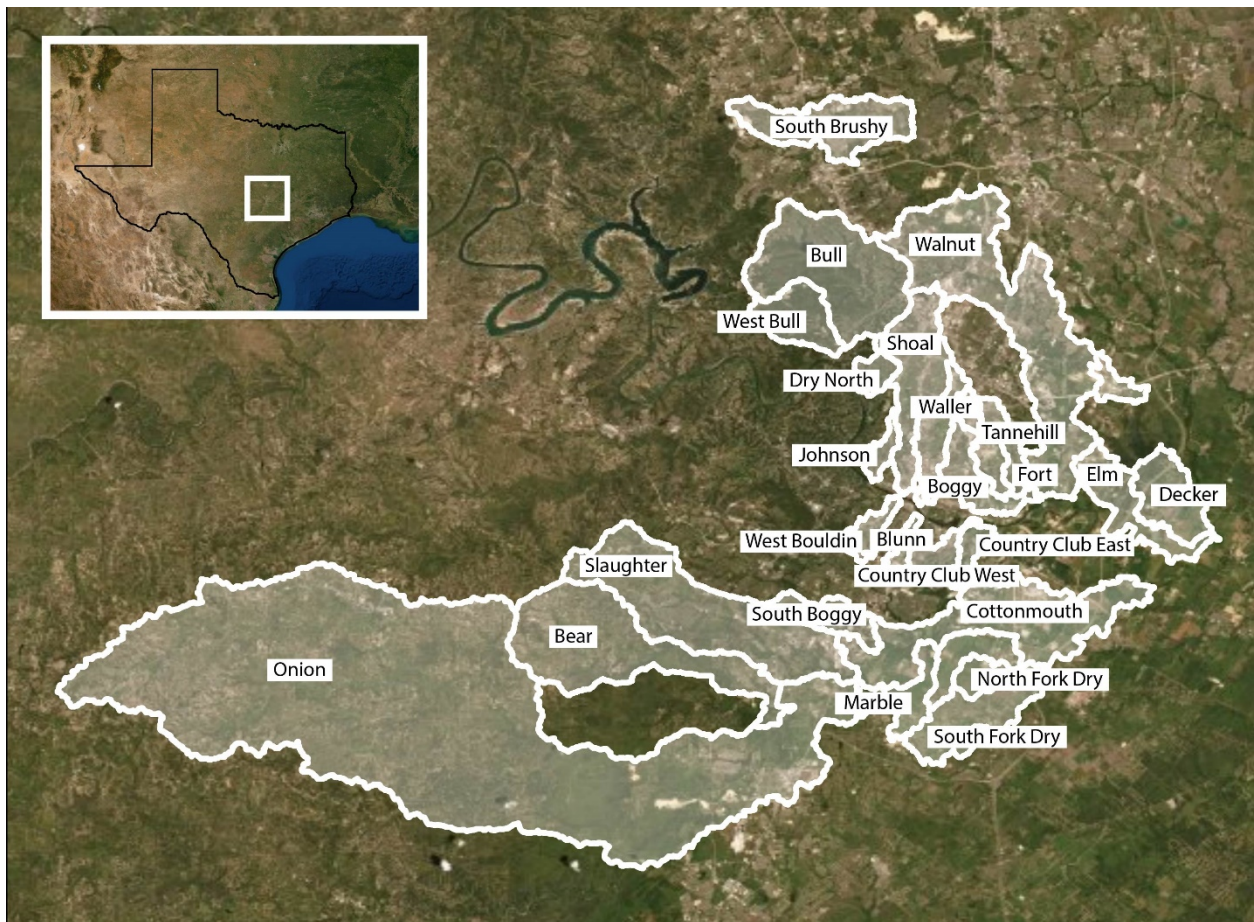


Figure 3.2 Watersheds in Travis County with available hydrologic and hydraulic models for flow parameter identification

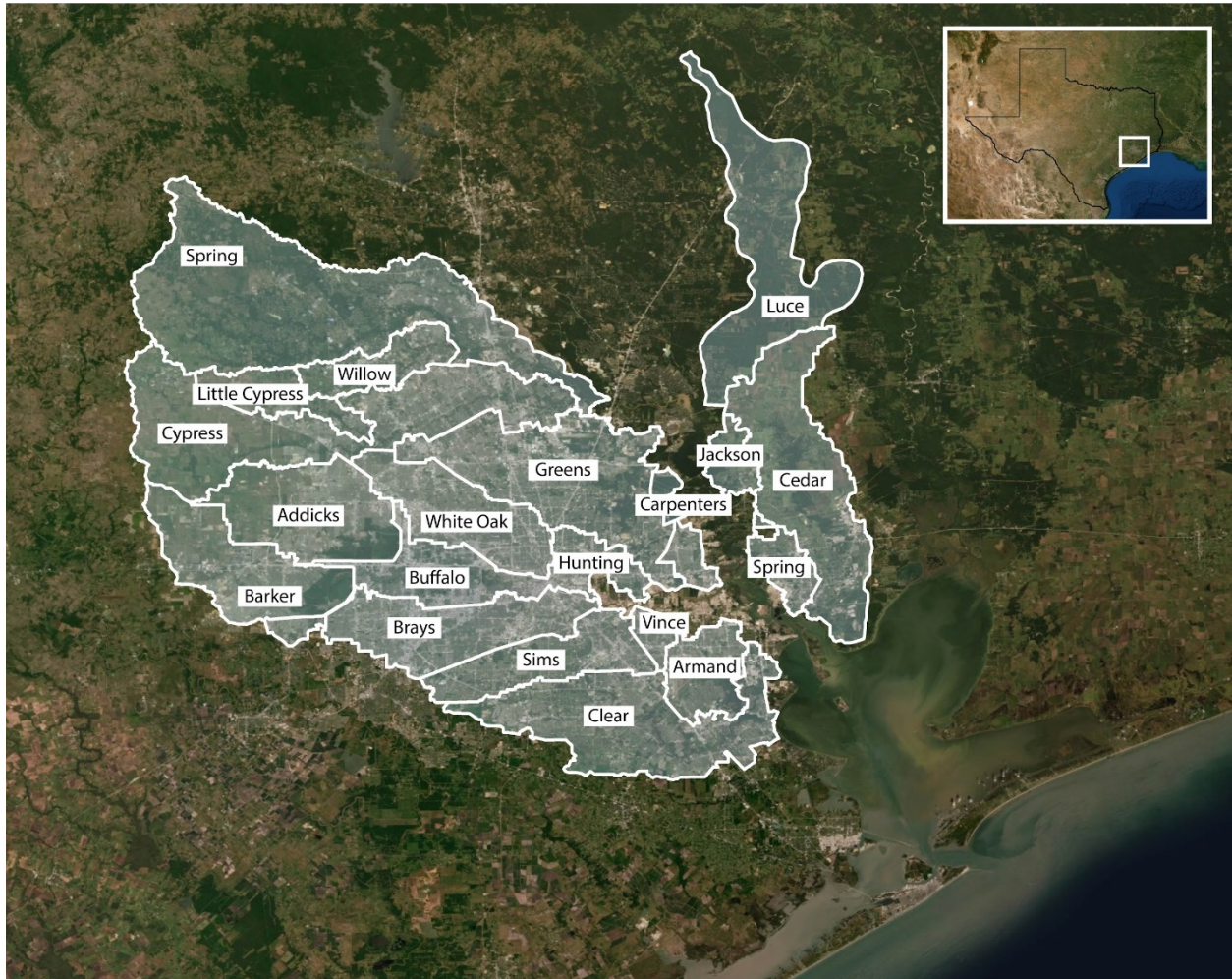


Figure 3.3 Watersheds in Harris County with available hydrologic and hydraulic models for flow parameter identification

Table 3.2 Summary of data sources and modeling methods for the City of Austin and HCFCFCD HEC-HMS and HEC-RAS models (FEMA, 2019a and 2020)

	Process/Parameter	City of Austin	HCFCFCD
HEC-HMS	Terrain	· LiDAR · Field surveys · NED DEM	· LiDAR · Field surveys
	Rainfall	· USGS depth-duration-frequency data · 24-hour storm duration	· USGS depth-duration-frequency data · 24-hour storm duration
	Soil	· NRCS SSURGO database	· NRCS SSURGO database
	Runoff losses	· NRCS Loss Rate Method	· Green & Ampt
	Imperviousness	· City of Austin impervious cover dataset	· Harris County Appraisal District parcel data
	Unit hydrograph	· NRCS dimensionless unit hydrograph	· Clark’s unit hydrograph
	Routing	· Modified Puls	· Modified Puls
HEC-RAS	Channel geometry	· LiDAR · Field surveys	· LiDAR · Field surveys
	Bridge geometry	· Field surveys	· Field surveys · Construction drawings
	Roughness	· Aerial photographs · Field reconnaissance	· Aerial photographs · Field reconnaissance

Key:

- LiDAR = Light Detection and Ranging
- NED DEM = National Elevation Dataset Digital Elevation Model
- NRCS = Natural Resources Conservation Service
- SSURGO = Soil Survey Geographic Dataset
- USGS = United States Geological Survey

Table 3.3 and 3.4 summarize the modeled watersheds and the number of bridges in each watershed in Travis County and Harris County, respectively. In some cases, not all river segments within each watershed were modeled, so data was extracted only from the available segments. All models include a simulation of the 1% AEP event for that watershed, which is the basis for FEMA flood mapping and insurance studies. Some models also include additional AEP simulations (e.g., 10% AEP, 2% AEP, or 0.2% AEP). For each modeled event, hydraulic parameters were extracted at cross-sections upstream and downstream of the bridge to characterize the flow in the vicinity of the structures. The parameters of interest include water surface elevation, velocity in the channel, maximum flow depth in the channel, Froude number in the channel, and elevation of the low chord of the bridge deck. Water surface elevations were compared with bridge low chord elevations to characterize the depth of flooding above the low chord.

Table 3.3 Watersheds in Travis County and the number of bridges modeled along the main stem (COA, 2019)

Creek	Area (sq mi)	Number of Bridges	Creek	Area (sq mi)	Number of Bridges
Bear	28	3	North Fork Dry	4	8
Blunn	1	9	Onion	211	23
Boggy	6	24	Shoal	13	28
Bull	23	8	Slaughter	31	8
Cottonmouth	5	4	South Boggy	5	8
Country Club			South Brushy	12	1
East	2	2	South Fork Dry	9	8
Country Club			Tannehill	4	11
West	3	6	Waller	6	14
Decker	10	3	Walnut	39	23
Dry Creek			West Bouldin	3	8
North	2	3	West Bull	7	12
Elm	8	5			
Fort	3	3			
Johnson	2	8			
Marble	4	2			

Table 3.4 Watersheds in Harris County and the number of bridges modeled along the main stem (HCFCD, 2020)

Creek	Area (sq mi)	Number of Bridges	Creek	Area (sq mi)	Number of Bridges
Clear	201	26	Willow	56	20
Armand	59	7	Carpenters	31	24
Sims	94	56	Spring Gully	33	18
Brays	129	74	Greens	211	75
White Oak	111	76	Cedar	199	14
Hunting	31	53	Jackson	26	5
Vince	15	21	Luce	195	3
Spring	386	20	Barker	129	10
Cypress	267	39	Addicks	139	14
Little Cypress	52	12	Buffalo	102	65

3.3.2 As-Built Drawings

As-built drawings for bridges designed with shear keys were provided by TxDOT. The drawings included bridges across the state that were bid out between 2013 and 2016. All drawings with complete hydraulic design information simulated the 1% AEP flow. Some drawings also simulated higher-frequency flows (e.g., 10% AEP, 4% AEP, or 2% AEP). Hydraulic design parameters,

including flow velocities and water surface elevations, were extracted from the drawings for all available AEPs. Water surface elevations immediately upstream of the bridge were compared with bridge low chord elevations to calculate the depth of flooding above the low chord.

3.3.3 Flow Parameters

Table 3.5 to 3.8 summarize the flow parameters extracted from the Travis County and Harris County HEC-RAS models, including channel velocity, flow depth in the channel, Froude number, and water depth above low chord. Also included are the number and percent of bridges along each modeled creek/stream at which the water surface in the channel reaches or exceeds the elevation of the low chord of the bridge. Note that bridges are designed for a specific AEP storm and thus are expected to be impacted by flooding during higher return period events.

In Travis County, maximum velocities in the vicinity of bridges range from 19.6 feet per second for the 10% AEP to 26.9 feet per second for the 0.2% AEP, with associated water depths above low chord between 12.3 feet and 23.9 feet. Maximum flow depths in the channel range from 25.9 feet for the 10% AEP to 44.8 feet for the 0.2% AEP. For the 1% AEP, Shoal Creek, Onion Creek, Waller Creek, and Walnut Creek have the highest number of impacted bridges.

In Harris County, maximum velocities in the vicinity of bridges range from 13.2 feet per second for the 10% AEP to 17.4 feet per second for the 0.2% AEP, with associated water depths above low chord between 13.2 feet and 20.0 feet. Maximum flow depths in the channel range from 42.9 feet for the 10% AEP to 56.8 feet for the 0.2% AEP. For the 1% AEP, Brays Bayou, White Oak Bayou, and Greens Bayou have the highest number of impacted bridges (over 40 bridges in each system).

Tables 3.9 and 3.10 summarize the water depth above low chord and velocity information extracted from TxDOT as-built drawings. Results generally fall within similar ranges as those modeled for Travis and Harris Counties, suggesting that the flow parameters are applicable to systems across Texas. Maximum water depth above low chord values ranged from -0.1 feet (no submergence) for the 4% AEP event to 11.5 feet for the 1% AEP event. Maximum channel velocities ranged from 7.0 feet per second for the 10% AEP event to 11.7 feet per second for the 1% AEP event. Table C.1 in Appendix C further summarizes the Froude numbers at bridge locations based on TxDOT as-built drawings. The range of Froude numbers is slightly lower than those reported for Harris and Travis counties, with a maximum Froude number of 0.87.

Table 3.5 Summary of flow parameters and bridge impacts for 10% AEP and 2% AEP flood events in Travis County watersheds

Creek	10% AEP						2% AEP					
	Max Channel Velocity (ft/s)	Max Flow Depth (ft)	Max Froude #	Max Water Depth above Low Chord (ft)	# of Bridges Partially or Fully Submerged	% of Bridges Partially or Fully Submerged	Max Channel Velocity (ft/s)	Max Flow Depth (ft)	Max Froude #	Max Water Depth above Low Chord (ft)	# of Bridges Partially or Fully Submerged	% of Bridges Partially or Fully Submerged
Bear	12.7	23.7	0.7	-4.5	0	0%	14.5	34.6	0.5	3.0	2	67%
Blunn	14.5	13.0	1.3	4.1	5	56%	13.4	15.0	1.0	5.9	6	67%
Boggy	13.0	25.5	1.0	9.4	7	29%	16.1	27.6	1.0	11.5	7	29%
Bull	19.6	17.1	1.0	5.9	1	13%	19.8	23.8	1.0	8.1	1	13%
Cottonmouth	13.3	12.5	0.8	3.5	2	50%	18.1	17.3	1.0	8.9	4	100%
Country Club East	6.5	11.1	1.0	3.3	1	50%	5.6	14.4	0.6	3.9	1	50%
Country Club West	10.5	11.8	1.0	-2.1	0	0%	11.5	14.5	0.9	1.1	2	33%
Decker	6.2	8.3	0.6	-3.6	0	0%	6.6	10.0	0.4	-2.3	0	0%
Dry Creek North	10.5	18.8	1.0	8.7	2	67%	12.1	20.5	1.0	10.3	2	67%
Elm	5.9	11.5	0.4	2.6	1	20%	7.0	12.2	0.4	3.1	1	20%
Fort	13.3	14.3	1.0	2.1	3	100%	14.6	16.3	1.0	3.7	3	100%
Johnson	13.9	11.0	1.0	0.7	2	25%	15.3	13.9	1.0	1.7	3	38%
Marble	4.8	8.3	0.4	-5.0	0	0%	7.7	11.3	0.5	-2.0	0	0%
North Fork Dry	8.4	12.4	0.6	4.3	4	50%	10.1	15.1	0.6	5.1	5	63%
Onion	13.3	21.6	1.0	5.5	7	30%	19.4	25.9	1.0	7.3	13	57%
Shoal	18.1	21.9	1.0	12.3	15	54%	20.2	25.0	1.0	15.1	17	61%
Slaughter	14.5	17.1	1.0	9.8	1	13%	14.4	21.7	0.9	15.4	2	25%
South Boggy	12.9	16.6	0.9	1.6	3	38%	14.0	23.3	1.0	8.5	4	50%
South Brushy	8.4	9.9	0.3	1.9	1	100%	6.5	10.3	0.3	2.3	1	100%
South Fork Dry	11.3	15.7	0.6	4.0	3	38%	14.2	20.2	0.6	5.3	4	50%
Tannehill	14.4	16.2	1.0	5.2	4	36%	15.7	16.8	1.0	5.8	6	55%
Waller	13.8	16.2	0.8	6.7	14	100%	17.7	19.6	0.8	8.9	14	100%
Walnut	11.9	25.9	0.6	6.8	5	22%	14.3	28.9	0.7	9.5	9	39%
West Bouldin	10.2	7.6	1.0	2.5	8	100%	8.7	8.1	0.9	2.9	8	100%
West Bull	14.6	12.8	1.0	0.6	1	8%	17.9	20.8	1.0	7.8	5	42%
Min	4.8	7.6	0.3	-5.0	-	-	5.6	8.1	0.3	-2.3	-	-
Avg	11.9	15.2	0.8	3.5	-	-	13.4	18.7	0.8	6.0	-	-
Max	19.6	25.9	1.3	12.3	-	-	20.2	34.6	1.0	15.4	-	-

Table 3.6 Summary of flow parameters and bridge impacts for 1% AEP and 0.2% AEP flood events in Travis County watersheds

Creek	1% AEP						0.2% AEP					
	Max Channel Velocity (ft/s)	Max Flow Depth (ft)	Max Froude #	Max Water Depth above Low Chord (ft)	# of Bridges Partially or Fully Submerged	% of Bridges Partially or Fully Submerged	Max Channel Velocity (ft/s)	Max Flow Depth (ft)	Max Froude #	Max Water Depth above Low Chord (ft)	# of Bridges Partially or Fully Submerged	% of Bridges Partially or Fully Submerged
Bear	18.1	37.8	0.7	6.1	2	67%	26.9	44.8	1.0	9.6	2	67%
Blunn	14.1	15.9	1.0	6.6	6	67%	15.5	19.9	1.0	8.1	7	78%
Boggy	17.5	28.5	1.0	12.3	7	29%	19.9	30.5	1.0	14.1	14	58%
Bull	21.3	26.1	1.0	8.8	2	25%	24.9	32.9	1.0	11.4	2	25%
Cottonmouth	15.7	18.9	0.8	9.4	4	100%	-	-	-	-	-	-
Country Club East	5.7	15.7	0.5	4.1	1	50%	5.2	18.7	0.4	4.7	2	100%
Country Club West	12.0	14.7	0.9	1.6	3	50%	14.3	16.8	1.0	3.2	5	83%
Decker	8.2	12.4	0.5	0.5	1	33%	9.0	12.5	0.6	0.7	1	33%
Dry Creek North	12.6	21.2	1.0	11.0	3	100%	-	-	-	-	-	-
Elm	7.4	12.4	0.5	3.4	1	20%	8.3	12.9	0.5	4.0	1	20%
Fort	14.7	16.4	1.0	4.5	3	100%	14.0	16.9	0.8	5.3	3	100%
Johnson	15.8	15.7	1.0	2.0	4	50%	-	-	-	-	-	-
Marble	8.8	12.3	0.5	-0.9	0	0%	13.9	14.5	0.8	1.5	1	50%
North Fork Dry	9.7	15.8	0.6	5.7	5	63%	10.4	17.3	0.6	7.1	5	63%
Onion	20.5	27.7	1.0	8.8	16	70%	22.9	32.0	1.0	12.1	20	87%
Shoal	21.0	26.2	1.0	16.2	18	64%	22.5	29.0	1.0	18.5	20	71%
Slaughter	17.4	23.0	0.9	18.0	3	38%	16.3	28.8	0.8	23.9	5	63%
South Boggy	14.6	24.2	1.0	9.2	5	63%	16.6	25.5	1.0	10.5	7	88%
South Brushy	6.0	10.8	0.3	2.8	1	100%	4.1	11.9	0.3	3.6	1	100%
South Fork Dry	14.8	20.4	0.6	6.0	6	75%	13.8	22.2	0.5	7.5	6	75%
Tannehill	16.1	17.3	1.0	6.3	6	55%	16.8	18.3	1.0	7.3	7	64%
Waller	19.2	20.9	0.8	10.1	14	100%	-	-	-	-	-	-
Walnut	15.4	31.9	0.6	10.9	14	61%	19.1	37.1	0.8	14.1	17	74%
West Bouldin	9.5	8.3	0.9	3.1	8	100%	9.8	8.6	1.0	3.4	8	100%
West Bull	19.2	22.6	1.0	9.7	6	50%	21.7	26.8	1.0	12.3	8	67%
Min	5.7	8.3	0.3	-0.9	-	-	4.1	8.6	0.3	0.7	-	-
Avg	14.2	19.9	0.8	7.1	-	-	15.5	22.8	0.8	8.7	-	-
Max	21.3	37.8	1.0	18.0	-	-	26.9	44.8	1.0	23.9	-	-

Table 3.7 Summary of flow parameters and bridge impacts for 10% AEP and 2% AEP flood events in Harris County watersheds

Creek	10% AEP						2% AEP					
	Max Channel Velocity (ft/s)	Max Flow Depth (ft)	Max Froude #	Max Water Depth above Low Chord (ft)	# of Bridges Partially or Fully Submerged	% of Bridges Partially or Fully Submerged	Max Channel Velocity (ft/s)	Max Flow Depth (ft)	Max Froude #	Max Water Depth above Low Chord (ft)	# of Bridges Partially or Fully Submerged	% of Bridges Partially or Fully Submerged
Clear	4.3	29.7	0.5	1.9	3	12%	6.1	32.4	0.4	4.8	8	31%
Armand	-	-	-	-	-	-	-	-	-	-	-	-
Sims	10.9	27.8	0.6	5.9	1	2%	11.8	34.1	0.5	10.5	4	7%
Brays	-	-	-	-	-	-	-	-	-	-	-	-
White Oak	-	-	-	-	-	-	-	-	-	-	-	-
Hunting	7.8	24.0	0.4	13.2	16	30%	8.7	26.5	0.4	15.8	32	60%
Vince	-	-	-	-	-	-	-	-	-	-	-	-
Spring	6.5	29.3	0.3	7.2	9	45%	8.5	35.5	0.4	10.9	13	65%
Cypress	-	-	-	-	-	-	-	-	-	-	-	-
Little Cypress	5.5	19.0	0.8	1.7	2	17%	6.5	20.9	0.5	3.1	5	42%
Willow	7.4	21.3	0.8	4.3	9	45%	7.7	24.5	0.6	6.8	11	55%
Carpenters	-	-	-	-	-	-	-	-	-	-	-	-
Spring Gully	-	-	-	-	-	-	-	-	-	-	-	-
Greens	-	-	-	-	-	-	-	-	-	-	-	-
Cedar	-	-	-	-	-	-	-	-	-	-	-	-
Jackson	-	-	-	-	-	-	-	-	-	-	-	-
Luce	-	-	-	-	-	-	-	-	-	-	-	-
Barker	-	-	-	-	-	-	-	-	-	-	-	-
Addicks	6.0	15.7	0.4	2.3	2	14%	6.9	18.5	0.4	3.2	3	21%
Buffalo	13.2	42.9	0.4	2.7	2	3%	14.5	48.3	0.4	8.2	17	26%
Min	4.3	15.7	0.3	1.7	-	-	6.1	18.5	0.4	3.1	-	-
Avg	7.7	24.4	0.5	4.9	-	-	8.8	28.4	0.5	7.7	-	-
Max	13.2	42.9	0.8	13.2	-	-	14.5	48.3	0.6	15.8	-	-

Table 3.8 Summary of flow parameters and bridge impacts for 1% AEP and 0.2% AEP flood events in Harris County watersheds

Creek	1% AEP						0.2% AEP					
	Max Channel Velocity (ft/s)	Max Flow Depth (ft)	Max Froude #	Max Water Depth above Low Chord (ft)	# of Bridges Partially or Fully Submerged	% of Bridges Partially or Fully Submerged	Max Channel Velocity (ft/s)	Max Flow Depth (ft)	Max Froude #	Max Water Depth above Low Chord (ft)	# of Bridges Partially or Fully Submerged	% of Bridges Partially or Fully Submerged
Clear	6.7	33.4	0.4	5.7	12	46%	8.7	35.9	0.3	7.6	18	69%
Armand	13.2	21.9	2.6	8.9	6	86%	-	-	-	-	-	-
Sims	11.0	37.6	0.5	12.6	17	30%	10.6	43.8	0.4	16.8	39	70%
Brays	11.8	51.3	0.5	16.4	57	77%	-	-	-	-	-	-
White Oak	12.3	43.9	0.5	11.5	52	68%	-	-	-	-	-	-
Hunting	8.6	27.9	0.4	17.2	35	66%	9.1	30.5	0.4	20.0	45	85%
Vince	9.0	24.4	0.6	11.9	17	81%	-	-	-	-	-	-
Spring	9.3	37.7	0.5	12.5	14	70%	11.4	43.8	0.5	16.3	17	85%
Cypress	8.2	41.8	0.4	11.0	11	28%	-	-	-	-	-	-
Little Cypress	8.7	21.6	0.7	3.7	5	42%	8.0	22.6	0.5	5.2	9	75%
Willow	9.7	25.7	0.6	7.6	14	70%	9.8	28.9	0.7	10.4	17	85%
Carpenters	7.3	24.0	0.4	6.1	7	29%	-	-	-	-	-	-
Spring Gully	9.4	21.2	0.7	3.7	5	28%	-	-	-	-	-	-
Greens	11.5	48.4	0.5	14.3	44	59%	-	-	-	-	-	-
Cedar	9.5	33.6	0.3	2.3	6	43%	-	-	-	-	-	-
Jackson	12.6	20.4	0.6	9.4	3	60%	-	-	-	-	-	-
Luce	6.0	33.9	0.2	7.5	3	100%	-	-	-	-	-	-
Barker	6.3	15.0	0.5	3.5	7	70%	-	-	-	-	-	-
Addicks	6.8	19.8	0.4	4.1	7	50%	6.5	22.1	0.4	6.8	12	86%
Buffalo	15.1	51.0	0.4	11.3	23	35%	17.4	56.8	0.5	17.0	41	63%
Min	6.0	15.0	0.2	2.3	-	-	6.5	22.1	0.3	5.2	-	-
Avg	9.6	30.8	0.6	8.9	-	-	9.9	33.8	0.5	12.2	-	-
Max	15.1	51.3	0.7	17.2	-	-	17.4	56.8	0.7	20.0	-	-

Table 3.9 Summary of water depth above bridge low chord values extracted from as-built drawings

Bridge	NBI Number	County	Water Depth above Low Chord (ft)			
			10% AEP	4% AEP	2% AEP	1% AEP
Bethel Draw	17-0260-0506-04-101	Burleson	-	-0.1	-	0.8
Bethel Creek	17-0260-0506-04-100	Burleson	-1.0	-	-	1.5
Hickory Creek	17-0260-0506-04-100	Burleson	-	-0.9	-	-0.3
Green Creek	02-073-0-AA02-66-003	Erath	-3.3	-1.2	-	3.0
Pedernales River	14-087-0-AA01-19-502	Gillespie	-	-	-	-7.1
Patrick Creek	02-184-0-314-01-229	Parker	-13.8	-	-	-6.5
Walnut Creek	02-184-0-AA05-47-004	Parker	-0.8	-	-	4.6
Kickapoo Creek	02-184-0-AA05-47-004	Parker	-	-	-	7.8
Dry Creek	02-184-0-AA05-47-004	Parker	1.9	-	-	4.9
Kickapoo Creek	17-094-0-AA0202-003	Grimes	-	-	2.3	2.8
Box Creek	10-001-0-AA04-71-001	Anderson	-	-	-	7.0
Colorado River	08-168-0-AA01-42-005	Mitchell	-	-2.5	-	0.8
Aquilla Creek	09-110-0-AA05-60-001	Hill	-	-	-	-1.6
Cobb Creek	09-110-0-AA08-93-002	Hill	-2.1	-	-	0.2
Salt Creek	03-252-0-AA01-08-001	Young	-	-	-	2.9
Plum Creek	03-252-0-AA03-06-001	Young	-	-	-	4.0
Willow Creek	14-227-0-0114-03-489	Travis	-	-3.0	-	-1.3
Atascosa River	16-149-0-AA0210001	Live Oak	1.0	-	-	11.5
Kickapoo Creek	01-194-0-0-0046-001-112	Red River	-	-1.3	-	-0.3
West Fork Pilot Grove Creek	01-092-0-0729-02-185	Grayson	-	-0.9	-	1.5
Shooter Creek	01-075-0-AA04-93-001	Grayson	-	-	-	-14.4
Mud Branch	01-075-AA04-51-001	Grayson	-	-	-	9.4
Pot Creek	01-075-0-AA02-37-002	Fannin	-	-	-	5.1
Noth Suphur River Tributary	01-075-0-AA02-37-001	Fannin	-2.0	-	-	1.1
Long John Creek	20-146-0-AA23-31-001	Liberty	-3.7	-	-1.9	-1.1
Leon Creek	15-015-0072-07-402	Bexar	0.0	-	4.8	5.5
Hickory Creek	01-139-0-AA04-34-001	Lamar	-	-	-	4.9
Tributary of Rowdy Creek	01-139-0-AA04-34-001	Lamar	-	-3.6	-	-1.7
West Tributary No.1	12-170-0338-11-114	Montgomery	-	-	-2.0	-1.5
West Tributary No.2	12-170-0338-11-115	Montgomery	-	-	-2.1	-1.7
Alligator Creek	12-170-0338-11-116	Montgomery	-	-	-1.9	-1.4
Silver Creek	02-220-0-ZS45-28-004	Tarrant	-	-	-	2.0
Clear Creek	12-102-0-3312-01-007	Harris/Galveston	-19.1	-	-17.3	-16.5
Rocky Creek	13-076-0-1441-01-005	Fayette	-1.2	-0.3	0.3	0.9
Redding Creek	01-113-0-AA04-44-001	Hopkins	-1.0	-	-	3.2
Panther Creek North	03-169-0-AA04-79-001	Montague	-	-0.1	-	4.1
Panther Creek South	03-169-0-AA04-79-002	Montague	-0.2	-	-	6.4
Salt Creek	03-169-0-AA01-73-001	Montague	-5.4	-	-	-2.8
Baker Creek	01-075-0-AA05-66-001	Fannin	-	-	-	1.7
Honey Grove Creek	01-075-0-AA02-52-001	Fannin	-1.8	-	-	5.2
Sanders Creek	01-075-0-AA04-91-001	Fannin	-	-	-	2.0
Leon River	230680057001151	Eastland	-	-0.8	-	2.5
Maximum Values			1.9	-0.1	4.8	11.5

Table 3.10 Summary of channel velocity values extracted from as-built drawings

Bridge	NBI Number	County	Channel Velocity (ft/s)			
			10% AEP	4% AEP	2% AEP	1% AEP
Bethel Draw	17-0260-0506-04-101	Burleson	-	7.7	-	11.7
Bethel Creek	17-0260-0506-04-100	Burleson	6.9	-	-	2.7
Hickory Creek	17-0260-0506-04-100	Burleson	-	5.0	-	6.4
Green Creek	02-073-0-AA02-66-003	Erath	6.7	7.8	-	8.9
Pedernales River	14-087-0-AA01-19-502	Gillespie	-	-	-	3.9
Patrick Creek	02-184-0-314-01-229	Parker	6.5	-	-	8.1
Walnut Creek	02-184-0-AA05-47-004	Parker	6.6	-	-	8.4
Kickapoo Creek	02-184-0-AA05-47-004	Parker	-	-	-	10.4
Dry Creek	02-184-0-AA05-47-004	Parker	3.9	-	-	4.6
Kickapoo Creek	17-094-0-AA0202-003	Grimes	-	-	7.6	8.0
Box Creek	10-001-0-AA04-71-001	Anderson	-	-	-	7.9
Colorado River	08-168-0-AA01-42-005	Mitchell	-	7.2	-	10.0
Aquilla Creek	09-110-0-AA05-60-001	Hill	-	-	-	6.1
Cobb Creek	09-110-0-AA08-93-002	Hill	3.1	-	-	2.3
Salt Creek	03-252-0-AA01-08-001	Young	-	-	-	2.9
Plum Creek	03-252-0-AA03-06-001	Young	-	-	-	1.5
Willow Creek	14-227-0-0114-03-489	Travis	-	4.2	-	5.5
Atascosa River	16-149-0-AA0210001	Live Oak	5.7	-	-	8.9
Kickapoo Creek	01-194-0-0-0046-001-112	Red River	-	7.6	-	9.2
West Fork Pilot Grove Creek	01-092-0-0729-02-185	Grayson	-	8.8	-	11.1
Shooter Creek	01-075-0-AA04-93-001	Grayson	-	-	-	5.4
Mud Branch	01-075-AA04-51-001	Grayson	-	-	-	9.1
Pot Creek	01-075-0-AA02-37-002	Fannin	-	-	-	7.4
Noth Suphur River Tributary	01-075-0-AA02-37-001	Fannin	4.4	-	-	6.7
Long John Creek	20-146-0-AA23-31-001	Liberty	4.5	-	4.9	5.0
Leon Creek	15-015-0072-07-402	Bexar	3.0	-	2.9	3.2
Hickory Creek	01-139-0-AA04-34-001	Lamar	-	-	-	3.4
Tributary of Rowdy Creek	01-139-0-AA04-34-001	Lamar	-	2.0	-	1.2
West Tributary No.1	12-170-0338-11-114	Montgomery	-	-	3.8	4.2
West Tributary No.2	12-170-0338-11-115	Montgomery	-	-	1.5	1.4
Alligator Creek	12-170-0338-11-116	Montgomery	-	-	4.1	4.4
Silver Creek	02-220-0-ZS45-28-004	Tarrant	-	-	-	3.5
Clear Creek	12-102-0-3312-01-007	Harris/Galveston	2.9	-	3.3	3.4
Rocky Creek	13-076-0-1441-01-005	Fayette	4.5	4.9	5.2	5.5
Redding Creek	01-113-0-AA04-44-001	Hopkins	3.7	-	-	4.0
Panther Creek North	03-169-0-AA04-79-001	Montague	-	6.5	-	6.1
Panther Creek South	03-169-0-AA04-79-002	Montague	5.2	-	-	2.5
Salt Creek	03-169-0-AA01-73-001	Montague	6.5	-	-	11.2
Baker Creek	01-075-0-AA05-66-001	Fannin	-	-	-	4.2
Honey Grove Creek	01-075-0-AA02-52-001	Fannin	7.0	-	-	5.8
Sanders Creek	01-075-0-AA04-91-001	Fannin	-	-	-	8.7
Leon River	230680057001151	Eastland	-	6.6	-	6.3
Maximum Values			7.0	8.8	7.6	11.7

3.4 Coastal Parameter Identification

Of Texas's 254 counties, 16 border the Gulf of Mexico or coastal estuaries (Figure 3.4). Bridges in these counties may be susceptible to coastal flood impacts. Several state-wide or national datasets are available to characterize coastal flooding driven by storm surge and wave effects. NHC has applied a storm surge model driven by simulated hurricane wind fields to probabilistically estimate storm surge magnitude and extent for Category 1-5 hurricanes along the entire U.S. East and Gulf coasts. This approach does not include wave effects.

The most recent state-wide coastal flood hazard modeling was developed as part of FEMA's FIS for Texas coastal counties (FEMA and USACE, 2011). This FIS used a series of numerical models, including a circulation model (ADCIRC), a wave setup model (STWAVE), and a wave runup model (WHAFIS), to simulate coastal inundation for a range of AEP storm events. The combined outputs of these models were used to map stillwater depths, wave heights, and total water depths along the Texas coast. Note that stillwater depths from FEMA include the effects of wave setup, while TxDOT's guidance on stillwater depth determination for coastal bridge design does not incorporate these effects.

Model outputs from both NHC and FEMA sources were utilized to assess coastal flood impacts on bridges in Texas. NHC data was available for all coastal areas in Texas. Complete FEMA datasets were available for all coastal counties except Kenedy County, Brazoria County, and Nueces County. The following sections provide additional information about the modeling approaches and summarize the coastal flood parameters.

3.4.1 Coastal Water Level and Wave Models

Numerical models of varying complexity have been applied to simulate coastal hydrodynamics and flooding. These include surge and circulation models (SLOSH and ADCIRC) and wave models (STWAVE and WHAFIS). The details of these models and their application for the Texas coast are described in the following sections.

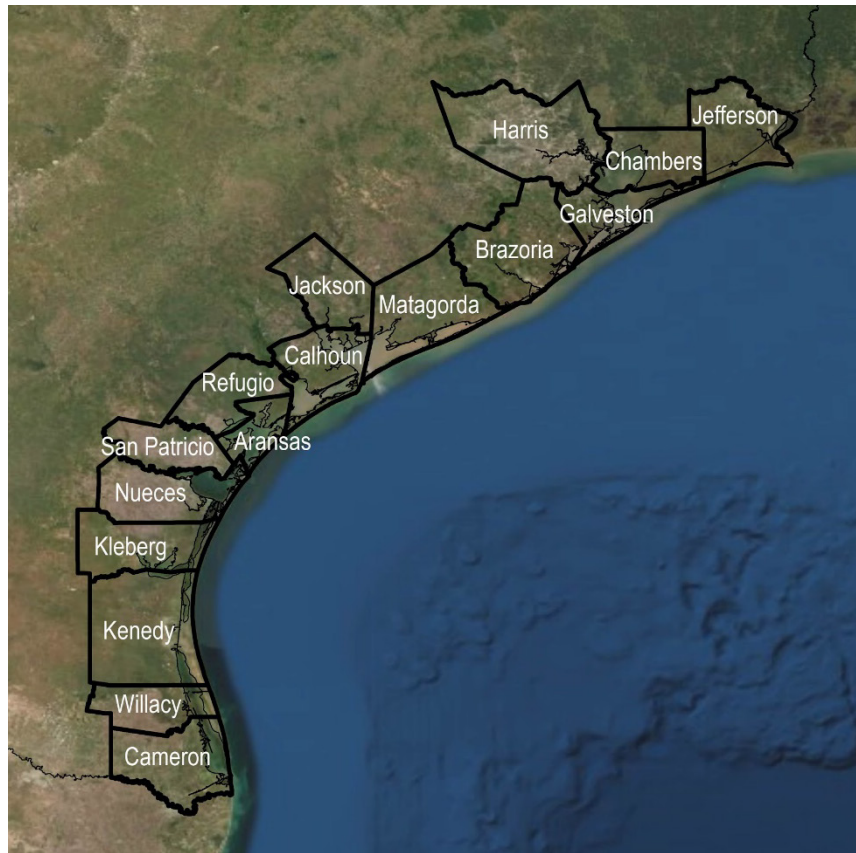


Figure 3.4 Coastal counties of Texas

SLOSH

The Sea, Lake and Overland Surges from Hurricanes (SLOSH) model is a physics-based model that can simulate local inundation due to hurricane-driven storm surge. The model can account for local shoreline geometry, including bay and river systems, as well as other physical infrastructure features that may impact flooding, such as levees and roadways. The SLOSH model is divided into 32 basins (Figure 3.5), which are typically centered on vulnerable coastal areas such as population centers, critical port locations, and areas with inlets or low topography. SLOSH can be applied deterministically or probabilistically. For the deterministic approach, a single simulation is used to forecast storm surge based on a specific set of hurricane parameters. For the probabilistic approach, statistics of past hurricane parameters are used to generate an ensemble of hypothetical hurricanes that are each simulated deterministically in the model (NOAA, 2020).

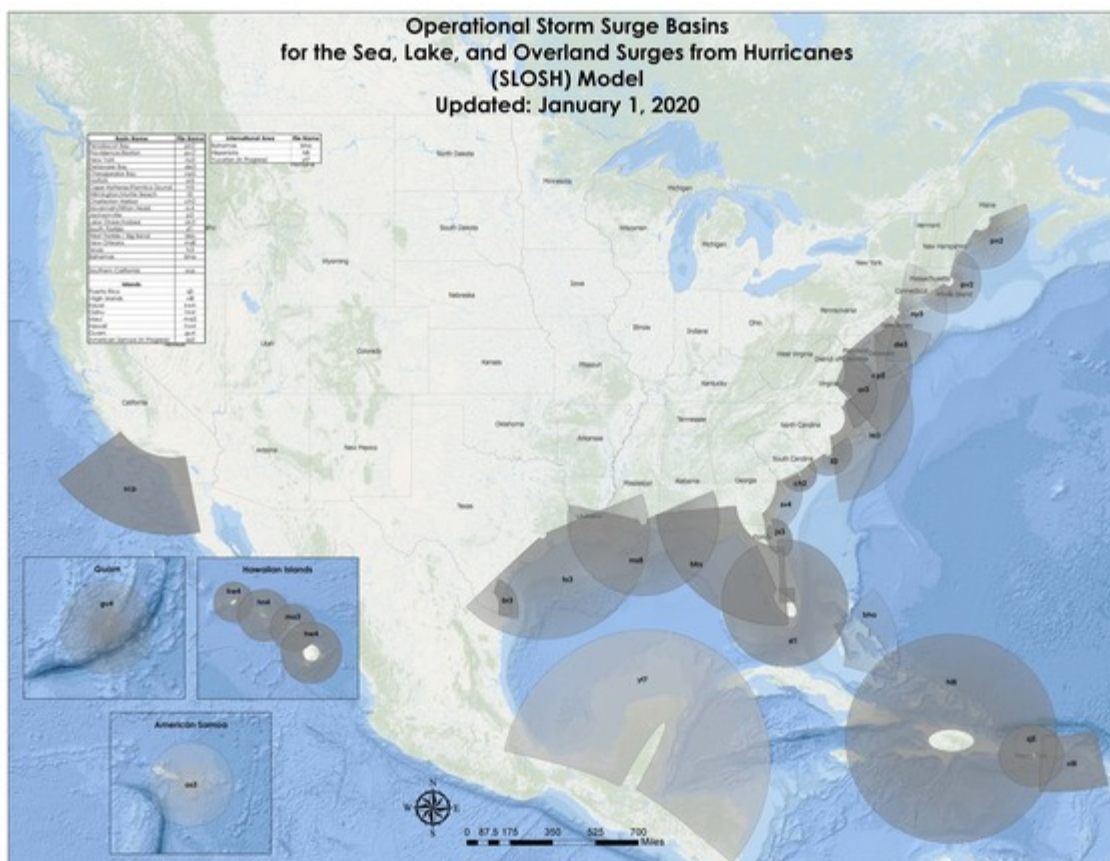


Figure 3.5 SLOSH model domains for the 32 operational storm surge basins (NOAA, 2020)

NHC generated maximum storm surge maps for each hurricane category by simulating thousands of hypothetical hurricanes using SLOSH. A Maximum Envelope of High Water (MEOW) was generated for each storm category, forward speed, trajectory, and initial tidal level, accounting for uncertainty in the location of landfall. These MEOWs were then combined to create a Maximum of the Maximum Envelope of High Water (MOM) for each storm category, which represents the worst-case high-water scenario for every point in the model domain (NOAA, 2020).

ADCIRC

The ADvanced CIRCulation model (ADCIRC) is a finite-element coastal hydrodynamic model that solves the three-dimensional equations of motion to simulate tidal circulation and storm surge propagation (Luettich and Westerink, 2012). The model can resolve open coastlines and bay shorelines in detail and is thus useful in assessing the exposure of coastal infrastructure to extreme events. For extreme water level analysis, hurricane wind and pressure data from historical or synthetic storms is used to drive the hydrodynamic response. ADCIRC outputs include the spatially-variable storm surge field for the model domain, as well as the wind field modified by land effects.

The FEMA surge modeling for the Texas coast utilized a consistent bathymetric-topographic representation and mesh domain for the entire coastline, from western Louisiana to the Mexican border. The model domain included offshore areas in the Atlantic Ocean and Gulf of Mexico, nearshore open coastlines and bays, and inland areas within the coastal floodplain, thus allowing for complete simulation of hurricane events, from generation in the Atlantic to landfall (FEMA and USACE 2011).

STWAVE

To account for wave setup, the STeady State Spectral WAVE model (STWAVE) was used in conjunction with ADCIRC. As its name implies, STWAVE is a steady-state spectral wave model that applies the finite difference method on a rectangular grid (Massey et al., 2011). The model can simulate wave height, peak wave period, mean wave direction, and two-dimensional wave spectra at selected locations. Because storm surge can significantly influence wave setup in shallow areas, the spatially-variable storm surge and wind fields generated by ADCIRC were used as input to STWAVE.

For FEMA's Texas coastal study, three large domains that extended offshore to an approximate depth of 100 feet were used to simulate nearshore waves. These grids used a half-plane version of STWAVE, which is limited to capturing cross-shore wave generation and propagation. Two nested grids for Galveston Bay and Corpus Christi Bay utilized the full-plane version of the model, which can simulate wind-driven waves in all directions but is more memory-intensive (FEMA and USACE, 2011).

After coupling STWAVE with ADCIRC, a Joint Probability Method Optimum Sampling (JPM-OS) approach was used to develop stillwater elevations for a range of AEP events. This method relies on the development of thousands of synthetic hurricane events, generated from statistical distributions of key hurricane parameters, including central pressure, radius to maximum wind speed, maximum wind speed, translation speed, and track heading. Optimum sampling was used to select the most probable combinations of these variables and to reduce the number of storms that were simulated using the coupled ADCIRC-STWAVE model. Statistical combinations of the model outputs were then used to generate the 10%, 2%, 1%, and 0.2% AEP stillwater levels, including tides, storm surge, and wave setup (FEMA and USACE, 2011).

WHAFIS

The Wave Height Analysis for Flood Insurance Studies model (WHAFIS) is a DOS-based program that computes wave crest elevations along one-dimensional cross-shore transects (FEMA 2019b). These transects account for local topography, vegetative cover, and built features. Wave heights were computed using stillwater elevations from the ADCIRC and STWAVE modeling and then interpolated between transects to generate two-dimensional gridded wave height data that accounts for overland wave propagation and runup. For FEMA's Texas coastal study, transects were defined along open coastlines, bay shorelines, and, in some cases, tidally influenced rivers and streams (FEMA and USACE, 2011).

3.4.2 Storm Surge and Wave Parameters

Maximum storm surge estimates for Category 1-5 hurricanes were obtained from NHC (Zachry, 2018). Modeled water levels were extracted at the location of coastal bridges in Texas to determine likely surge depths (in feet above ground level). The number of bridges in each coastal county that are susceptible to various storm surge depths are summarized in Table 3.11 for Category 1-5 hurricanes. Surge hazards are primarily limited to under 6 feet for Category 1 storms and under 12 feet for Category 2 storms. For Category 3, 4, and 5 hurricanes, surges above 12 feet are more common at bridge locations, with some surges in excess of 18 feet. Harris County has the highest number of bridges susceptible to storm surge across all hurricane categories. Many bridges in Brazoria, Galveston, and Jefferson counties are also exposed to storm surge.

Coastal stillwater depth and total water depth datasets derived from ADCIRC-STWAVE and WHAFIS simulations conducted by FEMA and USACE are available as county-level rasters from the FIS. Stillwater depths from ADCIRC-STWAVE, which include the effects of storm surge and wave setup, were available for the 1% AEP in all studied counties and, in some cases, were also available for additional AEPs (e.g., 10% AEP, 2% AEP, 0.2% AEP). Total water depth data, which also includes wave heights from WHAFIS, was only available for the 1% AEP (FEMA, 2013).

Table 3.11 Number of bridges in each coastal county that are susceptible to various storm surge depths for Category 1-5 hurricanes

County	Category 1				Category 2				Category 3				Category 4				Category 5			
	0-6ft	6-12ft	12-18ft	>18ft	0-6ft	6-12ft	12-18ft	>18ft	0-6ft	6-12ft	12-18ft	>18ft	0-6ft	6-12ft	12-18ft	>18ft	0-6ft	6-12ft	12-18ft	>18ft
Aransas	3	-	-	-	8	1	-	-	5	7	-	-	-	7	4	1	-	-	9	3
Brazoria	21	-	-	-	47	16	-	-	53	51	9	-	81	49	47	3	83	74	43	30
Calhoun	9	-	-	-	31	11	-	-	23	30	7	-	20	25	27	5	10	17	29	24
Cameron	2	-	-	-	7	1	-	-	29	7	-	-	42	23	5	-	56	45	20	1
Chambers	6	-	-	-	15	7	-	-	31	16	6	-	33	26	14	-	39	25	19	8
Galveston	29	-	-	-	67	21	-	-	81	70	9	-	66	86	40	2	45	79	81	16
Harris	32	-	-	-	76	31	-	-	145	89	33	-	208	133	77	18	242	177	105	52
Jackson	4	-	-	-	6	5	-	-	6	4	6	1	4	5	5	6	8	3	6	10
Jefferson	4	-	-	-	77	18	-	-	91	101	27	2	63	111	78	19	34	79	123	58
Kenedy	1	-	-	-	1	-	-	-	2	1	-	-	2	-	1	-	4	2	1	-
Kleberg	1	-	-	-	1	-	-	-	2	1	-	-	2	1	-	-	1	2	1	-
Matagorda	11	-	-	-	16	13	1	-	19	19	10	1	26	18	16	8	25	29	16	20
Nueces	6	-	-	-	26	1	-	-	13	24	-	-	30	17	18	-	40	27	21	6
Refugio	1	-	-	-	6	2	-	-	18	8	1	-	24	13	9	-	23	22	8	11
San Patricio	1	-	-	-	12	-	-	-	6	11	-	-	7	6	11	-	21	6	8	10
Willacy	-	-	-	-	1	-	-	-	3	1	-	-	11	4	-	-	12	9	1	-
Total	131	-	-	-	397	127	1	-	527	440	108	4	619	524	352	62	643	596	491	249

Stillwater depth rasters were used to represent the effects of storm surge and wave setup. To assess potential wave impacts, the stillwater depth rasters were subtracted from the total water level rasters to obtain spatially distributed wave heights. The resultant maxima of 1% AEP total water depths, stillwater depths, and wave heights are summarized by county in the left half of Table 3.12. To further refine these ranges to those that are likely to impact existing bridges, total water depths, stillwater depths, and wave heights were extracted at the location of bridges from TxDOT’s bridge inventory. These values are summarized by county in the right half of Table 3.12. At coastal bridge locations, wave heights of up to 20.0 feet and stillwater depths of 62.6 feet are possible. Total water depths reach as high as 70.9 feet for the 1% AEP coastal storm event.

Table 3.12 Maximum wave height, stillwater depth, and total water depth for each coastal county, as well as the maximum values in the vicinity of bridges

County	County-wide Maximum Values (ft)			Maximum Values at Bridge Locations (ft)		
	Wave Height	Stillwater Depth	Total Water Depth	Wave Height	Stillwater Depth	Total Water Depth
Aransas	24.7	272.2	255.1	12.8	30.9	37.0
Calhoun	34.4	169.5	188.5	20.0	48.9	68.9
Cameron	24.7	204.3	212.1	11.4	36.3	44.5
Chambers	47.7	81.0	98.1	17.8	39.4	57.1
Galveston	40.6	247.2	265.9	19.5	62.6	70.9
Harris	49.3	110.5	89.3	15.1	57.5	58.4
Jackson	22.0	78.5	92.9	11.2	43.2	54.4
Jefferson	28.2	228.5	232.3	15.4	49.2	56.4
Kleberg	23.1	192.2	85.3	4.6	26.1	12.0
Matagorda	30.6	368.5	381.3	10.5	47.2	57.7
Refugio	20.6	47.7	62.3	11.8	34.0	45.8
San Patricio	21.3	94.5	98.8	-	-	-
Willacy	25.6	199.3	126.0	-	-	-
All	49.3	368.5	381.3	20.0	62.6	70.9

3.5 Summary

This analysis utilized the results of hydraulic and hydrodynamic modeling studies to assess the magnitude of potential flood impacts on bridges in riverine and coastal areas in Texas. Bridges in two highly populated counties, Travis and Harris, were analyzed to extract riverine flow characteristics, including water surface elevations, flow regimes, and velocities. Coastal

hydrodynamic characteristics, including stillwater elevations and wave heights, were extracted for bridges in the 16 coastal counties in Texas.

The findings of this analysis reveal the potential for high-velocity flows and substantial inundation depths at bridges in the studied counties. For the 1% AEP event, maximum flow velocities exceeded 20 feet per second in Travis County and 15 feet per second in Harris County. Across both counties, maximum flow depths exceeded 37 feet. Even for less-extreme flood events, flow velocities and inundation depths can be large. For example, velocities exceeded 19 feet per second in Travis County and 13 feet per second in Harris County for the 10% AEP event, while flow depths exceeded 25 feet in both counties. Coastal bridges are also widely exposed to potential risks due to elevated water levels and waves. Surge heights in excess of 18 feet are possible for hurricanes with intensity above Category 3. For the 1% AEP coastal storm event, bridges in all studied coastal counties except Kleberg could experience wave heights greater than 10 feet.

The hydraulic and hydrodynamic parameters summarized in this report informed Tasks 4 and 5 of this project, which include physical and numerical modeling of bridge superstructures subject to flood loading. Scale modeling conducted in a river flume and wave tank drew upon the riverine and coastal flow data presented here to develop feasible scenarios for testing. This allowed for an assessment of the potential benefits of implementing shear keys as countermeasures to reduce the risk of bridge failure during flood events.

4 PHYSICAL MODELING OF RIVER CROSSING BRIDGES

4.1 Introduction

Physical models are commonly used to estimate the hydrodynamic forces on hydraulic structures such as bridges, culverts, spillways, etc. A physical model is a reduced-size representation of the prototype (i.e., full-scale structure) that is used during the design stage to optimize a structure and to ensure its safe operation. When surface tension and compressibility can be neglected in fluid dynamics, the Reynolds number (Re) and Froude number (Fr) are the most influential force ratios that should be considered in designing a physical model. These two dimensionless numbers represent inertia and gravity forces that govern flow in open channels. Drag coefficients do not change significantly across the range of the Reynolds numbers usually observed in the lab ($Re > 10^4$) and in field data ($Re > 10^6$) (Oudenbroek 2017). Therefore, Froude number scaling was used to design physical models of bridge elements in this study. The geometrical parameters of the bridge models were selected based on the experimental facility's ability to mimic the field conditions. The physical modeling of river-crossing bridges was simulated in a laboratory flume to provide the TxDOT with information on the effects of flood forces on superstructures and substructures, using typical TxDOT bridge details. The physical model study included the evaluation of forces on the TxGirder, Box Beam, and Slab Beam superstructures without and with substructures. The performance of 1:50 scaled-down bridge models with different deck system shapes was examined under different flow conditions, including:

- relative submergence (inundation ratio) from 0.25 to 3
- proximity ratio from 1.09 to 5.07
- Froude number from 0.22 to 0.34
- degree of flow blockage with debris from 0.11 to 0.39.

Experiments were conducted for 24' and 44' roadways (with deck widths of 26' and 46', respectively) and 0°, 15°, 30°, and 45° skewness to assess the effect of deck geometry on flood forces. Selected bridge structures were also tested under wave action. The effect of waves on vertical and horizontal forces was assessed under different wave conditions. The parameters tested include wave height and wave period, flow depth, and bridge location with reference to the streambed.

4.2 Physical Modeling Approach and Plan

The effects of flood forces on bridges were investigated through physical modeling in a laboratory setup. In consulting with the TxDOT project team, four typical TxDOT bridge details were selected for small-scale modeling. The bridge superstructure models included:

- Model 1: TX-28 I-Girder – 28" high
- Model 2: TX-54 I-Girder – 54" high
- Model 3: SB-15 Slab Beam – 15" high
- Model 4: BB-28 Box Beam – 28" high

Two common types of TxDOT roadways were considered: 24-ft roadway (26-ft wide deck) and 44-ft roadway (46-ft wide deck). The experiments were performed with and without bridge substructures. The effects of deck skewness on hydrodynamic forces were examined on bridges with 0°, 15°, 30°, and 45° skews. Selected bridge models were tested under wave action and debris loading. The coefficient of drag and lift forces and overturning moment are determined for bridge decks under various flow conditions. The experiments are grouped as follows:

- *Series A*: Bridge Model 1 to 4 with 26' and 46' wide decks with 0° skew
- *Series B*: Bridge Model 1 with 46' wide deck and 15°, 30°, and 45° skews
- *Series C*: Bridge Model 2 with 46' wide deck with debris
- *Series D*: Bridge Models 1 to 4 with 46' wide deck and substructure (no contact between beams and bent caps)
- *Series E*: Bridge Model 1 and 2 with 46' deck and substructure (beams in contact with bent caps)
- *Series F*: Bridge Model 2 with 26' and 46' wide decks under wave action

Test Series A to C replicate bridges that span across a stream without middle piers. In test Series D and E, the effects of substructures on flow conditions and forces acting on superstructures were examined for bridges span across a stream and have middle piers. The details of each bridge model are presented in the following. The procedure for experiments Series A to F is discussed in Section 4.4.2. The experiment conditions for each series are summarized in Table D.1, Appendix D.

4.3 Bridge and Debris Models

This section discusses the details of the bridge and debris models employed in this project.

4.3.1 Bridge Superstructure and Substructure

Bridge models are 1:50 scale of the TxDOT bridges. They were made of aluminum because it has a similar specific weight to reinforced concrete. The superstructures tested each had two bridge width configurations: 1) 26' wide deck and 2) 46' wide deck. The cross-sections of the

superstructures are shown in Appendix D Figure D.1 to D.4 including both deck types with TX28, TX54, Slab beam and Box beam. The railing used in the experiment is T221 that measures 32 inches in height, and like the other bridge components, it was machined out of aluminum (Figure D.5). The dimensions of bridge models are summarized in Tables D.2 to D.5 in Appendix D. The scale model of the bridge substructure consisted of three bent caps and twelve piers. A false bottom was used to hold piers together in the flume. The schematic of the bridge superstructure and substructure assembly is shown in Figure 4.1.

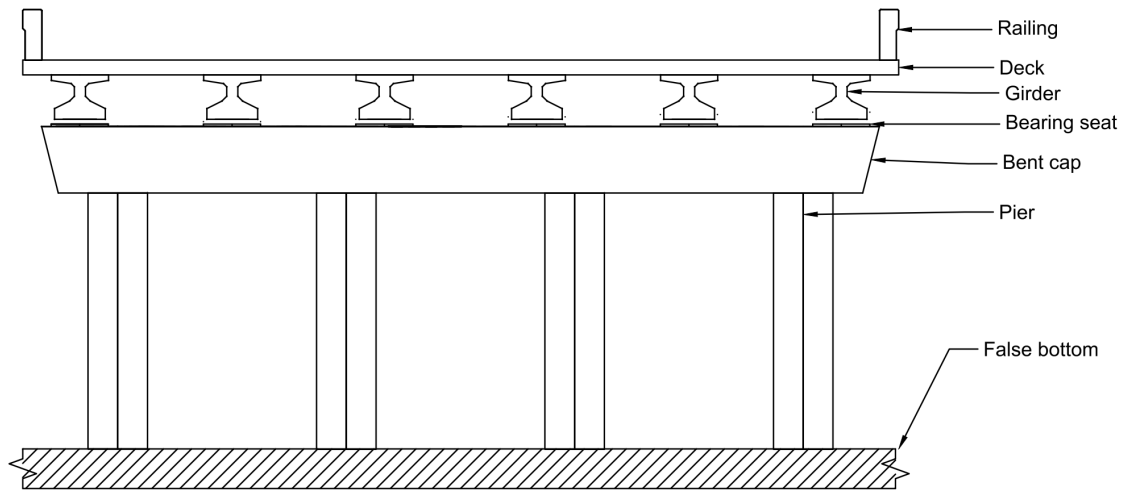


Figure 4.1 Schematic of the bridge substructure and superstructure

4.3.2 Debris

Two types of common debris mats were tested in experiments with debris:

- Flat plate
- Wedge debris

Flat Plate Debris

The flat plate debris consisted of a 0.12" thick steel plate rigidly fixed to the upstream side of the bridge deck. The flat plate resembled the vertical accumulation of debris upstream of bridges. Its height was set at 2.36" (9.8 ft high in prototype). The 9.8 ft is the maximum height of interlocking debris, such as tree limbs against a bridge superstructure (Wellwood and Fenwick, 1990). Its width matched the 11.9" width of the bridge deck section to ensure an even channel constriction. The geometry of the flat plate debris is shown in Figure 4.2a.

Wedge Debris

The wedge debris was made up of pinewood dowels fixed together with wood glue. These 0.75" diameter dowels represent, on average, the width of trees in the "Southern Forest Region" (Diehl, 1997) that Texas falls into. The wedge debris was modeled with a flume-width triangular cross-section, and its dimensions were 2.36" high and 7" long at a 1:50 scale (9.8 ft and 29 ft in

prototype). The wedge was positioned in front of the flat plate to provide better surface contact between the wedge debris and the deck and allowing the transfer of all forces from the wedge debris to the bridge. The geometry of the wedge debris is shown in Figure 4.2b.

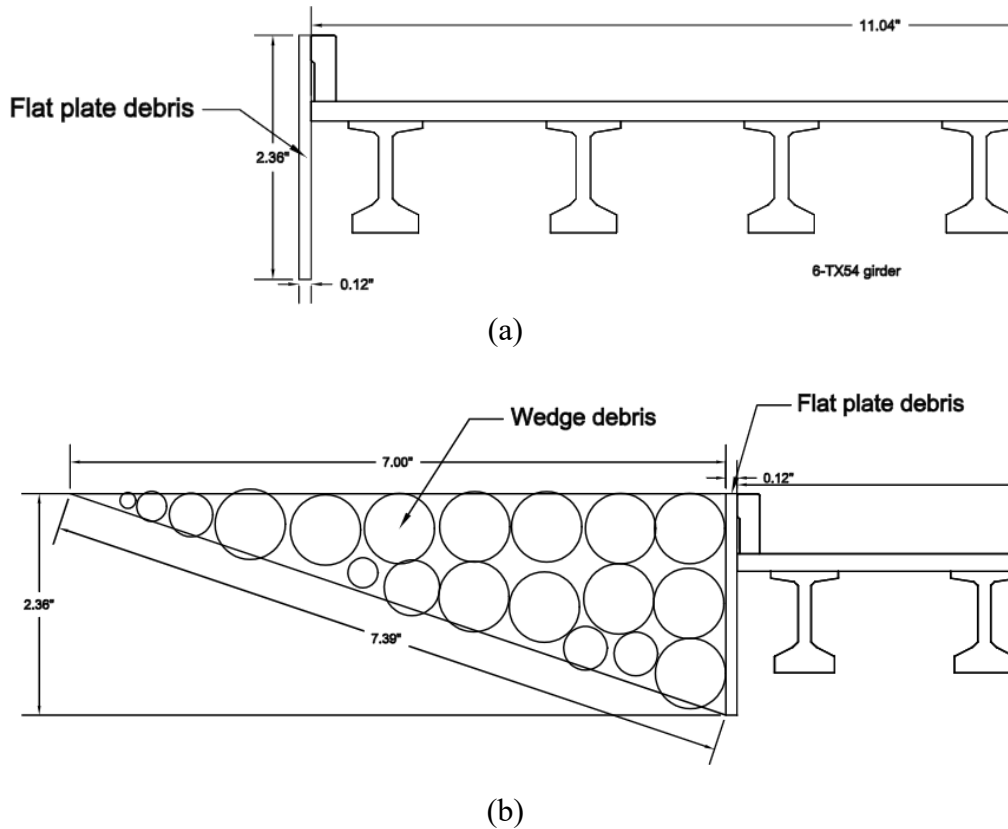


Figure 4.2 Schematic of the debris model: (a) flat plate debris and (b) wedge debris

4.4 Flow and Wave Parameters

This section discusses the flow parameters and wave parameters employed in this project to study the hydrodynamic loads on inundated bridges.

4.4.1 Flow Parameters

The drag, lift, and moment coefficients are dependent on flow parameters, including Reynolds number and Froud number, and the relative dimension of the bridge deck thickness to the flow depth, i.e., inundation ratio and proximity ratio.

Reynolds Number (Re)

Since the Reynolds number was above 10^4 in all experiments, the relationship between the drag coefficient value and the coefficients on the Reynolds number did not need to be investigated.

Froude Number (Fr)

The results of the analysis of 908 Texas Department of Transportation administered bridges showed an average channel Froude number of 0.39 with several bridge sites exceeding that amount up to 1.3 (Task 3 Technical Memorandum). The upper value is higher than the maximum Froude number of 0.34 that could be simulated in the laboratory flume due to the limitation of the experimental setup. As discussed in Section 6, this limitation may not be critical as long as the results provide calibration data for the computational fluid dynamic (CFD) models undertaken for the project (Chapter 5).

Inundation Ratio (h^*)

The inundation ratio ranged from 0.25 to 2.5 in experiments with bridge Models 1 and 4. The Bridge Model 2 was tested under inundation ratios up to 2.0 due to the experimental setup limitation. For bridge Model 3, it was possible to maintain the inundation ratio up to 3.0.

Proximity Ratio (Pr)

Chapter 3 exhibits that TxDOT bridges may have a range of proximity ratios from 0.63 to 5. The effects of the proximity of the superstructure to the flume bed on the coefficient of drag and lift forces and moments were investigated by conducting experiments using Model 1. Based on the finding from this experiment, a minimum proximity ratio of 3 was maintained in all experiments. The results of this investigation are presented in Section 4.7.

4.4.2 Wave Parameters

The effect of wave loading on bridges was investigated using Model 2 with 26' and 46' wide decks. Submergence depths and elevations are chosen such that the bridge model may be fully submerged, partially inundated, or fully elevated above still water level (SWL). The wave experiment setup is shown in Figure 4.3.

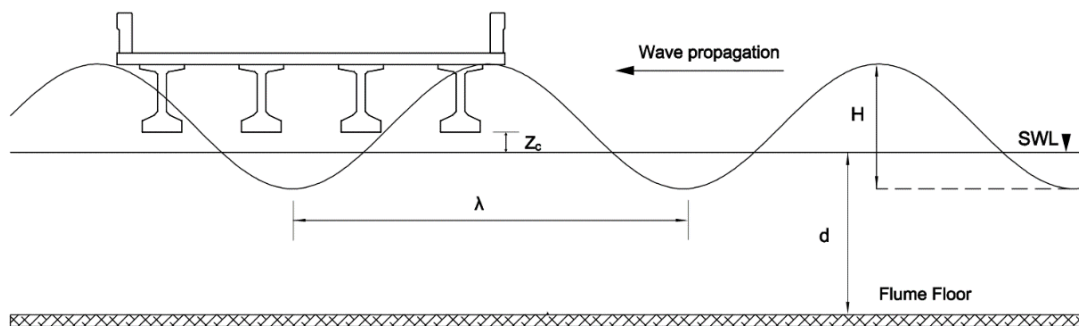


Figure 4.3 Wave experiment schematic (Model 2: TX54-26' wide deck)

Chapter 3 indicates that TxDOT bridges in coastal areas may experience wave height ranging from 4.6 ft to 20 ft, with the still water depth ranging from 26 to 63 ft. The experiments were conducted with wave heights of 1, 2, and 3 inches (4.2, 8.3, and 12.5 ft in prototype), which fall in the range of observed field data. The wave periods of 0.48, 0.61, and 0.94 sec (24, 30.5, and 47 sec in prototype) were also simulated. The water depth was changed from 8.5 to 9.5 inches (37.5 to 39.6 ft in prototype). The bridge location with reference to the still water level (SWL) was set at three different elevations to investigate the wave force effects at different bridge submergences. At these positions, the SWL was 0.5 inches above the low cord (Z_{c1}), at the low cord elevation (Z_{c2}), and 0.5 inches below the low cord (Z_{c3}), as shown in Figure 4.4. The maximum and minimum range of these parameters are summarized in Table 4.1.

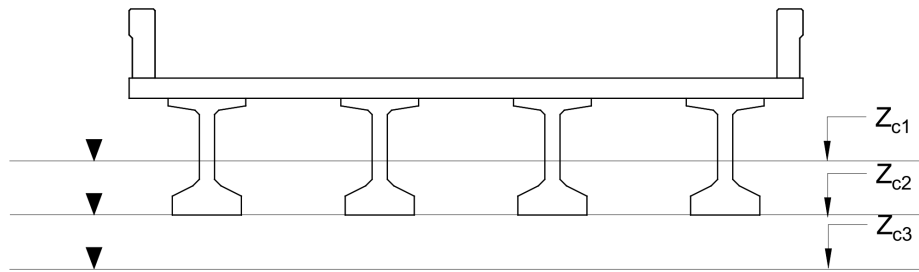


Figure 4.4 Bridge position with reference to the still water surface elevation during wave experiments (Model 2: TX54-26')

Table 4.1 Minimum and maximum wave experiment parameters

Parameter	Minimum		Maximum	
	Model	Prototype	Model	Prototype
Water depth, d (in)	8.5	425	9.5	475
Wave period, t (s)	0.48	24	0.94	47
Wave height, H (in)	1	50	3	150
Clearance height, Z_c (in)	-0.5	-25	0.5	25

4.5 Experimental Setup and Procedure

4.5.1 Experimental Setup

The experiments were conducted in a 16' long, 12" wide, and 18" deep rectangular plexiglass flume (Figure 4.5a). The flow capacity of the flume was 500 gallons per minute (gpm), maintained by the flume's recirculatory pumping system and two external pumps. The flume was set horizontal, and the water depth was controlled by an adjustable tailgate. The flow rate supplied by the external pumps was measured with a digital SonoTrac ST30 ultrasonic flowmeter attached to the flume's 4" inlet line. The orifice method was used to measure the discharge supplied by the

recirculatory pumping system. The point velocity upstream of the bridge was measured at the beginning of each experiment using a three-dimensional Acoustic Doppler Velocimeter (ADV). Flow depth was recorded using a point gauge upstream of the superstructure or by measuring tapes fixed to the flume wall. Loads in three different directions and moments were measured using an Interface-Model 3A100-100N-D11 with 100 N capacity load cell and an Interface-Model MRT2 Torque cell with 10 N-m capacity, respectively. A mounting frame was designed and constructed to house the load cell and torque cell and isolate the instruments from external vibrations and keep them well-elevated above the water surface due to their vulnerability to submersion. The cells were connected to the bridge deck via two vertical support plates (Figure 4.5b).

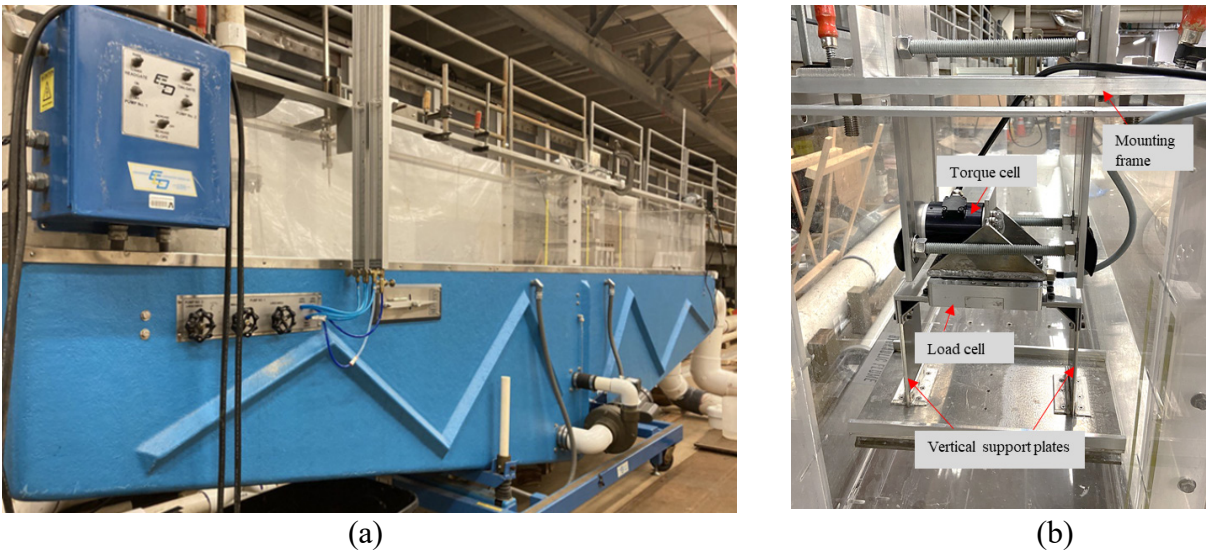


Figure 4.5 Photo of the: (a) experimental flume and (b) mounting frame, load and torque cells, and support plates

4.5.2 Experiments Procedure

Four distinct procedures were followed to conduct Series A to F experiments:

- Superstructure experiments (Series A and B)
- Debris experiments (Series C)
- Superstructure and substructure experiments (Series D and E)
- Wave experiments (Series F)

Superstructure Experiments

In this series of experiments, the bridge model superstructure was fixed to the mounting frame via two vertical support plates. The frame was firmly attached to the flume's top railing to prevent any movement and vibrations while transferring forces to the load and moment cells. Sample photos of the superstructure experiments are shown in Appendix D (Figure D.6 and D.7). The frame was secured to the flume with care taken to ensure that there was sufficient clearance between the flume

walls and both sides of the bridge deck. The bridge deck elevation was set to the desired height above the flume bottom, corresponding to the highest proximity ratio. The pumps were activated, and valves on the flume's inlet pipes were opened until the desired flow rate was achieved. Before recording force data, the load and moment cells' readings were zeroed, with the water level being kept below the bridge model. The height of the flume's tailgate was then set so that the lowest inundation ratio was reached. Once the model elevation and flow were set at the desired test conditions, the force and moment data were recorded for two minutes. The bridge elevation was lowered in steps to test the bridge model for higher inundation ratios. The same procedure was followed for each inundation ratio.

Debris Experiments

In experiments with debris, the flat plate and wedge debris were attached to the upstream side of superstructures alternatively. Sample photos of the debris experiments are shown in Figure D.8, Appendix D. The bridge model with debris was placed at the desired elevation (proximity ratio $Pr = 3.0$). Then, the pumps were activated, and valves on the flume's inlet pipes were opened until the desired flow rate was achieved. Before recording force data, the load and moment cells' readings were zeroed, with the water level being kept below the bridge model. The tailgate was then set so that the smallest inundation ratio and blockage ratio were reached. Once the model elevation and flow were set at the desired test conditions, the force and moment data were recorded for two minutes. The tailgate was raised in steps, and the flow rate was increased accordingly to test the bridge model for higher inundation and blockage ratios. The same procedure was followed for each blockage ratio.

Superstructure and Substructure Experiments

This series of experiments was conducted by placing both superstructure and substructure inside the experimental flume. The substructures consisted of bent caps and piers attached together and were fixed to a false bottom, replicating the connection between piers and the bridge foundation. The false bottom was rigidly fixed to the flume bottom. The bridge superstructure was placed on top of the substructure. Two scenarios were considered: a) a gap left between the girder's soffit and top of the bent cap (no-contact scenario), and b) the superstructure was placed directly on the top of the substructure (with-contact scenario).

Superstructure and Substructure Experiments (no-contact scenario)

In order to measure forces acting on the superstructure, the bridge model must be attached to the load and torque cells through the support plates. A small gap was left between the girders' soffit and the top of bent caps to ensure that there was no resisting force due to friction between the superstructure and substructure. Then, the pumps were activated, and valves on the flume's inlet pipes were opened until the desired flow rate was achieved. Before recording force data, the load and moment cells' readings were zeroed, with the water level being kept below the bridge model. The tailgate was then set so that the smallest inundation ratio was reached. Once the model elevation and flow were set at the desired test conditions, the force and moment data were recorded

for two minutes. The tailgate was raised in steps, and the flow rate was increased accordingly to test the bridge model for higher inundation ratios and Froude numbers. The same procedure was followed for each inundation ratio. Sample photos of the superstructure and substructure experiments are shown in Figure D.9, Appendix D.

Superstructure and Substructure Experiments (with-contact scenario)

In this test series, superstructures were placed directly on the top of the substructure. Rubber bearing pads were placed on the bearing seats to add friction between the superstructure and substructure. Sample photos of the superstructure and substructure experiments are shown in Appendix D (Figure D.10). The 50-durometer neoprene rubber was used as the bearing pad between the substructure and the superstructures (TxDOT Bridge Design Manual, 2020). The dimensions of the rubber pads were scaled down according to the physical model scale. The experiments were conducted under various flow conditions to induce bridge failure. Therefore, the bridge deck was not connected to the load and torque cells, and no force measurements were collected.

Wave Experiments

In this test series, a still water level pool was created by closing off the flume outlet. The bridge superstructure was mounted to the flume at the desired elevation. Sample photos of the wave experiments are shown in Appendix D (Figure D.11). The flume wave generator was used to create waves of various amplitudes, periods, and speeds. The bridge position was changed to different elevations to evaluate wave forces at different submergence conditions. The forces and moment readings were taken using the same procedure outlined in the superstructure experiment.

4.6 Results

The readouts of the load and torque cells were corrected to calculate the net hydrodynamic forces and moments exerted on the bridge models, and the hydrostatic (F_h) component of the total streamwise force was subtracted to calculate the drag force. The buoyant force (F_B) was deducted from the measured vertical force to calculate the net lift force acting on the bridge deck, and the torque cell readout moment was corrected to consider the centroidal moment (M_{cg}) with respect to the center of gravity of the bridge deck system. After these corrections were made, the drag (C_D), lift (C_L), and moment (C_M) coefficients were calculated using Equations 2.3 to 2.5. The results of experiments with different types of bridge superstructures are summarized and discussed in the following sections. The drag, lift, and moment design charts and equations for different bridge decks are developed. The effect of deck skewness, flow blockage by debris and substructures on these coefficients are quantified. The forces exerted on bridge decks by waves are assessed and compared with the flood-induced forces.

4.6.1 Superstructures with no Debris

The design charts for superstructures with different deck types, heights, and widths are presented in this section. Bridge decks are not skewed, and flow is not obstructed by substructures and debris.

The design charts for superstructures with I-girders TX28 and Tx54, Slab Beam SB15, and Box Beam BB28 are presented in Figures 4.6 to 4.9, respectively. The figures represent the result of the experiments performed with 26' and 46' wide decks under different Froude numbers. The experimental data were used to calculate parameters for fitting equations for each deck type for drag, lift, and moment coefficients (Equations 4.1 to 4.3). In these equations, h^* is inundation ratio, and C_D , C_L , C_M are the drag, lift, and moment coefficients. The upper and lower limits of each equation are determined by parameters a , b , and c that are given in Table 4.2.

$$C_D = a(e^{-2(h^*)^3}) - 2.3(e^{-b(h^*)^{3.5}}) + c \quad (4.1)$$

$$C_L = a(e^{-1.3(h^*)^4}) - 1.85(e^{-b(h^*)^3}) + c \quad (4.2)$$

$$C_M = 0.8(h^*)^{2.2}(e^{-1.8(h^*)^{1.5}}) + c \quad (4.3)$$

The upper limit of the drag and lift coefficients is bounded by data points from experiments conducted under the smaller Froude numbers, while the lower limit of these coefficients is bounded by data points from the higher Froude number experiments. These general trends were observed across all superstructures. The upper limit of the moment coefficient is bounded by data points from 26' wide deck tests, while the lower limit of the moment coefficient is bounded results from 46' wide deck experiments.

The results from all experiments are combined to develop universal design charts and equations for drag, lift, and moment coefficients. Figure 4.10 is produced using the data points from experiments with four deck types (TX28, TX54, SB15, BB28), two deck widths (26 ft, 46 ft), and three Froude numbers (0.2, 0.27, 0.34). Equations 4.1 to 4.3 also express the general trend of drag, lift, and moment coefficients as a function of the inundation ratio for all deck and girder types. The upper and lower boundaries of these coefficients can be calculated using constant parameters a , b , and c listed in Table 4.2.

4.6.2 Bridges with Skewed Decks

The effects of deck skewness on the design value of drag, lift, and moment coefficients are presented in this section. The results from experiments with TX28 with the skewed deck are compiled and shown in Figure 4.11. In this figure, the experimental data for a 46-ft wide deck with 15°, 30°, and 45° skewness is plotted along with the data collected for a bridge deck with no skewness. As can be seen from Figure 4.11, The coefficient of drag force decreased with an increase of deck angle of skewness. The decrease in the drag coefficient due to skewness is more significant for the inundation ratio h^* greater than 1. As shown in this figure, the results from the experiment with 45° and $Fr = 0.34$ define the lower boundary of the drag coefficient. The skewed deck results show a trend of increasing lift coefficient values with increasing angles of skewness. The results from the experiment with 45° represent the upper boundary of the lift coefficient. The moment coefficient also decreased with an increase in angles of skewness. This trend is more evident for the inundation ratio h^* greater than 1.25.

4.6.3 Bridges with Debris Loading

The effects of debris loading on the design value of drag, lift, and moment coefficients are presented in this section. These coefficients for a 46-ft deck and TX54 I-girders are shown in Figure 4.12. The results for the same superstructure and the same flow conditions and blockage and no debris are also shown for comparison. This figure shows that debris accumulation upstream of a bridge deck in the form of a vertical obstruction (simulated by flat plate debris mat) could significantly increase the drag coefficient. The increase in drag coefficient is more severe for smaller blockage ratios. The wedge mat debris, on the other hand, did not impose a significant increase in the drag coefficient. The lift coefficient showed similar values under smaller blockage ratios for with and without debris scenarios. As the blockage ratio increased, the lift coefficient showed a decreasing trend in wedge debris experiments, whereas it increased in the experiment with the flat plate debris. The results for the flat plate debris were, however, similar to the without debris scenario. The moment coefficients for the bridge deck without debris and with flat plate debris were almost the same for all blockage ratio testes; however, the wedge debris showed a decreasing trend with the increase in blockage ratio. Even though these conclusions are made based on the experiments on a deck with TX54 I-girders, they can be extended to other types of deck superstructures. The reason is the height of the debris mats was more than twice the height of the superstructure.

4.6.4 Bridges with Substructures

The effects of piers and bent caps on the design value of drag, lift, and moment coefficients are presented in this section. The results from experiments with TX28, BB28, and SB15 bridge models are combined and presented in Figure 4.13. The TX54 bridge model results were excluded since it was tested under a different proximity ratio. In this figure, the upper and lower limits of the superstructure-only scenario are also plotted for comparison. As can be seen, the presence of substructure increased the drag and lift coefficients significantly for $h^* > 1.25$. The moment coefficient was lower for the superstructure-substructure scenario but still within in range of upper and lower limits for the superstructure-only scenario.

4.6.5 Effect of Proximity Ratio (Pr)

The effect of proximity of the superstructure to the flume bed on the coefficient of drag and lift forces and moments was investigated. The experiments were conducted using TX28 with proximity ratios between 1.09 to 5.07 for inundation ratios of 1 and 2. It was found that the coefficients of forces and moment rapidly approached a plateau as the proximity ratio increased from 1.09 to 2.9 (Figure 4.14). For greater proximity ratios, all coefficients remained at relatively constant values. This pattern was consistent at both $h^* = 1.0$ and 2.0. Based on this finding, a minimum proximity ratio of 3 was maintained in all experiments.

4.6.6 Bridges with Wave Loading

The results are combined to determine the upper and lower boundaries of these forces under different wave heights and periods, and water depths. Figure 4.15 compares the vertical and

horizontal wave forces on two types of bridge decks with three separate elevations and varying wave height, water depth, and wave period. The vertical wave force on the 46-ft wide bridge deck was larger than the vertical wave force on a 26-ft wide bridge deck. The horizontal wave force did not exhibit a significant difference between the 46-ft and 26-ft decks. Additionally, the maximum wave force was observed when the bridge superstructure was submerged under the still water level, and the minimum wave force was observed when the bridge was located above the still water level. In general, both vertical and horizontal forces increased with the increase in wave height and water depth but decreased with an increase in the wave period. The maximum and minimum vertical and horizontal forces due to flood loading on TX54 bridge model with 26' and 46' wide deck (Series A experiments) are also shown in Figure 4.15. The comparison between flood and wave forces shows that the wave-induced vertical forces were higher than the flood-induced vertical forces while the horizontal forces were within the same range. It should be noted that the absolute values of vertical forces were used in this comparison. Both flood and wave loadings may impose positive or negative uplift forces. Therefore, vectoral summation of uplift and buoyant forces could be either positive or negative.

4.6.7 Superstructure and Substructure (contact scenarios)

The substructure and superstructure were simulated under the Fr of 0.20 to 0.34 with bridge submergence ranging from 0.25 to 2.5. Load and torque cells were not attached with the bridge superstructures, as the purpose of this test was only to observe the failure of the bridge. However, no bridge failure was observed under these flow conditions.

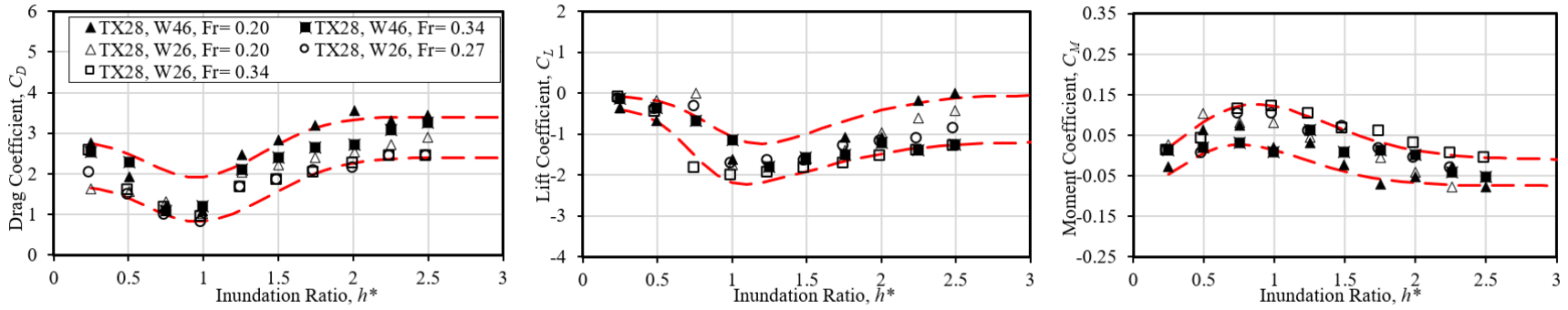


Figure 4.6 Design charts for drag, lift, and moment coefficient versus inundation ratio for superstructure I-girder TX28

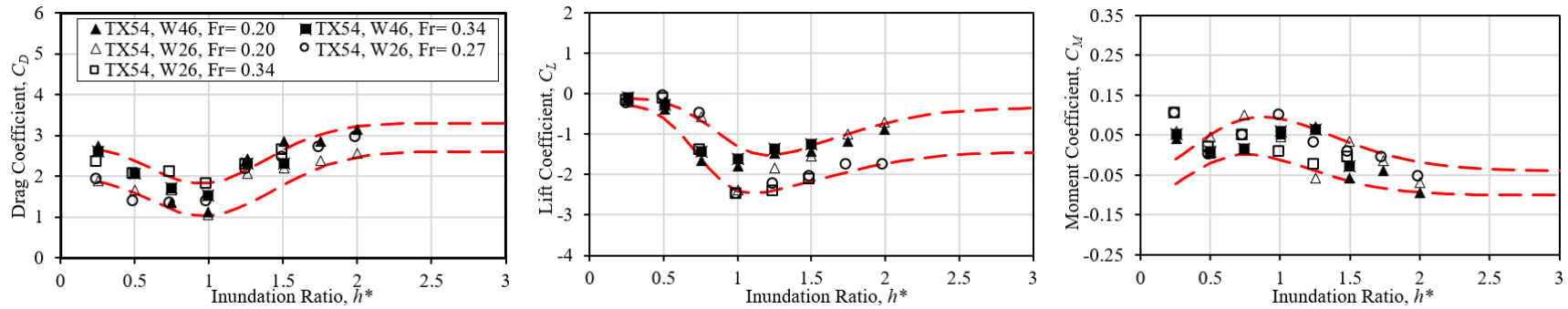


Figure 4.7 Design charts for drag, lift, and moment coefficient versus inundation ratio for superstructure I-girder TX54

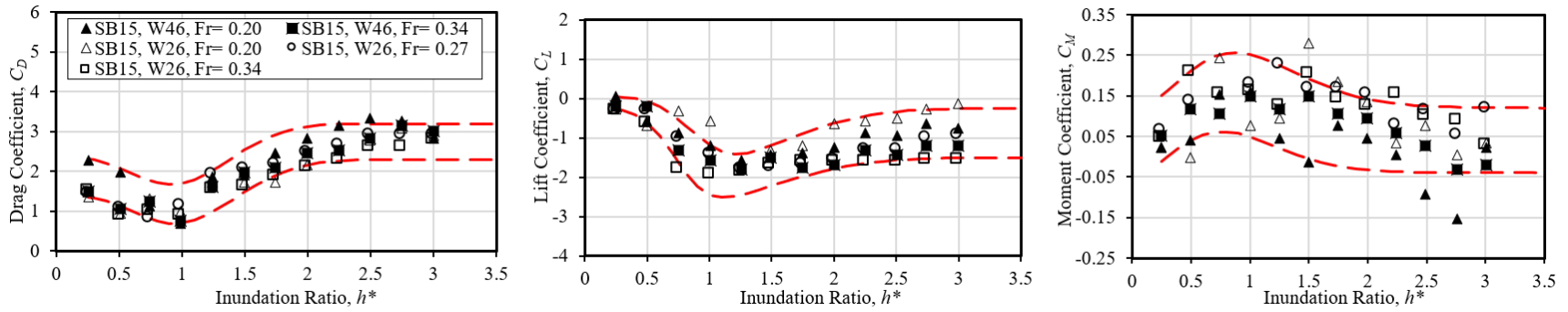


Figure 4.8 Design charts for drag, lift, and moment coefficient versus inundation ratio for superstructure Slab Beam SB15

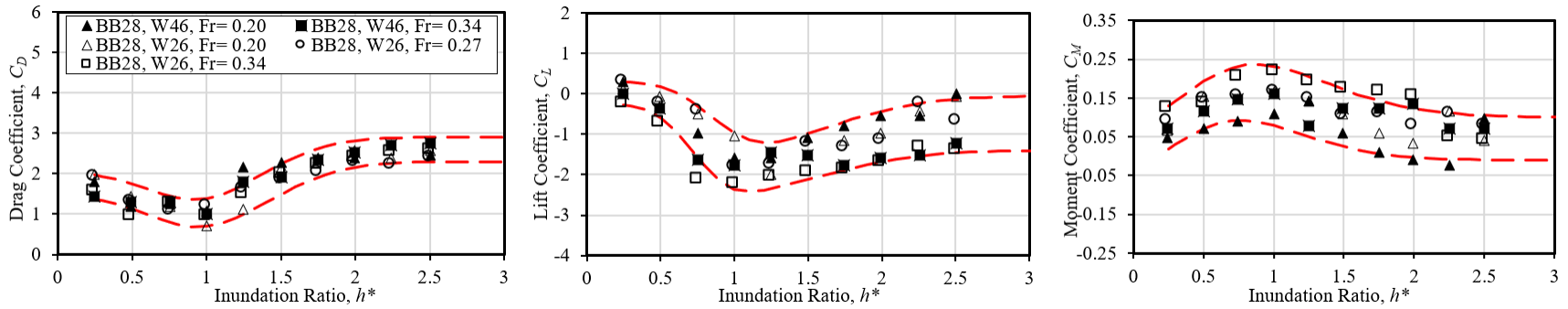


Figure 4.9 Design charts for drag, lift, and moment coefficient versus inundation ratio for superstructure Box Beam BB28

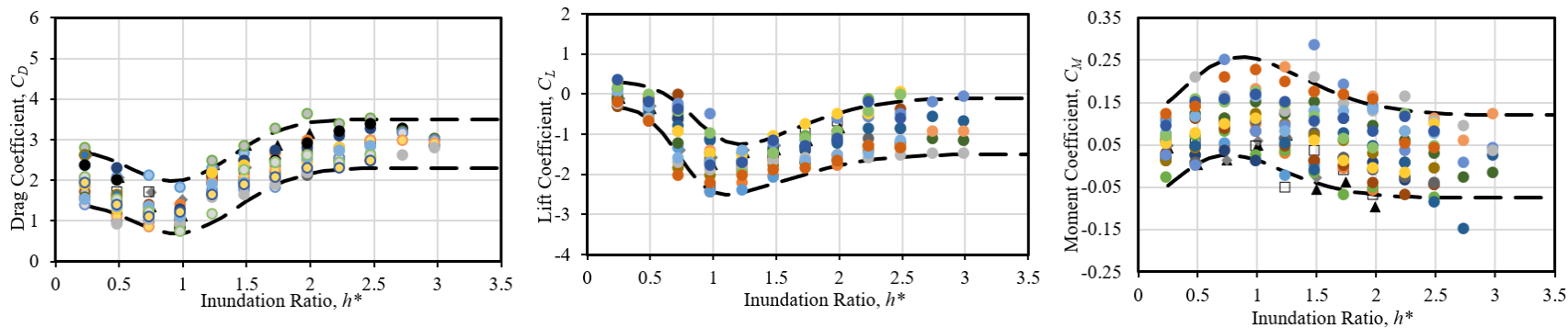


Figure 4.10 Design charts for drag, lift, and moment coefficient versus inundation ratio for all deck types

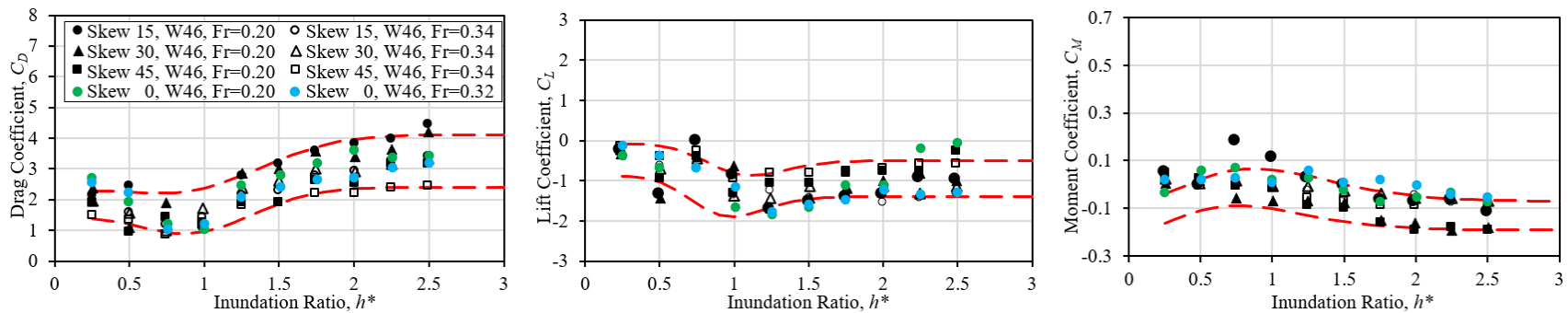


Figure 4.11 Effects of deck skewness on drag, lift, and moment coefficients

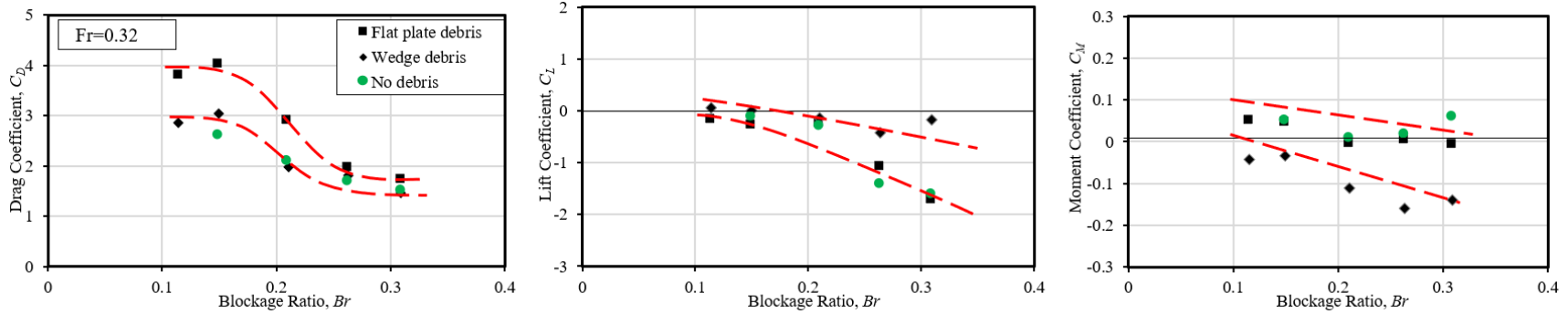


Figure 4.12 Effect of debris on drag, lift, and moment coefficients

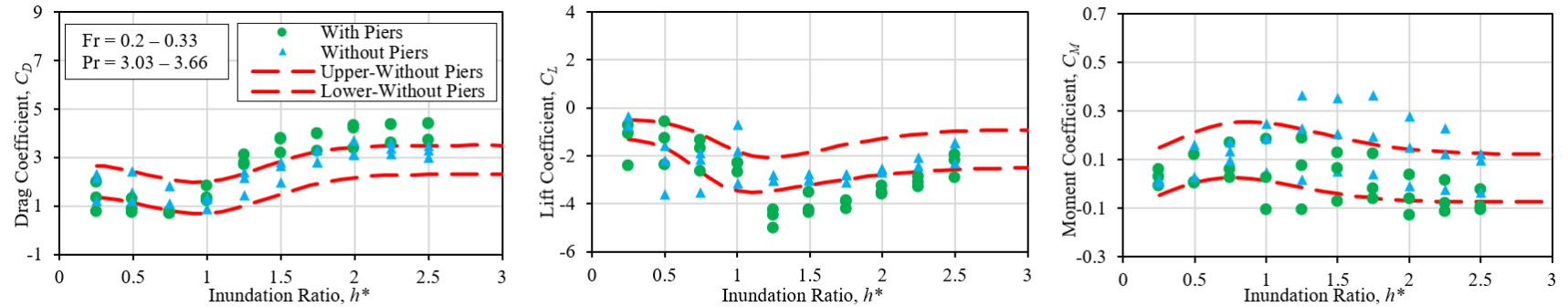


Figure 4.13 Effects of substructures on drag, lift, and moment coefficients

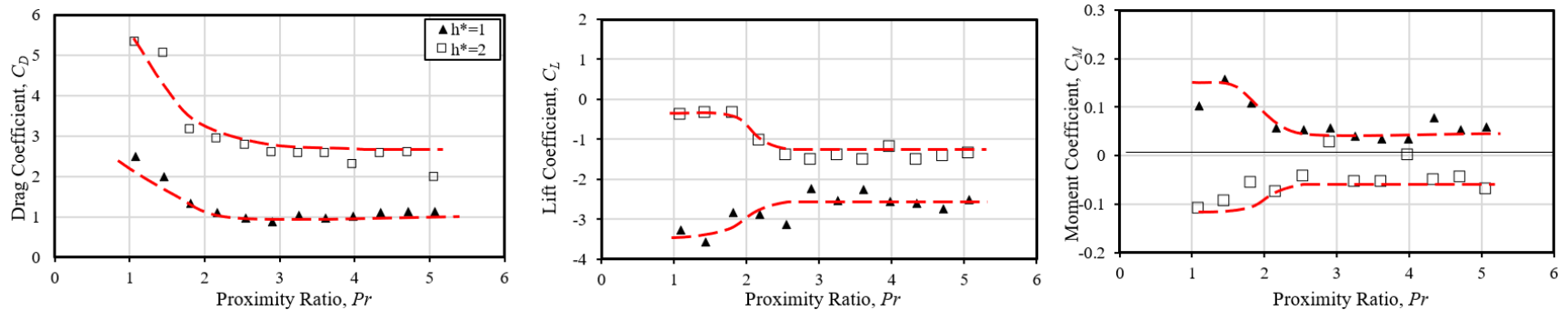


Figure 4.14 Dependency of drag coefficient, lift, and moment coefficient on proximity ratio (Model 1: TX-28 with 26' deck)

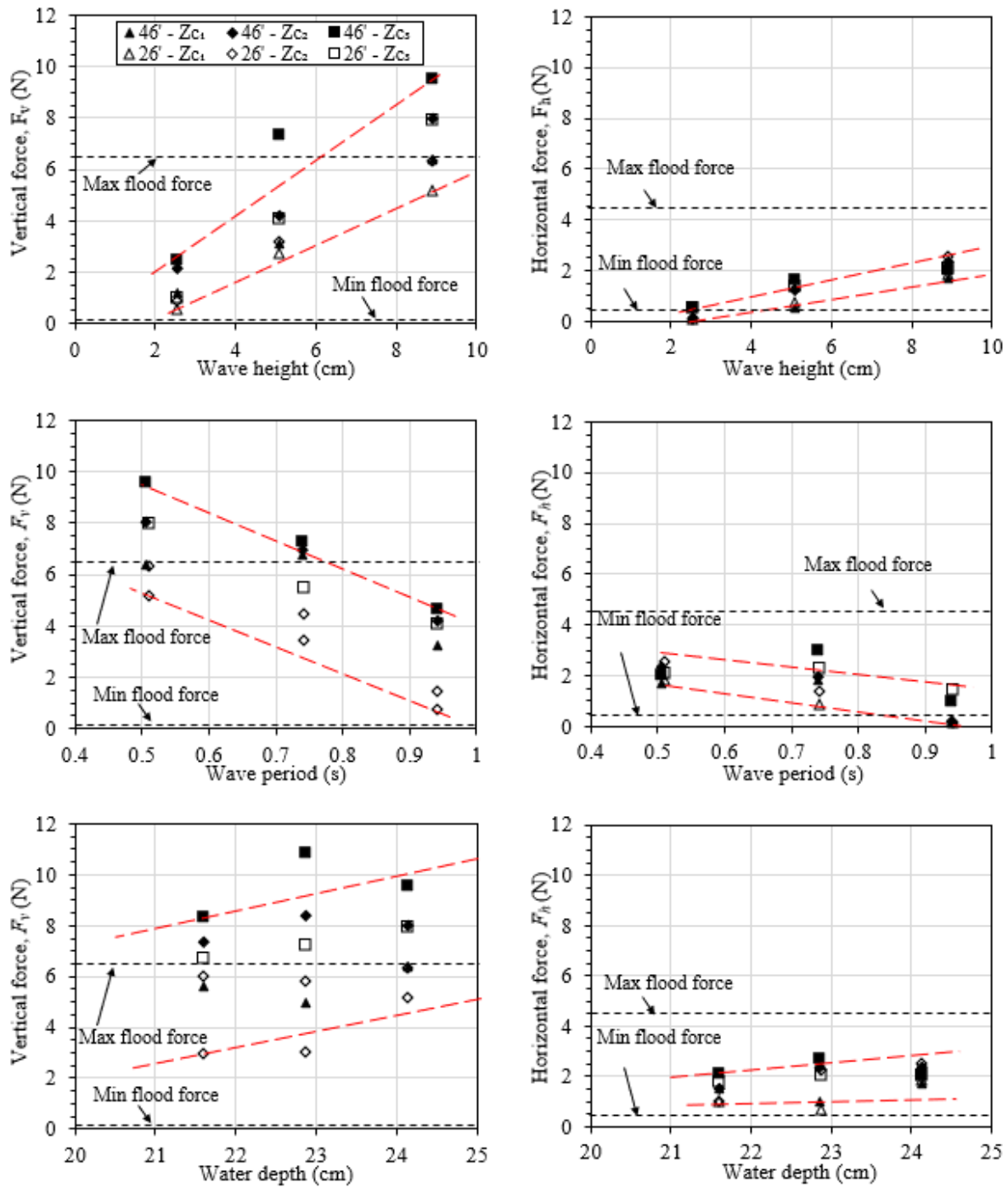


Figure 4.15 Comparison of vertical and horizontal wave and flood forces

Table 4.2 Summary of fitted equation parameters for Tx28, TX54, SB15, BB28, and all deck types

Deck Type	Parameter	<i>a</i>	<i>b</i>	<i>c</i>
I-girder (TX28)	$C_{D(Upper)}$	1.7	0.3	3.4
	$C_{D(Lower)}$	1.6	0.25	- 2.4
	$C_{L(Upper)}$	1.8	0.2	- 0.05
	$C_{L(Lower)}$	2.2	0.2	1.2
	$C_{M(Upper)}$	-	-	- 0.01
	$C_{M(Lower)}$	-	-	- 0.075
I-girder (TX54)	$C_{D(Upper)}$	1.7	0.3	3.3
	$C_{D(Lower)}$	1.6	0.25	2.6
	$C_{L(Upper)}$	2.1	0.2	- 0.35
	$C_{L(Lower)}$	2.6	0.2	- 1.45
	$C_{M(Upper)}$	-	-	-0.04
	$C_{M(Lower)}$	-	-	-0.1
Slab Beam (SB15)	$C_{D(Upper)}$	1.45	0.3	3.2
	$C_{D(Lower)}$	1.4	0.25	2.3
	$C_{L(Upper)}$	2.15	0.2	- 0.25
	$C_{L(Lower)}$	2.65	0.2	- 1.50
	$C_{M(Upper)}$	-	-	0.12
	$C_{M(Lower)}$	-	-	-0.04
Box Beam (BB28)	$C_{D(Upper)}$	1.4	0.3	3.2
	$C_{D(Lower)}$	1.4	0.25	2.3
	$C_{L(Upper)}$	2.2	0.2	- 0.25
	$C_{L(Lower)}$	2.55	0.2	- 1.50
	$C_{M(Upper)}$	-	-	0.1
	$C_{M(Lower)}$	-	-	-0.01
All Deck Types	$C_{D(Upper)}$	1.5	0.3	3.5
	$C_{D(Lower)}$	1.4	0.25	2.3
	$C_{L(Upper)}$	2.25	0.2	- 0.1
	$C_{L(Lower)}$	2.6	0.2	- 1.5
	$C_{M(Upper)}$	-	-	0.12
	$C_{M(Lower)}$	-	-	-0.075

4.7 Summary

A series of experiments were conducted in a laboratory flume to study hydrodynamic forces on bridges under flood and wave loading. The 1:50 scale models of the TxDOT's typical reinforced concrete bridge superstructures were tested in these experiments. The drag, lift, and moment design charts and equations were developed for TX28 and TX54 I-Girders, Box Beam BB28, and Slab Beam SB15 superstructures. The effects of deck skewness, debris, and substructure on these coefficients were evaluated and quantified. The key findings can be summarized as follows.

- The developed design charts and equations show the dependency of drag, lift, and moment coefficients to inundation ratio (h^*). The drag coefficient decrease as the inundation ratio

approaches 1 and then increases with a decreasing trend for smaller and larger inundation ratio.

- The drag and lift coefficients showed some dependency on the Froude number. The upper limit of the drag and lift coefficients design charts and equations is bounded by data points from experimental results under small Froude numbers, while the lower limit of these coefficients is bounded by data points from the higher Froude number experiments.
- The deck width showed some effect on the moment coefficients. The upper limit of the moment coefficient is bounded by data points from 26' wide deck tests, while the lower limit of the moment coefficient design charts and equations is bounded results from 46' wide deck experiments.
- The deck skewness would impact the hydrodynamic forces on bridges. It was observed that the coefficient of drag force decreased with an increase of deck angle of skewness. The skewed deck results showed a trend of increasing lift coefficient values with increasing angles of skewness.
- Accumulation of debris upstream of a bridge deck in the form of a vertical obstruction could significantly increase the drag coefficient. It was observed that the increase in drag coefficient was more severe for smaller blockage ratios. On the other hand, the wedge mat debris did not impose a significant increase in the drag coefficient. The lift coefficient showed similar values under smaller blockage ratios for flow scenarios with and without debris. With an increase in blockage ratio, the lift coefficient showed a decreasing trend in wedge debris experiments, whereas it increased in the experiment with the flat plate debris. However, the results for the flat plate debris were similar to the without debris scenario.
- The presence of substructure increased the drag and lift coefficients significantly for the inundation ratio greater than 1.25. The moment coefficient was lower for the superstructure-substructure scenario but still within in range of upper and lower limits for the superstructure-only scenario.
- The vertical wave forces on the bridges were larger for wider decks. The horizontal wave forces did not exhibit a significant change with the deck width. The comparison between flood- and wave-induced forces showed that the vertical wave forces were higher than the vertical flood forces while the horizontal forces were within the same range.

5 COMPUTATIONAL FLUID DYNAMICS MODELING OF RIVER CROSSING BRIDGES

5.1 Introduction

This chapter presents the results of Task 5 of Project 0-7068. Task 5 is titled: *Perform Structural Analysis to Assess Performance of the Proposed Countermeasures*. The main goal of this task was to conduct Computational Fluid Dynamics (CFD) modeling and structural analysis to estimate flood forces on typical TxDOT bridges and evaluate required resisting details that ensure adequate bridge performance during a design flood.

This chapter is structured as follows. Section 5.1 provides an introduction to this task. Section 5.2 provides an overview of typical CFD analysis approaches used to evaluate bridges subject to riverine or coastal flooding. Section 5.3 summarizes the governing equations for CFD modeling. Section 5.4 introduces the CFD modeling scenarios used for this study. Section 5.5 summarizes the model setup. Section 5.6 presents the results of the CFD modeling.

5.2 Background

In previous studies, the stability of bridges subjected to heavy flooding has been studied using scaled physical and numerical experiments (Guo et al., 2010; Malavasi & Guadagnini, 2003; Naderi, 2018; Nasim et al., 2019; Naudascher & Medlarz, 1983; Wang et al., 2015). Due to cost and time restrictions, these studies are typically constrained to a limited number of flood conditions and deck geometries. The rapid development of supercomputers, advancements in CFD methods, and the availability of commercial software such as ANSYS Fluent, Flow-3D, and Star-CCM+ have enabled numerical simulations of the flow around hydraulic structures, such as bridges, to become routine and standard practice to quantify hydrodynamic forces exerted on these structures.

The U.S. Federal Highway Administration (FHWA) conducted two- and three-dimensional CFD modeling of three- and six-girder bridge decks, using Fluent and Star-CD software. A series of simulation options, including different mesh resolutions, boundary conditions, and turbulence models, was performed to replicate flow conditions that matched with the results from physical model outputs. The results from both software programs were compared with the experimental data. The findings of the study concluded that the CFD model results did not accurately reproduce the experimental results. In contrast to the observations of the physical models, the results from the CFD models did not show any dependence on the Froude number (Fr) (Kerenyi et al., 2009).

Naderi (2018) used ANSYS Fluent to perform numerical simulations to compute hydrodynamic forces on inundated bridges. The objective of the study was to evaluate the failure mechanisms of bridges considering a range of water level, Fr , blockage ratio, proximity ratio, inclination, and aspect ratio conditions to facilitate the design of countermeasures. The results of the numerical

model were validated against the results of physical experiments conducted by Oudenbroek (2018). An incipient failure analysis was performed to determine hydrodynamic situations that would potentially cause bridge deck failure. It was found that regardless of the proximity ratio and Fr, the bridge deck collapsed when the inundation ratio was higher than 1.5. No bridge failure was observed for inundation ratios lower than 1.5, meaning that the deck would only fail if it was deeply submerged. The author concluded that decks are more susceptible to high water levels than to the flood velocity or the distance to the streambed.

Highway bridge failures in the Gulf Coast region during Hurricane Katrina were investigated by Chen et al. (2009). ADCIRC and SWAN models were used in their study to calculate surge height, velocity, and wave characteristics. The study concluded that wind-induced waves and storm surge were responsible for the reported bridge deck failures.

Although many studies to date have investigated hydrodynamic forces on bridge superstructures, none have applied numerical models on a full-scale bridge to investigate the impact of waves, floods, and debris on bridge deck stabilities. Previous studies also only considered limited types of bridge geometries and flow conditions (e.g., Guo et al., 2010; Naderi, 2018) and did not model deck skewness. To address these highlighted gaps in knowledge, this study performed scaled and full-scale CFD modeling to quantify potential hydrodynamic forces on different types of bridges. Results from the CFD modeling were used to determine the resisting details necessary to ensure adequate bridge performance for flood-durable designs.

5.3 Governing CFD Equations

The governing equations used in the CFD simulations are solved iteratively to predict the important properties and location of flow parameters for each time step in each computational cell. When the residuals are small enough, the solution is considered as converged, and the equations are solved for the next time step.

5.3.1 Navier Stokes Equations

The hydrodynamic simulation of bridges is based on the application of ANSYS Fluent, which solves conservation equations for mass and momentum. In general, the motion of a fluid can be expressed by the Navier-Stokes (N-S) equations for compressible Newtonian fluids (ANSYS, 2017):

$$\frac{\partial \rho}{\partial t} + \nabla \cdot (\rho u) = 0 \quad (5.1)$$

$$\rho \left(\frac{\partial u}{\partial t} + u \cdot \nabla u \right) = -\nabla P + \mu \nabla^2 \cdot u + F \quad (5.2)$$

For incompressible fluids, these equations can be rewritten as follows:

$$\frac{\partial U}{\partial x} + \frac{\partial V}{\partial y} + \frac{\partial W}{\partial z} = 0 \quad (5.3)$$

$$\frac{\partial U}{\partial t} + U \frac{\partial U}{\partial x} + V \frac{\partial U}{\partial y} + W \frac{\partial U}{\partial z} = -\frac{1}{\rho} \frac{\partial P}{\partial x} + \nu \left(\frac{\partial^2 U}{\partial x^2} + \frac{\partial^2 U}{\partial y^2} + \frac{\partial^2 U}{\partial z^2} \right) + F_x \quad (5.4)$$

$$\frac{\partial v}{\partial t} + U \frac{\partial v}{\partial x} + V \frac{\partial v}{\partial y} + W \frac{\partial v}{\partial z} = -\frac{1}{\rho} \frac{\partial P}{\partial y} + \nu \left(\frac{\partial^2 v}{\partial x^2} + \frac{\partial^2 v}{\partial y^2} + \frac{\partial^2 v}{\partial z^2} \right) + F_Y \quad (5.5)$$

$$\frac{\partial w}{\partial t} + U \frac{\partial w}{\partial x} + V \frac{\partial w}{\partial y} + W \frac{\partial w}{\partial z} = -\frac{1}{\rho} \frac{\partial P}{\partial z} + \nu \left(\frac{\partial^2 w}{\partial x^2} + \frac{\partial^2 w}{\partial y^2} + \frac{\partial^2 w}{\partial z^2} \right) + F_Z \quad (5.6)$$

In the above equations, P is pressure; U, V, and W are the components of velocity in the x-, y-, and z-directions, respectively; F_X , F_Y , and F_Z are the components of external forces in the x-, y-, and z-directions, respectively; ν is kinematic viscosity; t is time; ρ is fluid density; and μ is dynamic viscosity.

In equations 5.4, 5.5, and 5.6, the four terms on the left-hand side represent the inertial forces. On the right-hand side, the first term represents pressure forces, the second term represents viscous forces, and the last term represents external forces. If the magnitude of velocities and pressures at the boundaries of the domain is known, the CFD problem can be solved (Naderi, 2018)

5.3.2 Reynolds-Averaged Navier-Stokes (RANS) Equations

When the Reynolds number is high and flow is turbulent, as is often the case during riverine flood events, no precise solution to the N-S equations has yet been found, so only an approximated numerical solution is achievable. To solve this problem, three different methods can be considered as follows:

- Direct Numerical Simulations (DNS): In this method, the N-S equations are solved in an explicit way at all time and length scales. However, this method is limited to flows with low Reynolds numbers and is computationally very expensive.
- Large Eddy Simulations (LES): This method increases the efficiency of the numerical simulation by eliminating small length scales through a method of low-pass filtering of the N-S equations.
- Reynolds-Averaged Navier-Stokes (RANS): RANS is the most convenient and common method that gives a reasonable solution in a more pragmatic way (Naderi, 2018). RANS is used in this research and is described in the following paragraphs.

Reynolds decomposition is used to compute the RANS equation from the N-S equations. Velocity and pressure are decomposed into an average and a fluctuating part, as shown in equations 5.7 and 5.8.

$$u_i = \bar{u} + u' \quad (5.7)$$

$$P = \bar{p} + p' \quad (5.8)$$

The RANS equation is derived by substituting these Reynolds decompositions for velocity and pressure into the N-S equations and averaging them, as given below (ANSYS, 2017):

$$\rho \left(\frac{\partial}{\partial t} (\bar{u}_i) + \frac{\partial}{\partial x_j} (\bar{u}_i \bar{u}_j) \right) = -\frac{\partial \bar{p}}{\partial x_i} + \mu \frac{\partial^2 \bar{u}_i}{\partial x_j \partial x_i} + \bar{F}_i - \frac{\partial}{\partial x_j} (\rho \overline{u'_i u'_j}) \quad (5.9)$$

The above equation has an additional term as compared to the N-S equations. The last term on the right-hand side of the equation is related to Reynolds stresses.

The RANS equation can be further simplified by supposing that:

1. If the flow is turbulent, the pressure gradient is the leading term and is much larger than the normal stress gradient.
2. When the Reynolds number is high, turbulent shear stresses dominate over viscous shear stresses.

The simplified RANS equation by considering the above-mentioned assumptions can be written as:

$$\rho \left(\frac{\partial}{\partial t} (\bar{u}_i) + \frac{\partial}{\partial x_j} (\bar{u}_i \bar{u}_j) \right) = -\frac{\partial \bar{p}}{\partial x_i} + \bar{F}_i - \frac{\partial}{\partial x_j} (s_{ij}) \quad (5.10)$$

The inclusion of Reynolds stress terms in the equation leads to three unknowns, which causes a non-closed set of equations. Turbulence models are necessary to close this set of equations (Uijtewaal, 2018; Naderi, 2018). Each turbulence model has its own benefits and provides an approximation of Reynolds stresses, as explained in the next section.

5.3.3 Turbulence Models

The application of the turbulence model into the numerical scheme is significant and has a large impact on the simulation results. In general, turbulence models are classified based on the governing equations and numerical schemes employed to calculate turbulent viscosity, for which a solution is sought for turbulence parameters.

One of the most common turbulence models is the semi-empirical K- ϵ model (Deuflhard, 1974). It has been used for a large range of turbulent flow simulations because of its robustness and reasonable accuracy. The K- ϵ model assumes that the flow is totally turbulent, and the molecular viscosity is very small. The transport equations for the K- ϵ turbulence model are given below (ANSYS, 2017):

$$\frac{\partial}{\partial t} (\rho k) + \frac{\partial}{\partial x_j} (\rho k u_j) = \frac{\partial}{\partial x_j} \left[\left(\mu + \frac{\mu_t}{\sigma_k} \right) \frac{\partial k}{\partial x_j} \right] + G_k + G_b - \rho \epsilon - Y_M + S_k \quad (5.11)$$

$$\frac{\partial}{\partial t} (\rho \epsilon) + \frac{\partial}{\partial x_j} (\rho \epsilon u_j) = \frac{\partial}{\partial x_j} \left[\left(\mu + \frac{\mu_t}{\sigma_\epsilon} \right) \frac{\partial \epsilon}{\partial x_j} \right] + \rho C_1 S_\epsilon - \rho C_2 \frac{\epsilon^2}{k + \sqrt{\nu \epsilon}} + C_1 \epsilon \frac{\epsilon}{k} C_{3\epsilon} G_b + S_\epsilon \quad (5.12)$$

$$C_1 = \max \left[0.43, \frac{\eta}{\eta + 5} \right], \quad \eta = S \frac{k}{\epsilon}, \quad S = \sqrt{2 S_{ij} S_{ij}}$$

In these equations, k is turbulent kinetic energy; ϵ is the rate of dissipation of turbulent kinetic energy; G_k is the generation of turbulent kinetic energy due to the mean velocity gradients; G_b is the generation of turbulent kinetic energy due to buoyancy; Y_M is the contribution of the fluctuating dilatation in compressible turbulence to the overall dissipation rate; μ_t is the eddy viscosity;

$C_1, C_2, C_{1\epsilon}$ are constants; $\sigma_k, \sigma_\epsilon$ are the turbulent Prandtl numbers; and S_k, S_ϵ are user-defined source terms.

The other well-known turbulence model is the K- ω model (Wilcox, 2008). The K- ω shear stress transport (SST) model also includes transport of the turbulent shear stress. This advantage makes the K- ω SST model more accurate in predicting the magnitude and location of flow separation, although it takes longer to converge. The transport equations for the K- ω SST model are given below (ANSYS, 2017):

$$\frac{\partial}{\partial t}(\rho k) + \frac{\partial}{\partial x_i}(\rho k u_i) = \frac{\partial}{\partial x_j} \left(\Gamma_k \frac{\partial k}{\partial x_j} \right) + \tilde{G}_k - Y_k + S_k \quad (5.13)$$

$$\frac{\partial}{\partial t}(\rho \omega) + \frac{\partial}{\partial x_i}(\rho \omega u_i) = \frac{\partial}{\partial x_j} \left(\Gamma_\omega \frac{\partial \omega}{\partial x_j} \right) + G_\omega - Y_\omega + D_\omega + S_\omega \quad (5.14)$$

In these equations, k is the turbulent kinetic energy; ω is the specific turbulent dissipation rate; \tilde{G}_k is the generation of turbulent kinetic energy due to the mean velocity gradients; G_ω is the generation of ω ; Γ_ω is the effective diffusivity of k and ω ; Y_k, Y_ω represent the dissipation of k and ω ; D_ω is the cross-diffusion term; and S_k, S_ω are user-defined source terms.

Both turbulence models were tested in the CFD simulations to determine which provided the best accuracy for the modeling purposes.

5.3.4 Volume of Fluid Model

The numerical model used is based on the Volume of Fluid (VOF) method, which captures the free surface between water and air and tracks the surface through a grid mesh. For the multiphase numerical domain, a variable called fraction function (α) is defined for each cell. The fraction function for each phase defines what percentage of the cell is occupied by that phase, as shown in Figure 5.1. Interfaces between multiple phases are identified by a volume fraction falling between 0 and 1. The sum of fraction functions across all phases in each cell should be one.

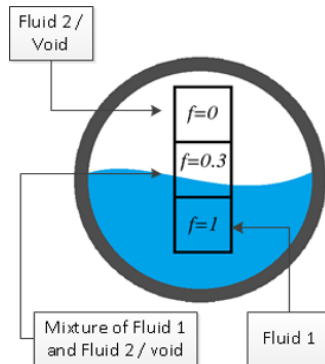


Figure 5.1 Fraction function for the blue phase in the VOF (Hirt & Nichols, 1988)

Based on the α factor, appropriate properties of the fluid are given to each cell. As an example, density follows this equation (Raja, 2012; Naderi 2018):

$$\rho = \alpha\rho_i + (1 - \alpha)\rho_j \quad (5.15)$$

Here ρ_i , ρ_j are the densities of phase i and phase j and α is the fraction function.

The conservation of mass equation for the fraction function of each phase is needed to locate the free surface. For the i^{th} phase, the volume fraction equation is given as:

$$\frac{1}{\rho_i} \left[\frac{\partial}{\partial t} (\alpha_i \rho_i) + \nabla(\alpha_i \rho_i u_i) \right] = s_{\alpha_i} + \sum_{j=1}^n (\dot{m}_{ij} - \dot{m}_{ji}) \quad (5.16)$$

Where \dot{m}_{ij} is the mass transfer from phase i to phase j and \dot{m}_{ji} is the mass transfer from phase j to phase i . s_{α_i} is a source term that is zero by default (ANSYS, 2017).

5.3.5 Wave Theories

In CFD models, the choice of a suitable wave theory and its order are the main criteria for wave modeling within stability limits. ANSYS Fluent software considered two main wave theories, as described below.

Stokes Wave Theory: Stokes wave theory, as implemented in ANSYS Fluent, is based on research by John D. Fenton (ANSYS, 2017). This wave theory is effective for very steep and finite amplitude waves in the intermediate- to deep-water depth range. The generalized wave equations for the fifth order Stokes theory are given as:

$$\zeta(X, t) = \frac{1}{k} \sum_{i=1}^5 \sum_{j=1}^i b_{ij} \xi^i \cos(jk(x - ct)) \quad (5.17)$$

where

$$\xi = \frac{kH}{2} = \frac{\pi H}{L} \text{ and } k = \frac{2\pi}{L}$$

$$c = \sqrt{\frac{g}{k} \tanh(kd)} \left(\sum_{i=1}^5 c_i \xi^i \right)$$

In these equation, c is wave celerity; k is wave number; H is wave height; L is wavelength; d is water depth; and b_{ij} , c_i are complex expressions of kH (Fenton, 1985).

Solitary Wave Theory: Solitary wave theory is primarily used for shallow depths. Solitary wave theory equations are derived by supposing that the waves have an infinite wavelength. Fifth order solitary wave equations are complex functions of relative wave height (H/d) (Fenton, 1972) and are too complicated to state here. Instead, first order solitary wave expressions, which form the basis for the fifth order equations, are given here. The expression of profile for a shallow wave is given as:

$$\zeta(X, t) = H \sec h^2 \left[\frac{k}{d} (x - x_0 - ct) \right] \quad (5.18)$$

Where wave celerity and wavenumbers are given as,

$$c = \sqrt{gd} \left(1 + \frac{H}{2d} \right) \text{ and } k = \frac{1}{d} \sqrt{\frac{3H}{4d}}$$

and x_0 is the initial position of the wave.

The fifth order solitary wave theory can be used for relative wave heights (H/d) of 0.55-0.60 as compared to the theoretical limit of 0.78. On the other hand, the fifth order Stokes wave theory can be used for wave steepness of 0.12 as compared to the theoretical limit of 0.14 (ANSYS, 2017). The water depth (h) and wavelength (L_w) considered during the numerical simulations presented here were 9.5" and 18", respectively. The criteria for defining the water depth in wave environment are shown in Table 5.1 (Jeong et al., 2019).

Table 5.1 Water depth classification in a wave environment

Water Depth	
Deep water	$h > \frac{L_w}{2}$
Intermediate zone	$\frac{L_w}{20} < h < \frac{L_w}{2}$
Shallow water	$h < \frac{L_w}{20}$

It is clear from the table that the considered water depth (h=9.5") is in the intermediate zone. The fifth order Stokes wave theory was thus considered for the simulations because it can capture the steepness of the waves and is valid for intermediate- to deep-water depths.

5.4 CFD Modeling Scenarios

Four typical TxDOT bridge details were selected for scaled and full-scale modeling. The bridge superstructure models included:

- TX-28 I-Girder – 28" high
- TX-54 I-Girder – 54" high
- SB-15 Slab Beam – 15" high
- BB-28 Box Beam – 28" high

Two common types of TxDOT roadways were considered: 24' roadway (26' wide deck) and 44' roadway (46' wide deck). Bridge substructures were not considered in the scaled experiments but were included in the full-scale modeling. The effect of deck skewness on hydrodynamic forces as examined on bridges with 0°, 15°, 30°, and 45° skews. Selected bridge models were also tested under debris loading and wave action. The drag, lift, and moment coefficients were determined for each scenario. Table 5.2 provides a summary of the modeled scenarios for Test Series A to D.

Table 5.2 Summary of experimental conditions for Test Series A to D (scaled models)

Test Series	Deck Width (ft)	Description	Froude No.	Inundation Ratios (h^*)
A	46	TX-28	0.20, 0.34	0.25 – 2.5
	26	TX-28	0.20, 0.27, 0.34, 0.5, 0.9	0.25 – 4
	46	TX-54	0.20, 0.32	0.25 – 2.0
	26	TX-54	0.20, 0.27	0.5 – 2.0
	26	Slab Beam	0.20, 0.27, 0.34	0.5 – 2.5
	26	Box Beam	0.20, 0.27, 0.34	0.5 – 2.5
B	46	TX-28 (15° Skew)	0.20, 0.34	0.5 – 2.5
		TX-28 (30° Skew)	0.20, 0.34	0.5 – 2.5
		TX-28 (45° Skew)	0.20, 0.34	0.5 – 2.5
C	46	TX-54 (Debris - Flat Plate)	0.32	0.25 – 1
		TX-54 (Debris - Fixed Wedge)	0.32	0.25 – 1
D	46	TX-28 (Wave Loading)	-	0.26, 0, - 0.26
	26	TX-28 (Wave Loading)	-	0.26, 0, - 0.26

Test Series E corresponds to the full-scale modeling. Table 5.3 provides a summary of the modeled scenarios for Test Series E. The details of each bridge model and procedure for experiments in Test Series A to E are presented in the following sections.

Table 5.3 Summary of experimental conditions for Test Series E (full-scale models)

Test Series	Deck Width (ft)	Description	Froude No.	Inundation Ratios (h^*)	
E	46	TX-28	0.9, 0.5, 0.34	2.5	
	26	TX-28	0.9, 0.5, 0.34	2.5	
	46	TX-54 (50' & 125' Span)	0.9, 0.5, 0.34	2.5	
	26	TX-54 (50' & 125' Span)	0.9, 0.5, 0.34	2.5	
	26	Slab Beam	0.9, 0.5, 0.34	2.5	
	26	Box Beam	0.9, 0.5, 0.34	2.5	
	46	46	TX-28 (15° Skew)	0.9, 0.5, 0.34	2.5
			TX-28 (30° Skew)	0.9, 0.5, 0.34	2.5
			TX-28 (45° Skew)	0.9, 0.5, 0.34	2.5
	46	46	Debris - Flat Plate (50' & 125' Span)	0.9, 0.5, 0.34	2.5
			Debris - Wedge (50' & 125' Span)	0.9, 0.5, 0.34	2.5
	26	TX-54 (Wave Loading)	-	0.75	

5.4.1 Bridge Models

Bridge models are 1:50 scale of the TxDOT bridges. The dimensions of each bridge model and railing are summarized in Appendix D.

5.4.2 Debris

Two types of common debris mats were tested in Test Series D, including flat plate and wedge shape debris.

Flat Plate Debris: The flat plate debris considered in this study consisted of a 0.12" thick plate rigidly fixed to the upstream side of the bridge deck. The flat plate debris is similar to the vertical accumulation of the debris upstream of bridges. Its height was set at 2.36" (9.8' high in full-scale modeling), which was reported as the maximum height of interlocking debris such as tree limbs against a bridge superstructure (Wellwood & Fenwick, 1990). The debris width corresponded to the 11.9" width of the bridge deck section to ensure an even channel constriction. The geometry of the flat plate debris is shown in Figure 4.2(a).

Wedge Shape Debris: The wedge shape debris considered in the physical modeling consisted of pinewood dowels fixed together with wood glue. These 0.75" diameter dowels represent, on average, the width of trees in the Southern Forest Region that Texas falls into (Diehl, 1997). Due to numerical modeling meshing restrictions, the wedge debris was modeled without dowels and assumed to be solid. The wedge shape considered in the numerical modeling was 2.36" wide and 7" high at a 1:50 scale (9.8' by 29.1' in full-scale modeling). The wedge was positioned in front of the flat plate as shown in Figure 4.2(b).

5.4.3 Flow Parameters

The drag, lift, and moment coefficients are dependent on the flow parameters (i.e., Froude number) and the relationship between the bridge deck thickness and the flow depth (i.e., inundation ratio and blockage ratio).

Froude Number (Fr): The results of the analysis of 598 TxDOT bridges in Chapter 3 showed an average channel Fr of 0.39, with several bridge sites exceeding that amount up to $Fr = 1.3$. The results of an analysis of 83 TxDOT bridges from as-built drawings showed an average channel Fr of 0.30, with several bridge sites exceeding that amount up to $Fr = 0.87$ (Appendix C). To compare with the results of the physical modeling, most of the scaled numerical experiments were conducted under $Fr = 0.20$, 0.27, and 0.34. For the TX-28 bridge with 26' deck, $Fr = 0.50$ and $Fr = 0.90$ were also considered. Full-scaled numerical modeling was conducted for $Fr = 0.34$, 0.5, and 0.9.

Inundation Ratio (h^*): The height of the water surface with respect to the flume bed and the position of the bridge deck can be describe in terms of the inundation ratio (h^*). The TX-28 bridge with 26' deck was tested for h^* up to 4, while the TX-54 bridge with 44' deck was simulated for h^* up to 2. For numerical experiments with box and slab beam bridges, h^* ranged from 0.25 to 2.5. Full-scaled numerical modeling was conducted under $h^* = 2.5$.

Blockage Ratio (Br):

In numerical modeling of the bridges with debris, Br ranged from 0.15 to 0.31.

5.4.4 Wave Parameters

The effect of wave loading on bridges was investigated using the TX-54 bridge with 26' and 46' decks. Submergence depths and elevations were chosen such that the bridge model was fully submerged, partially submerged, and fully elevated above stillwater level (SWL). The wave numerical modeling setup is shown in Figure 4.3.

Results from Task 3 (Chapter 3) indicated that TxDOT bridges in coastal areas may experience wave heights ranging from 4.6' to 20'. The numerical modeling was done with wave heights of 1" and 2" (4.2' and 8.3" in prototype), which fall in the range of observed field data. A wave period of 0.48 sec (47 sec in prototype) was simulated. The water depth was 9.5" (39.6' in prototype). The bridge location with reference to SWL was set at three different elevations to investigate the wave force effects at different bridge submergences. At these positions, the SWL was 0.5" above the low cord (Zc_1), at the low cord elevation (Zc_2), and 0.5" below the low cord (Zc_3), as shown in Figure 4.4.

5.5 Model Setup

An overview of the CFD modeling framework is shown in Figure 5.2. Flow parameters (i.e., water surface elevations and velocities) obtained from HEC-RAS modeling of Texas creeks conducted for Task 3 were subsequently used in defining the boundary conditions in the ANSYS Fluent modeling. Individual steps in the CFD modeling are described in more detail in the following sections.

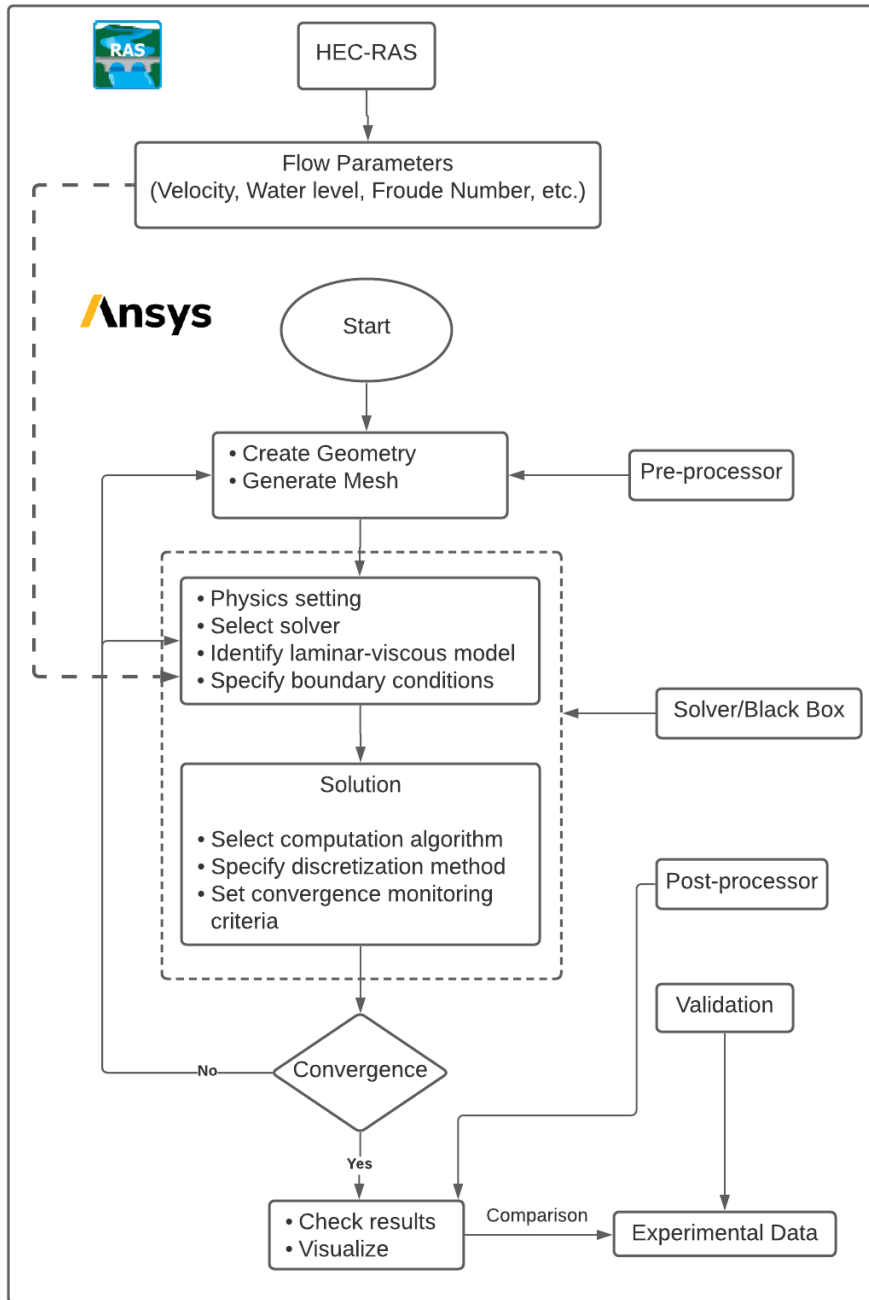


Figure 5.2 Schematic diagram of the steps of ANSYS Fluent CFD model set (Muiruri & Motsamai, 2018)

5.5.1 Overview of the Numerical Flume

The geometry of the bridge and numerical flume was first constructed in ANSYS Design Modeler software and was then exported to be used for meshing. The flume dimensions for scaled modeling are shown in Figure 5.3.

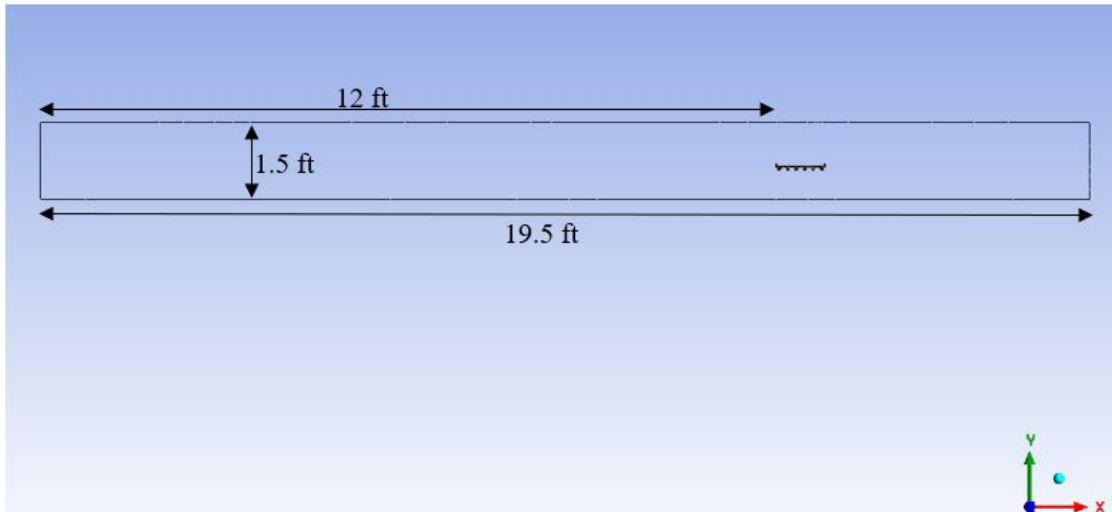


Figure 5.3 Geometry of scaled numerical flume

The height of the numerical flume was set equal to the height of the experimental flume (1.5'). The flume extended 12' upstream of the bridge for the development of a boundary layer and 7.5' downstream to allow enough space for the formation and transportation of the wake zone on the trailing side of the bridge. The numerical flume for the full-scale model was 230' long, 60' wide, and 115' high as shown in Figure 5.4.

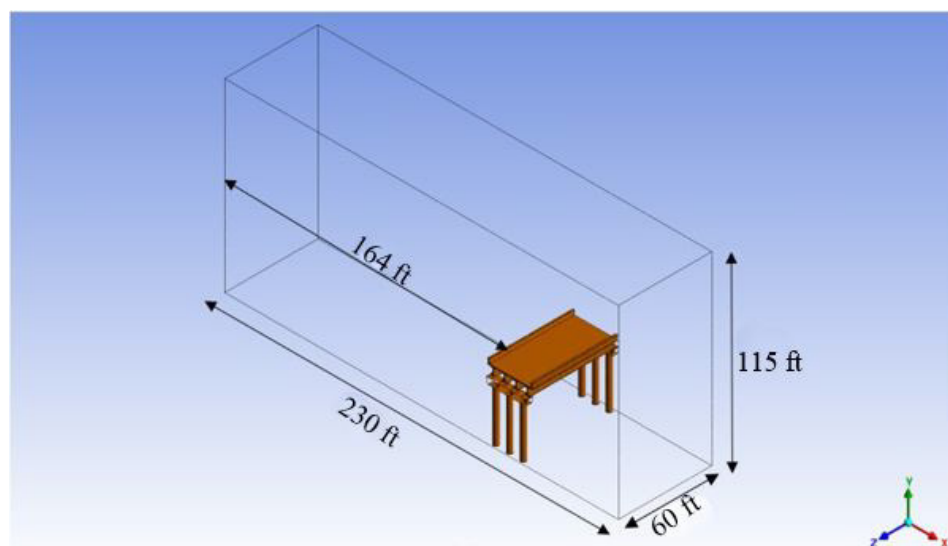


Figure 5.4 Geometry of full-scale numerical flume

The width of the flume was changed to 128' for the 125' span bridge. The bridge deck was located 164' downstream from the inlet of the flume, and a uniform velocity corresponding to $Fr = 0.34$, 0.5, and 0.9 was set at the inlet depending on the scenario. The depth of flow was maintained at $h^* = 2.5$.

5.5.2 Meshing

After constructing the geometry, the numerical mesh was developed using the ANSYS Fluent meshing software. In CFD modeling, an appropriate mesh size must be chosen to obtain accurate results while also balancing the required computational cost. A multi-block tetrahedral mesh was used for this study, with grid cells ranging from 0.78" at upstream and downstream locations to 0.15" near the bridge, where complex flow patterns occur. This resulted in a mesh with approximately 20,760,643 elements and 3,664,860 nodes (Figure 5.5). Mesh quality metrics, including minimum orthogonal quality, aspect ratio, and skewness, were carefully examined before the initialization of the numerical models.

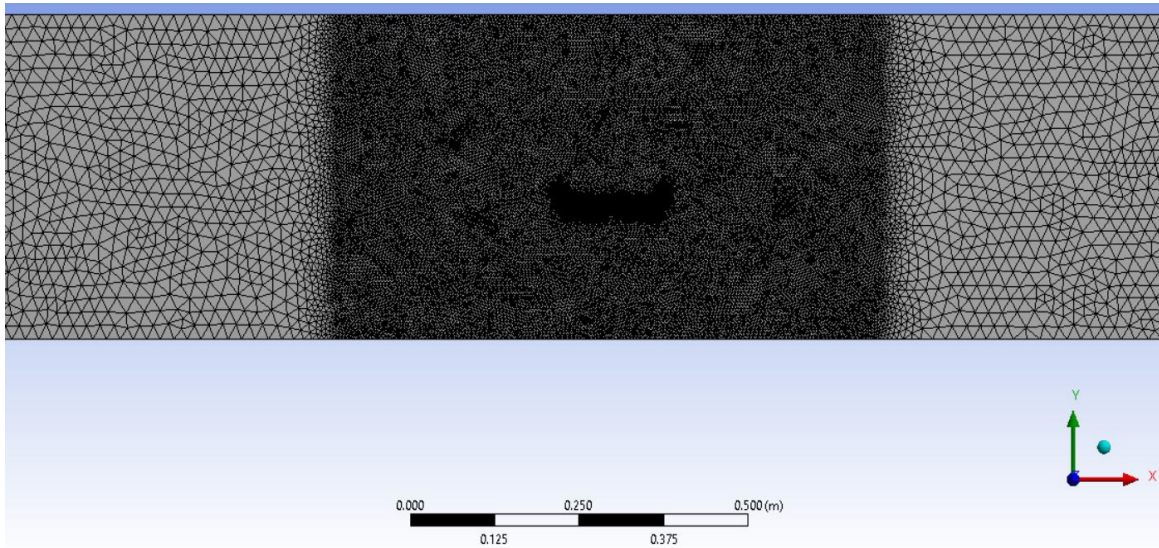


Figure 5.5 Mesh distribution around the scaled bridge

For the full-scaled modeling, the mesh size near the bridge of 24' deck with 50' span length was around 8" and gradually increased to a size of 10" away from the bridge deck. For 46' deck with 50' span length, mesh size near the bridge was 20" and 25" away from the bridge as shown in Figure 5.6.

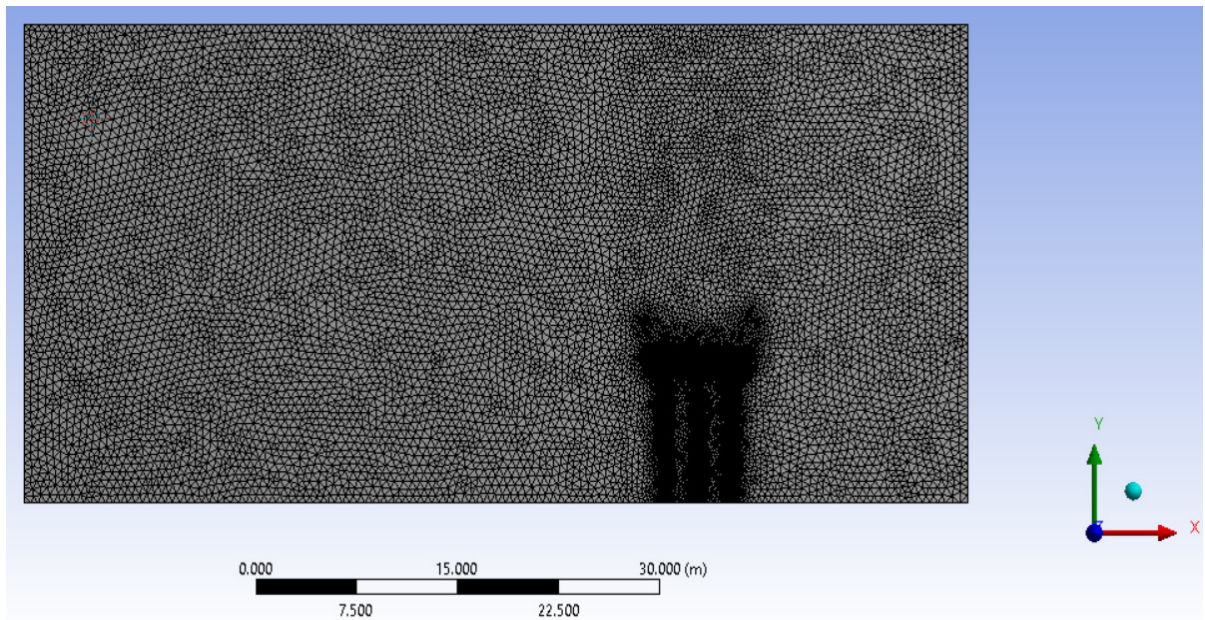


Figure 5.6 Mesh distribution around the full-scaled bridge

For the longer bridge spans (125'), the mesh size was around 30" and gradually increased to a size of 40" away from the bridge deck. A three-dimensional grid system with 3,842,488 nodes and 21,165,831 cells was generated.

5.5.3 Boundary Conditions and Solution Methods

The boundary conditions used in the numerical simulations are shown in Figure 5.7.

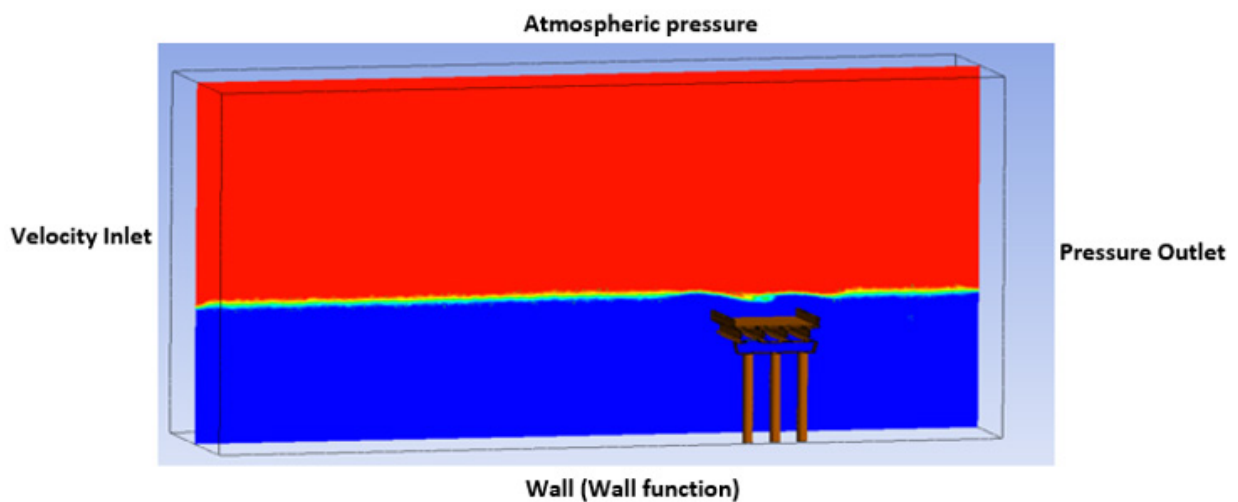


Figure 5.7 Boundary conditions of numerical simulations

At the inlet, a uniform velocity was defined with constant water depth based on the chosen Fr. The pressure at the top side of the domain was set at atmospheric pressure. An open channel boundary condition with a constant water depth was defined at the outlet. The bottom bed and bridge were defined as walls with a no-slip condition and default roughness. Near-wall treatment of the standard wall function was activated in the turbulence model. The simulations were completed using the VOF multiphase model and $k-\omega$ SST turbulence model. In the case of wave modeling, a numerical beach is defined in the region adjacent to the pressure outlet to suppress the numerical reflections propagating upstream.

Divergence in the numerical simulations can be caused by several factors, such as large mesh size, conservative under-relaxation factors, and complex flow physics. Furthermore, if the time step is too large as compared to the grid cell size, numerical smearing may occur, leading to numerical instability and in some cases divergence (ANSYS, 2017). To avoid issues with divergence, the time step size was set to 0.005 seconds based on the Courant number criteria, which should be less than 1 to ensure stability of the numerical models. Twenty iterations per time step were applied to reduce the residuals of the x- and y-velocities and the continuity equation. The residual for convergence of continuity and turbulence parameters was set to 10^{-6} . The Semi-Implicit Method for Pressure Linked Equations (SIMPLE) scheme was used to couple pressure and velocity (Runchal, 2008). A second-order upwind scheme was used to discretize momentum, turbulent kinetic energy, and turbulent dissipation rate. To obtain better convergence, the under-relaxation factor for pressure was 0.30, and other terms (i.e., density, momentum, turbulent kinetic energy, and specific dissipation rate) were reduced to 0.70. The drag force, lift force, and overturning moment were monitored for all scenarios. The simulations were run for 10 seconds and, due to the fluctuating values of drag, lift, and moment coefficients, the average value of the last 5 seconds was used. The operating pressure was set as atmospheric pressure (2,116 psf). The gravitational acceleration was set in the y-direction as -32.2 ft/s^2 and the operating density was set as 0.0750 lb/ft^3 . The solution was initialized from the inlet with a flat or wavy open channel initialization method for the simple open channel flow and wave modeling, respectively.

After obtaining solution convergence, results were post-processed and analyzed in ANSYS. All simulations were run on high-performance computing systems at the Texas Advanced Computing Center (TACC) and UT Arlington.

5.5.4 Sensitivity Analysis

Keeping in mind the accuracy and computational cost, the effects of several important modeling parameters were investigated with a sensitivity analysis. This analysis examined the effect of (1) the length of the numerical flume, (2) the mesh size, (3) the bottom roughness, and (4) the turbulence model. The results of this analysis are presented in the following sections.

Effect of length of the numerical flume

To be computationally efficient, a smaller length of the numerical flume is more favorable. However, the flume in front of the bridge should be long enough to allow the development of a

fully turbulent boundary layer. As a rule of thumb, the length of the flume should be at least 20 times the water depth (Naderi, 2018). To check the effect of the length of the flume on hydrodynamic forces, a simple open channel flow model was constructed with different upstream lengths from the bridge. All of the simulations were run for a TX-28 bridge with 26' deck at $h^* = 0.5$ and $Fr = 0.27$. Table 5.4 shows the effect of the upstream flume length on hydrodynamic forces. As indicated, the length of the flume does not have a significant impact on the calculated hydrodynamic forces. However, to ensure consistency with the standard practice that the upstream length be at least 20 times the water depth, an upstream flume length of 12' was chosen for all scaled numerical models.

Table 5.4 Effect of different upstream flume lengths on hydrodynamic forces

Distance (ft)	Drag Force (lbf) (ANSYS)	Lift Force (lbf) (ANSYS)
3	0.07	0.56
4	0.07	0.60
5	0.07	0.54
6	0.08	0.47
9	0.08	0.52
12	0.08	0.53

Effect of mesh size

Two different minimum mesh sizes (0.15" and 0.24") were tested to determine their effect on the measured forces on the bridge (Figure 5.8). For both mesh sizes, a TX-28 bridge with 26' deck was used, and simulations were performed at $h^* = 2$ and $Fr = 0.34$. As shown in Table 5.5, the mesh size near the bridge does not have a significant impact on the calculated hydrodynamic forces.

However, because the 0.24" mesh size produced unsatisfactory mesh quality metrics, the 0.15" mesh was selected for all scaled numerical models despite the additional computational requirement.

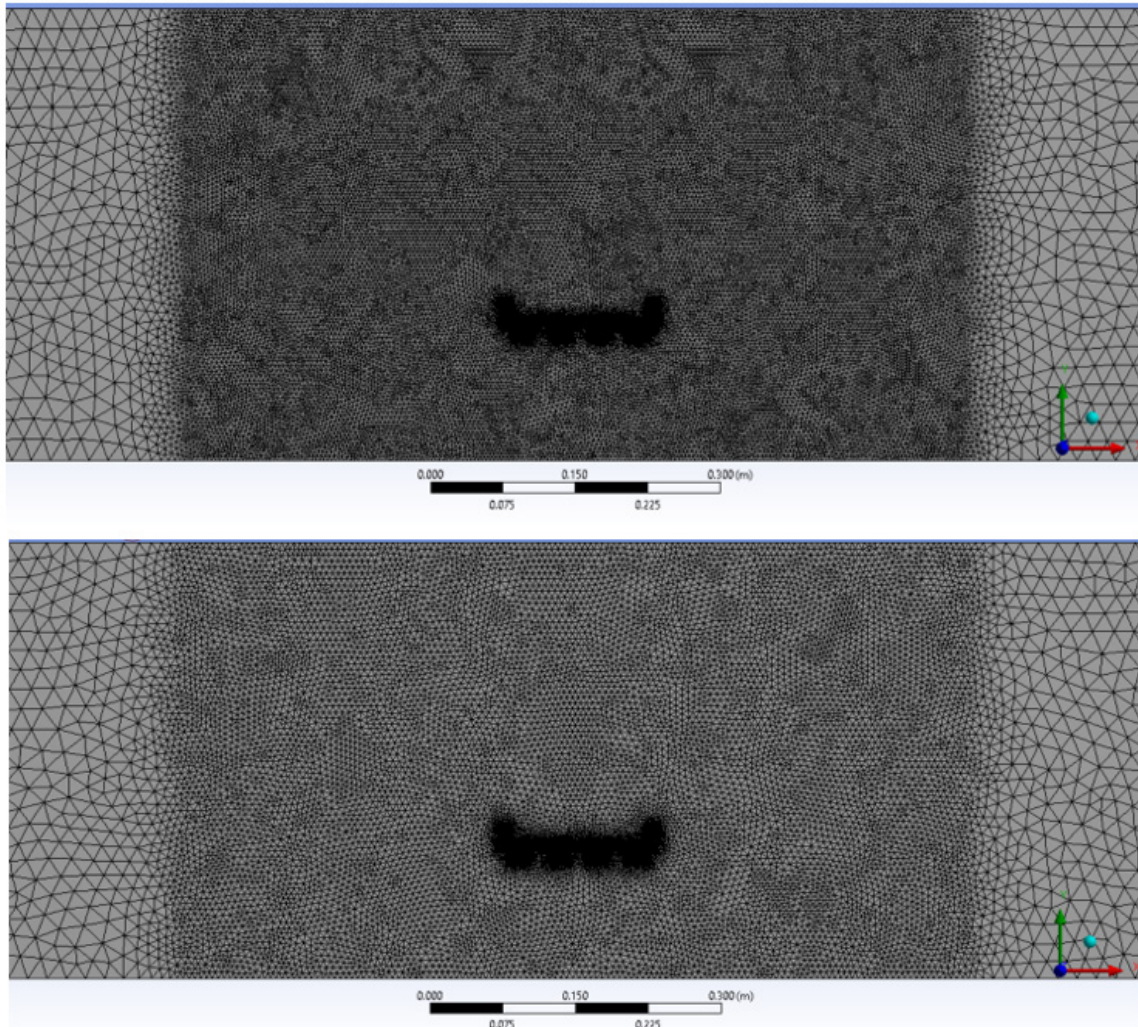


Figure 5.8 Mesh distribution around the bridge a) 0.15" b) 0.24"

Table 5.5 Drag and lift coefficient values for 0.15" and 0.24" mesh size

Mesh Size (in)	C_D (ANSYS)	C_L (ANSYS)
0.24	1.55	-0.82
0.15	1.57	-0.89

Effect of bottom roughness

To account for bottom roughness, ANSYS Fluent allows for the adjustment of a surface roughness height parameter (k_s) in the boundary conditions. The experimental flume used for the physical

modeling was made of plexiglass, which has a Manning’s roughness coefficient (n) value range between 0.008-0.01 (Sturm, 2001). The relationship between k_s (meters) and n can be expressed as (Smart, 1999):

$$n = 0.038 k_s^{1/6} \quad (5.19)$$

Using this relationship, k_s for plexiglass was computed as 0.00018. Simulations were run for different h^* (0.5-2) with $Fr = 0.20$ using the TX-54 bridge with 26’ deck. Table 5.6 shows a comparison between hydrodynamic forces computed by taking the default value of roughness height $k_s = 0$ in ANSYS Fluent and the computed roughness height for plexiglass. The bottom roughness of the flume has no substantial impact on the calculated hydrodynamic forces. As a result, the default k_s was used for all scaled numerical models.

Table 5.6 Effect of channel bottom roughness on hydrodynamic forces

h^*	Drag Force (lbf)	Drag Force with roughness (lbf)	Lift Force (lbf)	Lift Force with roughness (lbf)
0.5	0.05	0.05	0.39	0.39
1	0.28	0.28	0.74	0.73
1.5	0.32	0.32	0.83	0.82
2	0.35	0.34	1.03	1.03

Effect of turbulence model

Two of the most commonly used turbulence models, k- ϵ and k- ω SST, were tested for the numerical simulations using a TX-28 bridge with 26’ deck for a range of h^* (0.5-2.5) with $Fr = 0.34$. Drag and lift coefficient results for these two turbulence models were quite similar, as shown in Table 5.7. Because the k- ω SST turbulence model performs well in situations where separation flows and adverse pressure gradients exist and provides better results for drag and lift coefficients (Naderi, 2018), it was chosen for the simulations.

Table 5.7 Effect of turbulence models on drag and lift coefficients

h^*	C_D (K- ω SST)	C_D (K- ϵ Realizable)	C_L (K- ω SST)	C_L (K- ϵ Realizable)
0.5	1.10	1.11	-0.40	-0.38
2.5	1.58	1.62	-0.71	-0.67

5.5.5 Validation of Model Against Previous Studies

To test the validity of the numerical setup, a three-girder bridge tested experimentally by FHWA was simulated using the same hydrodynamic conditions. The dimensions of the three-girder deck and its railings are shown in Figures 5.9 and 5.10. The experimental flume was 23' long, 1.3' wide, and 1.64' high and was made of plexiglass.

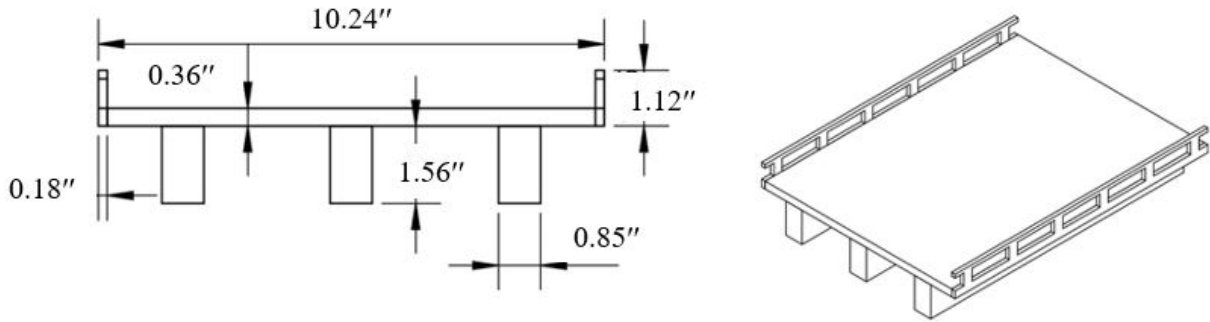


Figure 5.9 Dimensions of three girder bridge deck

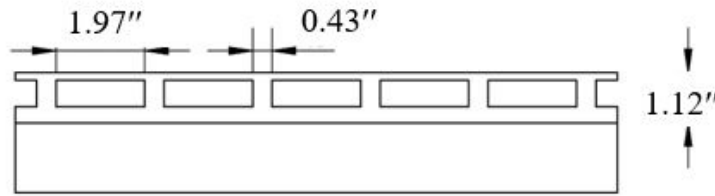


Figure 5.10 Railing of three-girder bridge deck

The drag, lift, and moment coefficients obtained in this study are plotted alongside the FHWA experimental results and results from past numerical modeling studies (Kerenyi et al., 2009; Naderi, 2018) in Figure 5.11. The ANSYS Fluent $k-\omega$ SST results show reasonable agreement with the FHWA experimental modeling results. In general, the drag coefficient increases with h^* , demonstrating the effect of increasing the frontal submergence area of the bridge. The lift coefficient is negative for all h^* , indicating that the flow is applying a pull-down force on the bridge. The lift coefficient becomes more negative as the bridge is fully submerged and then gradually returns near to zero as h^* continues to increase. The moment coefficients are close to zero for every h^* . The results show a clear agreement between numerical simulations and experimental data in the case of the drag and lift coefficients. However, the moment coefficients for the CFD simulations do not closely follow the experimental data. This lack of agreement was also described by Kerenyi et al. (2009) and Naderi (2018), who performed numerical simulations using ANSYS Fluent and STAR-CD.

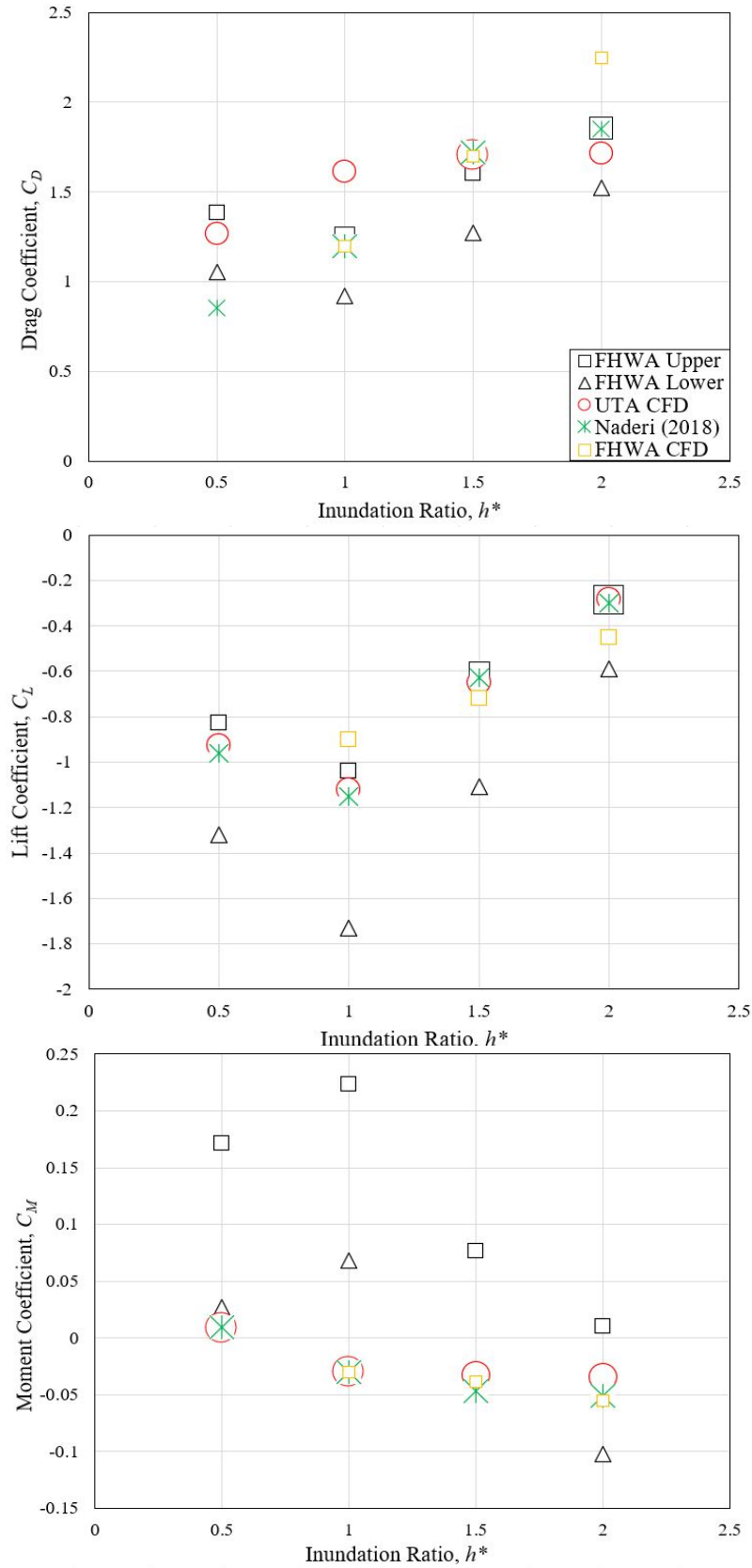


Figure 5.11 Comparison of drag, lift, and moment coefficients for FHWA 3-girder bridge

5.5.6 Validation of Model against Physical Modeling Performed at UTA

The numerical modeling results for different flow conditions and inundation ratios were compared with the physical modeling performed at UT Arlington (Task 4). For comparison, the following three scenarios were considered:

1. TX-28 with 26' deck (forces due to upstream flow field)
2. TX-28 with 46' deck (15° skewed deck)
3. TX-54 with 26' deck (wave loading)

TX-28 with 26' deck (forces due to upstream flow field): In this scenario, a TX-28 bridge with 26' deck was considered, and the drag, lift, and moment coefficients as a function of h^* and Fr were compared (Figure 5.12). In the case of drag coefficient, the CFD results for the scaled bridge deck agree with the physical modeling results at a lower h^* but do not closely follow the experimental results at $h^* > 1.5$. In the case of lift coefficient, to be consistent with the experiments, the component of buoyancy was subtracted from the lift force for all cases. The lift coefficient results agree with the physical modeling results in most of the simulations at both higher and lower h^* . The moment coefficients of the CFD simulation do not closely follow the experimental data. It can be observed that CFD simulation results underpredicted the moment coefficients. For the physical modeling, Fr affected the force and moment coefficients, but it did not greatly impact the shape of the response to the inundation ratio. On the other hand, the CFD model showed the dependence of the drag coefficient on Fr across the range of h^* tested.

TX-28 with 46' deck (15° skewed deck): In this scenario, a TX-28 bridge with 46' deck and 15° skew was considered, and the drag, lift, and moment coefficients as a function of h^* and Fr were compared (Figure 5.13). In the case of drag coefficient, the CFD results for the scaled bridge deck agree with the physical modeling results at lower h^* but do not closely follow the experimental results at $h^* > 1.5$, similar to what was observed for the 0° skew models. The lift coefficient results agree with the physical modeling results in most of the simulations at both higher and lower h^* . The moment coefficients of CFD simulations do not closely follow the experimental data, underpredicting at lower h^* and overpredicting at higher h^* . For the physical modeling, changes in Fr affect the force and moment coefficients at higher h^* but do not greatly impact the shape of the response to h^* . On the other hand, in the case of numerical modeling, Fr does not affect the force and moment coefficients, and it also does not greatly impact the shape of the response to h^* .

TX-54 with 26' deck (wave loading): In this scenario, a TX-54 bridge with 26' deck was considered, and the vertical and horizontal wave forces as a function of the wave height were compared as shown in Figure 5.14. In the case of wave modeling, CFD results for the scaled bridge deck agreed with the physical modeling results at the lower wave height but did not closely follow the experimental results at the higher wave height. This is due to limitations in ANSYS Fluent for modeling steep or breaking waves, which are more common at higher wave heights.

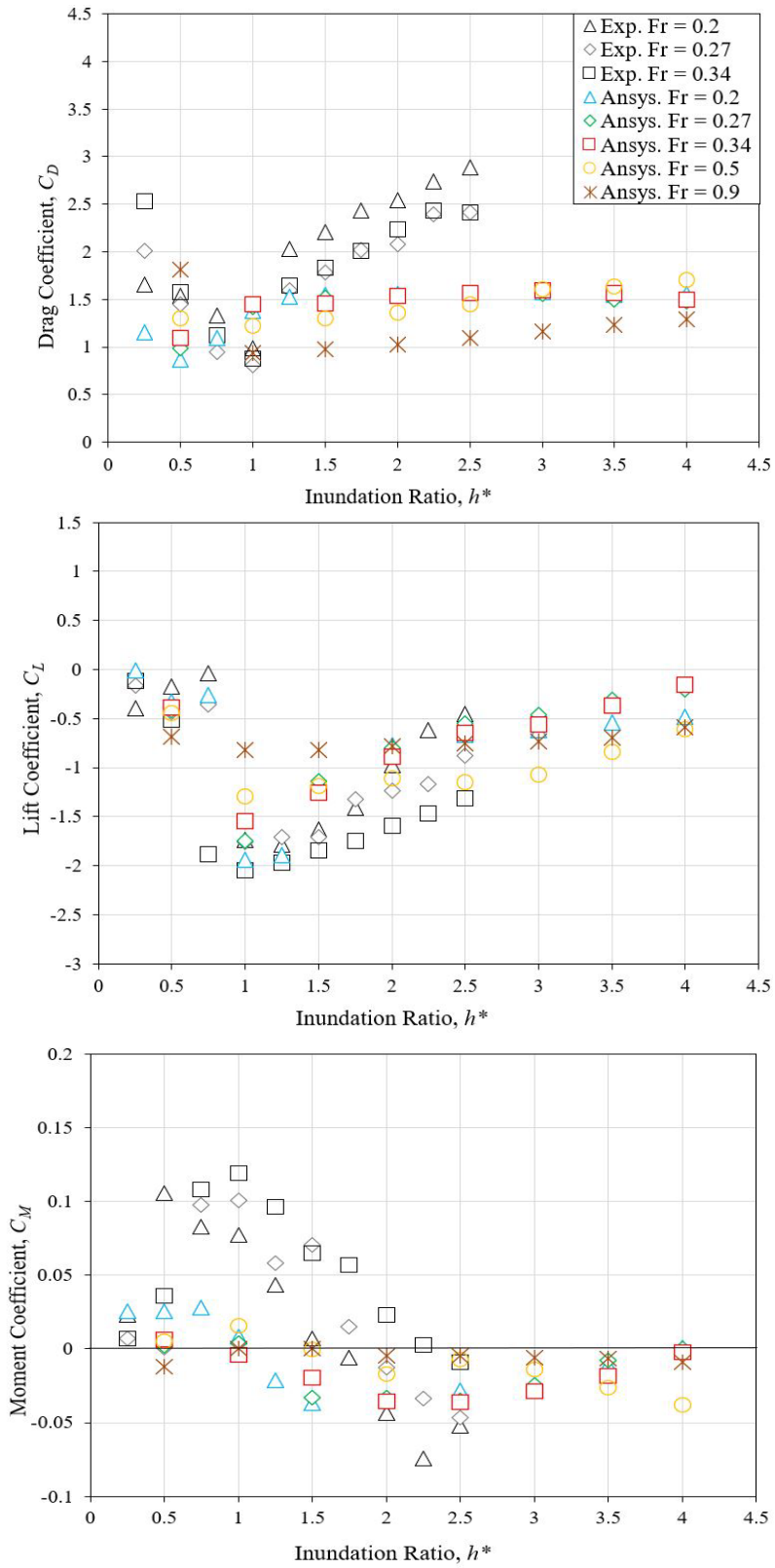


Figure 5.12 Comparison of drag, lift, and moment coefficients for bridge model (TX28 with 26' deck)

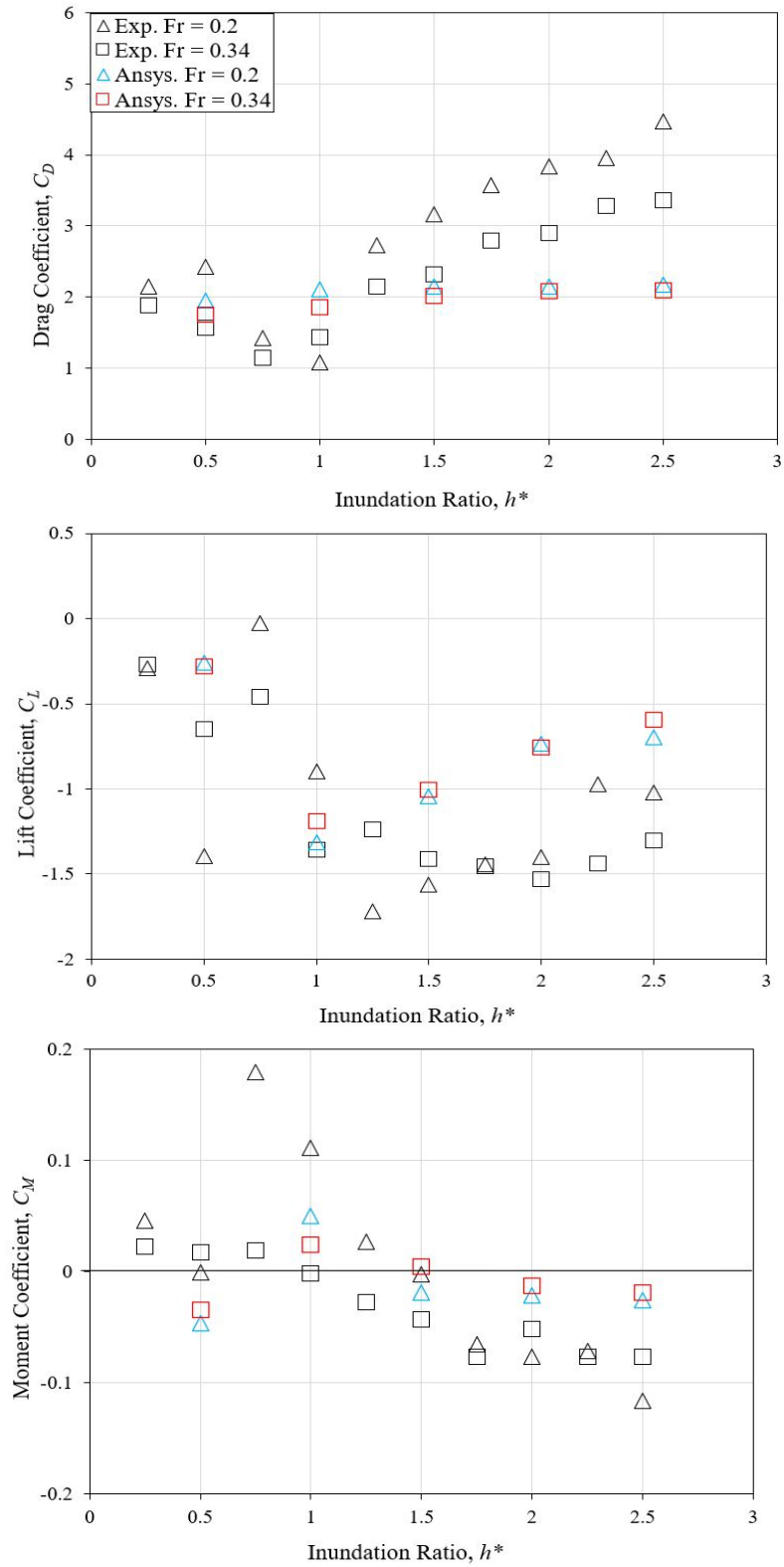


Figure 5.13 Comparison of Drag, lift, and moment coefficients for bridge model TX-28 with 46' deck (15° skewed deck)

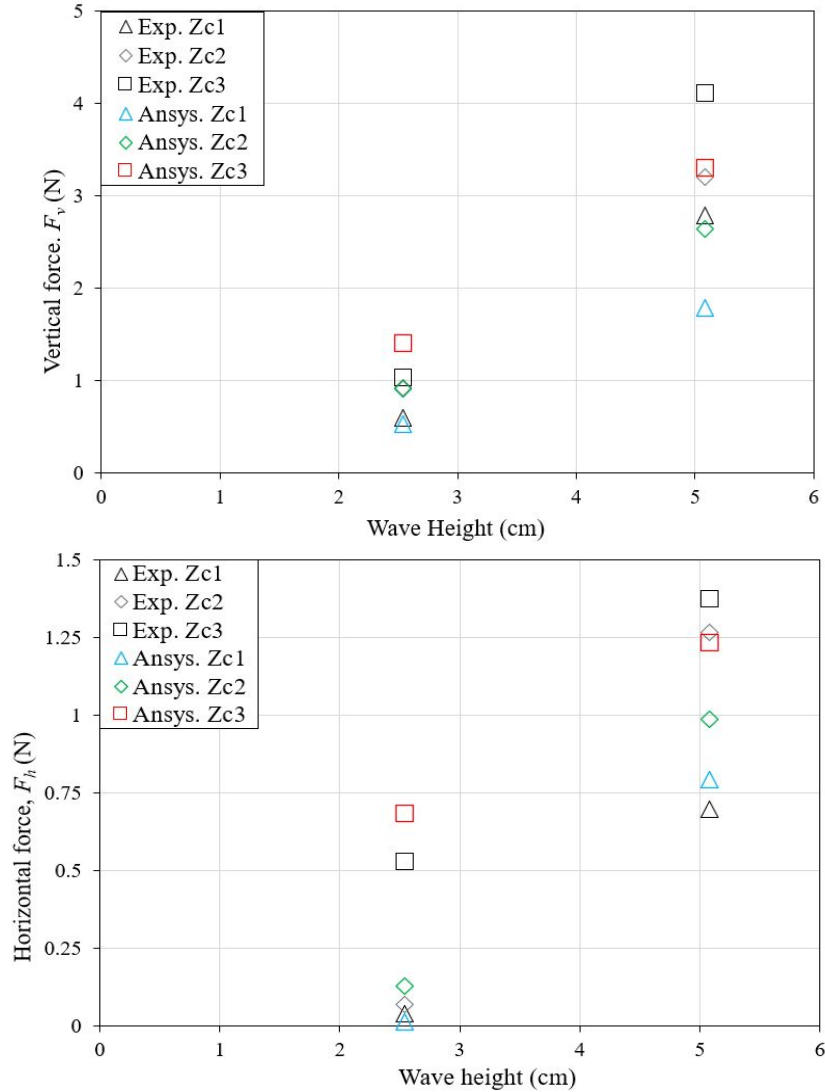


Figure 5.14 Comparison of vertical and horizontal forces under wave conditions for bridge model (TX-54 with 26' deck)

5.6 Results and Discussion

The results for all test series are presented in this section. The drag, lift, and moment coefficients were calculated for all bridge models under different flow conditions, deck widths, skewness, and debris loading. The vertical and horizontal forces exerted by waves of different characteristics are also calculated and presented.

5.6.1 Test Series A

Bridge models with I-beam girders (TX-28 and TX-54) were simulated with 26' and 46' wide decks and no debris. Slab beam and box beam bridge decks with 26' wide decks and no debris

were also modeled in this test series. The drag, lift, and moment coefficients as a function of h^* and Fr are shown in Figures 5.15 through 5.20.

A TX28 bridge with 26' deck was simulated for $Fr = 0.2, 0.27, 0.34, 0.5,$ and 0.9 and h^* from 0.5 to 4 . The drag, lift, and moment coefficients as a function of h^* and Fr are shown in Figure 5.15. For $Fr = 0.2$, additional simulations were also performed for $h^* = 0.25, 0.75,$ and 1.25 . The drag coefficient remains positive at all h^* , but there is a large dip in the drag coefficient graph at $h^*=0.5$. This resembles an event when the bridge deck is a little more than halfway submerged, possibly as the water depth is reaching the top of the girders and in the transition of starting to overtop the bridge deck. In the case of $Fr = 0.2, 0.27,$ and 0.34 , as h^* increases (i.e., $h^* > 1.5$), the drag coefficient values remain constant. However, for $Fr = 0.5$ and 0.9 , the drag coefficient continues to increase above the transition zone. Secondly, the CFD model results highlight that the drag coefficients and the shape of the response to the inundation ratio are dependent on Fr . For example, the curve shifted downward for $Fr = 0.5$ and 0.9 when $h^* > 0.5$. The lift coefficient remains negative for all the simulations performed. A negative lift coefficient means that flow exerts a pull-down force on the bridge deck. There is a major dip in the lift coefficient graph at $h^*=1$, but the lift coefficient approach zero as h^* continues to increase above 1 . The lift coefficient also shows dependence on Fr , as the curve flattens and shifts upward with an increase in Fr . The moment coefficient is positive for $Fr = 0.2, 0.27, 0.34,$ and 0.5 at $h^*=0.25-1$ and negative at $h^* > 1$. The moment coefficients also show dependence on the Fr , as the curve flattens and shifts upward with an increase in Fr .

A TX28 with 46' deck was simulated for $Fr = 0.2$ and 0.34 and $h^*=0.5-2.5$. The drag, lift, and moment coefficients as a function of h^* and Fr are shown in Figure 5.16. For the drag coefficients, the numerical simulation results display a shape similar to the results of the TX-28 bridge with 26' deck, but in this case, drag coefficients keep increasing for $h^* > 1.5$. The dip in the drag coefficient graph here occurs at $h^* = 0.75$ as compared to the previous case (TX54 bridge with 26' deck) where the dip is at $h^* = 0.5$. Secondly, the values of drag coefficient at all h^* are greater than the 26' deck bridge. The CFD model shows that Fr influences drag coefficients but does not influence the trend of the response to h^* . The lift coefficients remain negative for all the simulations performed and exhibit a shape similar to the results of the TX-28 bridge with 26' deck. The CFD model shows a very small dependence of the lift coefficient on Fr , although Fr does not influence the trend of the response to h^* . The response of the moment coefficients for the 46' wide deck bridge is different than the 26' wide deck bridge. The moment coefficient remains positive for both $Fr = 0.2$ and 0.34 at $h^*=1$, and the peak moment coefficient is observed when the bridge is fully inundated.

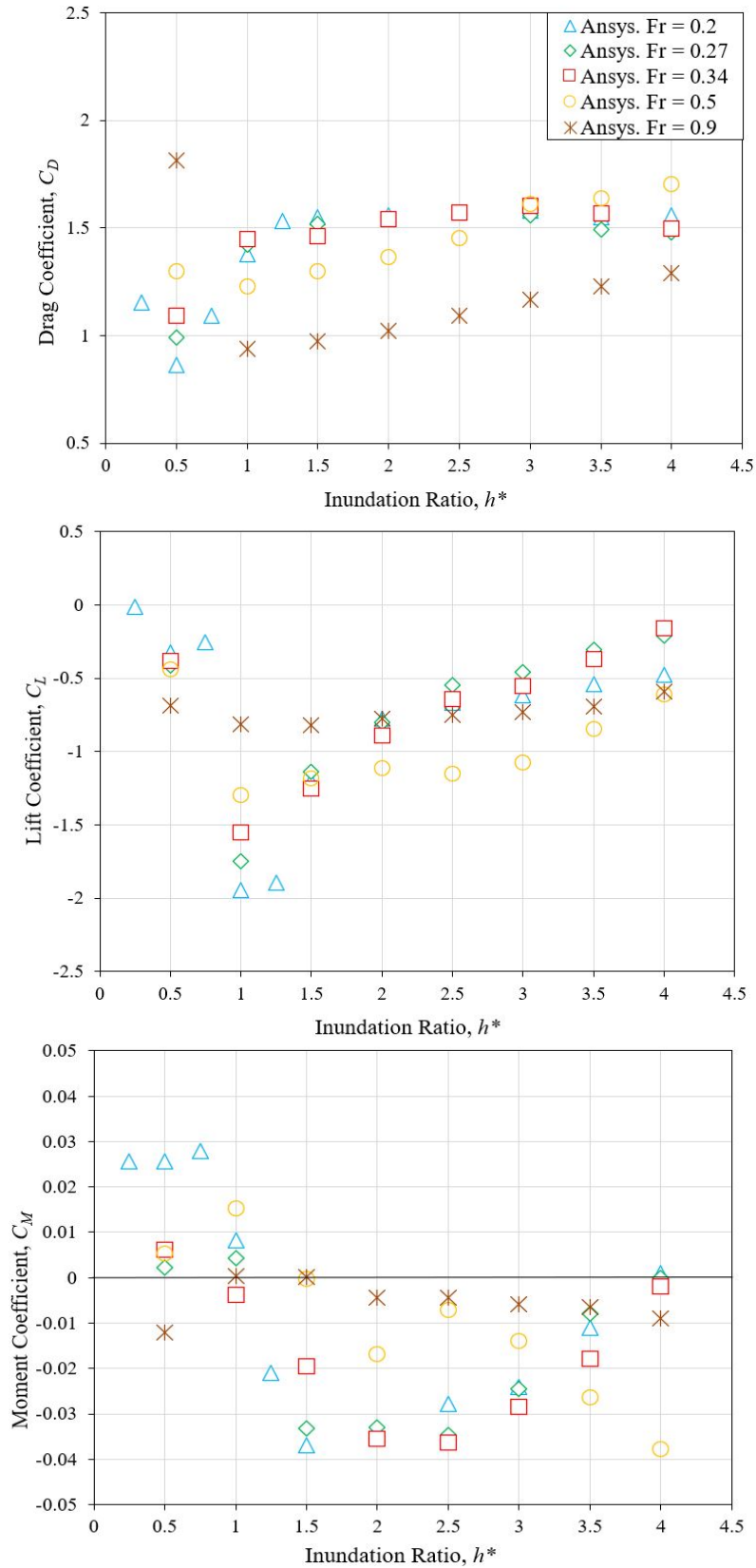


Figure 5.15 Drag, lift, and moment coefficients for bridge model (TX28-26' deck)

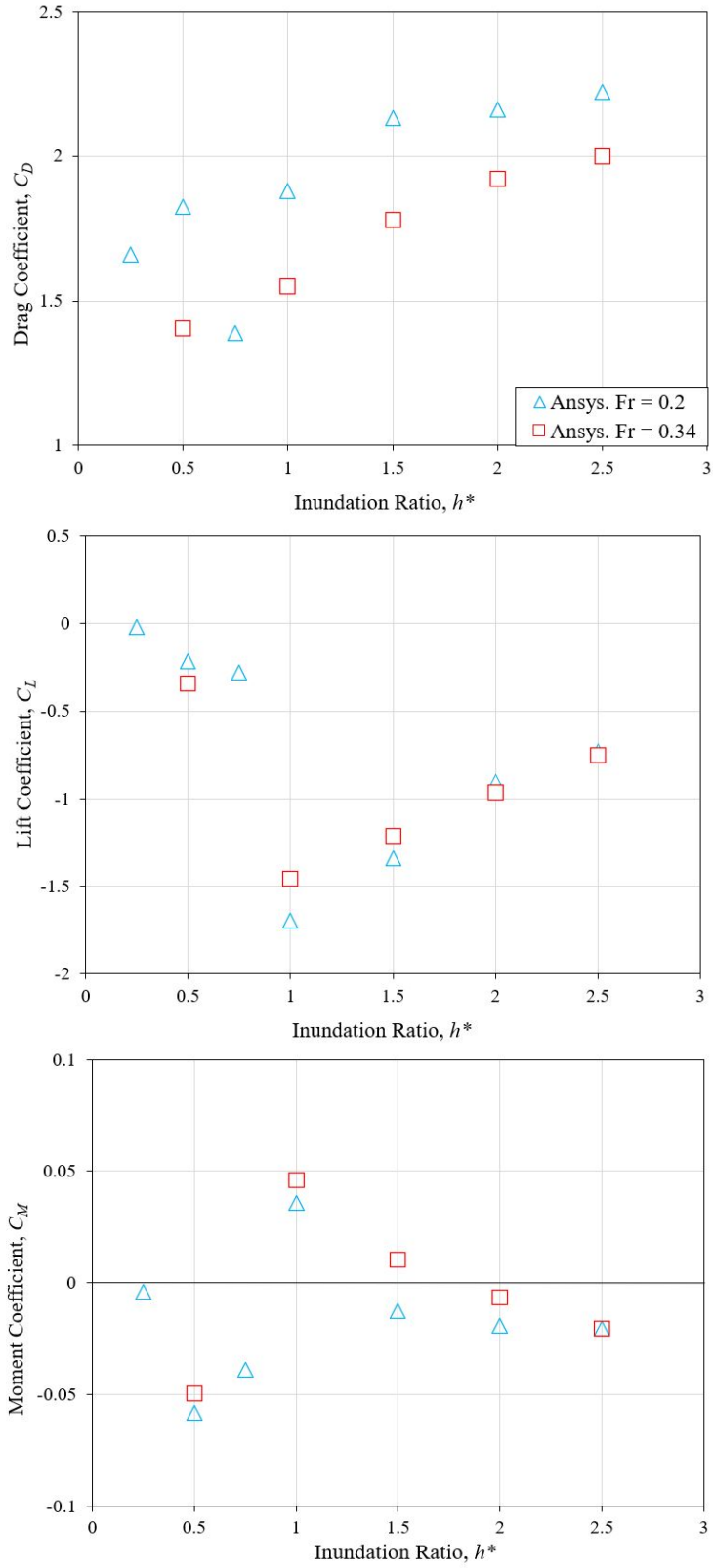


Figure 5.16 Drag, lift, and moment coefficients for bridge model (TX28-46' deck)

The TX-54 bridge with 26' deck was simulated for $Fr = 0.2$ and 0.34 and $h^* = 0.5-2$. The drag, lift, and moment coefficients as a function of h^* and Fr are shown in Figure 5.17. For the drag coefficients, the numerical simulation results showed that between $h^* = 0.5-1.5$, the drag coefficient increases with increasing h^* but after that, for $h^* = 2$, a small decline in the drag coefficient value is observed. In this case, Fr does not affect the drag coefficients or influence the trend of the response to h^* . The lift coefficient remains negative for all the simulations performed for this bridge and show the same trend as in the case of the TX-28 bridge model. The moment coefficients become more negative with increasing h^* , having peak magnitude at $h^* = 2$. The values of both lift and moment coefficients are almost the same for both $Fr = 0.2$ and 0.34 .

The TX-54 bridge with 46' deck was simulated for $Fr = 0.2$ and 0.27 and $h^* = 0.5-2$. The drag, lift, and moment coefficients as a function of h^* and Fr are shown in Figure 5.18. For $Fr = 0.2$, the additional simulations were also performed for $h^* = 0.25$ and 0.75 . The drag coefficients remain positive at all h^* , but there is a large dip in the drag coefficient graph at $h^* = 0.75$. The lift coefficients become more negative with increasing h^* , having the highest magnitude at the $h^* = 1$. Further increases in h^* cause a gradual decrease in lift coefficient magnitude. The drag and lift coefficients show a very small dependence on Fr , and Fr does not influence the trend of the response to the h^* . For $h^* = 0.25-0.75$, the moment coefficients become more negative with increasing h^* before reaching a peak magnitude at $h^* = 1$. For $h^* > 1$, the moment coefficients become more negative as h^* increases.

The slab-beam bridge with 26' deck was simulated for $Fr = 0.2$ and 0.34 and $h^* = 0.5-2.5$. The drag, lift, and moment coefficients as a function of h^* and Fr are shown in Figure 5.19. The drag coefficient is positive for all h^* . The drag coefficient increases with the increase in h^* up to $h^* = 1$ but remains constant at higher h^* . The CFD model shows some influence of Fr on drag coefficients as the curve shifts to lower values for $Fr = 0.34$ but does not influence the trend of the response to h^* . The lift coefficients become more negative with the increase in h^* , having the highest magnitude at $h^* = 1$. Further increases in h^* above 1 cause a gradual decrease in lift coefficient magnitudes. The moment coefficient plot shows that the moment coefficients are positive at all h^* and have a peak value at $h^* = 1$.

The box-beam bridge with 26' deck was simulated for $Fr = 0.2$ and 0.34 , and $h^* = 0.5-2.5$. The drag, lift, and moment coefficients as a function of h^* and Fr are shown in Figure 5.20. For the drag coefficients, the numerical simulation results show that up to $h^* = 0.5-1$, the drag coefficients increase with the increase in h^* but then exhibit a small decline. The CFD model shows the influence of Fr on drag coefficients at the lower inundation ratio ($h^* = 0.5$) but does not influence the trend of the response to h^* . The lift coefficients become more negative with the increase in h^* , having the highest magnitude at $h^* = 1$. Further increase in h^* causes a gradual decrease in lift coefficient magnitudes. The CFD model showed the influence of Fr on lift coefficient as the values increase with the increase in Fr . The moment coefficient plot exhibits that the moment coefficient has the highest value at $h^* = 1$, when the bridge is fully inundated.

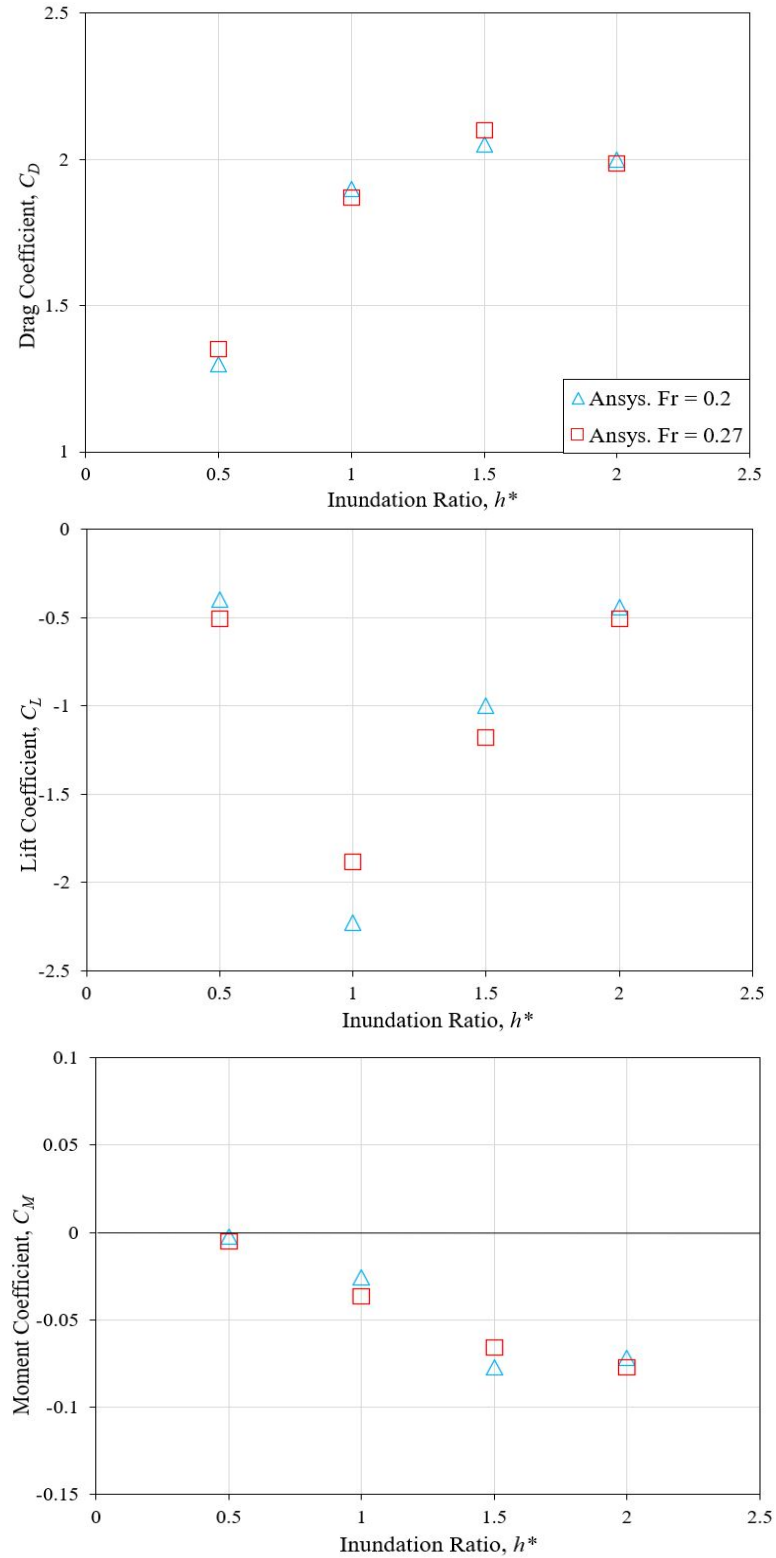


Figure 5.17 Drag, lift, and moment coefficients for bridge model (TX54-26' deck)

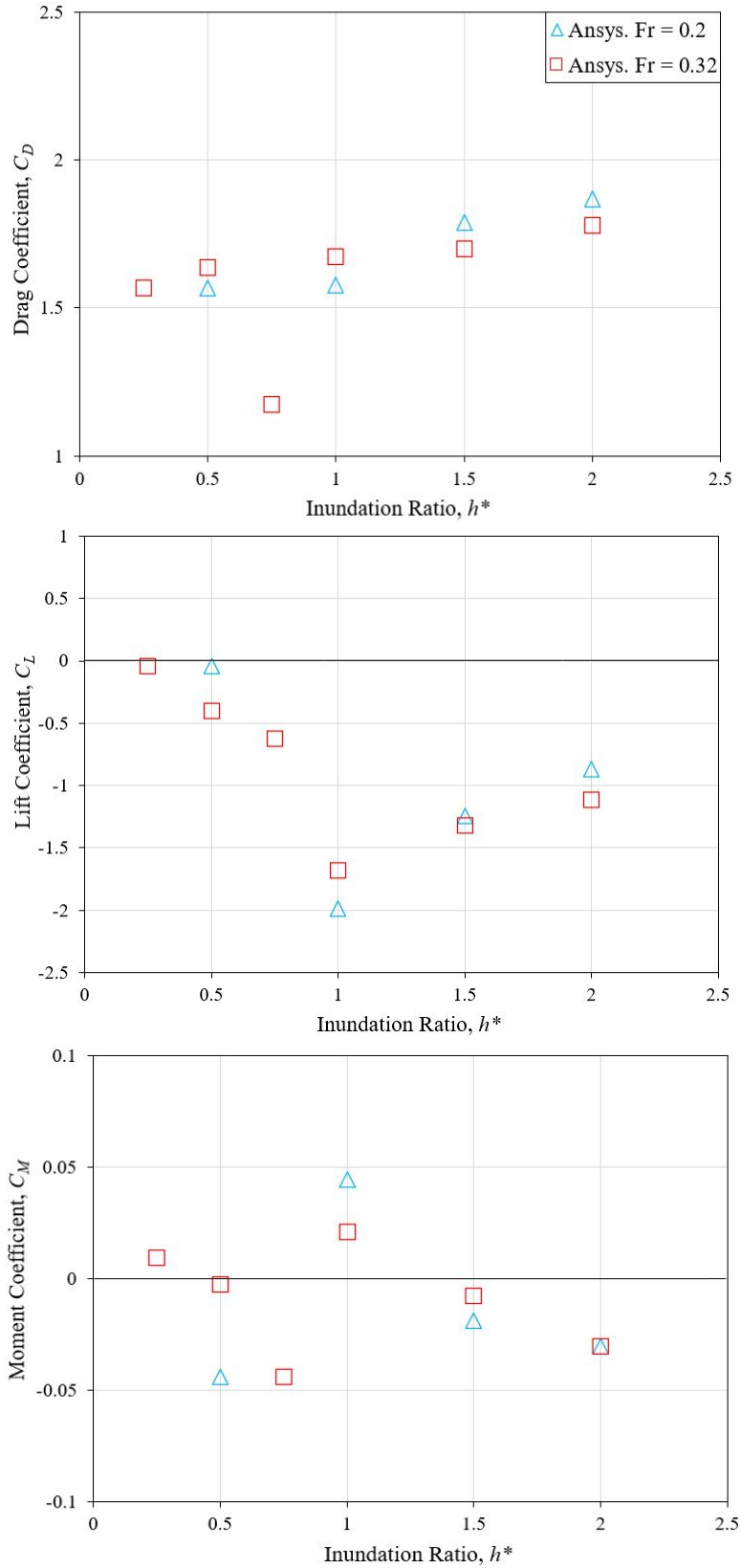


Figure 5.18 Drag, lift, and moment coefficients for bridge model (TX54-46' deck)

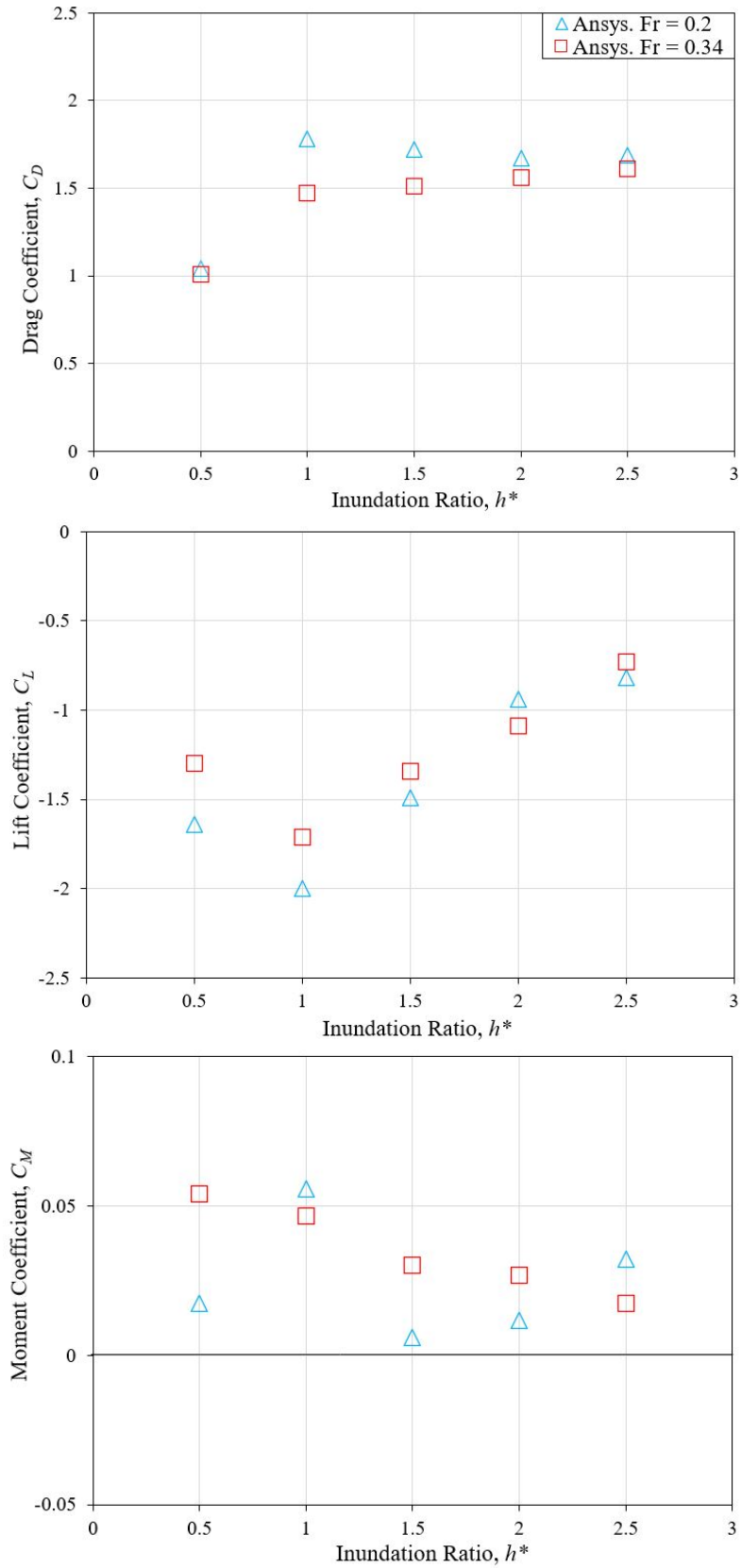


Figure 5.19 Drag, lift, and moment coefficients for bridge model (Slab Beam-26' deck)

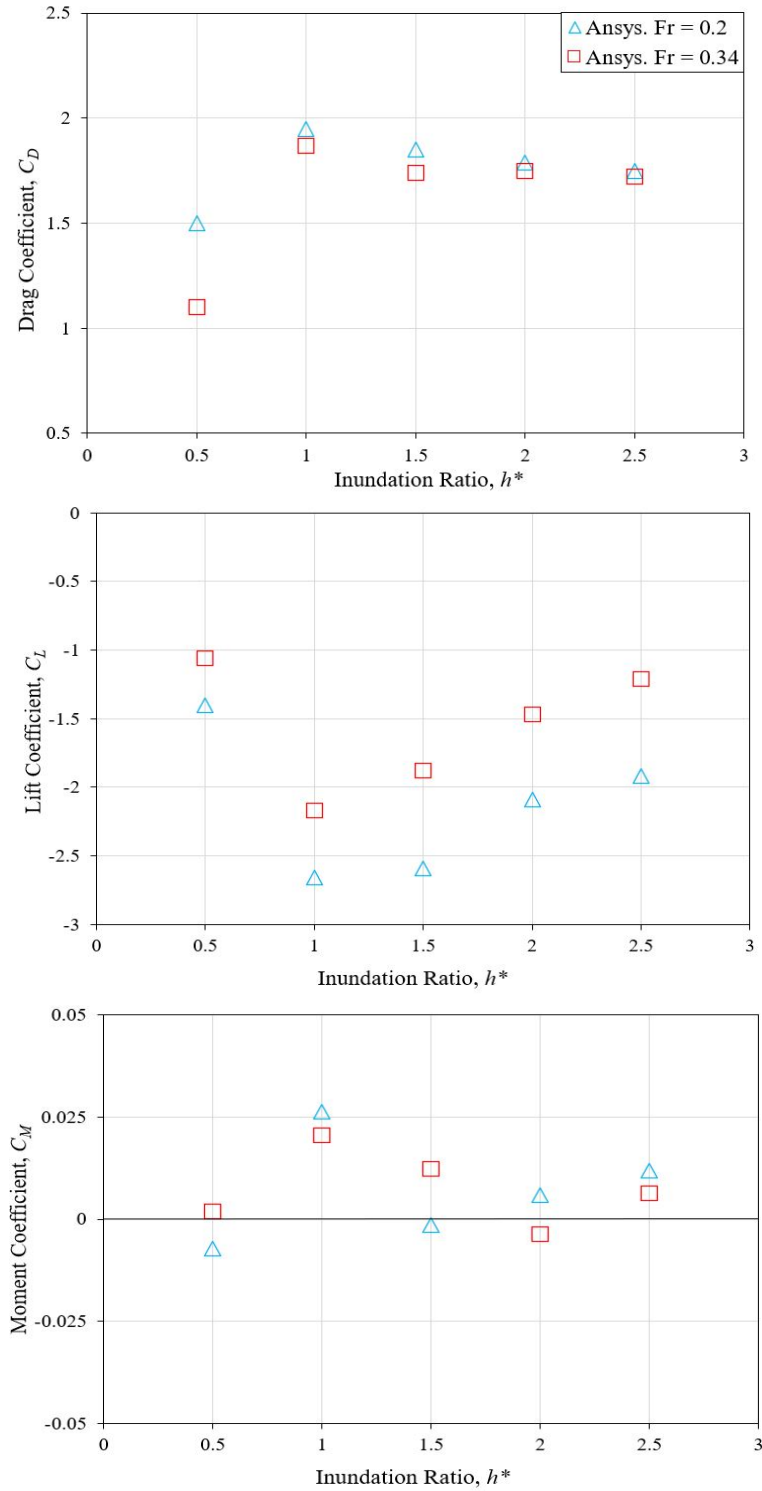


Figure 5.20 Drag, lift, and moment coefficients for bridge model (Box Beam-26' deck)

As demonstrated by the results from Test Series A, the bridge deck shape and dimensions have an impact on the force coefficient values. In general, the magnitude of drag and lift coefficients increase with the increase in deck width. The TX-54 bridge has higher magnitudes of hydrodynamic coefficients as compared to the TX-28, slab-beam, and box-beam decks, due to its larger size. The drag, lift, and moment coefficients exhibit a certain response to h^* , particularly for $h^* = 0.25-1$. In general, the magnitude of the drag coefficient decreases in this transition zone and then approaches a steady critical magnitude as h^* increases above 1. However, the values of lift and moment coefficients consistently increase in this transition zone. Fr values show some impact on the force and moment coefficients and also impact the trend of the response to the different h^* values for some bridge models. In general, a higher Fr decreases the drag coefficients at higher inundation ratios and increases the lift and moment coefficients, depending on the shape and dimensions of the bridge.

5.6.2 Test Series B

The effects of deck skewness on the drag, lift, and moment coefficients are presented in this section. The drag, lift, and moment coefficients as a function of h^* and Fr are shown in Figure 5.21. In these figures, the numerical modeling results for a TX-28 bridge with 46' deck and 0°, 15°, 30°, and 45° skewness were plotted for $Fr = 0.2$ and 0.34. The drag coefficient plot exhibits that the drag coefficient is positive at all h^* . The drag coefficients increase with the increase in h^* but at $h^* > 1.5$, the drag coefficient values remain constant for all the skewed decks. The coefficients of drag force generally decrease with an increase of deck angle of skewness. As shown in this figure, the bridge deck with 45° skew has the lowest values of the drag coefficient. The CFD model shows a very small influence of Fr on drag coefficients and also does not influence the trend of the response to h^* . The skewed deck results show a trend of increasing lift coefficient values with increasing angles of skewness. The results from the CFD modeling with 45° represent the upper boundary of the lift coefficient. The moment coefficients slightly decrease with an increase in angles of skewness. This trend is more prominent for $h^* = 1-1.5$.

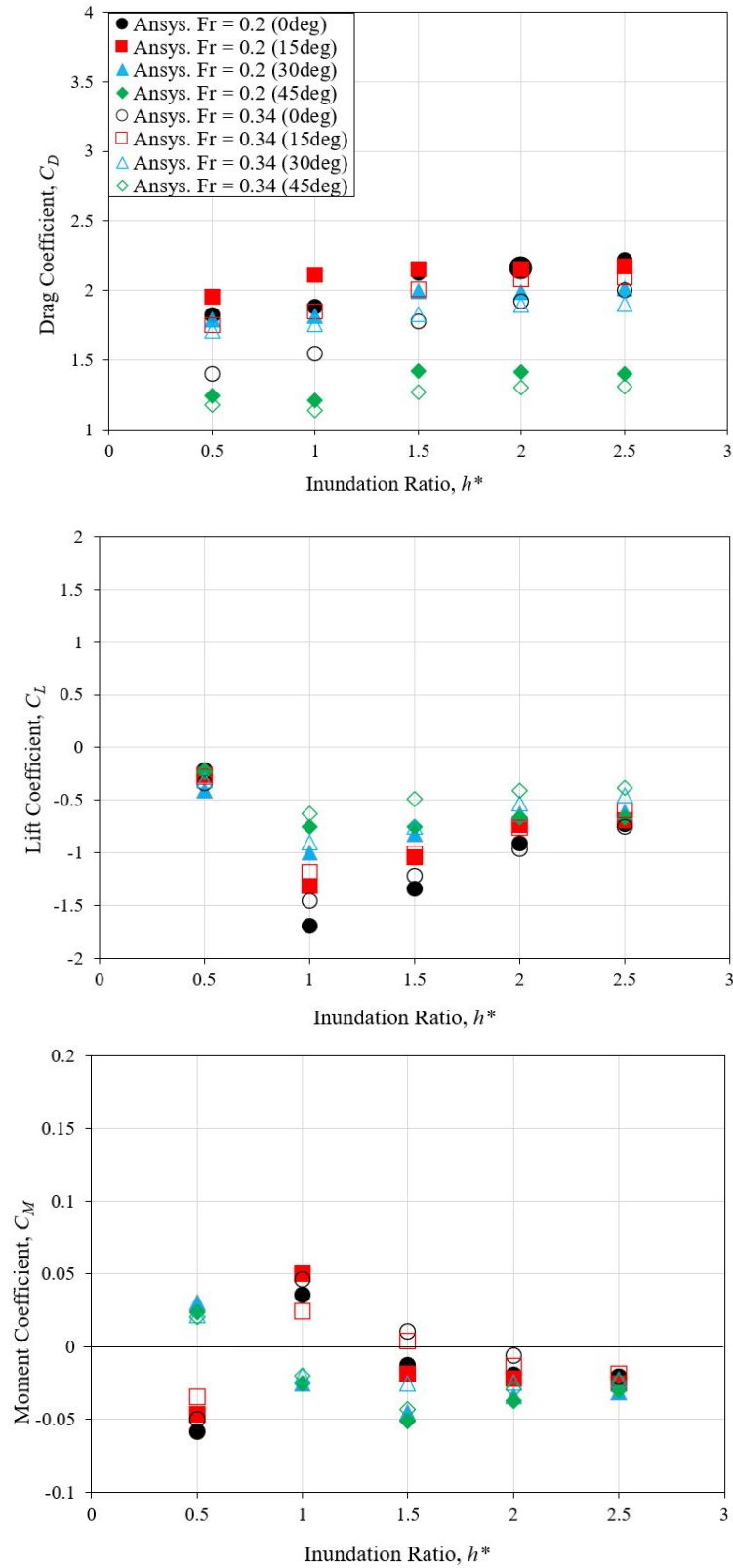


Figure 5.21 Effects of deck skewness on drag, lift, and moment coefficients for bridge model (TX28-46' deck)

5.6.3 Test Series C

In this series of experiments, a TX-54 bridge with 46' deck was simulated. The effects of flat plate and wedge shape debris configurations on the design value of drag, lift, and moment coefficients are presented in this section. The results for the same superstructure and flow conditions without debris are also shown for comparison in Figure 5.22. Debris accumulation upstream of a bridge deck in the form of a vertical obstruction (simulated by flat plate debris mat) significantly increases the drag coefficient. The increase in drag coefficient is more severe for smaller Br. The wedge mat debris, on the other hand, does not impose a significant increase in the drag coefficient. The lift coefficients show similar values under smaller Br with and without debris. As the blockage ratio increases, the lift coefficients become more negative for both the flat plate and wedge shape debris experiments and have a peak magnitude at $Br = 0.31$. The moment coefficients for the bridge deck without debris and with flat plate debris are almost the same for all Br tests; however, the wedge shape debris becomes more negative with the increase in Br and has a peak magnitude at $Br = 0.31$. Even though these conclusions are drawn based on the CFD modeling on a TX-54 bridge, they can generally be extended to other types of deck superstructures.

5.6.4 Test Series D

The effect of wave loading acting on bridge models was examined in this section. TX-54 bridges with 26' and 46' decks and no debris were selected for the numerical modeling. Figure 5.23 shows the comparison of the vertical and horizontal wave forces on two types of bridge decks with three separate elevations and varying wave heights. The vertical wave force on the 46' deck is larger than the vertical wave force on the 26' deck. The horizontal wave force does not exhibit a significant difference between the 46' and 26' decks. Additionally, the maximum wave force is observed when the bridge superstructure is located above the stillwater level, while the minimum wave force is observed when the bridge is submerged under the stillwater level. In general, both vertical and horizontal forces increase with the increase in wave height.

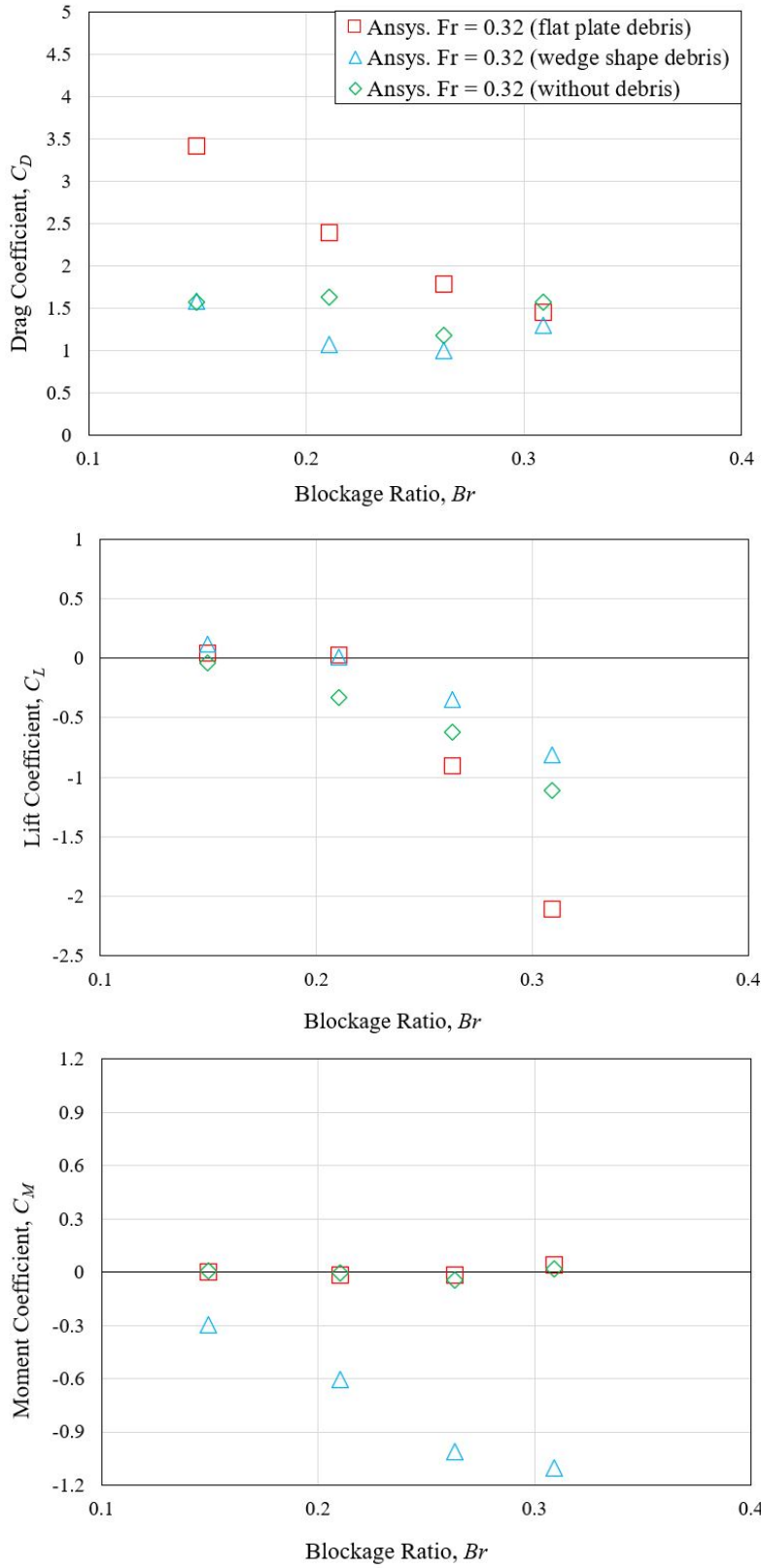


Figure 5.22 Effect of debris on drag, lift, and moment coefficients for bridge model (TX28-46' deck)

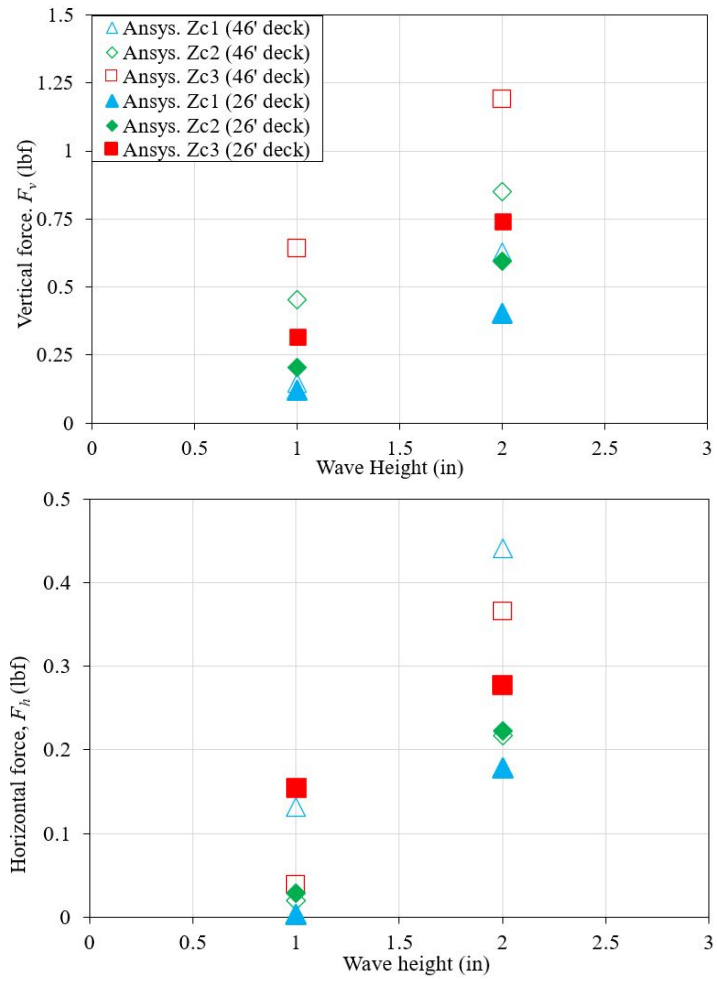


Figure 5.23 Effect of wave height on horizontal and vertical forces for bridge model (TX54-26' deck)

5.6.5 Test Series E: Full-Scale Modeling

The results of the full-scale modeling are shown in Tables 5.8 through 5.10. In general, the drag force (in the x-direction) increases with an increase in Fr . ANSYS Fluent calculates the vertical force (y-direction) as the summation of lift and buoyancy forces. It is clear from the tables that the vertical force becomes more negative and has a larger magnitude with the increase in Fr . The deck width and span length both impact the drag and vertical forces. The drag force is higher for the simulations of larger span and wider bridge decks but on the other hand, the vertical force values decrease. The skewness of the bridge deck also increases the drag force as compared to the no skewed deck. The maximum value is observed for a 30° skewed deck. In the case of wave modeling, the horizontal force (in the x-direction) is smaller as compared to the drag force produced by the upstream flow field alone, although the vertical force is larger. This indicates that, in the case of waves, the vertical force potentially impacts the stability of the bridges more than the flow field alone. The shape of debris also impacts the hydrodynamic forces. The accumulation of flat plate debris on the upstream face of the bridge increases the drag force as compared to the without debris scenario. In the case of accumulation of the wedge shape debris, the lift force increases. Among the simulations performed for Test Series E, the bridge with 125' deck width and the accumulation of flat plate debris has the largest drag force, while the bridge with 45° skewed deck has the largest vertical force magnitude. The results of the full-scale CFD modeling were used for the computational analysis of the bridge structures, which is described in the next section.

Table 5.8 Full-scale modeling results for $Fr = 0.9$ and $h^*=2.5$ ($h^*=0.75$ for wave modeling)

Froude number 0.9				
Bridge Type	Deck Width (ft)	Span Length (ft)	Drag Force (kips)	Lift + Buoyancy (kips)
TX-28	26	50	799	-50
TX-28	46	50	814	-297
TX-54	26	50	1,190	-191
TX-54	46	50	1,236	-324
TX-54	46	125	2,892	-401
TX-54	26	125	2,474	-312
Box-Beam	26	50	705	-102
Slab-Beam	26	50	517	-34
TX-28- 15° Skew	46	50	828	-492
TX-28- 30° Skew	46	50	1,036	-604
TX-28- 45° Skew	46	50	1,015	-802
TX-54 (Wave Modeling)	26	50	780	-527
TX-54 (Debris - Flat Plate)	46	50	1,659	-109
TX-54 (Debris - Wedge)	46	50	1,083	470
TX-54 (Debris - Flat Plate)	46	125	3,385	-259
TX-54 (Debris - Wedge)	46	125	2,306	729

Table 5.9 Full-scale modeling results for $Fr = 0.5$ and $h^*=2.5$ ($h^*=0.75$ for wave modeling)

Froude number 0.5				
Bridge Type	Deck Width (ft)	Span Length (ft)	Drag Force (kips)	Lift + Buoyancy (kips)
TX-28	26	50	250	-301
TX-28	46	50	275	-822
TX-54	26	50	357	-400
TX-54	46	50	374	-841
TX-54	46	125	937	-919
TX-54	26	125	913	-603
Box-Beam	26	50	243	-316
Slab-Beam	26	50	165	-245
TX-28-15° Skew	46	50	316	-1,072
TX-28-30° Skew	46	50	359	-1,170
TX-28-45° Skew	46	50	330	-1,471
TX-54 (Wave Modeling)	26	50	188	-947
TX-54 (Debris - Flat Plate)	46	50	700	-223
TX-54 (Debris - Wedge)	46	50	347	-360
TX-54 (Debris - Flat Plate)	46	125	1,244	-1,030
TX-54 (Debris - Wedge)	46	125	743	454

Table 5.10 Full-scale modeling results for $Fr = 0.34$ and $h^*=2.5$ ($h^*=0.75$ for wave modeling)

Froude number 0.34				
Bridge Type	Deck Width (ft)	Span Length (ft)	Drag Force (kips)	Lift + Buoyancy (kips)
TX-28	26	50	119	-413
TX-28	46	50	134	-928
TX-54	26	50	174	-473
TX-54	46	50	197	-1,053
TX-54	46	125	484	-1,105
TX-54	26	125	450	-653
Box-Beam	26	50	119	-388
Slab-Beam	26	50	85	-329
TX-28-15° Skew	46	50	148	-1,102
TX-28-30° Skew	46	50	174	-1,310
TX-28-45° Skew	46	50	155	-1,559
TX-54 (Wave Modeling)	26	50	87	-1,051
TX-54 (Debris - Flat Plate)	46	50	301	-311
TX-54 (Debris - Wedge)	46	50	163	-490
TX-54 (Debris - Flat Plate)	46	125	526	-1,185
TX-54 (Debris - Wedge)	46	125	358	353

5.6.6 Contour plots

Contour plots for velocity, turbulent kinetic energy, pressure, and wall shear stress are shown in Appendix E. Velocity contours of all the bridges illustrate an increase in velocity above and below the bridge deck due to the separation of the flow. There are also some areas of low velocities, which could influence the stability of the bridge deck. In general, the velocity profiles around all the bridges show good agreement with the anticipated velocity profile around a bluff body (Eckelmann et al., 2013). Turbulent kinetic energy contours illustrate that the maximum turbulent kinetic energy is at the point of separation when the high-velocity flow hits the bridge deck and further decays. Pressure contours show that the pressure is higher on the upstream face where water hits the bridge deck and lower at the downstream face. This pressure gradient can cause instability or failure of the bridge. Wall shear contours show that the shear stresses are higher at the front of the bridge deck and lower at the rear end of the bridge. The uneven distribution of the stresses can also cause instability of the bridge.

6 STRUCTURAL MODELING AND ANALYSIS OF RIVER CROSSING BRIDGES

6.1 Introduction

Lateral movement of superstructures can occur on water crossings due to flooding events and the movement can be restrained by concrete shear keys or earwalls which are either monolithically cast or composited with the bent cap. The shear key is provided on the upstream side of a bridge between the exterior girder and the next adjacent girder (TxDOT Bridge Design Manual, 2020). Figure 6.1 shows a typical shear key placed on the upstream side of the structure between the exterior girder and the next adjacent girder. Figures 6.2 and 6.3 schematically show the TxDOT I-girder shear key (IGSK) on a bent cap with no skew. A shear key is anchored in the bent cap by dowel bars which also serve as the interface shear reinforcement. The design of shear key is based on the interface shear resistance equation in AASHTO LRFD Specifications (2020) as described in Section 6.2. Since the shear key is provided in-between two girders, the length of the shear key depends on the spacing of the girder whereas the width of a shear key is limited to the width of the bent cap (Figure 6.2). The minimum height of the shear key should be at least 8.25 in. as per current TxDOT practice.



Figure 6.1 Shear key on bridge bent cap

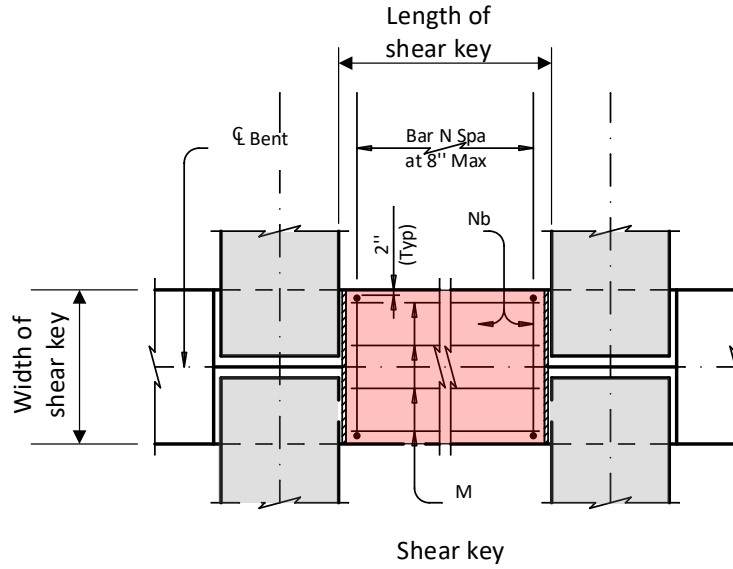
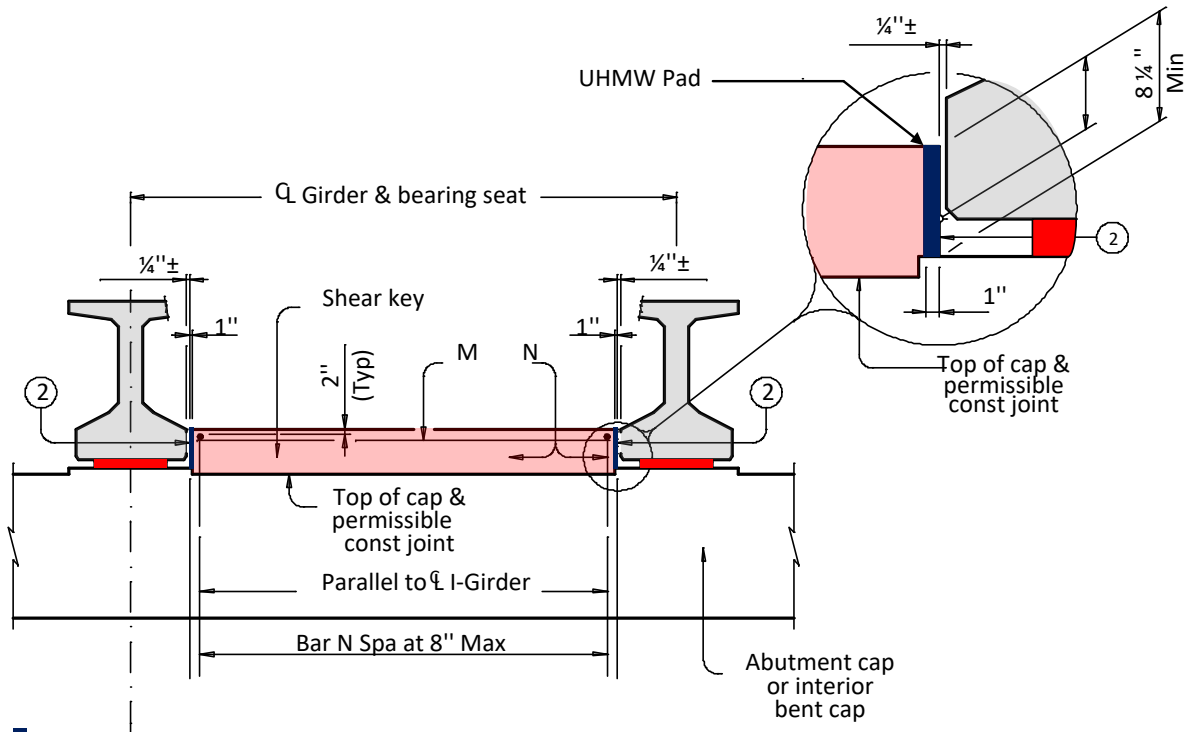


Figure 6.2 TxDOT shear key (plan view)



Ultra-high molecular weight (UHMW) polyethylene wear pad is inserted between the shear key and I-girders in accordance with ASTM D6712.

Figure 6.3 TxDOT shear key (elevation view)

In the case of slab beam bridges and box beam bridges, lateral restraint is provided by the earwalls on the bent cap as shown in Figures 6.4 to 6.6. The design of earwall is based on the interface shear resistance equation in AASHTO LRFD Specifications (2020) as described in Section 6.2. As per current TxDOT practice, the length of earwall is 12 in. and width of earwall is limited to the width of bent cap. The height of earwall is 7 in. for box beam bridges and 9 in. for slab beam bridges. Current TxDOT practice also uses 0.5 in.-thick preformed bituminous fiber materials between box/slab beam and earwall. Earwalls should be cast after the beams are erected in their final position (TxDOT Bridge Detailing Guide, August 2018).



Figure 6.4 Earwall on bridge

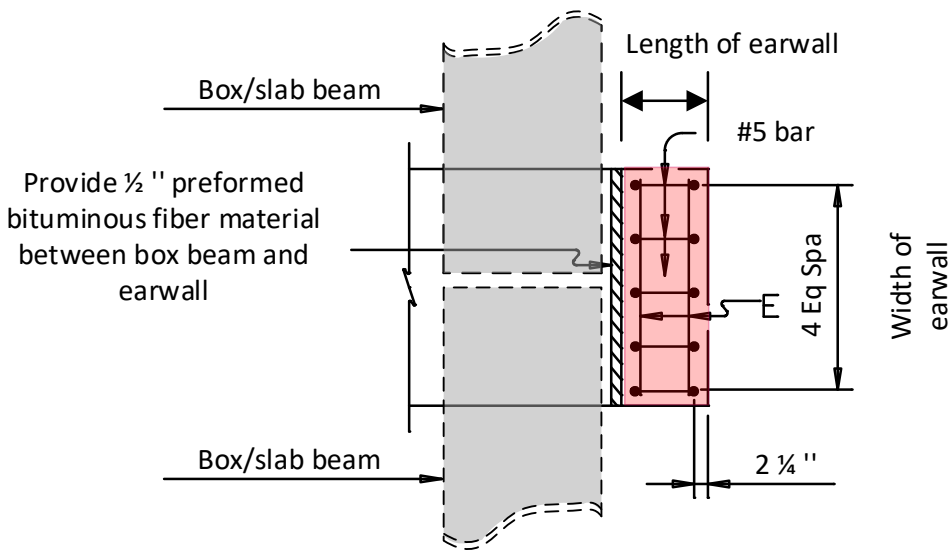


Figure 6.5 TxDOT earwall plan

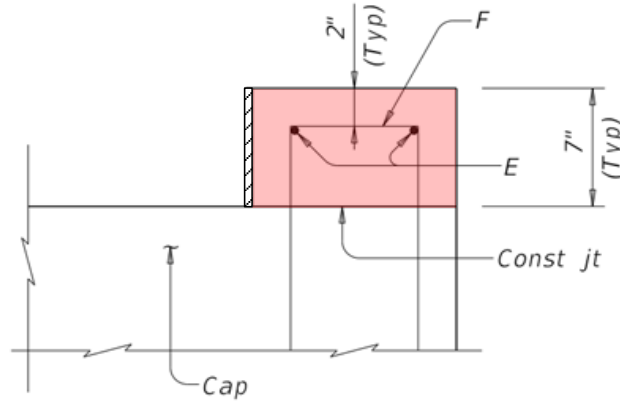


Figure 6.6 TxDOT earwall elevation

The goal of this task was to conduct finite element (FE) modeling of TxDOT bridges with typical I-girders, box beams, and slab beams. The FE models were then analyzed by computational fluid dynamics (CFD) to obtain the forces on the bridge due to flood forces and debris, which were used to examine the interface shear resistance of the shear keys and ear walls according to the shear-friction capacity by AASHTO LRFD Specifications (AASHTO, 2020). If the interface shear strength is not sufficient, several approaches are proposed to increase the capacity of shear key or earwall.

6.2 Interface Shear Resistance

Interface shear resistance described in AASHTO LRFD Specifications (2020) is based on the concept of shear-friction analogy, which describes how shear is transferred across a cracked interface.

According to the shear-friction concept in Article 5.7.4 of AASHTO (2020):

$$\begin{aligned}
 V_{ni} &= c A_{cv} + \mu (A_{vf} f_y + P_c) & (6.1a) \\
 &= c A_{cv} \text{ (cohesion and/or aggregate interlock) (i)} \\
 &\quad + \mu P_c \text{ (friction between the crack faces) (ii)} \\
 &\quad + A_{vf} f_y \text{ (dowel action of the reinforcement) (iii)}
 \end{aligned}$$

The nominal shear resistance, V_{ni} , used in the design shall not be greater than the lesser of:

$$V_{ni} \leq K_1 f'_c A_{cv} \quad (6.1b)$$

or

$$V_{ni} \leq K_2 A_{cv} \quad (6.1c)$$

where A_{cv} is the area of concrete considered to be engaged in interface shear transfer, A_{vf} is the area of interface shear reinforcement crossing the shear plane within the area A_{cv} ; f_y is the yield strength of the interface reinforcement not more than 60 ksi; P_c is the net permanent compression

force normal to the interface; μ is a friction factor; and c is a cohesion factor. K_1 is fraction of concrete strength available to resist interface shear, and K_2 is limiting interface shear resistance. Article 5.7.4.4 of AASHTO provides recommendations for cohesion and friction factors, as well as K_1 and K_2 factors.

Figure 6.7 illustrates the shear-friction concept used by AASHTO. It shows that a wedging action develops in the crack when the opposite sides of the crack are subjected to a shear force. This wedging action results in not only a slip along the interface, but also a dilatation perpendicular to the cracked plane. Due to this dilatation, the reinforcing bar crossing the crack is stressed in tension and clamps both parts together. The equilibrium compression on concrete leads to frictional force. The maximum capacity of the frictional force is reached when the reinforcing bar starts yielding. In addition to the friction, the protrusions of the aggregates on the cracked surface provide an interlock action to the shear resistance (Waweru et al., 2018). Past researchers have used “cohesion” for aggregate interlock.

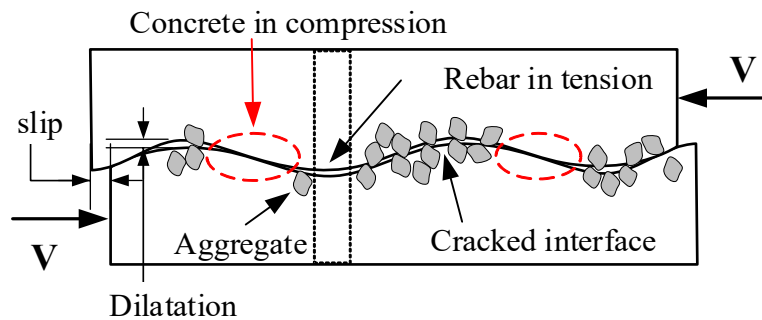


Figure 6.7 Shear friction mechanism (Waweru et al., 2018)

Cohesion (or aggregate interlock) forms the resistance of the protrusions on the crack faces (Mattock and Hawkins 1972; Ali and White 1999; AASHTO, 2020). This can be achieved by artificially roughening the interface, providing a bonding agent (Bass et al., 1989). Friction resistance diminishes rapidly when the crack width (dilatation) increases due to the increased slip (or shear displacement), unless the opening of crack is controlled by effective clamping or restraining forces (Park and Paulay, 1975). Reinforcing bars (that is, interface shear reinforcement) are generally placed at right angles to the shear plane to provide a clamping force between the two potential sliding surfaces. These bars must be adequately anchored to ensure yielding before their debonding and pullout. However, to engage the clamping action of the interface shear reinforcement, the crack between the surfaces must slightly open (Scholz, 2004). Because of the relative slip at the interface, the interface shear reinforcement will also be subjected to shear displacement, which mobilizes the dowel action to transfer a certain amount of shear.

6.3 Finite Element Modeling

In this study, finite element (FE) models for single span TxDOT bridges with typical I-girders, box beams, and slab beams were developed using ANSYS version 2019 R3 (Figure 6.8). The

developed models were then used for CFD analysis to find the drag force on shear key/earwall for different flow conditions. For the structural analysis, full-scale bridges were modeled in ANSYS static structural modules. The materials properties used are summarized in Section 6.4 and the contact interface properties are summarized in Section 6.5.

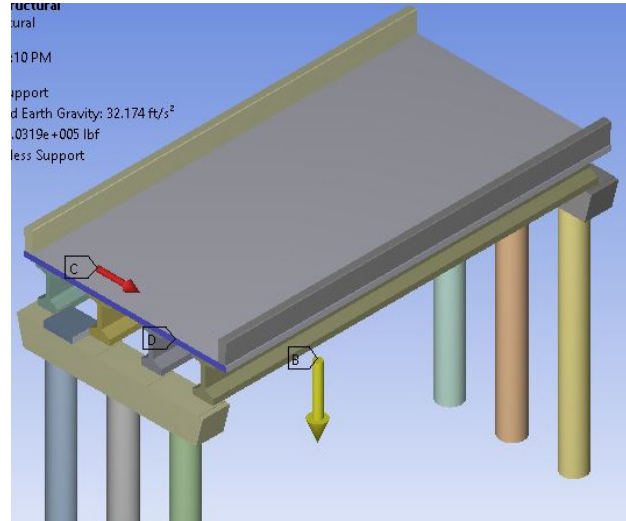


Figure 6.8 Finite element (FE) model of a bridge

6.4 Material Properties

- a. TX28 I-girders, TX54 I-girders, TxDOT box beams (BB-B28), and TxDOT slab beams (5SB15)
 - Concrete compressive strength: 8 ksi
- b. Piers, pier caps, decks, railings, shear keys, and earwalls
 - Concrete compressive strength: 3.6 ksi
- c. Elastomeric bearing pad
 - Shear modulus: 0.120 ksi, based on 2020 AASTHO LRFD Specifications
- d. Ultra-high molecular weight (UHMW) polyethylene wear pads (accordance with ASTM D6712)
 - Compressive strength: 3 ksi
 - Tensile strength: 5.8 ksi
 - Modulus of elasticity: 87 ksi
 - The mechanical properties of UHMW wearing pad were obtained from a local supplier (Nationwide Plastics, Inc. a division of Curbell Plastics | 2001 Timberlake Drive, Arlington, TX 76010)
- e. Prefomed bituminous fiber material between slab beam/box beam and earwall with reference to ASTM D1751.

Figure 6.9 shows the elements of TxDOT I-girder bridge, and Figure 6.10 shows the elements of TxDOT box beam bridge.

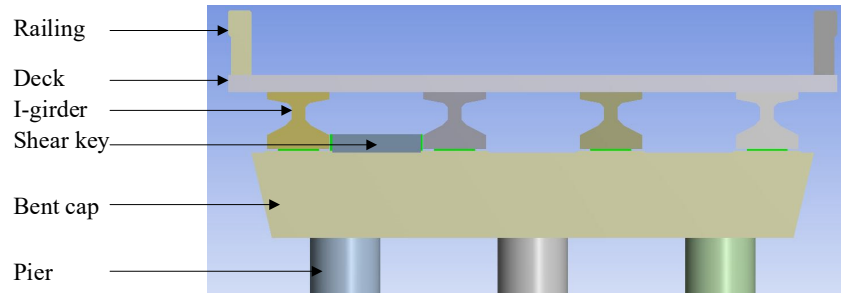


Figure 6.9 Elements of I-girder bridge

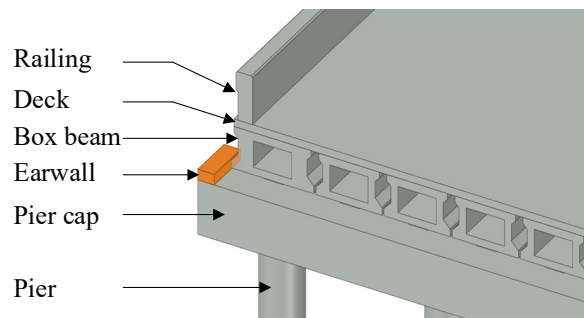


Figure 6.10 Elements of box beam bridge

6.5 Contact Properties

Table 6.1 summarizes the contact interface properties between different members in contact. The contact between railing and deck, deck and girders/beams are assumed bonded so that no sliding or separation occurs during the application of drag force. However, the contact between girder and bearing pad, and bearing pad and bent cap is frictional so they may slide relatively to each other if the drag force exceeds the frictional resistance between the interfaces. In addition, the contact between bent cap and shear key/earwall is also bonded and they act as a composite.

Table 6.1 Contact Properties

Members in Contact		Contact interface property
Railing	Deck	Bonded*
Deck	Girders/Beams	Bonded*
Girder	Bearing pad	Frictional with friction factor 0.2 [§]
Bearing pad	Bent Cap	Frictional with friction factor 0.2 [§]
Bent cap	Shear key	Bonded*
Bent cap	Earwall	Bonded*

* Bonded contacts have zero degrees of freedom between interfacing components. If contact regions are bonded, then no sliding or separation between faces or edges is allowed. This type of contact allows for a linear solution since the contact length/area will not change during the application of the load.

[§] Value provided by the TxDOT project team.

6.6 Calculations of Interface Area of Shear Keys/Earwalls and Corresponding Area of Interface Reinforcement

Length of the shear key depends on the spacing between I-girders and skew angle of the bridge, and width of the shear key is limited to the maximum width of the bent cap. Length and width of different shear keys are calculated in Sections 6.6.1 to 6.6.5. Length and width of earwalls for slab beam bridges and box beam bridges are summarized in Sections 6.6.6 and 6.6.7, respectively.

6.6.1 Length of Shear Key for 24-ft Roadway Bridge (TxDOT Detail BIG-24)

Figure 6.11(a) shows a shear key between two I-girders. 1.0-in.-thick wearing pad is provided between I-girder and the shear key. In general, a ± 0.25 -in. gap is left between girder and face of the wearing pad as shown in Figure 6.11(a). Figure 6.11(b) shows the layout of interface shear reinforcement in a shear key without skew and with a 45° skew angle. An increase in skewness increases the shear key length which allows more space to increase the amount of the interface shear reinforcement.

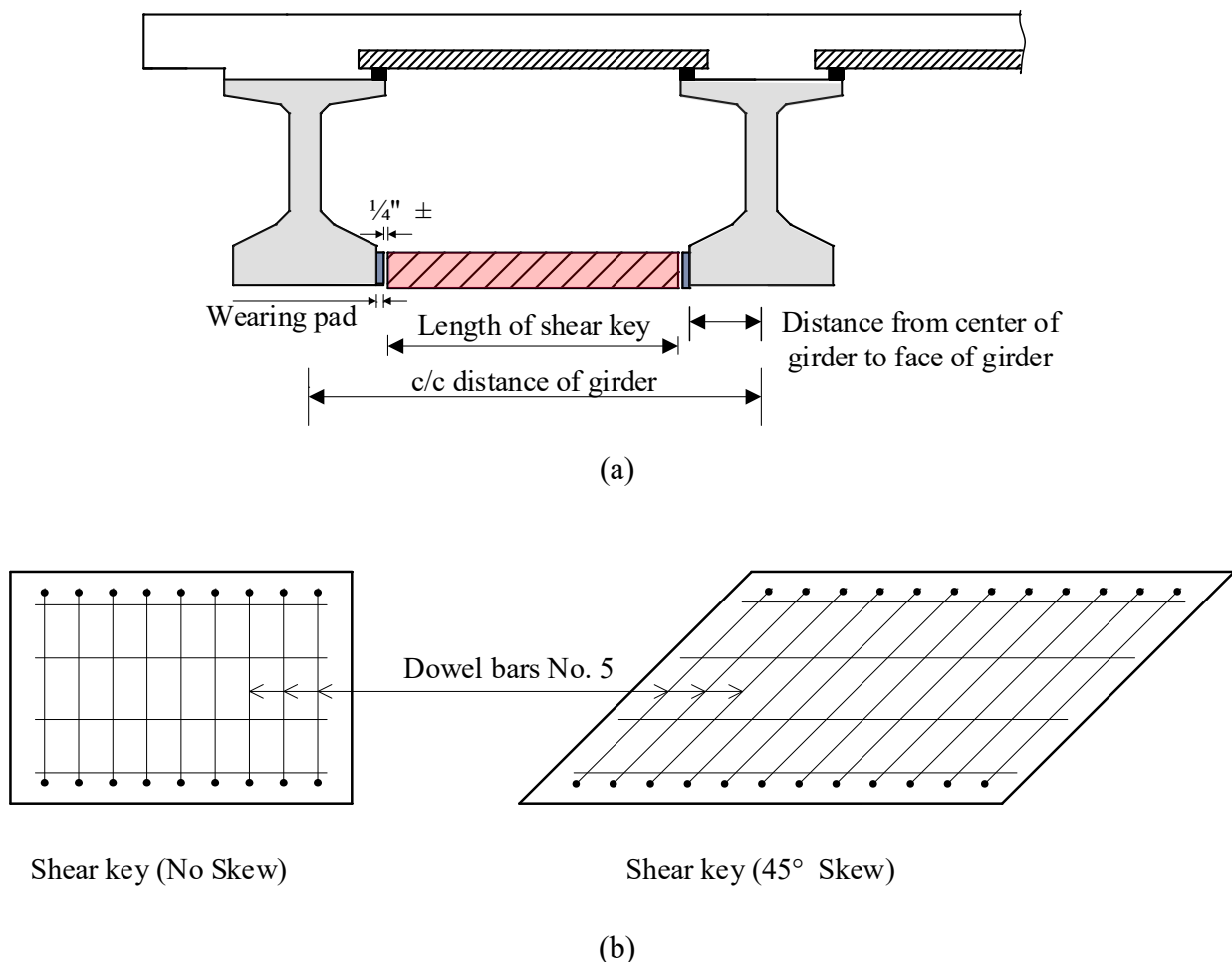


Figure 6.11 (a) Shear key and other elements (b) Interface shear reinforcement in shear key

Figure 6.12 shows a bent cap for a 24-ft roadway with I-girders from TX28 thru TX54. The spacing of girders is 80 in. center-to-center and the width of the bent cap is 42 in. Length of the shear key between the two girders is calculated as follows.

$L = \text{Center-to-center spacing of girders} - \text{distance from center of girder to face of girder} - \text{thickness of two wearing pads} - \text{minimum gap between wearing pad and face of girder}$

$$L = 80 - 2 \times 16 - 2 \times 1 - 2 \times 0.25 = 45.5 \text{ in}$$

Width of shear key: 42 in (width of bent cap)

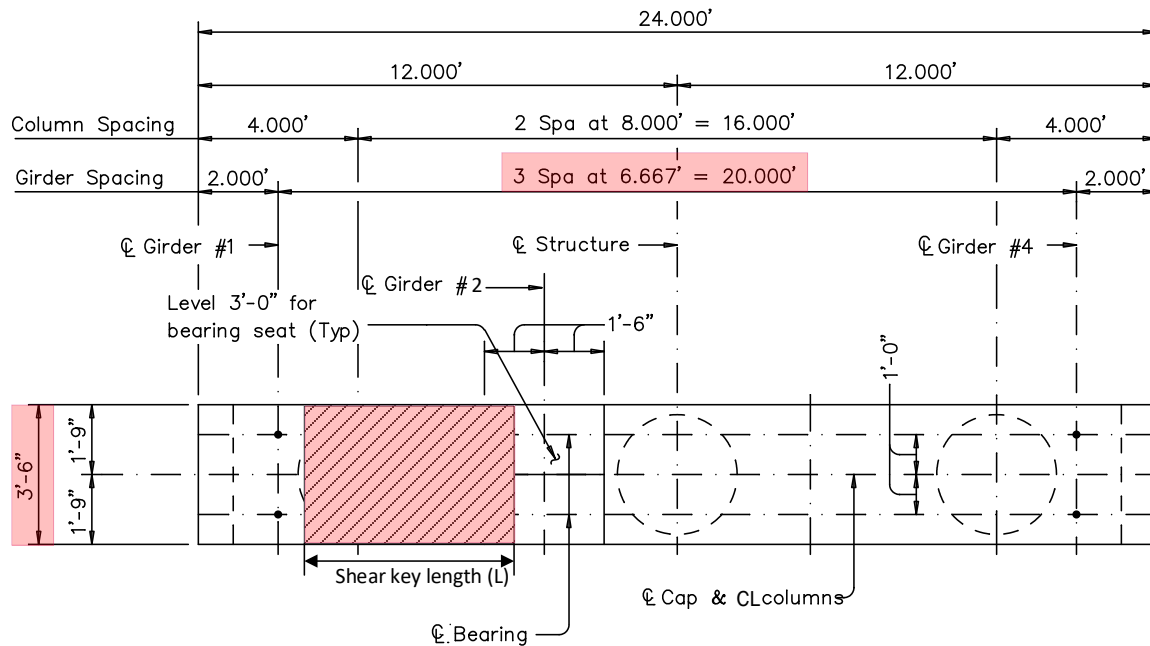


Figure 6.12 Bent cap for 24-ft roadway I-girder bridge

6.6.2 Length of Shear Key for 44-ft Roadway Bridge (TxDOT Detail BIG-44)

Figure 6.13 shows an interior bent for a 44-ft roadway with I-girders from TX28 thru TX54. The spacing of girders is 96 in center-to-center and the width of the bent cap is 42 in. Length of the shear key between the two girders is calculated as follows.

$L = \text{Center-to-center spacing of girders} - \text{distance from center of girder to face of girder} - \text{thickness of two wearing pads} - \text{minimum gap between wearing pad and face of girder}$

$$L = 96 - 2 \times 16 - 2 \times 1 - 2 \times 0.25 = 61.5 \text{ in}$$

Width of shear key: 42 in (width of bent cap)

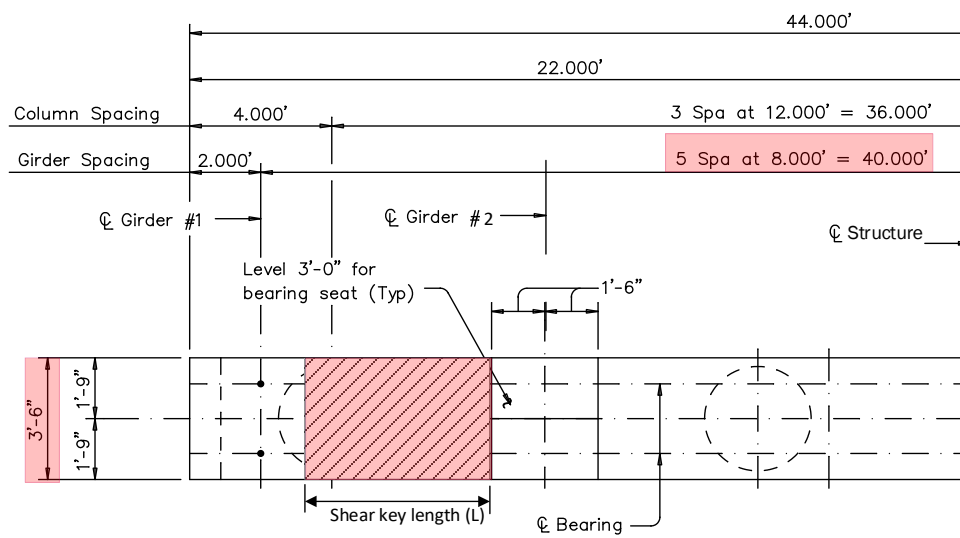


Figure 6.13 Bent cap for 44-ft roadway I-girder bridge

6.6.3 Length of Shear Key for 44-ft Roadway and 15-degree Skew Bridge (TxDOT Detail BIG-44-15)

Figure 6.14 shows an interior bent for a 15° skew, 44-ft roadway with I-girders from TX28 thru TX54. The spacing of girders is 8.282 ft center-to-center and the width of the bent cap is 42 in. Length of the shear key between the two girders is calculated as follows.

L = Center-to-center spacing of girders – distance from center of girder to face of girder – thickness of two wearing pads – minimum gap between wearing pad and face of girder

$$L = 99.4 - 2 \times 16 / \cos(15^\circ) - 2 \times 1 - 2 \times 0.25 = 63.8 \text{ in}$$

Width of shear key: 42 in (width of bent cap)

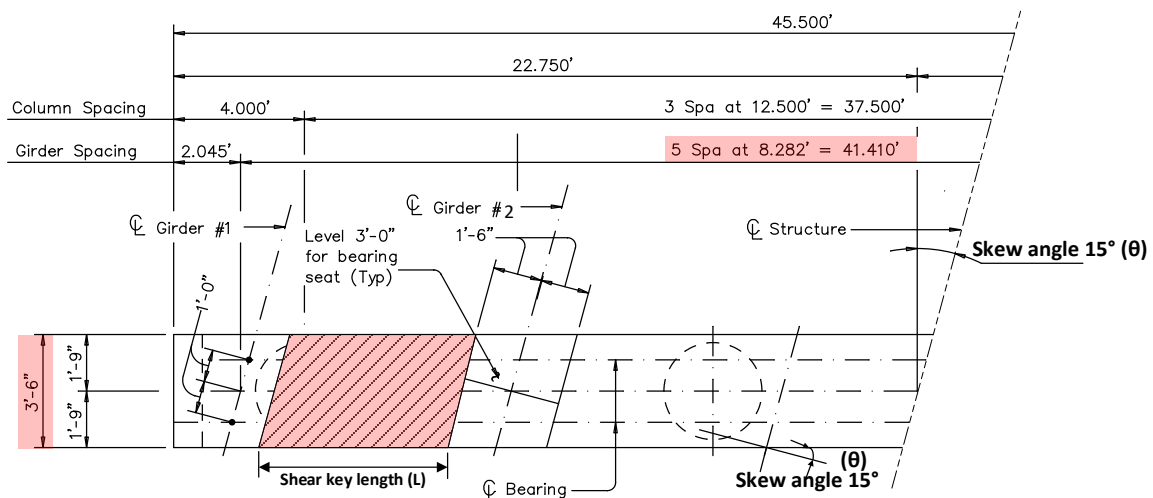


Figure 6.14 Bent cap for 44-ft roadway 15-degree skew I-girder bridge

6.6.4 Length of Shear Key for 44-ft Roadway and 30-degree Skew Bridge (TxDOT Detail BIG-44-30)

Figure 6.15 shows an interior bent for a 30° skew, 44-ft roadway with I-girders from TX28 thru TX54. The spacing of girders is 9.238 ft center-to-center and the width of the bent cap is 42 in. Length of the shear key between two girders is calculated as follows.

L = Center-to-center spacing of girders – distance from center of girder to face of girder – thickness of two wearing pads – minimum gap between wearing pad and face of girder

$$L = 110.9 - 2 \times 16 / \cos(30^\circ) - 2 \times 1 - 2 \times 0.25 = 71.5 \text{ in}$$

Width of shear key: 42 in. (width of bent cap)

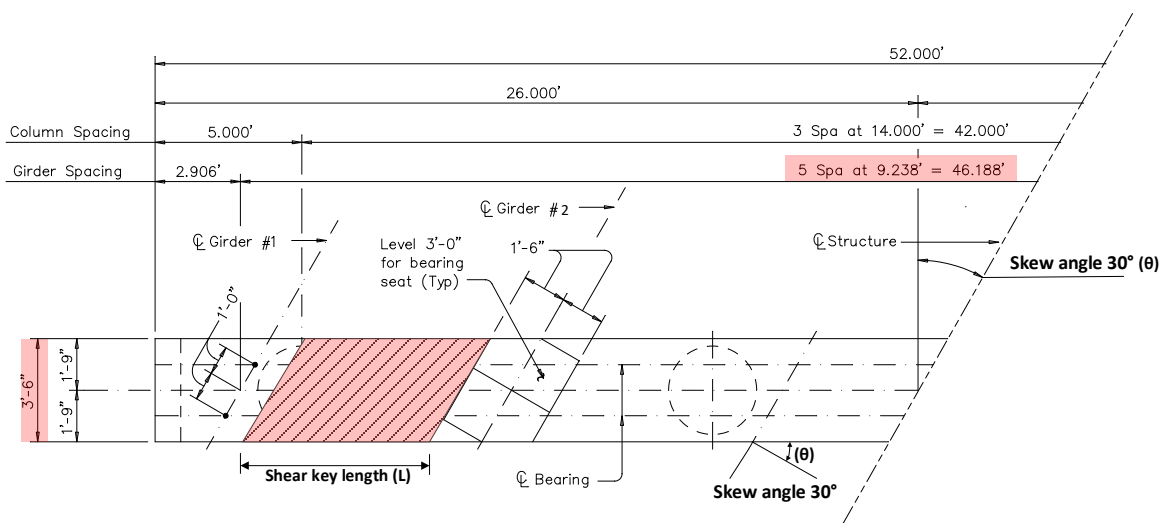


Figure 6.15 Bent cap for 44-ft roadway 30-degree skew I-girder bridge

6.6.5 Length of Shear Key for 44-ft Roadway and 45-degree Skew Bridge (TxDOT Detail BIG-44-45)

Figure 6.16 shows an interior bent for a 45° skew, 44-ft roadway with I-girders from TX28 thru TX54. The spacing of girders is 11.314 ft center-to-center and the width of the bent cap is 42 in. Length of the shear key between two girders is calculated as follows.

L = Center-to-center spacing of girders – distance from center of girder to face of girder – thickness of two wearing pads – minimum gap between wearing pad and face of girder

$$L = 135.8 - 2 \times 16 / \cos(45^\circ) - 2 \times 1 - 2 \times 0.25 = 88.1 \text{ in}$$

Width of shear key: 42 in (width of bent cap)

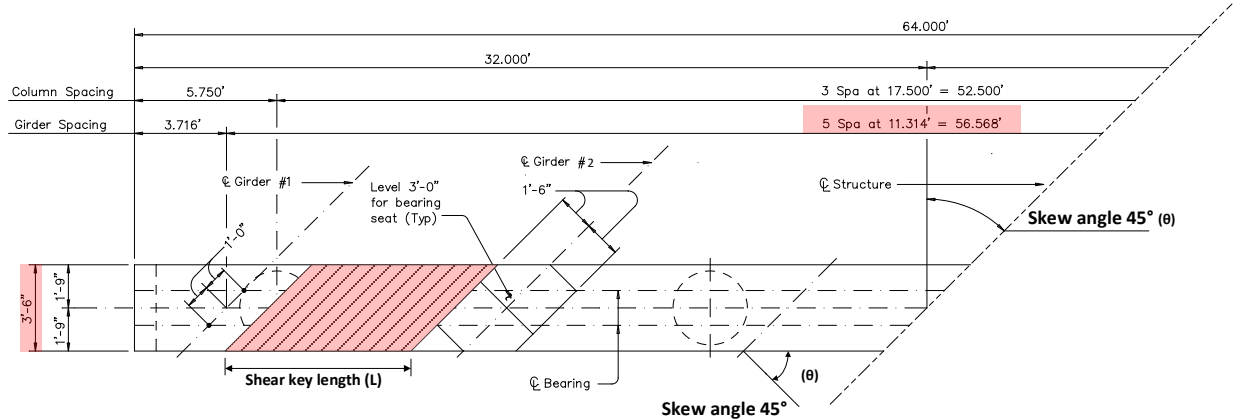


Figure 6.16 Bent cap for 44-ft roadway 45-degree skew I-girder bridge

6.6.6 Length of Earwall for Slab Beam Bridge (TxDOT Detail BPSP-24)

Figure 6.17 shows an interior bent for a 24-ft roadway SB12 or SB15 slab beam bridge.

Length: 12 in. Width of earwalls: 30 in (width of bent cap)

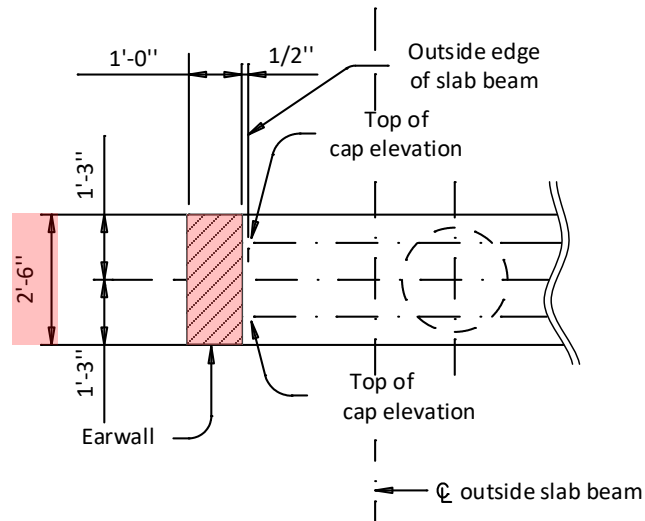


Figure 6.17 Bent cap for slab beam bridge

6.6.7 Length of Earwall for Box Beam Bridge (TxDOT Detail BBB-24)

Figure 6.18 shows an interior bent for a 24-ft roadway with box beam span of 30-ft thru 90-ft.

Length: 12 in. Width of earwalls: 30 in (width of bent cap)

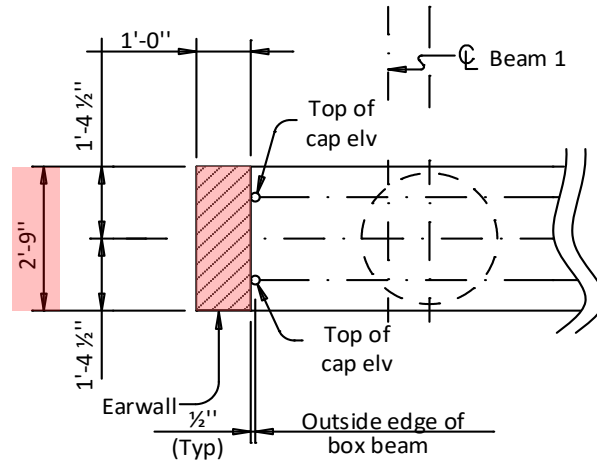


Figure 6.18 Bent cap for box beam bridge

Based on the length and width of shear key and earwall, Table 6.2 summarizes the interface area and area of interface shear reinforcement.

Table 6.2 Summary of area of shear keys/earwalls and area of reinforcement used

Shear keys/earwalls area calculations						
Bents for	TxDOT Std name	Length (in)	Breath (in)	Area, A_{cv} (in ²)	Number of bars/size	Area of reinforcement, A_{vf} (in ²)
24' Roadway (TX28 thru TX54 girders) (Figure 6.12)	BIG-24	45.5	42.0	1911.0	7 #5	4.34
44' Roadway (TX28 thru TX54 girders) (Figure 6.13)	BIG-44	61.5	42.0	2583.0	9 #5	5.58
44' Roadway, 15° skew (TX28 thru TX54 girders) (Figure 6.14)	BIG-44-15	63.8	42.0	2678.8	9 #5	5.58
44' Roadway, 30° skew (TX28 thru TX54 girders) (Figure 6.15)	BIG-44-30	71.5	42.0	3000.9	10 #5	6.20
44' Roadway, 45° skew (TX28 thru TX54 girders) (Figure 6.16)	BIG-44-45	88.1	42.0	3698.1	12 #5	7.44
Slab beam (Ty SB12 or SB15) (Figure 6.17)	BPSP-24	12.0	30.0	360.0	7 #4	2.80
Box beam (30' thru 95' Spans) (Figure 6.18)	BBB-24	12.0	33.0	396.0	5 #5	3.10

6.7 Interface Shear Strengths of Shear Key and Earwall

Article 5.7.4.4 of AASTHO LRFD Specifications (AASHTO, 2020) provides various recommended values for cohesion factor c , friction factor μ , fraction of concrete strength available to resist interface shear K_1 , and the limiting interface shear resistance K_2 . Following conditions are considered when estimating the interface shear strength of the shear key and earwall.

- Cast-in-place concrete slab on clean concrete girder surfaces, free of laitance with surface roughened to an amplitude of 0.25 in.
- Normal weight concrete placed monolithically.

Both cast-in-place concrete slab on clean concrete girder surfaces, and monolithic casting has been considered for the calculations and lower value is conservatively used for the analysis.

- P_c is the net permanent compression force normal to the interface. P_c is essentially the weight of the shear key or earwall which is negligible compared to the other terms; hence it is assumed to be zero.

a. For a cast-in-place concrete slab on clean concrete girder surfaces, free of laitance with surface roughened to an amplitude of 0.25 in

$$c = 0.28 \text{ ksi}$$

$$\mu = 1.0$$

$$K_1 = 0.3$$

$$K_2 = 1.8 \text{ ksi for normal weight concrete}$$

$$= 1.3 \text{ ksi for lightweight concrete}$$

b. For normal weight concrete placed monolithically

$$c = 0.40 \text{ ksi}$$

$$\mu = 1.4$$

$$K_1 = 0.25$$

$$K_2 = 1.5 \text{ ksi for normal weight concrete}$$

6.7.1 Shear Key Resistance for 24-ft Roadway (TX28 Thru TX54 Girders)

a. For normal weight concrete placed monolithically

$$V_{ni} = c A_{cv} + \mu (A_{vf} f_y + P_c) \quad (\text{Eq. 5.7.4-3 in 2020 AASTHO})$$

$$V_{ni} = 0.4 \times 1,911 + 1.4 \times 4.34 \times 60 \text{ (values taken from Table 6.2)}$$

$$V_{ni} = 1,129 \text{ kips}$$

$$V_{ni} \leq K_1 f'_c A_{cv},$$

$$V_{ni} \leq 0.25 \times 3.6 \times 1,911$$

$$V_{ni} \leq 1,720 \text{ kips OK}$$

$$V_{ni} \leq K_2 A_{cv}$$

$$V_{ni} \leq 1.5 \times 1,911$$

$$V_{ni} \leq 2,867 \text{ kips OK}$$

$$\phi V_{ni} = 0.9 \times 1,129$$

$$\phi V_{ni} = 1,016 \text{ kips}$$

- b. For a cast-in-place concrete slab on clean concrete girder surfaces, free of laitance with surface roughened to an amplitude of 0.25 in**

$$V_{ni} = c A_{cv} + \mu (A_{vf} f_y + P_c) \quad (\text{Eq. 5.7.4-3 in 2020 AASTHO})$$

$$V_{ni} = 0.28 \times 1,911 + 1 \times 4.34 \times 60 \text{ (values taken from Table 6.2)}$$

$$V_{ni} = 795 \text{ kips}$$

$$V_{ni} \leq K_1 f_c A_{cv}$$

$$V_{ni} \leq 0.3 \times 3.6 \times 1,911$$

$$V_{ni} \leq 2,064 \text{ kips OK}$$

$$V_{ni} \leq K_2 A_{cv}$$

$$V_{ni} \leq 1.8 \times 1,911$$

$$V_{ni} \leq 3,440 \text{ kips OK}$$

$$\phi V_{ni} = 0.9 \times 795$$

$$\phi V_{ni} = 716 \text{ kips} < 1,016 \text{ kips Controls}$$

6.7.2 Shear Key Resistance for 44-ft Roadway (TX28 Thru TX54 Girders)

- a. For normal weight concrete placed monolithically**

$$V_{ni} = c A_{cv} + \mu (A_{vf} f_y + P_c) \quad (\text{Eq. 5.7.4-3 in 2020 AASTHO})$$

$$V_{ni} = 0.4 \times 2,583 + 1.4 \times 5.58 \times 60 \text{ (values taken from Table 6.2)}$$

$$V_{ni} = 1,502 \text{ kips}$$

$$V_{ni} \leq K_1 f_c A_{cv}$$

$$V_{ni} \leq 0.25 \times 3.6 \times 2,583$$

$$V_{ni} \leq 2,325 \text{ kips OK}$$

$$V_{ni} \leq K_2 A_{cv}$$

$$V_{ni} \leq 1.5 \times 2,583$$

$$V_{ni} \leq 3,875 \text{ kips OK}$$

$$\phi V_{ni} = 0.9 \times 1,502$$

$$\phi V_{ni} = 1,352 \text{ kips}$$

- b. For a cast-in-place concrete slab on clean concrete girder surfaces, free of laitance with surface roughened to an amplitude of 0.25 in**

$$V_{ni} = c A_{cv} + \mu (A_{vf} f_y + P_c) \quad (\text{Eq. 5.7.4-3 in 2020 AASTHO})$$

$$V_{ni} = 0.28 \times 2,583 + 1 \times 5.58 \times 60 \text{ (values taken from Table 6.2)}$$

$$V_{ni} = 1,058 \text{ kips}$$

$$V_{ni} \leq K_1 f'_c A_{cv},$$

$$V_{ni} \leq 0.3 \times 3.6 \times 2,583$$

$$V_{ni} \leq 2,790 \text{ kips OK}$$

$$V_{ni} \leq K_2 A_{cv}$$

$$V_{ni} \leq 1.8 \times 2,583$$

$$V_{ni} \leq 4,649 \text{ kips OK}$$

$$\phi V_{ni} = 0.9 \times 1,058$$

$$\phi V_{ni} = 952 \text{ kips} \leq 1,352 \text{ kips Controls}$$

6.7.3 Shear Key Resistance for 44' Roadway, 15° Skew (TX28 Thru TX54 Girders)

- a. For normal weight concrete placed monolithically**

$$V_{ni} = c A_{cv} + \mu (A_{vf} f_y + P_c) \quad (\text{Eq. 5.7.4-3 in 2020 AASTHO})$$

$$V_{ni} = 0.4 \times 2,678 + 1.4 \times 5.58 \times 60 \text{ (values taken from Table 6.2)}$$

$$V_{ni} = 1,540 \text{ kips}$$

$$V_{ni} \leq K_1 f'_c A_{cv},$$

$$V_{ni} \leq 0.25 \times 3.6 \times 2,678$$

$$V_{ni} \leq 2,411 \text{ kips OK}$$

$$V_{ni} \leq K_2 A_{cv}$$

$$V_{ni} \leq 1.5 \times 2,678$$

$$V_{ni} \leq 4,018 \text{ kips OK}$$

$$\phi V_{ni} = 0.9 \times 1,540$$

$$\phi V_{ni} = 1,386 \text{ kips}$$

- b. For a cast-in-place concrete slab on clean concrete girder surfaces, free of laitance with surface roughened to an amplitude of 0.25 in**

$$V_{ni} = c A_{cv} + \mu (A_{vf} f_y + P_c) \quad (\text{Eq. 5.7.4-3 in 2020 AASTHO})$$

$$V_{ni} = 0.28 \times 2,678 + 1 \times 5.58 \times 60 \text{ (values taken from Table 6.2)}$$

$$V_{ni} = 1,085 \text{ kips}$$

$$V_{ni} \leq K_1 f_c A_{cv},$$

$$V_{ni} \leq 0.3 \times 3.6 \times 2,678$$

$$V_{ni} \leq 2,893 \text{ kips OK}$$

$$V_{ni} \leq K_2 A_{cv}$$

$$V_{ni} \leq 1.8 \times 2,678$$

$$V_{ni} \leq 4,822 \text{ kips OK}$$

$$\phi V_{ni} = 0.9 \times 1,085$$

$$\phi V_{ni} = 976 \text{ kips} \leq 1,386 \text{ kips Controls}$$

6.7.4 Shear Key Resistance for 44' Roadway, 30° Skew (TX28 Thru TX54 Girders)

- a. For normal weight concrete placed monolithically**

$$V_{ni} = c A_{cv} + \mu (A_{vf} f_y + P_c) \quad (\text{Eq. 5.7.4-3 in 2020 AASTHO})$$

$$V_{ni} = 0.4 \times 3,000 + 1.4 \times 6.20 \times 60 \text{ (values taken from Table 6.2)}$$

$$V_{ni} = 1,721 \text{ kips}$$

$$V_{ni} \leq K_1 f_c A_{cv},$$

$$V_{ni} \leq 0.25 \times 3.6 \times 3,000$$

$$V_{ni} \leq 2,701 \text{ kips OK}$$

$$V_{ni} \leq K_2 A_{cv}$$

$$V_{ni} \leq 1.5 \times 3,000$$

$$V_{ni} \leq 4,500 \text{ kips OK}$$

$$\phi V_{ni} = 0.9 \times 1,721$$

$$\phi V_{ni} = 1,549 \text{ kips}$$

- b. For a cast-in-place concrete slab on clean concrete girder surfaces, free of laitance with surface roughened to an amplitude of 0.25 in**

$$V_{ni} = c A_{cv} + \mu (A_{vf} f_y + P_c) \quad (\text{Eq. 5.7.4-3 in 2020 AASTHO})$$

$$V_{ni} = 0.28 \times 3,000 + 1 \times 6.20 \times 60 \text{ (values taken from Table 6.2)}$$

$$V_{ni} = 1,212 \text{ kips}$$

$$V_{ni} \leq K_1 f_c A_{cv},$$

$$V_{ni} \leq 0.3 \times 3.6 \times 3,000$$

$$V_{ni} \leq 3,241 \text{ kips OK}$$

$$V_{ni} \leq K_2 A_{cv}$$

$$V_{ni} \leq 1.8 \times 3,000$$

$$V_{ni} \leq 5,401 \text{ kips OK}$$

$$\phi V_{ni} = 0.9 \times 1,212$$

$$\phi V_{ni} = 1,091 \text{ kips} \leq 1,549 \text{ kips Controls}$$

6.7.5 Shear Key Resistance for 44' Roadway, 45° Skew (TX28 Thru TX54 Girders)

- a. For normal weight concrete placed monolithically**

$$V_{ni} = c A_{cv} + \mu (A_{vf} f_y + P_c) \quad (\text{Eq. 5.7.4-3 in 2020 AASTHO})$$

$$V_{ni} = 0.4 \times 3,698 + 1.4 \times 7.44 \times 60 \text{ (values taken from Table 6.2)}$$

$$V_{ni} = 2,104 \text{ kips}$$

$$V_{ni} \leq K_1 f_c A_{cv},$$

$$V_{ni} \leq 0.25 \times 3.6 \times 3,698$$

$$V_{ni} \leq 3,328 \text{ kips OK}$$

$$V_{ni} \leq K_2 A_{cv}$$

$$V_{ni} \leq 1.5 \times 3,698$$

$$V_{ni} \leq 5,547 \text{ kips OK}$$

$$\phi V_{ni} = 0.9 \times 2,104$$

$$\phi V_{ni} = 1,894 \text{ kips}$$

- b. For a cast-in-place concrete slab on clean concrete girder surfaces, free of laitance with surface roughened to an amplitude of 0.25 in**

$$V_{ni} = c A_{cv} + \mu (A_{vf} f_y + P_c) \quad (\text{Eq. 5.7.4-3 in 2020 AASTHO})$$

$$V_{ni} = 0.28 \times 3,698 + 1 \times 7.44 \times 60 \quad (\text{values taken from Table 6.2})$$

$$V_{ni} = 1,482 \text{ kips}$$

$$V_{ni} \leq K_1 f_c A_{cv},$$

$$V_{ni} \leq 0.3 \times 3.6 \times 3,698$$

$$V_{ni} \leq 3,994 \text{ kips OK}$$

$$V_{ni} \leq K_2 A_{cv}$$

$$V_{ni} \leq 1.8 \times 3,698 \text{ OK}$$

$$V_{ni} \leq 6,657 \text{ kips}$$

$$\phi V_{ni} = 0.9 \times 1,482$$

$$\phi V_{ni} = 1,334 \text{ kips} \leq 1,894 \text{ kips Controls}$$

6.7.6 Earwall Resistance for 24' Roadway Box Beam Bridge (30' Thru 95' Spans)

- a. For normal weight concrete placed monolithically**

$$V_{ni} = c A_{cv} + \mu (A_{vf} f_y + P_c) \quad (\text{Eq. 5.7.4-3 in 2020 AASTHO})$$

$$V_{ni} = 0.4 \times 396 + 1.4 \times 3.10 \times 60 \quad (\text{values taken from Table 6.2})$$

$$V_{ni} = 419 \text{ kips}$$

$$V_{ni} \leq K_1 f_c A_{cv},$$

$$V_{ni} \leq 0.25 \times 3.6 \times 396$$

$$V_{ni} \leq 356 \text{ kips NG}$$

$$V_{ni} \leq K_2 A_{cv}$$

$$V_{ni} \leq 1.5 \times 396$$

$$V_{ni} \leq 594 \text{ kips OK}$$

$$\phi V_{ni} = 0.9 \times 356$$

$$\phi V_{ni} = 320 \text{ kips}$$

- b. For a cast-in-place concrete slab on clean concrete girder surfaces, free of laitance with surface roughened to an amplitude of 0.25 in**

$$V_{ni} = c A_{cv} + \mu (A_{vf} f_y + P_c) \quad (\text{Eq. 5.7.4-3 in 2020 AASTHO})$$

$$V_{ni} = 0.28 \times 396 + 1 \times 3.10 \times 60 \text{ (values taken from Table 6.2)}$$

$$V_{ni} = 297 \text{ kips}$$

$$V_{ni} \leq K_1 f'_c A_{cv},$$

$$V_{ni} \leq 0.3 \times 3.6 \times 396$$

$$V_{ni} \leq 428 \text{ kips OK}$$

$$V_{ni} \leq K_2 A_{cv}$$

$$V_{ni} \leq 1.8 \times 396$$

$$V_{ni} \leq 713 \text{ kips OK}$$

$$\phi V_{ni} = 0.9 \times 297$$

$$\phi V_{ni} = 267 \text{ kips} \leq 320 \text{ kips Controls}$$

6.7.7 Earwall Resistance for 24' Roadway Slab Beam Bridge (TX SB12 or SB15)

a. For normal weight concrete placed monolithically

$$V_{ni} = c A_{cv} + \mu (A_{vf} f_y + P_c) \quad \text{(Eq. 5.7.4-3 in 2020 AASTHO)}$$

$$V_{ni} = 0.4 \times 360 + 1.4 \times 2.8 \times 60 \text{ (values taken from Table 6.2)}$$

$$V_{ni} = 379 \text{ kips}$$

$$V_{ni} \leq K_1 f'_c A_{cv},$$

$$V_{ni} \leq 0.25 \times 3.6 \times 360$$

$$V_{ni} \leq 324 \text{ kips NG}$$

$$V_{ni} \leq K_2 A_{cv}$$

$$V_{ni} \leq 1.5 \times 360$$

$$V_{ni} \leq 540 \text{ kips OK}$$

$$\phi V_{ni} = 0.9 \times 324$$

$$\phi V_{ni} = 292 \text{ kips}$$

b. For a cast-in-place concrete slab on clean concrete girder surfaces, free of laitance with surface roughened to an amplitude of 0.25 in

$$V_{ni} = c A_{cv} + \mu (A_{vf} f_y + P_c) \quad \text{(Eq. 5.7.4-3 in 2020 AASTHO)}$$

$$V_{ni} = 0.28 \times 360 + 1 \times 2.8 \times 60 \text{ (values taken from Table 6.2)}$$

$$V_{ni} = 269 \text{ kips}$$

$$V_{ni} \leq K_1 f'_c A_{cv},$$

$$V_{ni} \leq 0.3 \times 3.6 \times 360$$

$$V_{ni} \leq 389 \text{ kips NG}$$

$$V_{ni} \leq K_2 A_{cv}$$

$$V_{ni} \leq 1.8 \times 360$$

$$V_{ni} \leq 648 \text{ kips OK}$$

$$\phi V_{ni} = 0.9 \times 269$$

$$\phi V_{ni} = 242 \text{ kips} \leq 292 \text{ kips Controls}$$

6.7.8 Summary of Shear Keys/Earwalls Resistance

Table 6.3 summarizes the calculated shear key/earwall area, area of interface shear reinforcement, and the interface shear strength of shear keys/earwalls.

Table 6.3 Summary of shear keys/earwalls resistance

Shear keys/earwalls	TxDOT Std name	Area of shear key/ earwall A_{cv} (in ²)	Area of reinforcement A_{vf} (in ²)	Shear key/earwall capacity (kips)
Shear keys				
24' Roadway (TX28 thru TX54 girders) (Figure 6.12)	BIG-24	1,911	4.34	716
44' roadway (TX28 thru TX54 girders) (Figure 6.13)	BIG-44	2,583	5.58	952
44' roadway, 15° skew (TX28 thru TX54 girders) (Figure 6.14)	BIG-44-15	2,678.8	5.58	976
44' roadway, 30° skew (TX28 thru TX54 girders) (Figure 6.15)	BIG-44-30	3,000.9	6.2	1,091
44' roadway, 45° skew (TX28 thru TX54 girders) (Figure 6.16)	BIG-44-45	3,698.1	7.44	1,334
Earwalls				
Slab beam (Tx SB12 or SB15) (Figure 6.17)	BPSP-24	360	2.8	242
Box beam (30' thru 95' spans) (Figure 6.18)	BBB-24	396	3.1	267

6.8 Force Transfer on Shear Key and Earwall

As shown in Figure 6.19, a shear key or an earwall should resist the drag forces coming from two adjacent spans. The summation of half of the drag force generated from span 1 and half of the drag force generated from span 2 goes to the shear key.

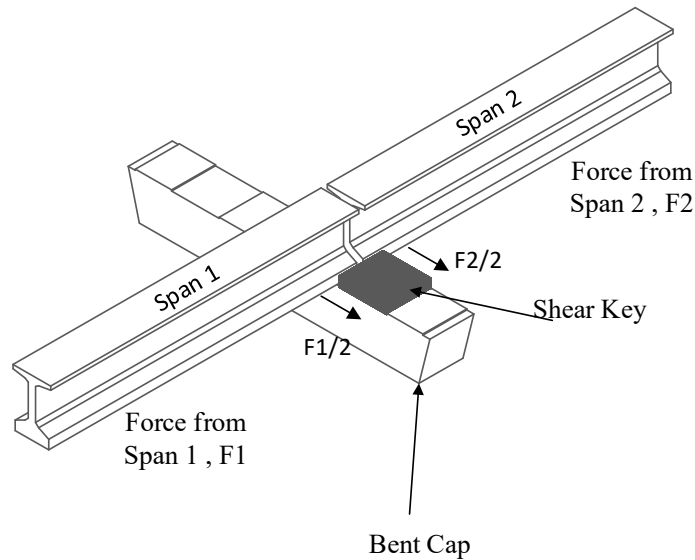


Figure 6.19 Force transfer in shear key

When the drag force is applied on the bridge superstructure, frictional force opposite to the drag force is generated at the interface between the bearing pad and bottom of the girder/bent cap. The frictional force depends on the weight of the superstructure and the coefficient of friction between bearing pad material and concrete. During the fully flooded condition, the water also produces an upward force due to uplift. Downward self-weight (\downarrow) of the superstructure could be balanced by the uplift force and buoyancy (\uparrow). Therefore, in this analysis, frictional resistance between bearing pad and girder/bent cap is conservatively ignored. Consequently, all the drag force is resisted by the shear keys (or the earwall of the box beam or slab beam bridges). Figures 6.20 and 6.21 show the drag force transfer for an I-girder bridge and a box beam bridge, respectively, where drag force coming from flood is first resisted by the bridge superstructure and then transfer to the shear key. Similarly, drag force coming from flood is first resisted by the bridge superstructure and then transferred to the earwall. Although in practice earwalls are commonly provided on both the upstream and downstream sides of a bent cap, only the earwall on the downstream side of the bent cap resists the lateral force.

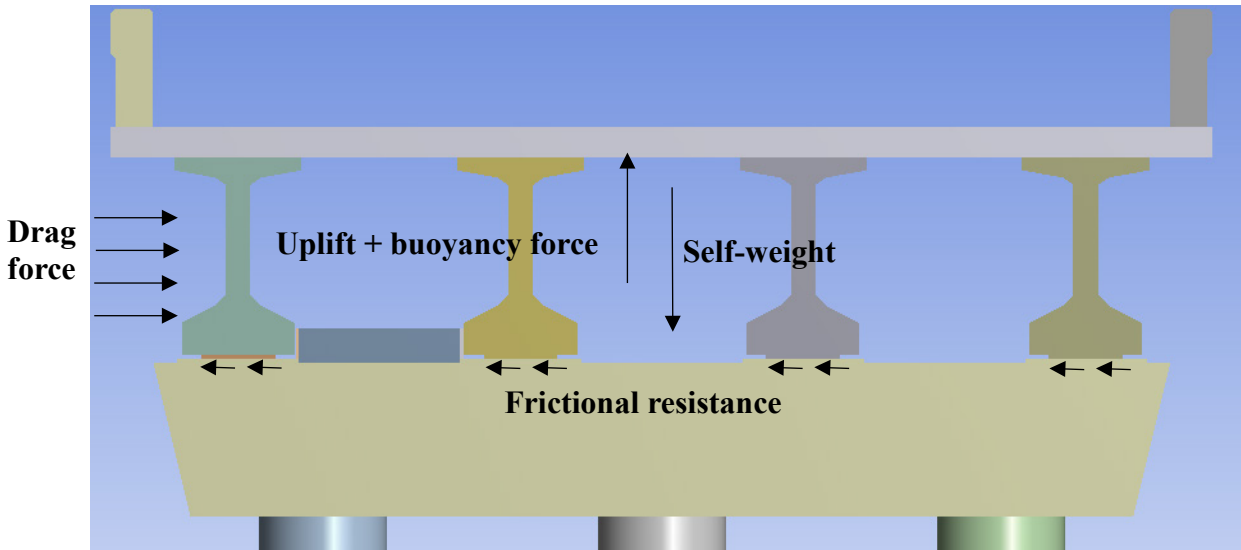


Figure 6.20 Lateral force transfer in I-girder bridge

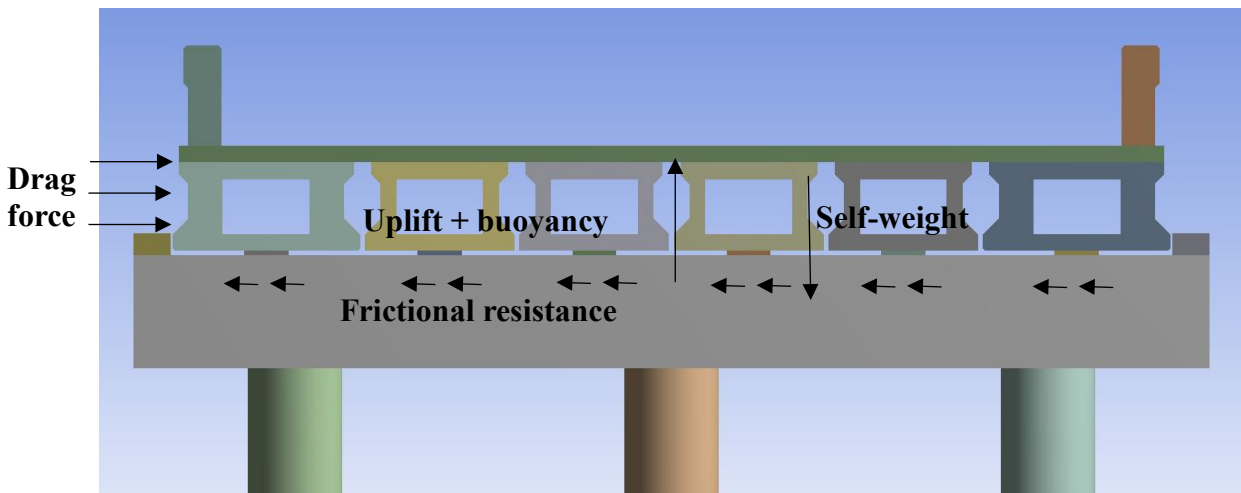


Figure 6.21 Lateral force transfer in box beam bridge

6.9 Analysis Results

Full-scale finite element (FE) models for single span TxDOT bridges with TX28 and TX54 I-girders, TxDOT B28 box beams, and TxDOT S15 slab beams were developed using ANSYS 2019 and analyzed by computational fluid dynamics (CFD) to obtain the forces on the bridge due to flood forces. Sections 6.9.1 to 6.9.5 summarize the computed forces for different flow conditions.

6.9.1 Summary of Full-scale Bridge Model Results for TX28 I-girder Bridge

TX28 I-girder bridge with a span length of 50-ft and two different roadway widths of 24-ft and 44-ft were analyzed. Center-to-center spacing of I-girders for the 24-ft roadway bridge is 6.667-ft

and center-to-center spacing for the 44-ft roadway bridge is 8-ft. The center-to-center spacing of girders for skew bridge varies with skew angles. For the 15-degree-skew, 24-ft wide roadway bridge the spacing of girders is 8.282-ft; for 30-degree skew, 24-ft roadway bridge the spacing of girders is 9.238-ft, and for 45-degree-skew, 24-ft roadway bridge the spacing of girders is 11.314-ft. The capacity of each shear key has been calculated in Section 6.7, and the force on each shear key is obtained from the CFD analysis. Table 6.4 compares the capacity and drag force on the shear key. Drag forces for three different Froude numbers of 0.34, 0.5, and 0.9 are calculated but the comparison is made only with the largest force given by Froude number of 0.9. Figure 6.22 shows the TX28 24-ft roadway I-girder bridge, Figure 6.23 shows TX28 44-ft roadway I-girder bridge, Figure 6.24 shows 15-degree skew, 44-ft roadway TX28 I-girder bridge, Figure 6.25 shows 30-degree skew, 44-ft roadway TX28 I-girder bridge, and Figure 6.26 shows 45-degree skew, 44-ft roadway TX28 I-girder bridge.

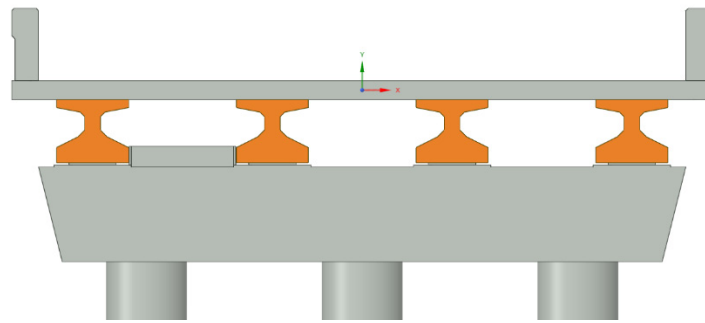


Figure 6.22 24-ft roadway TX28 I-girder bridge

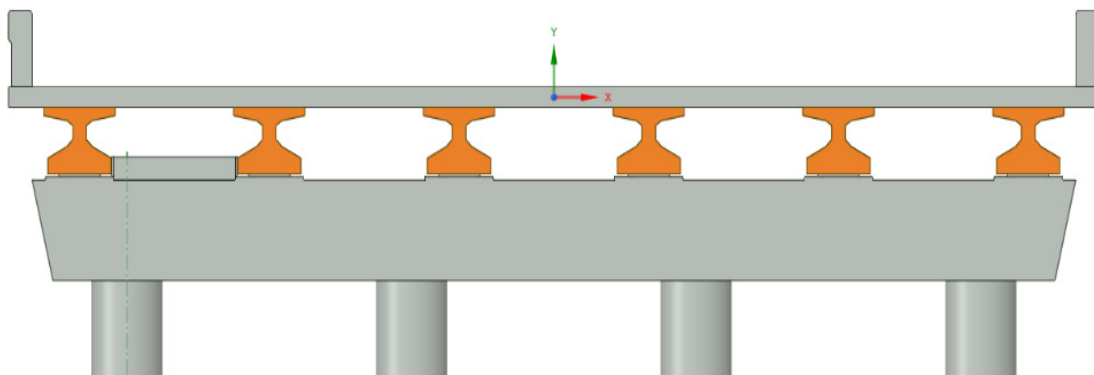


Figure 6.23 44-ft roadway TX28 I-girder bridge

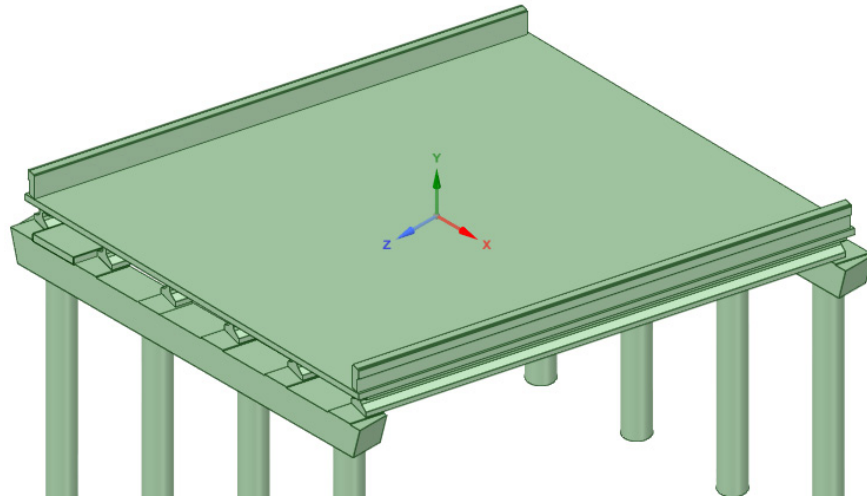


Figure 6.24 15-degree skew, 44-ft roadway TX28 I-girder bridge

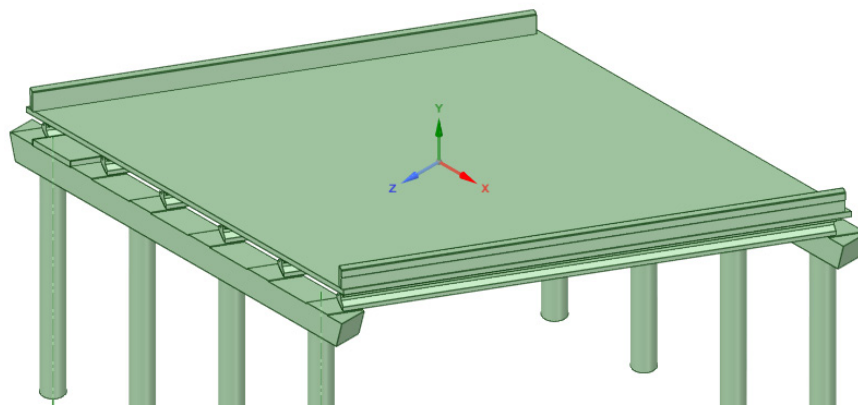


Figure 6.25 30-degree skew, 44-ft roadway TX28 I-girder bridge

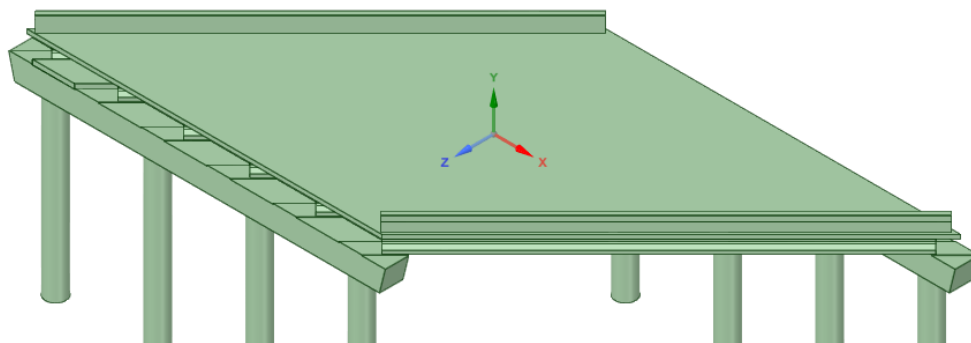


Figure 6.26 45-degree skew, 44-ft roadway TX28 I-girder bridge

Full-scale TX28 I-girder bridges with 24-ft roadway and 44-ft roadway for span length of 50-ft were analyzed by CFD for three different Froude numbers of 0.34, 0.5, and 0.9. Based on the FE analyses, the drag force on a 44-ft roadway is 2%-12% higher compared to the drag force on a 24-ft roadway. On the other hand, increased roadway width allows a greater spacing between girders, which increases interface shear area and interface shear reinforcement hence increases the interface shear resistance. Although an increased roadway width also has a larger drag force for the 44-ft roadway bridge, the interface shear strength of the shear key is sufficient for TX28 I-girder bridges with the 44-ft roadway for every Froude number analyzed. However, the interface shear resistance is not sufficient for TX28 I-girder bridges with the 24-ft roadway for Froude number of 0.9. Recommended modifications of the shear key details for a higher capacity are presented in Section 6.10.1.

Table 6.4 Summary of full-scale bridge model results for TX28 I-girder bridge and capacity comparison

Bridge type	Froude No. 0.34	Froude No. 0.5	Froude No. 0.9	Shear key (kips)	Remarks	Check
	Drag force on shear key (kips)	Drag force on shear key (kips)	Drag force on shear key (kips)			
TX28 girders, 24' Roadway, 50' span (Figure 6.22)	119	250	799	716	Capacity < Force	Redesign shear key
TX28 girders, 44' Roadway, 50' span (Figure 6.23)	134	275	814	952	Capacity > Force	OK
TX28 girders, 24' Roadway, 15° skew, 50' span (Figure 6.24)	148	316	828	976	Capacity > Force	OK
TX28 girders, 24' Roadway, 30° skew, 50' span (Figure 6.25)	174	359	1,036	1,091	Capacity > Force	OK
TX28 girders, 24' Roadway, 45° skew, 50' span (Figure 6.26)	155	330	1,015	1,334	Capacity > Force	OK

6.9.2 Summary of Full-scale Bridge Model Results for TX54 I-girder Bridge

TX54 I-girder bridges with a span length of 50-ft and 125-ft and two different roadway widths of 24-ft and 44-ft were analyzed. Center-to-center spacing of girders for the 24-ft roadway bridge is

6.667-ft and center-to-center spacing for the 44-ft roadway bridge is 8-ft. The capacity of each shear key has been calculated in Section 6.7, and the force on each shear key is obtained from CFD analysis. Figure 6.27 shows 24-ft roadway TX54 I-girder bridge, and Figure 6.28 shows 44-ft roadway TX54 I-girder bridge. Table 6.5 compares the interface shear capacity of the shear key and the drag force on the shear key. Drag forces for three different Froude numbers of 0.34, 0.5, and 0.9 have been calculated but the comparison is made only with the largest force which is given by Froude number of 0.9.

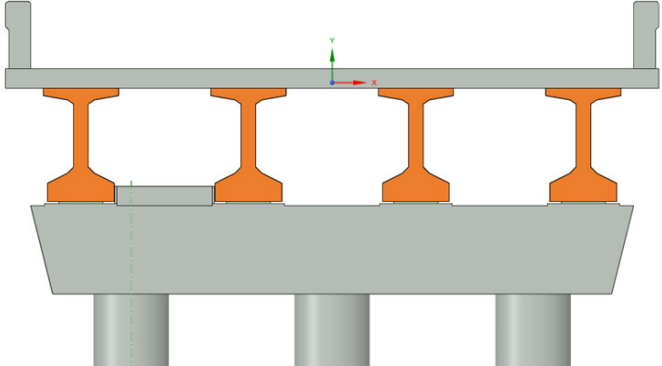


Figure 6.27 24-ft roadway TX54 I-girder bridge

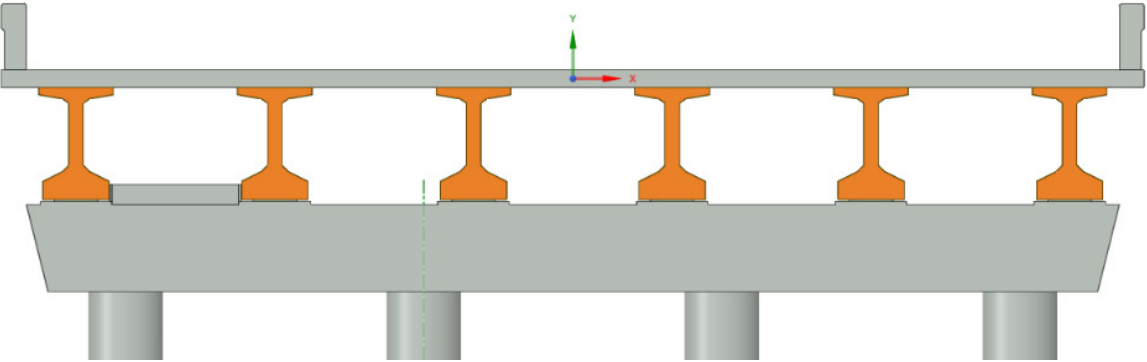


Figure 6.28 44-ft roadway TX54 I-girder bridge

Table 6.5 Summary of full-scale bridge model results for TX54 I-girder bridge and capacity comparison

Bridge type	Froude No. 0.34	Froude No. 0.5	Froude No. 0.9	Shear key resistance (kips)	Remarks	Check
	Drag force on shear key (kips)	Drag force on shear key (kips)	Drag force on shear key (kips)			
TX54 girders, 24' Roadway, 50' span (Figure 6.27)	173	357	1,190	716	Capacity < Force	Shear key should be redesigned
TX54 girders, 44' Roadway, 50' span (Figure 6.28)	197	374	1,236	952	Capacity < Force	Shear key should be redesigned
TX54 girders, 24' Roadway, 125' span (Figure 6.27)	450	913	2,474	716	Capacity < Force	Shear key should be redesigned
TX54 girders, 44' roadway, 125' span (Figure 6.28)	484	937	2,892	952	Capacity < Force	Shear key should be redesigned

6.9.3 Summary of the Full-scale Bridge Model Results for TX54 I-girder Bridge with Debris and 10-ft Wave

TX54 I-girder bridge with a span length of 50-ft and 125-ft and two different roadway widths of 24-ft and 44-ft were used. Center-to-center spacing of girders for the 24-ft roadway bridge is 6.667-ft and center-to-center spacing for the 44-ft roadway bridge is 8-ft. The capacity of each shear key has been calculated in Section 6.7 and the force on each shear key is obtained from CFD analysis. Table 6.6 compares the capacity and the drag force on the shear key. Drag forces for two different debris conditions; that is, flat plate debris and wedge-shaped debris are computed for the 44-ft roadway TX54 I-girder bridges (see Section 5.3.2). Figures 6.29 and 6.30 show the flat plate debris model and Figures 6.31 and 6.32 show the wedge-shaped debris model. Also, the drag force for 24-ft roadway TX54 I-girders bridge with a 10-ft wave modeling is also computed. Drag forces for three different Froude numbers of 0.34, 0.5, and 0.9 have been calculated but the comparison has been made only with the largest force given by Froude number of 0.9.

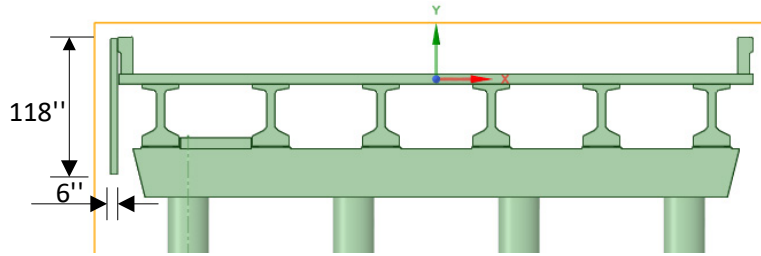


Figure 6.29 I-girder bridge with flat plate debris (section)

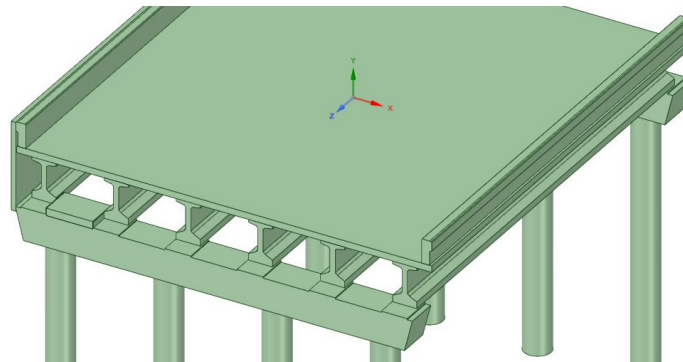


Figure 6.30 I-girder bridge with flat plate debris (elevation)

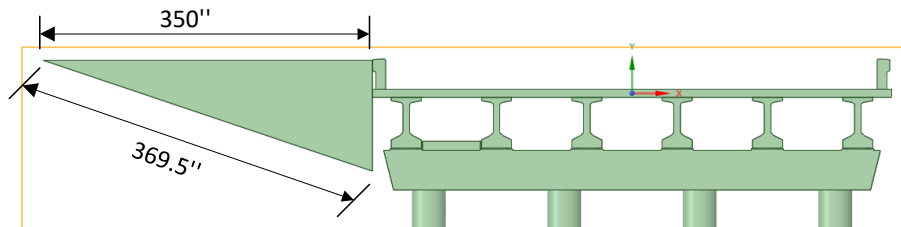


Figure 6.31 I-girder bridge with wedge shape debris (section)

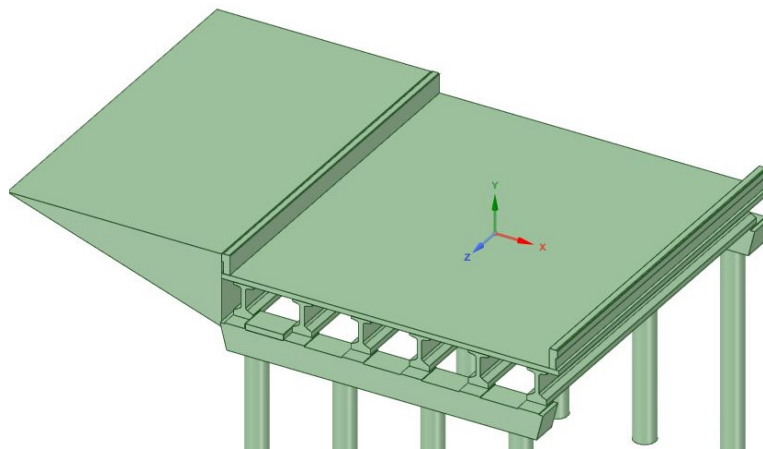


Figure 6.32 I-girder bridge with wedge shape debris (elevation)

Table 6.6 Summary of the full-scale bridge model results for TX54 I-girder bridge with debris and wave

Bridge type	Froude No. 0.34	Froude No. 0.5	Froude No. 0.9	Shear key resistance (kips)	Remarks	Check
	Drag force on shear key (kips)	Drag force on shear key (kips)	Drag force on shear key (kips)			
TX54 girders, 44' Roadway, 50' span (Flat plate debris) (Figures 6.29 and 6.30)	301	700	1,659	952	Capacity < Force	Shear key should be redesigned
TX54 girders, 44' Roadway, 50' span (Wedge debris) (Figures 6.31 and 6.32)	163	347	1,083	952	Capacity < Force	Shear key should be redesigned
TX54 girders, 44' Roadway, 125' span (Flat plate debris) (Figures 6.29 and 6.30)	526	1,244	3,385	952	Capacity < Force	Shear key should be redesigned
TX54 girders, 44' Roadway, 125' span (Wedge debris) (Figures 6.31 and 6.32)	358	743	2,306	952	Capacity < Force	Shear key should be redesigned
TX54 girders, 24' Roadway, 50' span (10-ft wave)*	87	188	780	716	Capacity < Force	Shear key should be redesigned

*See Section 5.4.4

6.9.4 Summary of Full-scale Bridge Model Results for Box Beam Bridge

Figure 6.33 shows the analyzed TxDOT box beam bridge with a span length of 50-ft and roadway width of 24-ft.

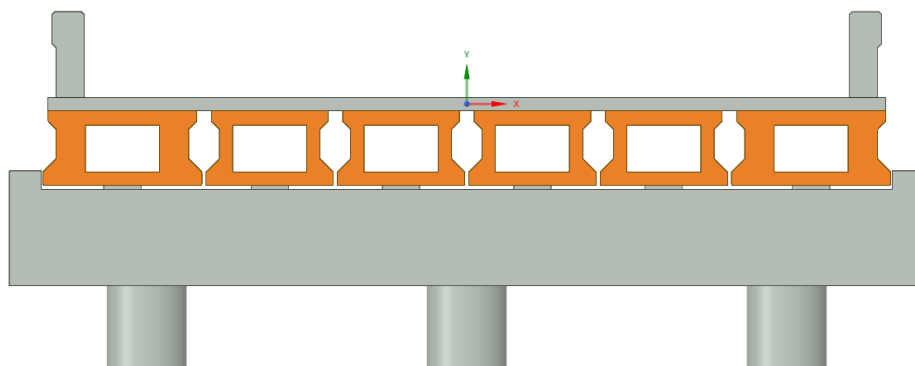


Figure 6.33 TxDOT 24-ft roadway box beam bridge

Two 5BB28 box beams as exterior beams on two sides and four 4BB28 beams as interior beams were placed side-by-side with a minimum spacing of 3.5 in. The capacity of each earwall has been calculated in Section 6.7 and the force on each earwall is obtained from CFD analysis. Table 6.7 compares the interface shear strength of the earwall and the drag force on the earwall. Drag forces for three different Froude numbers of 0.34, 0.5, and 0.9 are calculated but the comparison is made only with the largest force given by Froude number of 0.9.

Table 6.7 Summary of the full-scale bridge model results for box beam bridge

Bridge type	Froude No. 0.34	Froude No. 0.5	Froude No. 0.9	Earwall resistance (kips)	Remarks	Check
	Drag force on earwall (kips)	Drag force on earwall (kips)	Drag force on earwall (kips)			
Box beams B28, 24' Eoadway, 50' span (Figure 6.33)	119	243	705	267	Capacity < Force	Earwall should be redesigned

6.9.5 Summary of Full-scale Bridge Model Results for Slab Beam Bridge

Figure 6.34 shows the analyzed TxDOT slab beam bridge with a span length of 50-ft and roadway width of 24-ft. Five SB15 slab beams with a center-to-center distance of 5.255-ft (side-by-side spacing of 3.3 in.) were used. The capacity of each earwall has been calculated in Section 6.7 and the drag force on each earwall is obtained from the CFD analysis. Table 6.8 compares the capacity and drag force on the earwall. Drag forces for three different Froude numbers of 0.34, 0.5, and 0.9 are computed but the comparison has been made only with the largest force given by Froude number of 0.9.

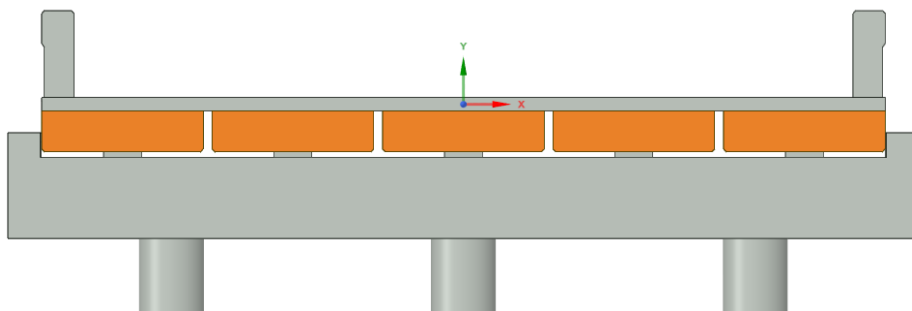


Figure 6.34 TxDOT 24-ft roadway slab beam bridge

Table 6.8 Summary of the full-scale bridge model results for slab beam bridge

Bridge type	Froude No. 0.34	Froude No. 0.5	Froude No. 0.9	Earwall resistance (kips)	Remarks	Check
	Drag force on earwall (kips)	Drag force on earwall (kips)	Drag force on earwall (kips)			
Slab beams 5SB15, 24' Roadway, 50' span (Figure 6.34)	85	165	517	242	Capacity < Force	Earwall should be redesigned

6.10 Recommended Modifications of Shear Key/Earwall

Drag force obtained from the CFD analysis and interface shear strength of the shear key or earwall are summarized and compared in Section 6.9. If the interface shear strength is not sufficient, several approaches can be used to increase the capacity: (1) increase the size and/or quantity of the interface shear reinforcement, (2) increase the quantity of the shear key, and (3) increase the length of the bent cap hence the length of the earwall.

6.10.1 Examples of Recommended Modifications to Shear Key on Bent Cap for TX28 I-girder Bridges

From the summary in Table 6.4, the interface shear strength of the shear key for the TX28 I-girder bridges with 24-ft roadway is not sufficient to resist the drag force for Froude number of 0.9. The interface shear strength is 716 kips whereas the drag force is 799 kips. Two approaches are recommended: (1) increase the interface shear reinforcement, or (2) increase the number of shear keys.

a. Increase the number of shear keys to two with same existing reinforcement details

As shown in Figure 6.35, the shear key is in-between two beams, hence the length of the shear key cannot be increased. On the other hand, increasing the width of the shear key needs to increase the width of the bent cap, which may not be economical. Therefore, it is recommended to increase the number of shear keys to two from one with the current TxDOT reinforcement detailing:

- Capacity of single shear key (716 kips) < Maximum drag force (799 kips)
- Capacity of two shear key (1,432 kips) > Maximum drag force (799 kips)

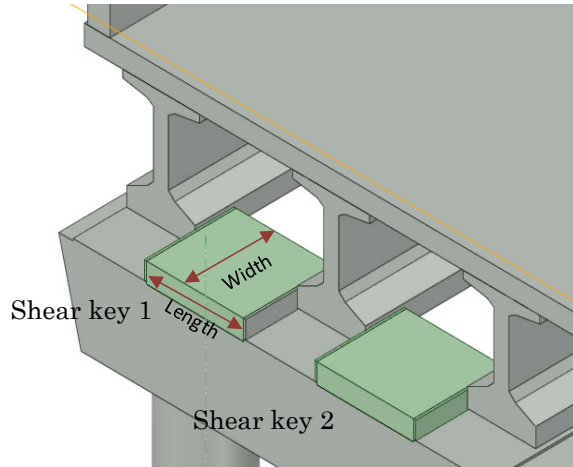


Figure 6.35 Two shear keys in bent cap

b. Increase the reinforcement to from 2-legs per line to 4-legs per line

Current TxDOT practice uses No. 5 bars with 2-legs of dowel bars at a maximum spacing of 8 in., as shown in Figures 6.36 and 6.37. If 4-legs of dowel bars as shown in Figures 6.38 and 6.39 with the same spacing of 8 in. are used, the interface reinforcement area is doubled which increase the interface shear capacity. Since the size of the bent cap is 42 in., it can easily accommodate 4-legs of dowel bars:

- Capacity of shear key with 2-legs per line of dowel bars (716 kips) < Maximum drag force (799 kips)
- Capacity of shear key with 4-legs per line of dowel bars (900 kips) (24-ft roadway bridge) > Maximum drag force (799 kips)

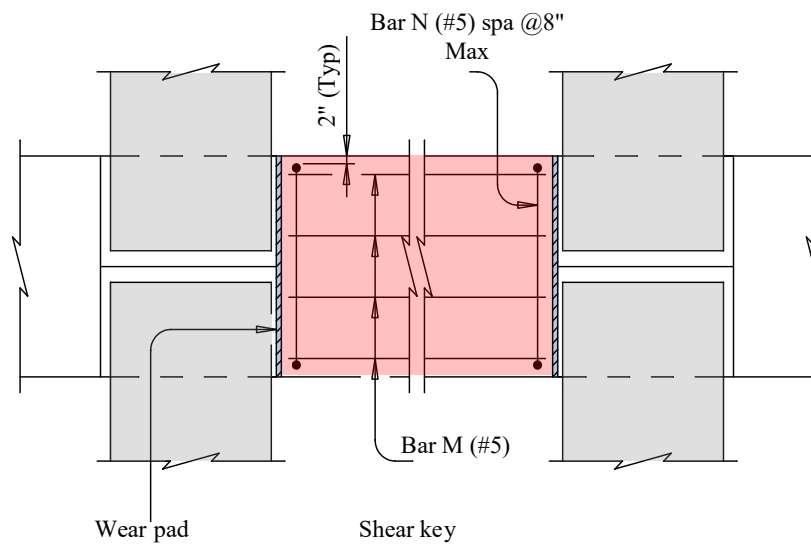


Figure 6.36 Existing shear key details (plan)

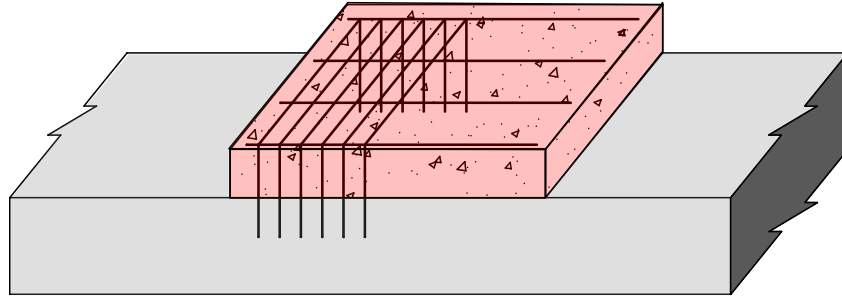


Figure 6.37 Existing shear key details (3D view)

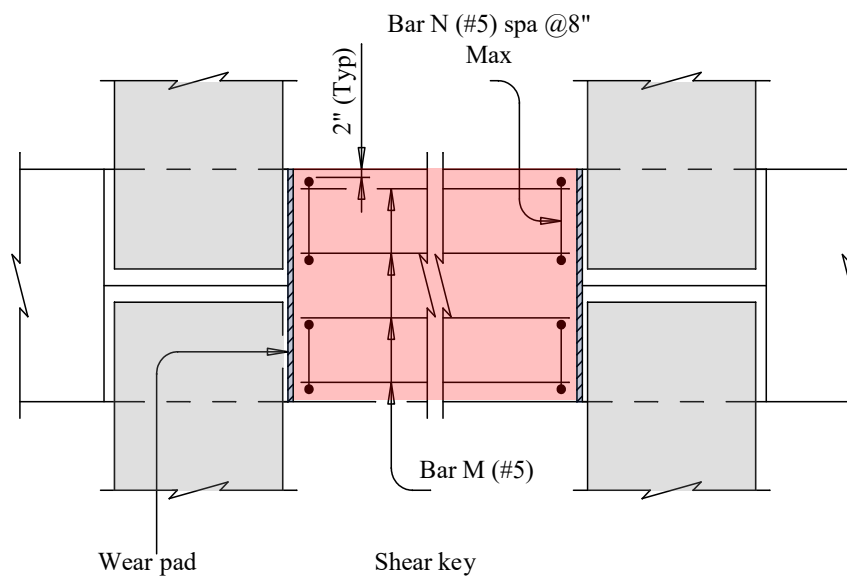


Figure 6.38 Modified shear key details (plan)

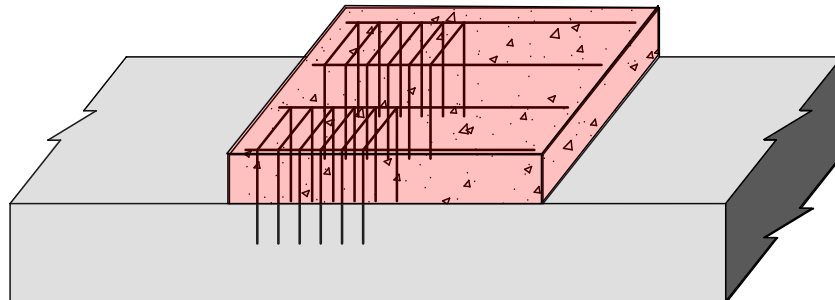


Figure 6.39 Modified shear key details (3D view)

6.10.2 Examples of Recommended Modifications to Shear Key on Bent Cap for TX54 I-girder Bridges

From the summary in Tables 6.5 and 6.6, the interface shear strength of shear keys for the TX54 I-girder bridges is not sufficient to resist the drag force for either the 24-ft roadway or the 44-ft roadway bridge for Froude number of 0.9. The interface shear strength of the shear key is 716 kips for the 24-ft roadway bridge and 952 kips for the 44-ft roadway bridge. However, the maximum drag force developed is more than 4 times for the 44-ft roadway bridge with 125-ft span having flat plate debris accumulated on the upstream side of the bridge. Two remedial approaches are recommended: (1) increase the interface shear reinforcement, or (2) increase the number of shear keys.

a. Increase the number of shear keys to four with the same reinforcement detailing

As shown in Figure 6.40, because the shear key is in-between two beams, the length of the shear key cannot be increased. On the other hand, increasing the width of the shear key needs to increase the width of the bent cap, which is not economical. So, increasing the number of shear keys to four from one with the current TxDOT reinforcement detailing is recommended:

- Capacity of single shear key (952 kips) < Maximum drag force (3,385 kips)
- Capacity of four shear keys (3,808 kips) > Maximum drag force (3,385 kips)

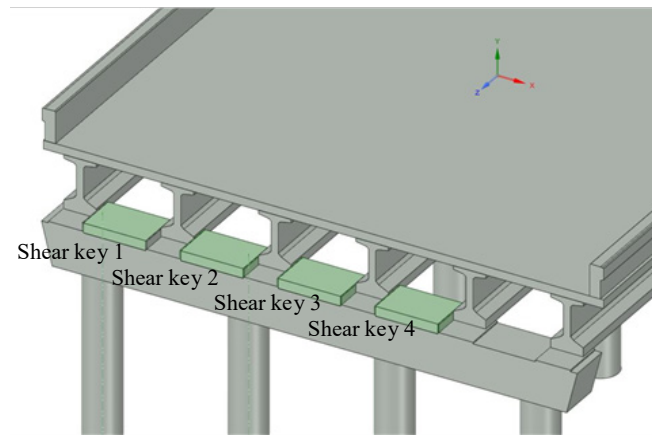


Figure 6.40 Bridge having 4 shear keys

b. Increase the reinforcement to from 2-legs per line to 4-legs per line and increase the shear keys to three 3

Current TxDOT practice uses No. 5 bars with 2-legs of dowel bars at maximum spacing of 8 in., as shown in Figures 6.36 and 6.37. If 4-legs of dowel bars as shown in Figures 6.38 and 6.39 with the same spacing of 8 in. are used, the interface reinforcement area is doubled which increases the interface shear capacity. Since the size of the bent cap is 42 in. which can easily accommodate 4-

legs of dowel bars. If a shear key with 4-legs of dowel bars per line is used, three shear keys as shown in Figure 6.41 are sufficient to resist the maximum drag force developed.

- Capacity of shear key with 4-legs per line of dowel bars (1,254 kips) (44-ft roadway bridge)
- Capacity of three shear key with double reinforcement: 3,761 kips > Maximum drag force (3,385 kips)

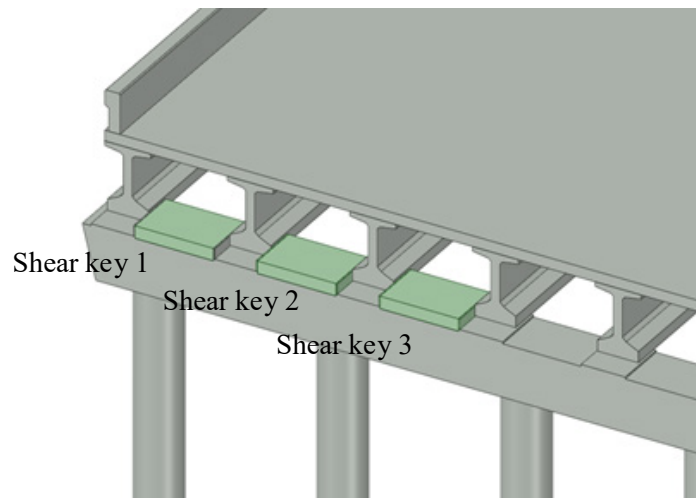


Figure 6.41 Bridge having 3 shear keys

6.10.3 Examples of Recommended Modifications to Earwall on Bent Cap for Box Beam Bridges

From the summary in Table 6.7 the interface shear strength of the earwall is not sufficient to resist the developed drag force for the 24-ft roadway TxDOT box beam bridge subjected to Froude number of 0.9. The interface shear strength of the earwall is 267 kips while the maximum drag force developed is more than 2.5 times. Current TxDOT reinforcement detailing uses five (5) No. 5 bars with 2-legs per line as shown in Figure 6.42. Since developed drag force is much higher compared to the interface shear capacity of the earwall, it is recommended to increase in earwall length by 18 in. and use seven (7) No. 5 bars with 4-legs per line interface shear reinforcement to provide sufficient capacity. The recommended modifications are illustrated in Figures 6.43 and 6.44.

- Existing earwall capacity (267 kips) < Maximum drag fore (705 kips)
- Modified earwall capacity (718 kips) > Maximum drag fore (705 kips)

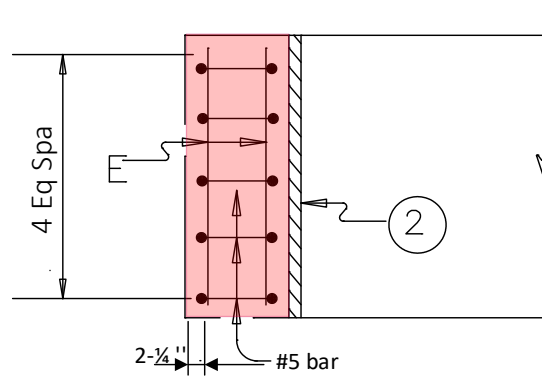


Figure 6.42 Existing earwall for box beam bridge

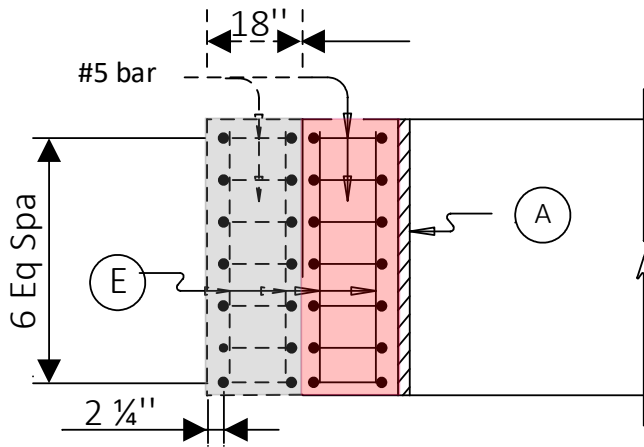


Figure 6.43 Proposed earwall for box beam bridge (plan)

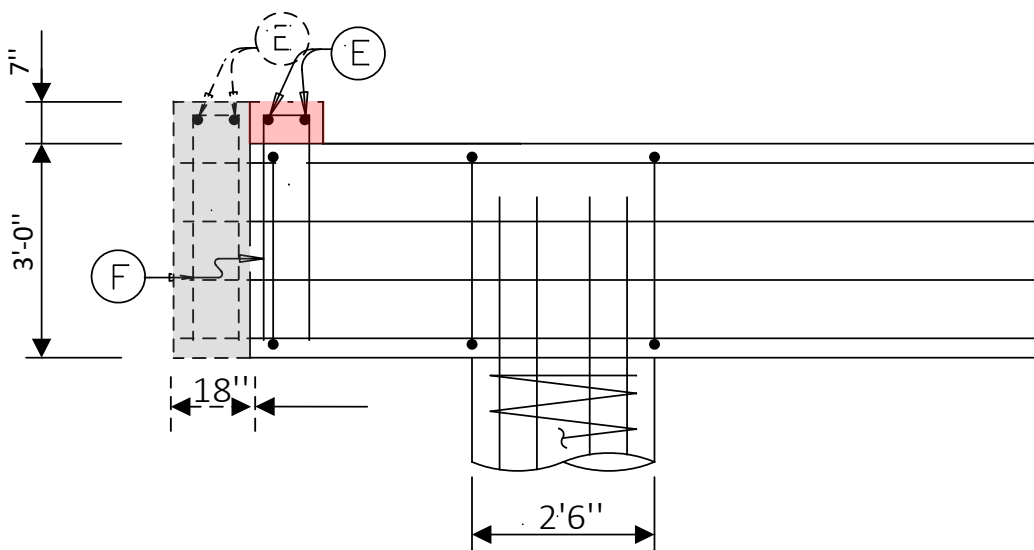


Figure 6.44 Proposed earwall for box beam bridge (elevation)

6.10.4 Examples of Recommended Modifications to Earwall on Bent Cap for Slab Beam Bridges

From the summary in Table 6.8 the interface shear strength of earwall is not sufficient to resist the developed drag force for the 24-ft roadway TxDOT slab beam bridge subjected to Froude number of 0.9. The interface shear strength of the earwall is 242 kips while the maximum drag force developed is more than two times. Current TxDOT reinforcement detailing uses seven (7) No. 4 bars with 2-legs per line as shown in Figure 6.45. Two modifications are recommended: (1) increase the interface shear area with increased bar size, or (2) increase the interface shear reinforcement.

a. Option I: This option has same reinforcement detailing as current TxDOT practice but using No. 5 bars instead of No. 4 and extending the cap and earwall for 24 in

Current TxDOT practice uses seven (7) No. 4 dowel bars. The existing interface shear capacity with No. 4 bars is 242 kips while the interface shear capacity increases to 325 kips if No. 5 bars are used instead of No. 4 bars. Still, the capacity is not sufficient to resist the maximum drag force (517 kips) so an additional increase of 24 in. in the length of the earwall is also recommended. Figures 6.46 and 6.47 illustrate the recommendation. This modification increases the interface shear capacity to 507 kips which is nearly equal to the maximum drag force.

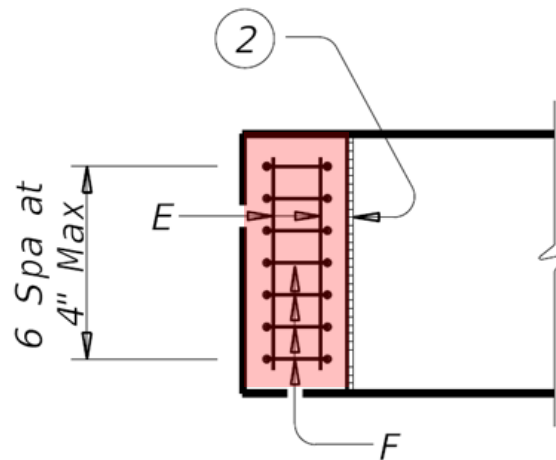


Figure 6.45 Existing earwall for slab beam bridge

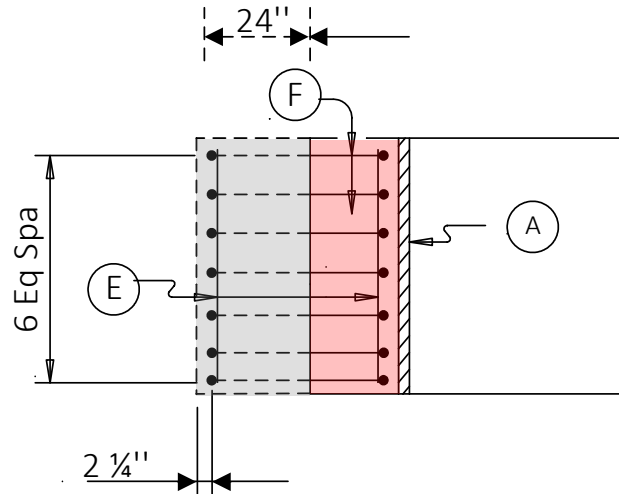


Figure 6.46 Modified earwall for slab beam bridge (plan)

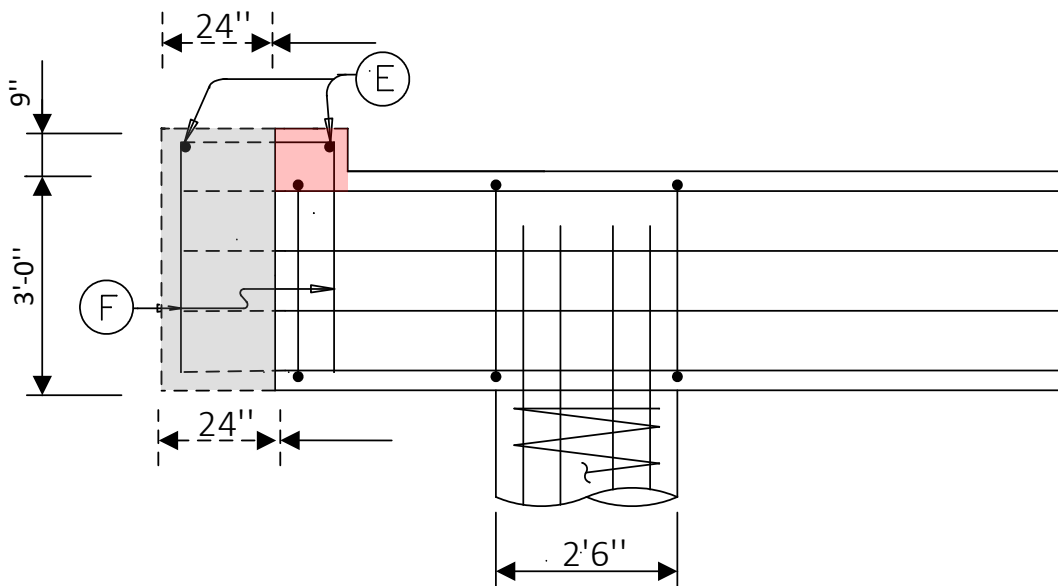


Figure 6.47 Modified earwall for slab beam bridge (elevation)

b. Option II: Extending the cap and earwall for 18 in. No. 5 bars, and double the amount of interface shear reinforcement

Current TxDOT practice uses seven (7) No. 4 dowel bars with 2-legs per line as shown in Figure 6.45. If 4-legs per line of No. 5 dowel bars with increased earwall length of 10 in. is used, the capacity increases to 635 kips which is sufficient to resist the maximum drag force (517 kips) developed. Figures 6.48 and 6.49 illustrate the recommendation.

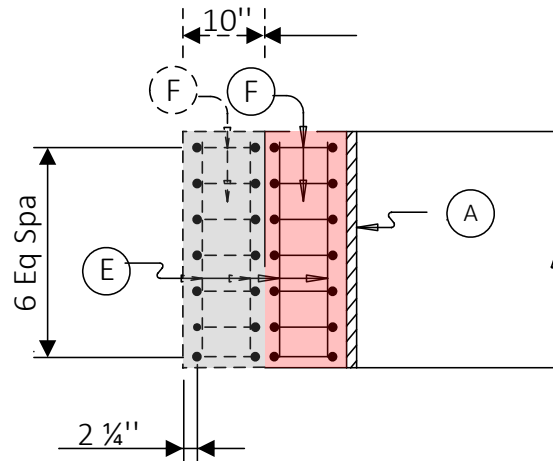


Figure 6.48 Modified earwall for slab beam bridge (plan)

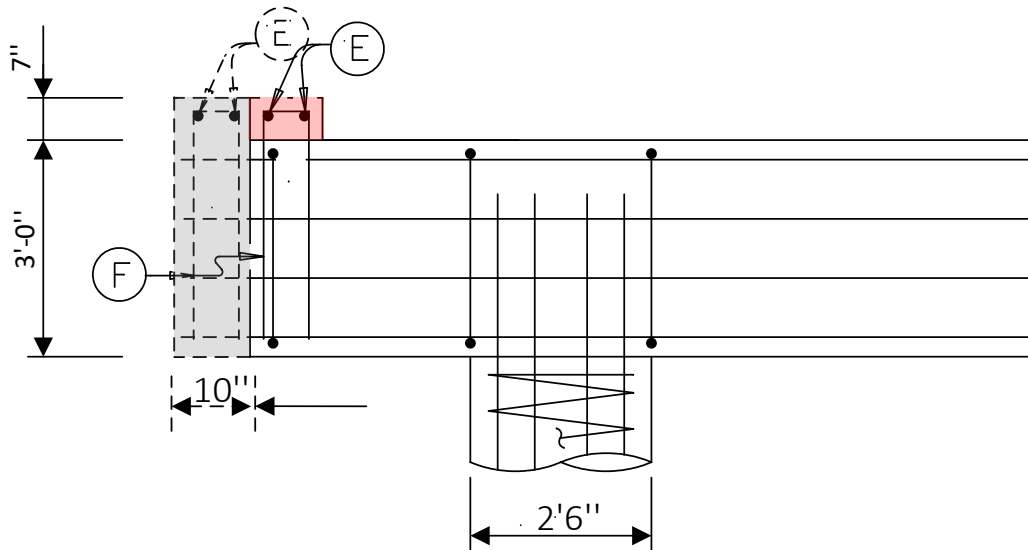


Figure 6.49 Modified earwall for slab beam bridge (elevation)

6.11 Limitations of the Study

- This study assumes the height of the shear key and earwall is sufficient, so the girder/beam always engages with the shear key/earwall during a flood. (note: height of shear key: 8.25 in.; height of earwall: 7 in. for box beam bridge; height of slab beams: 9 in. for slab beam bridge). Should the uplift force be too high and lead to disengagement of the girder and the shear key/earwall, the bridge can be damaged even with the increased the strength of shear key/earwall.
- CFD analysis is based on a single-span bridge. Thus, all the drag force computations are based on a single-span bridge.

7 CONCLUSIONS AND RECOMMENDATIONS

The current guidelines and standards for calculating hydrodynamic forces are applicable only to bridge piers. During high flow events, the bridge deck may become fully or partially submerged, and the flood exerts significant hydrodynamic forces on the bridge superstructure, resulting in shearing and overturning the bridge deck, which may cause bridge failure. No specific design guideline is available in the U.S. to calculate hydrodynamic forces on the bridge superstructure. Additionally, the effectiveness of structural countermeasures, such as shear keys, to hydraulic failure of bridges is unknown. The objectives of this study were to identify bridges that have the potential to become inundated during high-velocity flow events, estimate flood force effects on superstructures and substructures, using typical TxDOT bridge details, and determine if shear key details are adequate or whether additional countermeasures are warranted.

The approach in this study included experimental and numerical modeling of hydrodynamic forces on bridges under flood and wave loading, and structural modeling and analysis of current TxDOT countermeasure, including shear keys and earwalls. The dependency of drag, lift, and moment coefficients to inundation ratio, Froude number, deck width, types of beam/girders, and bridge skew angle was assessed. The hydrodynamic forces that were considered included flood, surge, and debris loading. Structural modeling and analysis of the current TxDOT countermeasure were conducted to assess the efficacy of these measures during high flood events. If the capacity of these measures was not sufficient, several approaches have been recommended to increase the capacity.

A series of experimental laboratory tests were conducted to measure hydrodynamic forces on bridges under flood and wave loading. The 1:50 scale models of the TxDOT's typical reinforced concrete bridge superstructures were tested in these experiments. The drag, lift, and moment design charts and equations were developed for TX28 and TX54 I-Girders, Box Beam BB28, and Slab Beam SB15 superstructures. The effects of deck skewness, debris, and substructure on these coefficients were evaluated and quantified.

The numerical modeling of hydrodynamic forces on bridge decks using ANSYS Fluent displayed a reasonable potential for assessing the performance of submerged bridge decks. Although the numerical models did not catch the full range of behavior shown in the physical modeling results (i.e., the values of drag coefficients for higher inundation ratios), the estimation of hydrodynamic forces exhibited sufficient similarity to draw conclusions about the impacts of flood forces on bridge structures. Furthermore, the CFD modeling approach allows for flexibility in simulating a variety of flow and inundation scenarios, thus providing an important complement to physical modeling. Further sensitivity analysis (e.g., by changing under-relaxation parameters and convergence criteria) or comparisons with particle image velocimetry data collected in the lab could provide additional enhancements to the modeling presented here.

Finite element (FE) models for single span TxDOT bridges with typical I-girders, box beams, and slab beams were developed using ANSYS version 2019 R3. The developed models were then used for CFD analysis to find the drag force on shear key/earwall for different flow conditions. The computed force from CFD analysis was then compared with the factored interface shear resistance of shear key/earwall calculated based on Equation 5.7.4.3-1 of 2020 AASTHO LRFD Specifications. Following are the conclusions and recommendations based on the full-scale FE analyses and calculated interface resistance.

- All the bridge models were analyzed for three different Froude numbers of 0.34, 0.5, and 0.9. Drag force for bridge models analyzed with Froude numbers of 0.34 and 0.5 is less than the interface shear strengths of respective shear keys/earwalls.
- Full-scale TX28 I-girder bridges with 24-ft roadway and 44-ft roadway for span length of 50-ft were analyzed by CFD for three different Froude numbers of 0.34, 0.5, and 0.9. Based on the FEA, the drag force on the 44-ft roadway is 2%-12% higher compared to the drag force on the 24-ft roadway.
- Interface shear resistance of shear key for TX28 I-girder bridges with 24-ft roadway is not sufficient to resist the drag force for Froude number of 0.9. To provide a solution, two different modifications are recommended: (1) increase the number of shear keys to two, or (2) increase the No. 5 interface shear reinforcement to 4-legs per line from 2-legs per line.
- Full-scale TX28 I-girder bridges with 44-ft roadway with 15°, 30°, and 45° skew angles were analyzed by CFD for three different Froude numbers of 0.34, 0.5, and 0.9. Drag force increases from skew angle 15° to 30° but drag force decreases from 30° to 45°. An increase in skewness increases the shear key length which allows more space to place the interface shear reinforcement area. Both factors result in higher interface shear strength. Full-scale TX28 I-girder bridges with 44-ft roadway with 15°, 30°, and 45° skew angles are sufficient to resist the computed drag force for every Froude number analyzed.
- Full-scale TX54 I-girder bridges with 24-ft roadway and 44-ft roadway for span length of 125-ft were analyzed by CFD for three different Froude numbers of 0.34, 0.5, and 0.9. Based on the FEA, the drag force on a 44-ft roadway bridge is 2%-16% higher compared to the drag force on a 24-ft roadway bridge. The same bridge models were analyzed for flat plate debris, wedge shaped debris, or a 10-ft wave modeling. The maximum drag force obtained was for full-scale TX54 I-girder bridges with 44-ft roadway and Froude number of 0.9. The computed drag force is more than four times the existing capacity of the shear key. Two modifications are proposed: (1) provide at least four shear keys with current TxDOT reinforcement detailing, or (2) increase the No. 5 interface shear reinforcement to 4-legs per line from 2-legs per line and increase the shear key's quantity to three.
- Full-scale box beam (BB28) bridge with 24-ft roadway for a span length of 50-ft was analyzed by CFD for three different Froude numbers of 0.34, 0.5, and 0.9. Drag force for Froude number of 0.9 is nearly 200% greater than the interface shear strength of the

earwall. The recommendation is to increase the length of earwall at least 15 in and increase the No. 5 interface shear reinforcement to 4-legs per line from 2-legs per line, and decrease the spacing of the bar to allow at least 7 lines of rebar across the bent cap.

- Full-scale slab beam (SB15) bridge with 24-ft roadway for a span length of 50-ft was analyzed by CFD for three different Froude numbers of 0.34, 0.5, and 0.9. Drag force for Froude number of 0.9 is nearly 160% greater than the interface shear strength of the earwall. Two modifications are recommended: (1) increase the length of earwall by 24 in. with the current TxDOT reinforcement detailing but using No. 5 bars instead of current practice No. 4 bars, or (2) increase the reinforcement to 4-legs per line from 2-legs per line with No. 5 bars and increase the length of the earwall by 10 in.

REFERENCES

- AASHTO, 2017, “*AASHTO LRFD Bridge Design Specifications*,” Eight edition. American Association of State Highway and Transportation Officials, Washington, D.C.
- AASHTO, 2020, “*LRFD Bridge Design Specifications*,” Ninth edition, American Association of State Highway and Transportation Officials (AASHTO), Washington, DC.
- Ali, M. A., and White, R. N., 1999, “Enhanced Contact Model for Shear Friction of Normal and High-Strength Concrete,” *ACI Structural Journal*, V. 96, No. 3, May-June, pp. 348-360.
- Almodovar-Rosario, N., Dorney, C., Flood, M., Lennon, J., and Lockman, J.T., 2014. MnDOT Flash Flood Vulnerability and Adaptation Assessment Pilot Project.
- Akhtar, A.A., Esquivel, A., Sharma, M., and Tandon, V., 2018. Understanding climate change impact on highway hydraulic design procedures (No. SPTC14. 1-97-F).
- Ansys, I., 2017. Ansys Fluent Theory Guide. Release 18.2.
- ARTBA, 2020. *Bridge Report*, s.l.: American Road & Transportation Builders Association.
- Bass, R. A.; Carrasquillo, R. L.; and Jirsa, J. O., 1989, “Shear Transfer across New and Existing Concrete Interfaces,” *ACI Structural Journal*, V. 86, No. 4, July-Aug., pp. 383-393.
- Bozorgnia, M., 2012. Computational fluid dynamic analysis of highway bridge superstructures exposed to hurricane waves. (Doctoral dissertation, University of Southern California).
- Bundy, F., 2021. *How Much Does it Cost to Build a Bridge? [2021 Updated]*. [Online] Available at: <https://howmuchly.com/cost-to-build-a-bridge> [Accessed 26 August 2021].
- Briaud, J.L. and Chedid, M., 2019. *Allowable Limit Contraction and Abutment Scour at Bridges: Technical Report* (No. FHWA/TX-18/0-6935-R1). Texas A&M Transportation Institute.
- Byrne, K. Major flooding on Llano River triggers bridge collapse near Kingsland, Texas [Online] Available at: <https://www.accuweather.com/en/weather-news/major-flooding-on-llano-river-triggers-bridge-collapse-near-kingsland-texas/342859> [Accessed: 2 February 2020].
- Chen, G., Witt III, E.C., Hoffman, D., Luna, R. and Sevi, A., 2005. Analysis of the Interstate 10 twin bridge’s collapse during Hurricane Katrina. *Science and the Storms: The USGS Response to the Hurricanes of*, pp.35-42.
- Chen, Q., Wang, L. and Zhao, H., 2009. Hydrodynamic investigation of coastal bridge collapse during Hurricane Katrina. *Journal of Hydraulic Engineering*, 135(3), pp.175-186.
- Chu, C.R., Huang, C.J., Wu, T.R. and Wang, C.Y., 2012. Numerical simulation of hydrodynamic loading on submerged rectangular bridge decks. *The 7th International Colloquium on Bluff Body Aerodynamics and Applications (BBAA7) Shanghai, China*; September 2-6, 2012.
- Chu, C.R., Chung, C.H., Wu, T.R. and Wang, C.Y., 2016. Numerical analysis of free surface flow over a submerged rectangular bridge deck. *Journal of Hydraulic Engineering*, 142(12), p.04016060.
- Church, J.A., Clark, P.U., Cazenave, A., Gregory, J.M., Jevrejeva, S., Levermann, A., Merrifield, M.A., Milne, G.A., Nerem, R.S., Nunn, P.D. and Payne, A.J., 2013. *Sea level change*. PM Cambridge University Press.
- Cook, W., Barr, P.J. and Halling, M.W., 2015. Bridge failure rate. *Journal of Performance of Constructed Facilities*, 29(3), p.04014080.
- Cook, W., 2014. *Bridge Failure Rates, Consequences, and Predictive Trends.*, Ph.D. Thesis.
- Deng, L., Wang, W. and Yu, Y., 2016. State-of-the-art review on the causes and mechanisms of bridge collapse. *Journal of Performance of Constructed Facilities*, 30(2), p.04015005.

- Diehl, T.H., 1997. *Potential drift accumulation at bridges*. US Department of Transportation, Federal Highway Administration, Research and Development, Turner-Fairbank Highway Research Center.
- Deuffhard, P., 1974. A modified Newton method for the solution of ill-conditioned systems of nonlinear equations with application to multiple shooting. *Numerische Mathematik*, 22(4), pp.289-315.
- Doney, S.C., Ruckelshaus, M., Duffy, J.E., Barry, J.P., Chan, F., English, C.A., Galindo, H.M., Grebmeier, J.M., Hollowed, A.B., Knowlton, N. and Polovina, J., 2011. Climate change impacts on marine ecosystems.
- Dráb, A., Duchan, D., Špano, M., Pavlíček, M., Zubík, P. and Štěpánková, P., 2019. Determination of the hydrodynamic load on an inundated bridge deck by measurements performed on a physical model. *International Journal of Civil Engineering*, 17(10), pp.1491-1502.
- EN, B.S., 1991. 1-6: 2005 Eurocode 1: Actions on Structures—Part 1-6: General Actions—Actions on Structures Exposed to Fire. *British Standards*.
- Fang, Q., Hong, R., Guo, A., Stansby, P.K. and Li, H., 2018. Analysis of hydrodynamic forces acting on submerged decks of coastal bridges under oblique wave action based on potential flow theory. *Ocean Engineering*, 169, pp.242-252.
- Fechter, J. 2015. TXDoT: Two bridges completely wrecked in Central Texas floods, others damaged [Online] Available at: <https://www.mysanantonio.com/news/local/article/TXDoT-Two-bridges-wrecked-in-the-Central-Texas-6294892.php> [Accessed: 2 March 2020].
- Fenton, J., 1972. A ninth-order solution for the solitary wave. *Journal of fluid mechanics*, 53(2), pp.257-271.
- Fenton, J.D., 1985. A fifth-order Stokes theory for steady waves. *Journal of waterway, port, coastal, and ocean engineering*, 111(2), pp.216-234.
- FHWA (Federal Highway Administration), 2009. Bridges, Structures, and Hydraulics. *23 CFR 650, subpart C*.
- Flint, M.M., Fringer, O., Billington, S.L., Freyberg, D. and Diffenbaugh, N.S., 2017. Historical analysis of hydraulic bridge collapses in the continental United States. *Journal of infrastructure systems*, 23(3), p.04017005.
- Jeong, Y.J., Park, M.S., Kim, J. and Song, S.H., 2019. Wave Force Characteristics of Large-Sized Offshore Wind Support Structures to Sea Levels and Wave Conditions. *Applied Sciences*, 9(9), p.1855.
- Guo, J., Admiraal, D.M. and Zhang, T.C., 2010. Computational design tool for bridge hydrodynamic loading in inundated flows of Midwest rivers.
- IRC6:2016, *Standard Specifications and Code of Practice for Road Bridges Section: II Loads and Load Combinations (7th Revision)* (Indian Road Congress, New Delhi, 2016).
- Japan Road Association (JRA). 2002. Specifications for Highway Bridges Part I Common, pp. 52-57
- Jempson, M., 2000. Flood and debris loads on bridges. (Doctoral Dissertation). The University of Queensland, Australia.
- Kara, S., Stoesser, T., Sturm, T.W. and Mulahasan, S., 2015. Flow dynamics through a submerged bridge opening with overtopping. *Journal of Hydraulic Research*, 53(2), pp.186-195.
- Kerenyi, K., Sofu, T., Guo, J., 2009. Hydrodynamic forces on inundated bridge decks, Rep. No. FHWA-HRT-09-028. McLean, VA.

- Landsea, C., 2016. TCFAQ E TROPICAL CYCLONE RECORDS [Online] Available at: <https://www.aoml.noaa.gov/hrd/tcfaq/tcfaqE.html> [Accessed: 2 March 2020].
- Lin, C. and Kao, M.J., 2014. Flow types around and vortex structure beneath inundated bridge deck. *Journal of Engineering, National Chung Hsing University*, Vol. 25, No. 3, pp. 65-84.
- Lee, G.C. and Sternberg, E., 2008. A new system for preventing bridge collapses. *Issues in Science and Technology*, 24(3), p.31.
- Lee, G.C., Mohan, S., Huang, C. and Fard, B.N., 2013. A study of US bridge failures (1980-2012). MCEER.
- Malavasi, S. and Guadagnini, A., 2003. Hydrodynamic loading on river bridges. *Journal of Hydraulic Engineering*, 129(11), pp.854-861.
- Malavasi, S. and Trabucchi, N., 2008, July. Numerical investigation of the flow around a rectangular cylinder near a solid wall. In *BBAA VI International Colloquium on: Bluff*
- Mattock, A. H., and Hawkins, N. M., 1972, "Shear Transfer in Reinforced Concrete— Recent Research," *PCI Journal*, V. 17, No. 2, pp. 55-75. doi: 10.15554/pcij.03011972.55.75
- Meegoda, J.N., Juliano, T.M. and Tang, C., 2009. Culvert information management system. *Transportation Research Record*, 2108(1), pp.3-12.
- Naderi, N., 2018. Numerical simulation of hydrodynamic forces on bridge decks. MSc Thesis. *TU Delft, Nederland*.
- Nasim, M., Setunge, S., Zhou, S. and Mohseni, H., 2019. An investigation of water-flow pressure distribution on bridge piers under flood loading. *Structure and Infrastructure Engineering*, 15(2), pp.219-229.
- Naudascher, E. and Medlarz, H.J., 1983. Hydrodynamic loading and backwater effect of partially submerged bridges. *Journal of Hydraulic Research*, 21(3), pp.213-232.
- Oudenbroek, K., 2018. Experimental research on hydrodynamic failure of river bridges on spread footings. (Master Thesis, TU Delft).
- Oudenbroek, K., Naderi, N., Bricker, J.D., Yang, Y., Van der Veen, C., Uijtewaal, W., Moriguchi, S. and Jonkman, S.N., 2018. Hydrodynamic and debris-damming failure of bridge decks and piers in steady flow. *Geosciences*, 8(11), p.409.
- Parola, A.C., Apelt, C.J. and Jempson, M.A., 2000. Debris forces on highway bridges (No. 445). *Transportation Research Board*.
- Park, P., and Paulay, T., 1975, *Reinforced Concrete Structures*, John Wiley & Sons, Inc., New York, 769 pp.
- Patil, S., Kostic, M. and Majumdar, P., 2009. Computational fluid dynamics simulation of open-channel flows over bridge-decks under various flooding conditions. In *Proceedings of the 6th WSEAS International Conference on FLUID MECHANICS (FLUIDS'09), Ningbo, China January 10* (Vol. 12, No. 2009, pp. 114-120).
- Raja, R.S., 2012. Coupled fluid structure interaction analysis on a cylinder exposed to ocean wave loading.
- Roberts, J.D., Freer-Hewish, R.J. and Knight, D.W., 1983, August. Modelling of hydraulic drag forces on submersible bridge decks. In *Road Engineering Association of Asia and Australasia, Conference, 4th, 1983, Jakarta, Indonesia* (Vol. 2).
- Scholz, D. P., 2004, "Performance Criteria Recommendations for Mortars used in Full-Depth Precast Concrete Bridge Deck Panels Systems," master's thesis, Virginia Polytechnic Institute and State University, Blacksburg, VA

- Schrank, D., Albert, L., Eisele, B. & Lomax, T., 2021. *2021 URBAN MOBILITY REPORT*, s.l.: The Texas A&M Transportation Institute and INRIX.
- Schrank, D., Eisele, B., Lomax, T. & Bak, J., 2015. *2015 Urban Mobility Scorecard*, s.l.: Texas A&M Transportation Institute and INRIX.
- Smart, G.M., 1999. COEFFICIENT OF FRICTION FOR FLOW RESISTANCE IN ALLUVIAL CHANNELS. *Proceedings of the Institution of Civil Engineers-Water Maritime and Energy*, 136(4), pp.205-210.
- Standards Australia., 2004. AS 5100.1, Bridge Design - Scope and General. Sydney, Australia.
- Storey, C. and Delatte, N., 2003. Lessons from the collapse of the Schoharie Creek bridge. In *Forensic Engineering (2003)* (pp. 158-167).
- Sturm, T.W., 2001. *Open channel hydraulics* (Vol. 1, p. 1). New York: McGraw-Hill.
- Takle, G. and Anderson, C., 2015. *Iowa's bridge and highway climate change and extreme weather vulnerability assessment pilot: [tech transfer summary]* (No. HEPN-707). Iowa State University. Institute for Transportation.
- Taricska, M., 2014. *An analysis of recent bridge failures (2000-2012)*. Master Thesis, The Ohio State University.
- Thai, T.K.C., 2019. Numerical simulation of the turbulent flow over submerged bridge decks. *Magazine of Civil Engineering*, 85(1).
- Texas Department of Transportation (TxDOT), 2019, "Hydraulic Design Manual", September.
- Texas Department of Transportation (TxDOT), 2020, "Bridge Design Manual- LRFD", January.
- Texas Department of Transportation, 2020. *Report on Texas Bridges - Fiscal Year 2020*, TxDOT Bridge Division.
- Wardhana, K. and Hadipriono, F.C., 2003. Analysis of recent bridge failures in the United States. *Journal of performance of constructed facilities*, 17(3), pp.144-150.
- Wang, Y.H., Zou, Y.S., Xu, L.Q. and Luo, Z., 2015. Analysis of water flow pressure on bridge piers considering the impact effect. *Mathematical Problems in Engineering*, 2015.
- Waweru, R.N., Palacios, G. and Chao, S.H., 2018. Strength of interface shear reinforcement with limited development length. *ACI Structural Journal*, 115(4), pp.983-996.
- Wellwood, N. and Fenwick, J., 1990. A flood loading methodology for bridges. In *Australian Road Research Board (ARRB) Conference, 15th, 1990, Darwin, Northern Territory* (Vol. 15, No. 3).
- Wilcox, D.C., 2008. Formulation of the kw turbulence model revisited. *AIAA journal*, 46(11), pp.2823-2838.
- Wong, S. M., Onof, C. J. & Hobbs, R. E., 2005. Models for evaluating the costs of bridge failure. *Bridge Engineering*, September, 158(3), pp. 117-128.
- Zevenbergen, L.W., Arneson, L.A., Hunt, J.H. and Miller, A.C., 2012. Hydraulic design of safe bridges (No. FHWA-HIF-12-018). United States. Federal Highway Administration.
- Zhang, G., Hoshikuma, J.I. and Usui, T., 2012. An experimental study on countermeasure for mitigating tsunami effect on highway bridge. *15WCEE, LISBOA*.

APPENDIX A

Value of Research

The goals of the project were to 1) develop an improved prediction of magnitude of potential hydrodynamic forces on bridge superstructures, 2) determine the effectiveness of current TxDOT countermeasures, particularly shear keys, and 3) recommend additional measures to enhance stability and resistance of bridges during flood events. Several approaches are recommended as the outcome of this research that can be implemented to increase the interface shear capacity of shear key and earwalls of bridges and reduce the risk of failure. Table A.1 lists the research value and benefits areas selected by the Texas Department of Transportation (TxDOT). The benefit areas include both qualitative and economic (quantitative) benefits. In the absence of documented costs and benefits associated with each area, the average overall cost (direct and indirect) of failure of a bridge is considered to determine the value of research. The research value and benefits areas are presented in the following.

Table A. 1 The Project Value of Research (VoR)

Benefit Area	Qual	Eco	Both	TxDOT	State	Both
Level of knowledge	×			×		
System reliability		×		×		
Increased service life		×		×		
Traffic and congestion reduction		×			×	
Reduced construction, operation, and maintenance cost		×			×	
Infrastructure condition		×				×

Notes: Qual: Qualitative; Econ: Economic; TxDOT: Texas Department of Transportation; State: State of Texas

A.1 Economic Value

Stream-crossing bridges are crucial elements of road infrastructures that are vulnerable to flooding. Bridge superstructures may become fully or partially submerged during high flow events, and the hydrodynamic forces may result in shearing and overturning bridge elements. Bridge failures cause significant economic losses and delay the rescue and reconstruction of disaster-stricken areas (Fang et al., 2018). The implementation of recommended measures in this project for existing and future bridges in Texas would prevent such extreme losses and reduce structural damage during floods.

The economic value is calculated assuming that the recommended approaches will be incorporated in new bridges that will be constructed in the next 20 years as well as in existing bridges with the age of ≤ 20 years.

New Bridges

The net cash inflow from this project when implemented to new bridges is calculated based on the following information and assumptions.

- The average overall cost (direct and indirect) associated with the failure of a bridge is estimated to be around \$2,000,000 (Briaud and Chedid, 2019).
- 28.65% of bridge failures in the U.S. have been reported due to flooding and debris loading, which is about 8 bridges per year (Cook, 2014).
- Texas has 55,000 bridges (Report on Texas Bridges, Fiscal Year 2020), which is 8.9% of the U.S. bridges.
- 350 new bridges are added to Texas' inventory per year (Report on Texas Bridges, Fiscal Year 2020).
- The cost of implementing recommended measures in new bridges is insignificant comparing to the total cost of a bridge due to the simple design of these measures (Chapter 6).

The saving from avoiding failure of new bridges is calculated based on the above assumptions and information. Examples of these calculations for Year 1, Year 2, and Year 20 are presented herein.

$$\begin{aligned} \text{Saving in Year 1} &= \$2,000,000 \times (8)(0.089)(350/55000) = \$9061 \\ \text{Saving in Year 2} &= \$2,000,000 \times (8)(0.089)(2 \times 350/55000) = \$18,123 \\ \text{Saving in Year 20} &= \$2,000,000 \times (8)(0.089)(20 \times 350/55000) = \$181,236 \end{aligned}$$

Savings for Year 3 to Year 19 can be calculated similarly.

Existing Bridges with the Age of ≤ 20 Years

The net cash inflow from this project when implemented to the existing bridges with the age of ≤ 20 years is calculated based on the following information and assumptions.

- The average overall cost (direct and indirect) associated with the failure of a bridge is estimated to be around \$2,000,000 (Briaud and Chedid, 2019).
- 13,700 of the Texas bridges are younger than 20 years (Report on Texas Bridges, Fiscal Year 2020), that is 26.7% of total bridges.
- Hydraulic conditions at 908 bridges located in several Texas' counties are investigated (Chapter 3). 50 of these bridges (5.5%) would be at risk during floods with recurrence intervals of 100 years or smaller. These bridges would be inundated and experience high flow velocity and Froude number ($Fr > 0.5$). Some of these bridges may fail during such flood conditions and require additional measures against flood forces (Chapter 6).
- Assuming that 5.5% of the 13,700 bridges with the age of ≤ 20 years experience high inundation and Froude number, a total of 753 bridges might be at risk of failing. Assuming

only 1/3 of these bridges cannot resist flood forces, 251 bridges need to be retrofitted. This subset may include bridges with longer span and wider deck, and those under the combination of flood and debris loading (Chapter 6).

- Assuming 251 bridges will be retrofitted in 20 years, i.e., 12.5 bridges/year with the cost of \$20,000 per bridge.

The savings from avoiding failure of existing bridges is calculated based on the above assumptions and information as follows.

$$\begin{aligned} \text{The annual savings from avoiding bridge failure in Texas} &= \$2,000,000 \times (8)(0.089)(0.267) \\ &= \$380,208 \end{aligned}$$

$$\text{Total annual cost of bridge retrofitting} = 12.5 \times \$20,000 = \$250,000$$

The net cash inflow from this project when implemented to new bridges and existing bridges with the age of ≤ 20 years are calculated for Year 1, Year 2, and Year 20 are presented herein


$$\text{Annual cash inflow year 1} = \$9061 + \$380,208 - \$250,000 = \$139,269$$

$$\text{Annual cash inflow year 2} = \$18,123 + \$380,208 - \$250,000 = \$148,330$$

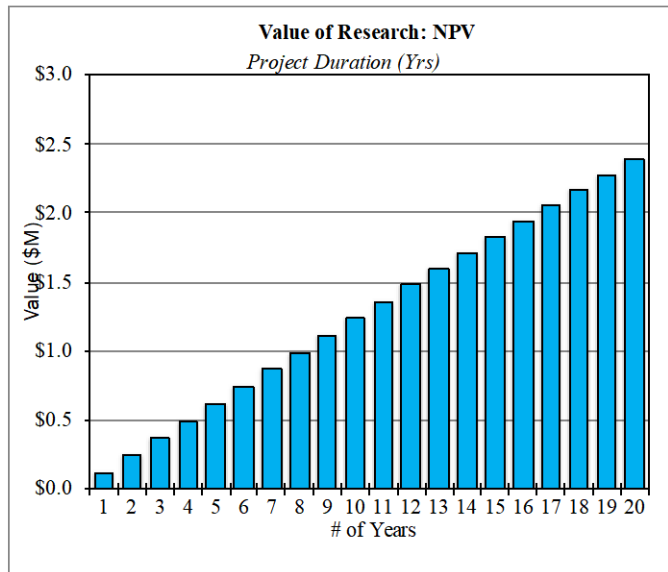
$$\text{Annual cash inflow year 20} = \$181,236 + \$380,208 - \$250,000 = \$311,444$$

Annual cash inflows for Year 3 to Year 19 are calculated and presented in Figure A.1.

The net present value for this research in a 20-year period and discount rate of 5% will be \$2,383,676. The cost of the project is \$223,743. Therefore, the cost-benefit ratio is 11 which shows the overall value of TxDOT investment on the project.

	Project #	0-7068		
	Project Name:	Identify and Analyze Inundated Bridge Superstructures in High Velocity Flood Events		
	Agency:	UTA	Project Budget	\$ 223,743
	Project Duration (Yrs)	2.0	Exp. Value (per Yr)	\$ 139,269
Expected Value Duration (Yrs)		20	Discount Rate	5%
Economic Value				
Total Savings:	\$ 1,355,875	Net Present Value (NPV):	\$ 2,383,676	
Payback Period (Yrs):	1.606549	Cost Benefit Ratio (CBR, \$1 : \$):	\$ 11	

Years	Expected Value
1	\$139,269
2	\$148,330
3	\$157,391
4	\$166,452
5	\$175,513
6	\$184,574
7	\$193,635
8	\$202,696
9	\$211,757
10	\$220,818
11	\$229,879
12	\$238,940
13	\$248,001
14	\$257,062
15	\$266,123
16	\$275,184
17	\$284,245
18	\$293,306
19	\$302,367
20	\$311,428



Years	Expected Value	Expected Value	Expected Value	NPV
1	\$139,269	\$139,269	\$0.14	\$0.12
2	\$148,330	\$287,599	\$0.29	\$0.24
3	\$157,391	\$444,990	\$0.44	\$0.37
4	\$166,452	\$611,442	\$0.61	\$0.49
5	\$175,513	\$786,955	\$0.79	\$0.61
6	\$184,574	\$971,529	\$0.97	\$0.74
7	\$193,635	\$1,165,164	\$1.17	\$0.86
8	\$202,696	\$1,367,860	\$1.37	\$0.99
9	\$211,757	\$1,579,617	\$1.58	\$1.11
10	\$220,818	\$1,800,435	\$1.80	\$1.24
11	\$229,879	\$2,030,314	\$2.03	\$1.36
12	\$238,940	\$2,269,254	\$2.27	\$1.48
13	\$248,001	\$2,517,255	\$2.52	\$1.60
14	\$257,062	\$2,774,317	\$2.77	\$1.72
15	\$266,123	\$3,040,440	\$3.04	\$1.83
16	\$275,184	\$3,315,624	\$3.32	\$1.95
17	\$284,245	\$3,599,869	\$3.60	\$2.06
18	\$293,306	\$3,893,175	\$3.89	\$2.17
19	\$302,367	\$4,195,542	\$4.20	\$2.28
20	\$311,428	\$4,506,970	\$4.51	\$2.38

Figure A.1 Value of Identify and Analyze Inundated Bridge Superstructures in High Velocity Flood Events

A.2 Level of Knowledge

In the U.S., all bridges and structures over waterways are designed in accordance with AASHTO-LRFD Bridge Design Specifications and DOT's bridge design guidelines and standards. Even though these guidelines and standards specify the use of the 100-year flood for analyzing the overtopping of modern interstate bridges receiving federal funding, many bridge failures in the U.S. occur during floods with return periods smaller than 100 years. AASHTO (2017) defines forces exerted by flood and waves on bridges; however, it only addresses forces on substructures and recommends constant coefficients for drag and lift forces on bridge piers. Besides, previous studies on calculating hydrodynamic forces on bridges do not accurately estimate the flood loading. These studies did not consider the effects of bridge deck width, height, shape, and skew angle on hydrodynamic force and overturning moment coefficients. The effectiveness of structural countermeasures, such as shear keys, for hydrodynamic failure of substructures and superstructures is also unknown. This project uniquely combined the results from laboratory experiments, computational fluid dynamics, and structural analysis of inundated bridges to investigate the hydrodynamic forces exerted on partially or fully submerged bridges and to assess their integrity during flooding. This study evaluated the general response of the drag, lift and moment coefficients to bridge geometry (deck type, width, and skewness), flow conditions (inundation ratio, Froude number), flow blockage by debris and substructures, and wave loading. Design charts and equations are developed for four typical TxDOT bridge deck details. The results of all bridge deck types are combined to develop universal design charts and equations for all bridge deck geometries. Furthermore, the efficacy of using TxDOT countermeasures, particularly shear keys and earwalls, to reduce the risk of bridge failure during flood events were assessed to determine whether current measures are adequate, or if modified details are warranted. Specifically, the drag force obtained from CFD analysis was compared with the interface shear strength of the shear key or earwall, which was estimated according to the shear-friction equations in 2020 AASHTO LRFD Specifications. For the cases where the interface shear strength is not sufficient, several approaches are recommended to increase the interface shear capacity

This study improves the level of knowledge by eliminating gaps in the current bridge design standard. It improved the prediction of magnitude of potential hydrodynamic forces on bridges to determine the efficacy of using countermeasures to provide enhanced stability and resistance against failure during flood events. In addition to TxDOT, other DOT's or federal transportation agencies may benefit from the results of this project to update the current national bridge design standards, AASHTO standards and FHWA guidelines.

A.3 System Reliability and Increased Service Life

Bridge failures due to high-velocity flood events and hurricane-driven surge and wave loading have highlighted the importance of designing countermeasures to improve the reliability of bridge structures subject to hydraulic and hydrodynamic forcing. This research project provides value by identifying and analyzing bridge superstructures with different geometric shapes and required countermeasures in high velocity flood events. To counter the lateral force exerted by high velocity

floods, this study recommended modification to the current shear key and earwall details. Implementing the findings of this study will significantly lower the chances of bridge failures due to hydraulic events and consequently increase the service life of Texas stream-crossing bridges.

A.4 Traffic and Congestion Reduction

Bridges are a major transportation medium, and their failures can lead to severe traffic congestion, detours, and delays. In 2015, traffic congestion caused people in the U.S. to travel 6.9 billion extra hours and purchase 3.1 billion additional gallons of fuel which was equivalent to \$160 billion (Schrank et al., 2015). According to Cook (2014), at least one bridge with an ADT of 70,000 (Average Daily Traffic) or greater fails annually in the U.S. In 2015 during the Memorial Weekend flood, the Fischer Store Road bridge collapsed and that cut off a major route west of Wimberley. It forced those who used to use the road to make a 50-mile detour. Such incidences may affect supply and demand for goods and services in a region as well. The per-hour commercial value of time in Texas is \$55.24, and average state gasoline cost is \$2.05/gallon (Schrank et al., 2021). These data show the cost of a bridge failure due to the amount of time and fuel lost. Since the majority of bridge failures (almost 55%) in the U.S. result from hydraulic events like flood and scour, this project will contribute to congestion, detour, and delay reduction by increasing the bridge safety against high velocity flood events.

A.5 Reduced Construction, Operation, and Maintenance Cost

Texas has the largest inventory of bridges when compared to other states in the U.S. This includes both on-system bridges (those owned or maintained by TxDOT) and off-system bridges (owned or maintained by another entity) (Texas Department of Transportation, 2020). Bridge construction/re-construction is necessary when a bridge totally collapses. A total collapse is when the primary members of the bridge undergo severe deformation and thus are no longer able to service the traffic flows. A partial collapse refers to an incident when the bridge undergoes some deformation or section loss but is still able to service the traffic flows (Taricska, 2014). When a bridge collapses partially, it needs to be repaired. The cost required for bridge repair can be considered as maintenance cost. Typically, construction of a highway bridge in the U.S. costs within \$10,00,000–\$50,00,000 (Bundy, 2021). A study conducted by American Road and Transportation Builders Association estimated nearly \$164 billion is required to make major repair works on structurally deficient bridges in U.S. (ARTBA, 2020). Implementing the results of this research and recommended countermeasures will increase the capacity of new bridges to withstand more intense flood events, which will eventually lead to the reduction of construction, operations, and maintenance costs.

A.7 Infrastructure Condition

Bridge failure is the leading problem facing U.S. infrastructure. Bridge failures have a devastating impact on commerce, economic growth, logistics, and casualties (Taricska, 2014). Bridges connect two sides of a river; therefore, their failure can disrupt traffic and other services. For example, some highway bridges carry infrastructure services such as electricity, telephone cables, and water supply pipelines (Wong et al., 2005). This research project provides value by identifying existing

bridges prone to hydraulic failure and recommends approaches to retrofit these bridges. Implementing this research also helps design and build more reliable and safer bridges and prevent damages to adjacent infrastructure facilities.

APPENDIX B

DOT's Current Bridge Design Standards, Policies, and Guidelines for the Design of Countermeasures to Hydrodynamic Forces

Alabama (February 2019)

The ALDOT's Bridge and Hydraulic Design Manual mentions the use of FEMA and AASHTO standards for hydraulic and hydrological analyses of bridges.

Alaska (September 2017)

Alaska DOT's Bridges and Structures Manual provides the current AASHTO LRFD bridge design policies and practices for use in the DOT & PF (Public health) projects. Revisions to this manual are released on an annual basis after being approved by the FHWA (Federal Highway Administration).

Countermeasures

- Countermeasures for scouring risks are provided by addressing an adequate waterway opening and designing a bridge foundation that must not fail or be damaged in the event of a 100-year or 500-year flood.
- Shear keys or blocks are used to transmit the superstructure's lateral force to the substructures.

Arizona (July 2001)

ADOT's Bridge Design Manual refers to AASHTO LRFD Bridge Design Specifications for calculations of hydrodynamic loads.

Countermeasures

- For the scour countermeasure, concrete block floors with cut-off walls upstream and downstream of the bridge
- The use of shear key is suggested to resist lateral imposed loads, i.e., seismic loads.

Arkansas (September 2017)

The ARDOT follows AASHTO LRFD and FHWA Bridge Design Specifications and Standards.

California (August 2019)

All bridges and structures over waterways in the state highway system (SHS) are designed in accordance with AASHTO-LRFD Bridge Design Specifications, current Bridge Design Standard California Amendments (AASHTO-BDS-CA), and the Highway Design Manual (HDM).

Countermeasure

Shear keys are used for reducing seismic effects as per the Caltrans seismic design criteria.

Colorado (February 2020)

The CDOT Bridge Design Manual refers to AASHTO Bridge Design Specifications for the design, rehabilitation, and repair of bridges.

Countermeasure

- The shear key is required at piers and abutments to provide adequate sliding resistance.

Connecticut (December 2019)

The CTDOT conforms to the requirements set forth in the latest publications of the CTDOT Bridge Manual and AASHTO LRFD Bridge Design Specifications.

Countermeasure

The CTDOT designs the foundations of bridges to reduce the effects of scour from a super flood and protect the substructure units with riprap or similar armoring layers.

Delaware (January 2019)

The Delaware Department of Transportation (DelDOT) developed a Bridge Design Manual to provide guidance and assistance for the construction and maintenance of bridges. The AASHTO LRFD Bridge Design Specifications provide the basis for highway bridges designed for the DelDOT.

Countermeasure

According to the DelDOT, a scour countermeasure is properly designed and installed when it is in accordance with the procedures outlined in HEC-23 and NCHRP Report 587.

Florida (January 2018)

The FDOT Structure Design Guidelines (SDG) incorporate technical design criteria, and include additions, deletions, or modifications to the requirements of the AASHTO LRFD Bridge Design Specifications (LRFD). The SDG provides engineering standards, criteria, and guidelines for developing and designing bridges and retaining walls for which the Structures Design Office (SDO) and District Structures Design Office (DSDO) have overall responsibility.

Georgia (March 2019)

The GDOT incorporates standard specification guidance from the LRFD Bridge Manual into the GDOT Bridge and Structures Design Manual to produce a consolidated manual for bridge design.

Countermeasures

For scour risks, the depth of a bridge foundation shall be determined, based on the 500-year storm event and the associated 500-year scour line.

Hawaii (December 2005)

The HDOT is responsible for designing its own bridges in the state of Hawaii.

Idaho (November 2019)

The Idaho DOT provides the Idaho Transportation Department LRFD Bridge Design Manual to supplement the AASHTO LRFD Bridge Design Specifications, as well as to provide guidance for designers, checkers, and consultants.

Illinois (January 2012)

The IDOT is currently transitioning from the AASHTO Standard Specification for Highway Bridges - Division I & IA (LFD or ASD) to the AASHTO LRFD Bridge Design Specifications (LRFD) for new bridge constructions.

Countermeasures

- Riprap can be used to mitigate the estimated scour at piers *only* if additional alternatives are also employed.
- Shear key is suggested for preventing differential beam movement.

Indiana (December 2012)

The INDOT follows the LRFD's policy for hydrodynamic load estimation of river-crossing bridges.

Countermeasures

- To prevent scour around a bridge pier, the protective material is laid on the streambed, which includes a floor lining of concrete, timber, or riprap.
- Shear connectors and vertical ties between the deck and its supporting members should be designed for force effects calculated on the basis of full composite action.

Iowa (February 2020)

The latest Iowa DOT Bridge design standards state that after October 1, 2007, all new bridges shall be designed by LRFD specifications. They also indicate that states have the option of using LRFD specifications or the specifications of the original design for modifications of existing structures.

Countermeasures

The IOWA DOT follows HEC-18 instructions for an in-depth discussion of when and how to use countermeasures for scouring.

Kansas (October 2016)

The KDOT follows the AASHTO LRFD Bridge Design Specifications published in 2016.

Kentucky (June 2019)

The Kentucky DOT uses LRFD (Load Resistance Factor Design) for all new bridges begun after October 1, 2007.

Louisiana (August 2019)

The LA DOTD follows the AASHTO LRFD Bridge Design Specifications for the design of all new bridges begun after October 2006. However, for extreme events with scour they follow the NCHRP report 489, Design of Highway Bridges with Extreme Events; for extreme events with storm surges and waves, they follow the latest AASHTO Guide Specifications for Bridges Vulnerable to Coastal Storms.

Maine (June 2018)

The Maine DOT utilizes several tools for hydraulic analysis of bridge structures, including the Army Corp of Engineers Program HEC-RAS, the U.S.G.S Computer Program "WSPRO," and principles of open channel hydraulics.

Countermeasures

- The Maine DOT follows the HEC-18 manual when evaluating scour.
- Shear key is recommended for resisting seismic loads.

Maryland (January 2020)

The Federal Highway Administration (FHWA), under the Department of Transportation (DOT), is responsible for reviewing and approving highway bridges for the MDOT.

Massachusetts (June 2013)

MassDOT follows the AASHTO LRFD Bridge Manual (2013) design guidelines when developing a bridge project process, finalizing the bridge design, preparing the construction drawings, and rating the bridge.

Countermeasures

Shear key is suggested for providing resistance against sliding.

Michigan (December 2019)

The Michigan DOT requires that the most recent edition of LRFD Bridge Design Specifications published by AASHTO and FHWA standards be followed for the design of waterway-crossing bridges.

Countermeasures

Countermeasures to prevent scour are incorporated according to FHWA and AASHTO standards.

Minnesota (July 2019)

The MNDOT's Bridge Design Manual employs the load and resistance factor design (LRFD) methodology established by AASHTO.

Mississippi (March 2010)

The bridge design manual for Mississippi focuses on the structural aspects of design and refers to AASHTO guidelines for hydrology and hydraulics requirements.

Missouri (October 2010)

The MoDOT states that all preliminary engineering for bridges after October 1, 2017 shall be designed according to LRFD specifications.

Montana (August 2002)

Montana's Bridge Design Manual focuses on the structural aspects of design, and all hydrology and hydraulics requirements refer to the drainage manual, which was adapted from AASHTO guidelines.

Countermeasures

The nonductile shear key is considered to provide resistance against the transverse movement of the deck.

Nebraska (December 2016)

The Nebraska Bridge Design Manual requires that new structures be designed based on AASHTO LRFD Bridge Design Specifications.

Countermeasures

Bridge general scour, local scour, and abutment scour are analyzed per publication No. FHWA-HIF-12-003; Hydraulic Engineering Circular No. 18, Evaluating Scour at Bridges; and by using engineering judgment. The minimum 100-year general scours used for bridge design is three (3) feet for cohesive soils and six (6) feet for sand-bed streams. The minimum 500-year scour elevation is six (6) feet below the flow line for cohesive soils and 12 feet below the flow line for sand-bed streams.

Nevada (March 2019)

The NDOT Structures Manual follows the 4th edition of the AASHTO LRFD Bridge Design Specifications.

Countermeasure

To resist seismic force, concrete shear key is provided on the outside edges of the bridge.

New Hampshire (January 2015)

The New Hampshire DOT states that bridges and transportation-related structures shall be designed in accordance with the latest edition of the following specifications:

- AASHTO LRFD Bridge Design Specifications,
- AASHTO Standard Specifications for Highway Bridges, and
- NHDOT Standard for Road and Bridge Construction.

Countermeasures

- The NHDOT states that all foundations must be designed to withstand the conditions of scour for the design flood of a 100-year event and the check flood of a 500-year event.
- Shear keys are recommended between a superstructure and an abutment.

New Jersey (October 2016)

The NJDOT Bridge Design Manual refers to the AASHTO LRFD manual for design purposes. However, while the design manual establishes the standards for designing bridge structures in New Jersey, designers are encouraged to explore innovative methods for providing NJDOT project bridge designs.

Countermeasures

- The NJDOT follows HEC 23 design guidelines for bridge scour and stream instability countermeasures. It also mentions that foundations of new bridges should be designed to resist scour for 100-year flood criteria or a flood of a lesser interval. The foundation shall also be checked for a 500-year check flood.
- The shear key is employed to provide resistance against seismic events.

New Mexico (February 2018)

The New Mexico Department of Transportation (NMDOT) uses the current edition of the AASHTO Load and Resistance Factor Design (LRFD) Bridge Design Specifications and the current interims as the primary standards.

Countermeasures

- Expected scour should be designed for 50-year, 100-year, and 500-year flood events. To prevent scour at streambeds, riprap should extend a minimum of 2 feet above the design flood elevation and should be buried in the stream bed to the contraction scour depth if possible.
- Shear key is provided to resist sliding decks and girders.

New York (May 2019)

The NYSDOT states that structural design shall be in accordance with the NSYDOT LRFD Bridge Design Specifications for all new and replacement bridges. The NYSDOT Standard Specifications for Highway Bridges may be used for rehabilitation of existing bridges, with DCES (Deputy Chief Engineer for Structures Design and Consideration) approval.

Countermeasures

Scour depth needs to be investigated for 100-year and 500-year flood events. During bridge replacement projects, new abutments are often built behind the old abutments, with the old abutments left in place for scour protection.

North Carolina (June 2019)

Unless otherwise noted, the NCDOT design for bridge loads shall be in accordance with the AASHTO LRFD Bridge Design Specifications.

North Dakota (July 2019)

The NDDOT Bridge Design Manual follows the AASHTO guidelines for all load calculations except Strength II and Extreme event I.

Countermeasures

Countermeasures such as riprap, guide banks (spur dikes), or other features shall be used to control potential scour.

Ohio (January 2020)

The ODOT Bridge Design Manual refers to AASHTO's standard design specifications for highway bridges, including all issued interim specifications, the ODOT Construction and Material Specifications, and the Office of Structural Engineering's standard drawings and design datasheets.

Oklahoma (December 2016)

The Oklahoma DOT Roadway Design Manual refers to FEMA and AASHTO guidelines for hydrology and hydraulic designs of bridges.

Oregon (May 2019)

The ODOT Bridge Design Manual refers to AASHTO LRFD Bridge Design Specifications (8th edition, 2017), Oregon standard specifications for construction, and Oregon standard drawings for load calculations.

Pennsylvania (December 2019)

PennDOT requires that all design criteria meet FHWA, AASHTO and U.S. Coast Guard guidelines.

Countermeasures

Proposed scour countermeasures include underpinning, riprap placement, streambed paving, etc.

Rhode Island (December 2007)

The RIDOT Bridge Design Manual primarily uses a compilation of design procedures that include AASHTO LRFD bridge design specifications and the standard practice and guidelines of RIDOT policies.

Countermeasure

For the design of new bridge structures, the use of riprap or other scour countermeasures as a means of scour protection is not permitted. All foundations must be designed to withstand the conditions of scouring for the design flood and the check flood.

South Carolina (June 2006)

The SCDOT Bridge Design Manual refers to AASHTO standard specifications for the design requirements of hydrodynamic loads.

Countermeasure

To accommodate seismic and other lateral loads, beam or girder spans may be detailed with shear keys cast on the cap to provide a shear transfer between the superstructure and the substructure.

South Dakota (January 2020)

The SDDOT Bridge Design Manual refers to AASHTO LRFD bridge design specifications, the SDDOT Road Design Manual, and FHWA requirements and practices.

Countermeasure

Abutment scour is mitigated at end support by appropriate countermeasures designed for a 100-year recurrence event.

Tennessee (December 2012)

The hydraulic design of bridges in Tennessee follows the Federal Highway Administration's (FHWA) guidelines. The Tennessee Department of Transportation also utilizes the FHWA/USGS program, WSPRO, to analyze most bridges.

Texas (January 2020)

The TxDOT Bridge Design Manual follows the AASHTO LRFD Bridge Design Specifications (2017). The Federal Highway Administration (FHWA) mandated the use of LRFD for all bridges for which the Texas Department of Transportation initiated preliminary engineering after October 2007.

Countermeasure

The Texas Department of Transportation (TxDOT) issued a design policy that requires shear keys in bridges Crossings Rivers and streams, based on a freeboard 100-year flood level.

Utah (September 2017)

The UDOT Bridge Design Manual refers to LRFD specifications (AASHTO) for design and load calculations.

Countermeasures

The UDOT recommends the use of the shear key to providing lateral resistance to any type of load. They also suggest that the shear key can be added to transfer transverse forces to substructures.

Vermont (October 2010)

The VTRANS Bridge Design Manual refers to AASHTO, FHWA, and the U.S. Coast Guard design specification for load calculations and considerations for river-crossing bridges.

Countermeasures

Foundations, including abutments and piers, shall be evaluated at the service limit states, considering the effects of scour on the design flood.

Virginia (May 2016)

The VDOT Bridge and Structure Hydraulics Design Manual for Bridges refers to AASHTO, FHWA, and the U.S. Coast Guard references for the design of river-crossing bridges.

Countermeasures

Riprap may be used as a scour countermeasure at existing bridge piers, new or existing abutments, and lateral encroachments.

Washington (July 2019)

The WSDOT follows the current editions of the following AASHTO specifications to design highway bridges and structures:

- AASHTO LRFD Bridge Design Specifications (LRFD-BDS), and
- AASHTO Guide Specifications for LRFD Seismic Bridge Design (LRFD-SGS).

Countermeasures

- The shear key is used as a countermeasure for lateral loads, as well as reinforcement for girders.
- Deep foundations, minimum cover to the top of the footing, riprap, pier alignment to streamflow, closure walls between columns, etc. are used as countermeasures to protect piers from scour activity or accumulation of drift.

West Virginia (March 2006)

The West Virginia DOT Bridge Design Manual follows the FHWA, U.S. Coast Guard, and AASHTO requirements for all waterway-crossing bridge designs.

Countermeasures

The deck section should be structurally attached to the girder by a shear key that will be used for transferring moments and shears.

Wisconsin (January 2019)

All bridges in Wisconsin carrying highway traffic are to be designed according to the American Association of State Highway and Transportation Officials (AASHTO) LRFD Design Specifications, American Society for Testing and Material (ASTM), American Welding Society (AWS), and Wisconsin Department of Transportation Standards.

Countermeasures

Debris protection is provided where a physical study of the drainage area indicates considerable debris collection. Sample debris protection devices are presented in the FHWA publication, HEC-9.

Wyoming (April 2003)

The Wyoming Bridge Design Manual requires that AASHTO specifications and requirements be met for all bridges.

APPENDIX C

Identification of Flow Parameters from TxDOT As-built Drawings

Table C. 1 Identification of flow parameters from TxDOT As-built Drawings

Serial No.	TxDOT Drawing	Creek name	Bed level (ft)	Water Surface Level (ft)	Water depth (ft)	Velocity (ft/s)	Froude Number (<i>Fr</i>)
1		Box Creek	273	286.72	13.72	7.85	0.37
2	Anderson 0910-08-040	Indian Creek	358	371.49	13.49	9.48	0.45
3		Stills Creek	271.5	285.99	14.49	11.99	0.56
4	Bastrop 0914-18-102	Paint Creek	433.22	448.68	15.46	6.93	0.31
5		Nichols Creek	1131.66	1143.52	11.86	3.2	0.16
6	Bexar 0072-07-059		1129.25	1137.38	8.13	10.3	0.64
7		Leon Creek	1115	1138.47	23.47	3.2	0.12
8			1112.5	1131.01	18.51	6.7	0.27
9	Brazoria 0912-31-282	Bayou Water Canal	503.23	526.31	23.08	3.42	0.13
10		Betheldraw	217	227.44	10.44	4.25	0.23
11	Burleson 0506-04-022	Bethel Creek	211.5	224.06	12.56	2.68	0.13
12		Hickory Creek	283	291.97	8.97	6.4	0.38
13	Caldwell 0152-03-056	Caldwell	429.12	450.76	21.64	6.95	0.26
14	Comache 0923-17-073	Comanche	1000	1031.35	31.35	10.92	0.34
15	Coryell 0724-01-044	Buttermilk Creek	919	928.29	9.29	15.11	0.87
16		Cowhouse Creek	742	779.08	37.08	9.54	0.28
17	Cottle 0760-01-024	Salt Creek	1740	1749.01	9.01	2.14	0.13
18	Eastland 0570-01-019	Leon River	1273	1293.81	20.81	5.18	0.20
19	Erath 0902-49-063	Green Creek	1057	1082.49	25.49	8.9	0.31
20	Fannin 0901-32-043	Pot Creek	582	599.27	17.27	7.44	0.32
21		Baker Creek	575	584.36	9.36	4.23	0.24
22	Fannin 0901-32-054	Honey Grove Creek	527.5	549.11	21.61	5.81	0.22
23		Sanders Creek	598	607.71	9.71	8.69	0.49
24	Fayette 1441-01-012	Fayette	357	370.38	13.38	5.21	0.25
25	Fisher 0908-23-030	Sweetwater Creek	1905	1920.35	15.35	8.02	0.36
26	Gillespie 0914-19-022	Pedernales River	1547	1564.14	17.14	8.88	0.38
27	Grayson 0705-01-027	Shawnee Creek	511	528.1	17.1	5.51	0.23
28		Grove Creek	620	638	18	10.96	0.46
29	Grayson 0729-02-026	Shooter Creek	557	570.6	13.6	5.27	0.25
30		Mud Branch	453	473.15	20.15	9.06	0.36
31		Grace Creek	335	343.65	8.65	1.32	0.08
32	Gregg 2158-01-011	Grace Creek Trib	335	345.05	10.05	3.68	0.20
33		Kickapoo Creek	305	316.97	11.97	3.3	0.17
34	Grimes 0917-17-043	Ragan Creek	287.5	300.02	12.52	7.9	0.39
35	Grimes 0917-17-063	Navasota River	213	238.01	25.01	2.45	0.09
36	Hardeman 0925-07-	Groesbeck Creek	1510	1530.32	20.32	8.74	0.34
37	029	Unnamed Creek	1916	1926.39	10.39	1.14	0.06
38	Harris 0912-72-230	White Oak Bayou	7	45.25	38.25	5.79	0.16
39	Harris Galveston 3312-01-008	Clear Creek	1.5	8.4	6.9	3.4	0.23
40	Hartley 0238-01-030	Punta De Agua Creek	3952	3967.54	15.54	7.22	0.32
41		Rita Blanca Creek	3910	3934.27	24.27	8.96	0.32

42	Hill 0909-37-056	Aquilla Creek	460	470.73	10.73	3.88	0.21
43		Cobb Creek	607	614.73	7.73	3.11	0.20
44	Hopkins 0901-28-086	Redding Creek	435	452.18	17.18	3.95	0.17
45	Knox 0925-17-013	China Creek	1540	1549.05	9.05	1.64	0.10
46		Caney Creek	421	432.71	11.71	5.98	0.31
47		East Caney Creek	376	393.93	17.93	2.87	0.12
48	Lamar 0688-03-023-2	Hickory Creek	368	387.83	19.83	17.34	0.69
49		Peters Creek	322.5	339.54	17.04	10.5	0.45
50		Parsons Creek	450	460.66	10.66	12.3	0.66
51		Cane Creek	507	519.76	12.76	10.16	0.50
52	Lamar 0901-29-065	Hickory Creek	421	435.82	14.82	3.36	0.15
53		Rowdy Creek	535	539.64	4.64	1.17	0.10
54			535	537.88	2.88	8.02	0.83
55	Leon 1147-03-014	Two Mile Creek	224	243.72	19.72	5.3	0.21
56	Liberty 0920-02-087	Long John Creek	15.82	25.54	9.72	5.01	0.28
57	Lipscomb 2078-02-007	North Fork Kiowa Creek	2513	2526.57	13.57	6.11	0.29
58	Live Oak 0916-29-012	Atascosa River	123	165.39	42.39	8.9	0.24
59	Lubbock 1041-02-039	Brazos River	2912.6	2920.73	8.13	4.5	0.28
60	Mills 0923-23-028	Pompey Creek	1299	1320.71	21.71	11.9	0.45
61	Mitchell 0908-21-016	Colorado River	1962.5	1994.09	31.59	9.97	0.31
62		Panther Creek	810	828.42	18.42	9.83	0.40
63	Montague 0903-28-043	Salt Creek	810	829.08	19.08	10.44	0.42
64		West Fork San	125	133.61	8.61	4.2	0.25
65		Jacinto River	121.5	132.61	11.11	1.5	0.08
66	Montgomery 0338- 11-051		130	140.38	10.38	2.2	0.12
67		Alligator Creek	133	143.06	10.06	4.4	0.24
68			129	130.6	1.6	3.7	0.52
69	Parker 0314-01-077	Patrick Creek	892	907.61	15.61	13.39	0.60
70		Walnut Creek	735	752.77	17.77	9.1	0.38
71	Parker 0902-38-076	Kickapoo Creek	696	722.78	26.78	10.63	0.36
72		Dry Creek	971	993.92	22.92	6.1	0.22
73	Red River 0046-01-061	Kickapoo Creek	342	355.55	13.55	8	0.38
74	Robertson 0262-03- 025	Little Brazos River	252	277.7	25.7	1.97	0.07
75	Tarrant 0902-48-742	Silver Creek	598	612.4	14.4	2.2	0.10
76	Travis 0114-03-05	Willow Creek	437	455.61	18.61	5.8	0.24
77	Travis 1200-03-028	Lower Colorado River	385	415.53	30.53	10.71	0.34
78	Wheeler 0761-05-013	Sweetwater Creek	2233	2247.03	14.03	5.56	0.26
79		Salt Creek	1178	1187.3	9.3	1.06	0.06
80	Young 0903-27-026	Loving Creek	1062	1070.94	8.94	4.03	0.24
81	17-082-1327-02- 007_AsBuilts_2013	Washburn Branch	473	483.67	10.67	5.23	0.28
82	17-239-1299-01- 004_AsBuilts_2008	Red Gully	137.5	154.78	17.28	9.8	0.42
83	17-23-1299-01- 005_AsBuilts_2008	New Year Creek	134	157.52	23.52	11.7	0.43

APPENDIX D

Experimental Modeling-Additional Information

Table D.1 Summary of experimental conditions for test Series A to F

Test Series	Model	Deck Width (ft)	Description	Froude No.	Inundation Ratios (or Blockage Ratio for Debris Tests)	Proximity Ratios
A	1	46	TX-28	0.20, 0.34	0.25 – 2.5	3 – 5.25
		26	TX-28	0.20, 0.27, 0.34	0.25 – 2.5	3 – 5.25
	2	46	TX-54	0.20, 0.32	0.25 – 2.0	3 – 4.75
		26	TX-54	0.20, 0.27, 0.32	0.25 – 2.0	3 – 4.75
	3	46	Slab beam	0.20, 0.34	0.25 – 3.0	3 – 5.25
		26	Slab beam	0.20, 0.27, 0.34	0.25 – 3.0	3 – 5.25
	4	46	Box beam	0.20, 0.34	0.25 – 2.5	3 – 5.25
		26	Box beam	0.20, 0.27, 0.34	0.25 – 2.5	3 – 5.25
B	1	46	15° Skew	0.20, 0.34	0.25 – 2.5	3 – 5.25
			30° Skew	0.20, 0.34	0.25 – 2.5	3 – 5.25
			45° Skew	0.20, 0.34	0.25 – 2.5	3 – 5.25
C	2	46	Debris – Flat Plate	0.32	0.11 -0.31	3
			Debris – Fixed Wedge	0.32	0.11 - 0.31	3
D	1	46	Unattached Substructure	0.20 – 0.33	0.25 – 2.5	3.03
	2	46	Unattached Substructure	0.25 – 0.28	0.25 – 2.0	2.20
	3	46	Unattached Substructure	0.30 – 0.33	0.25 – 3.0	3.66
	4	46	Unattached Substructure	0.20 – 0.33	0.25 – 2.5	3.03
E	1	46	Attached Substructure	0.20 – 0.33	0.25 – 2.5	3.03
	2	46	Attached Substructure	0.20 – 0.33	0.25 – 2.0	2.20
F	2	46	Wave Loading		0.26, 0, - 0.26	
		26	Wave Loading		0.26,0, -0.26	

Table D.2 Bridge Dimensions (Bridge Model 1: TX-28)

Attribute	Actual Dimension (in)	Scale Dimension (in)	Scale Dimension (mm)
Deck thickness (<i>s</i>)	9.38	0.19	4.8
Bridge Length (<i>L</i>)	595	11.9	302
Width (W) - 26 ft deck	312	6.24	160
Width (W) - 46 ft deck	552	11.04	280
Girder height	28	0.56	14
Railing height	32	0.64	16
Superstructure height (<i>S</i>)	69.88	1.39	34.8

Table D.3 Bridge Dimensions (Bridge Model 2: TX-54)

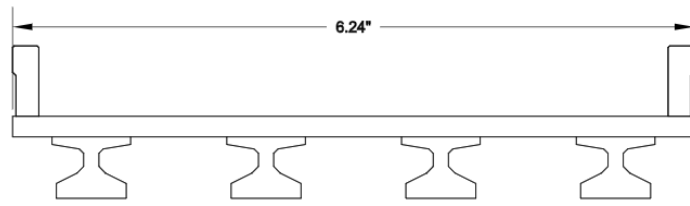
Attribute	Actual Dimension (in)	Scale Dimension (in)	Scale Dimension (mm)
Deck thickness (<i>s</i>)	9.38	0.19	4.8
Bridge Length (<i>L</i>)	595	11.9	302
Width (W) - 26 ft deck	312	6.24	160
Width (W) - 46 ft deck	552	11.04	280
Girder height	54	1.08	27
Railing height	32	0.64	16
Superstructure height (<i>S</i>)	86	1.72	43

Table D.4 Bridge Dimensions (Bridge Model 3: SB-15 Slab Beam)

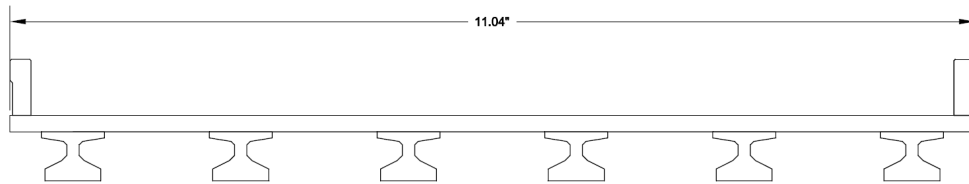
Attribute	Actual Dimension (in)	Scale Dimension (in)	Scale Dimension (m)
Deck thickness (<i>s</i>)	9.38	0.19	4.8
Bridge Length (<i>L</i>)	595	11.9	302
Width (W) - 26 ft deck	312	6.24	160
Width (W) - 46 ft deck	552	11.04	280
Beam height	15	0.3	7.6
Railing height	32	0.64	16
Superstructure height (<i>S</i>)	40.5	0.81	16.4

Table D.5 Bridge Dimensions (Bridge Model 4: BB-28 Box Beam)

Attribute	Actual Dimension (in)	Scale Dimension (in)	Scale Dimension (mm)
Deck thickness (<i>s</i>)	9.38	0.19	4.8
Bridge Length (<i>L</i>)	595	11.9	302
Width (W) - 26 ft deck	312	6.24	160
Width (W) - 46 ft deck	552	11.04	280
Beam height	28.1	0.56	14.3
Railing height	32	0.64	16
Superstructure height (<i>S</i>)	60.1	1.20	31

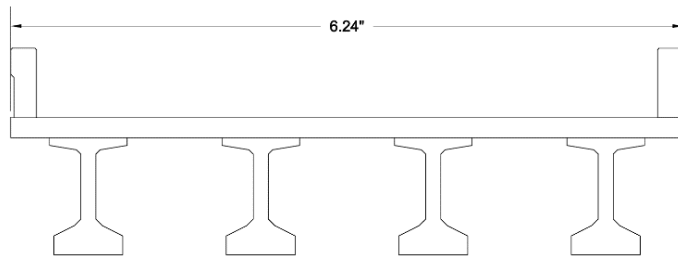


(a)

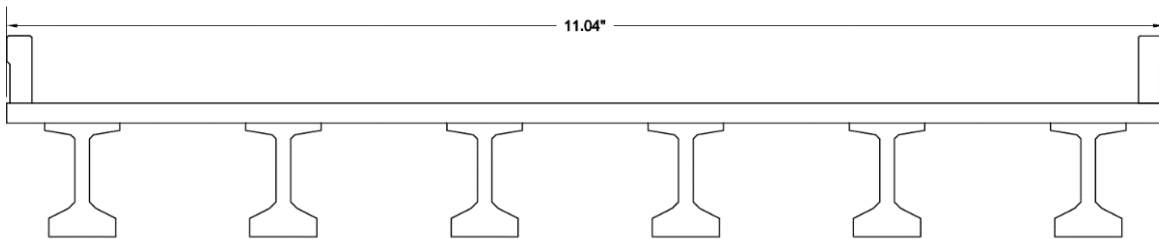


(b)

Figure D.1 Bridge Model 1: a) 26' deck with four TX-28 girders, b) 46' deck with six TX-28 girders

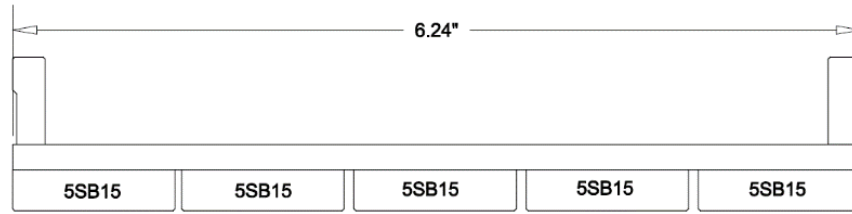


(a)

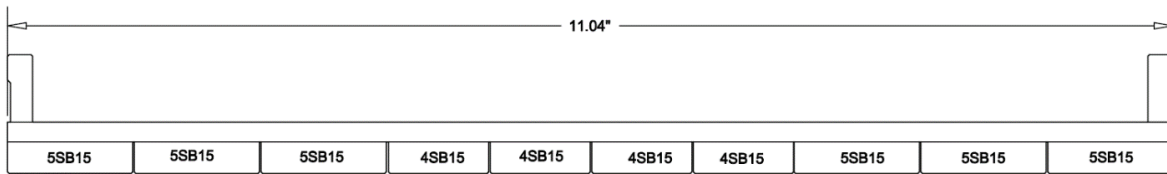


(b)

Figure D.2 Bridge Model 2: a) 26' deck with four TX-54 girders, b) 46' deck with six TX-54 girders



(a)

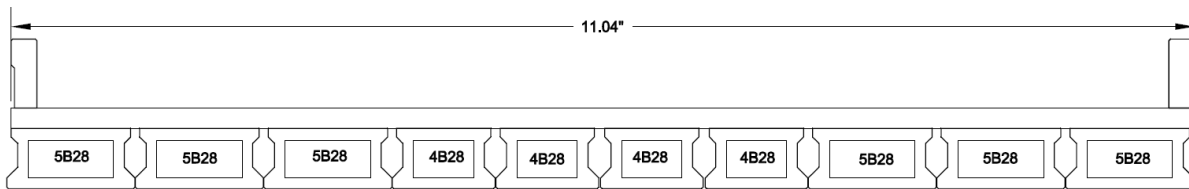


(b)

Figure D.3 Bridge Model 3: a) 26' deck with four 5SB-15 slab beams, b) 46' deck with six 5SB-15 and four 4SB-15 slab beams



(a)



(b)

Figure D.4 Bridge Model 4: a) 26' deck with four 5BB-28 box beams, b) 46' deck with six 5BB-28 and four 4BB-28 box beams

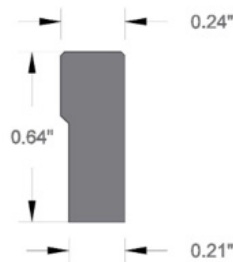


Figure D.5 T221 Bridge railing model

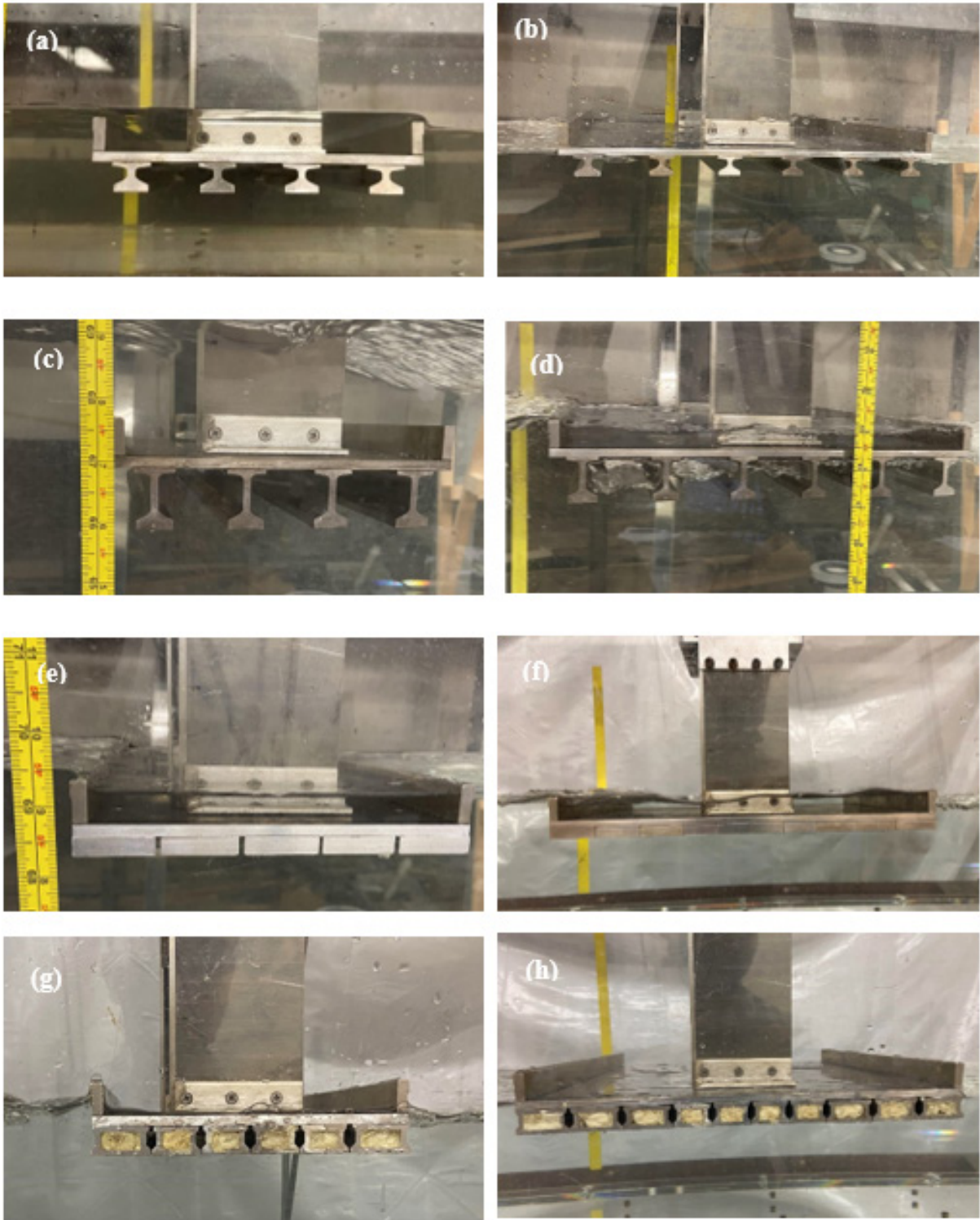


Figure D.6 Test Series A: Bridge Models: (a) 26-ft deck TX-28, (b) 46-ft deck TX-28, (c) 26-ft deck TX-54, (d) 46-ft deck TX-54, (e) 26-ft deck SB-15, (f) 46-ft deck SB-15, (g) 26-ft deck BB-28, (h) 46-ft deck BB-28

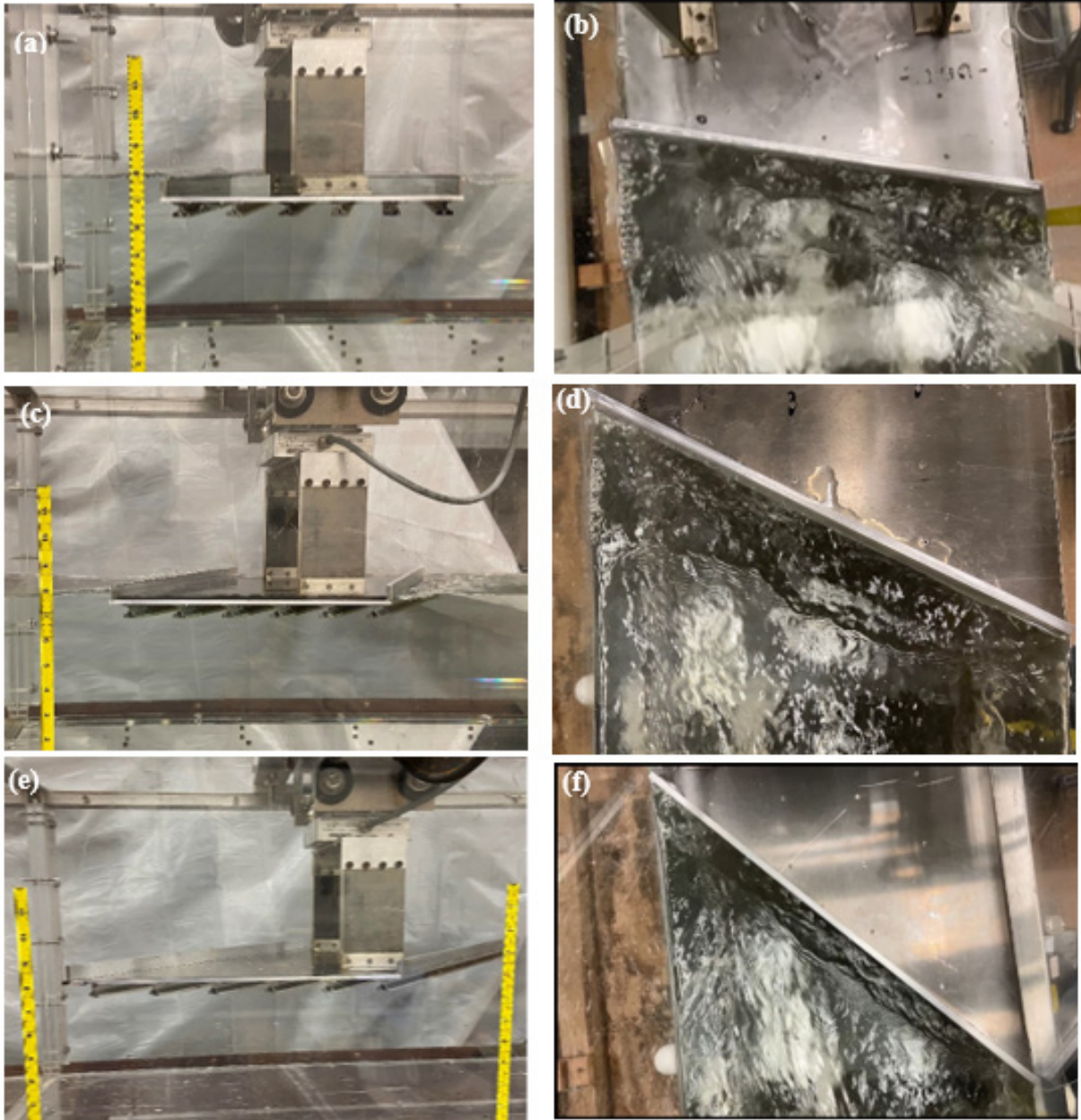
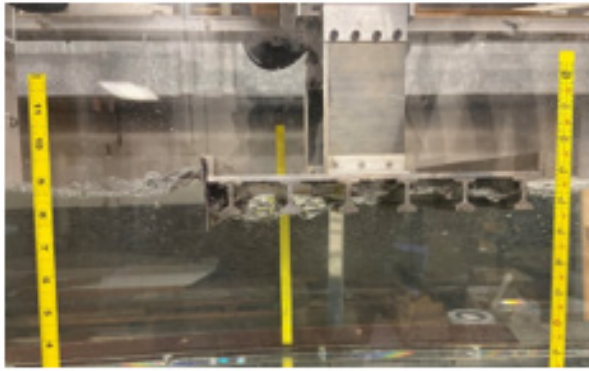
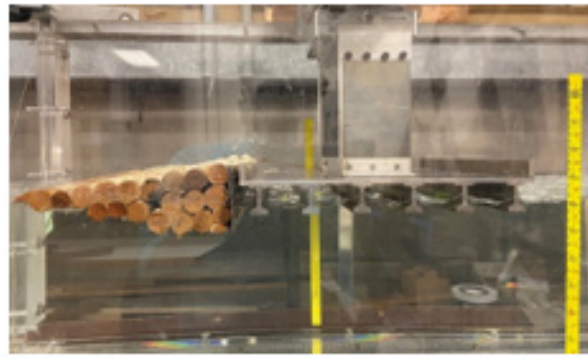


Figure D.7 Test Series B: Bridge Model 1 with skew deck; (a) 15-deg skew deck side view (b) 15-deg skew deck top view, (c) 30-deg skew deck side view, (d) 30-deg skew deck side view, (e) 45-deg skew deck side view, (f) 45-deg skew deck top view



(a)



(b)

Figure D.8 Test Series C: Bridge Model 2 with derbies; (a) with flat plate debris, (b) with wedge debris

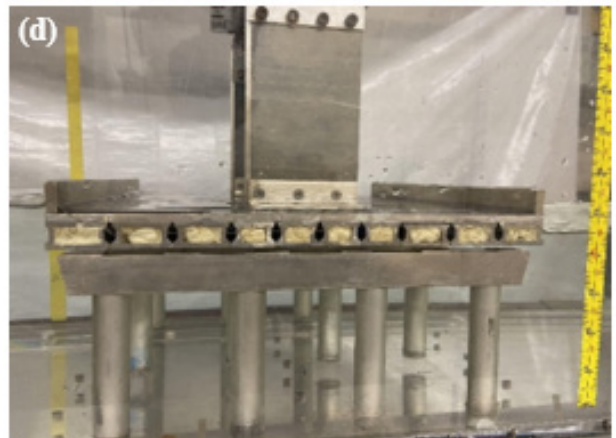
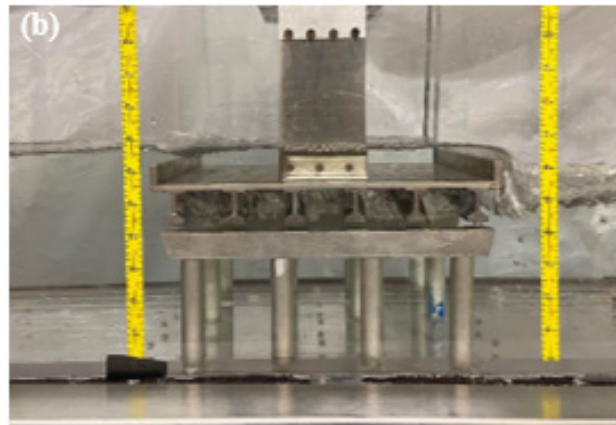
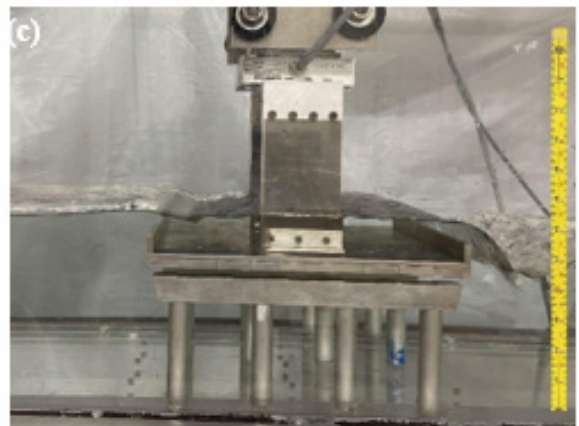
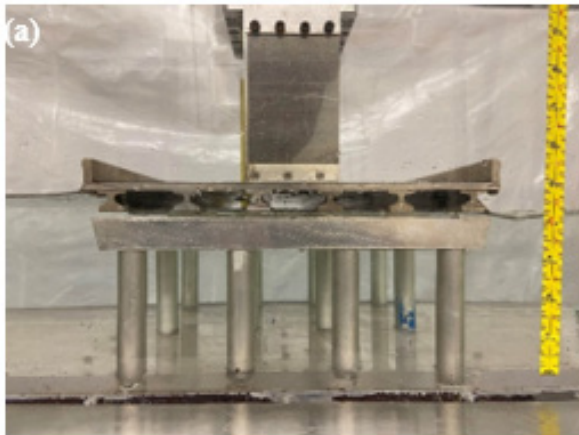
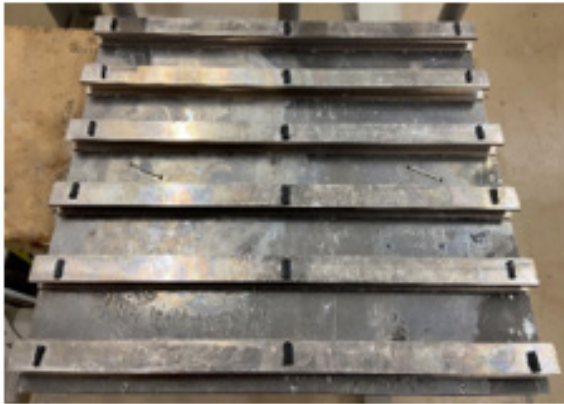


Figure D.9 Test Series D: Bridge Models 1 to 4 with substructures; (a) Bridge Model 1 (TX-28), (b) Bridge Model 2 (TX-54), (c) Bridge Model 3 (SB-15), (d) Bridge Model 4 (BB-28)



(a)

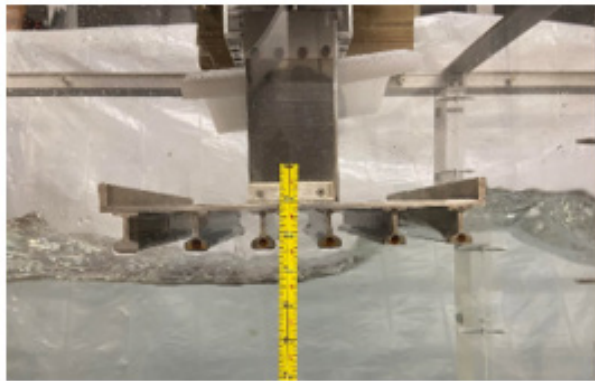


(b)

Figure D.10 Test series E: (a) bearing pad installation and (b) substructure test configuration



(a)



(b)

Figure D.11 Test Series F: Bridge Models 2 under wave loading; (a) TX54-26' deck, (b) TX54-46' deck

APPENDIX E

Numerical Modeling-Additional Information

I. Contour Plots for Variables Around Scaled Bridge Decks

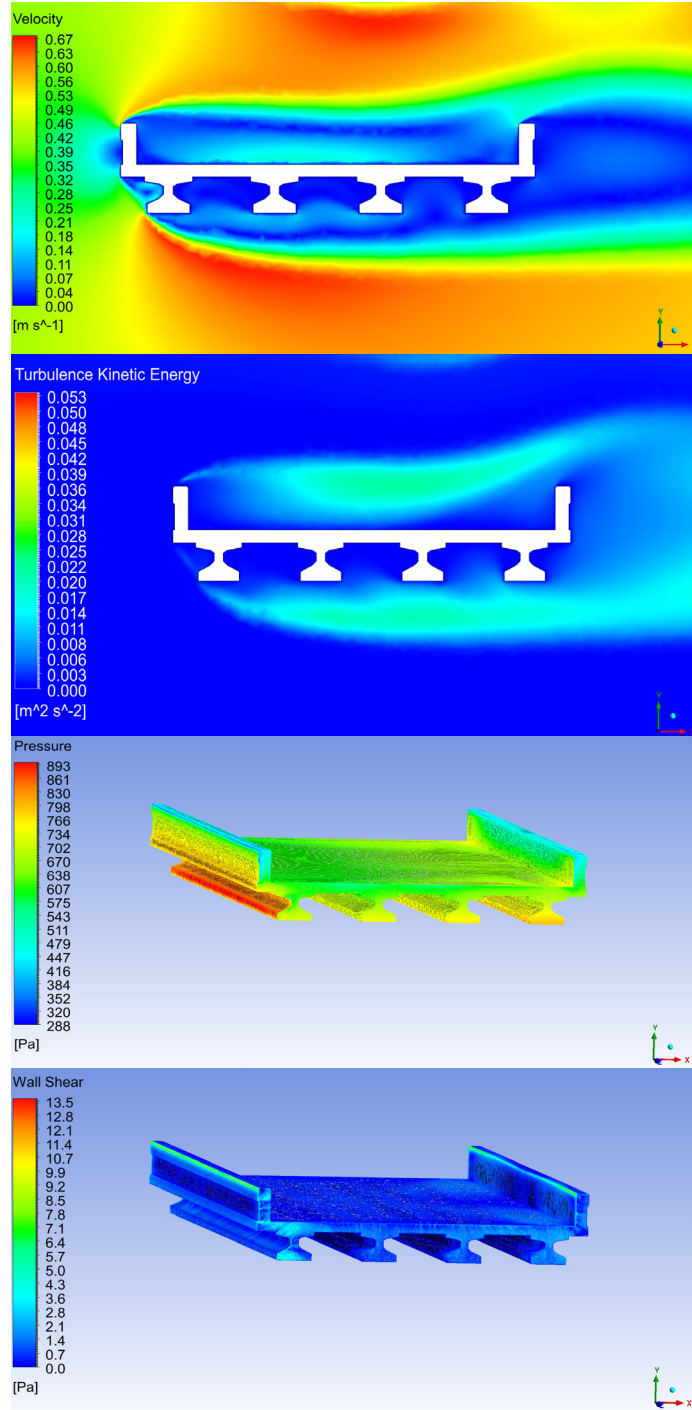


Figure E.1 Bridge Model TX28-26' wide Deck ($h^* = 2.5$, $Fr = 0.34$)

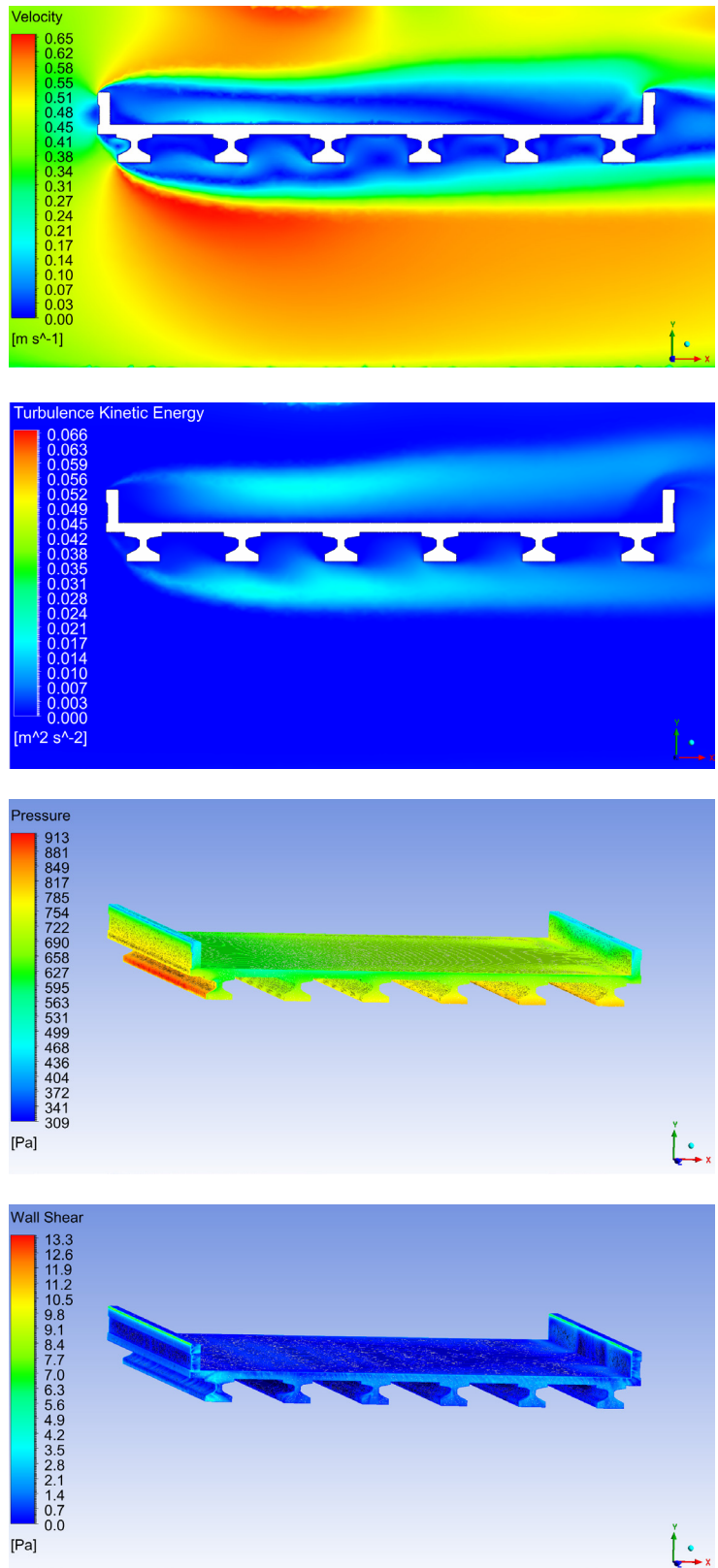


Figure E.2 Bridge Model TX28-46' wide Deck ($h^* = 2.5$, $Fr = 0.34$)

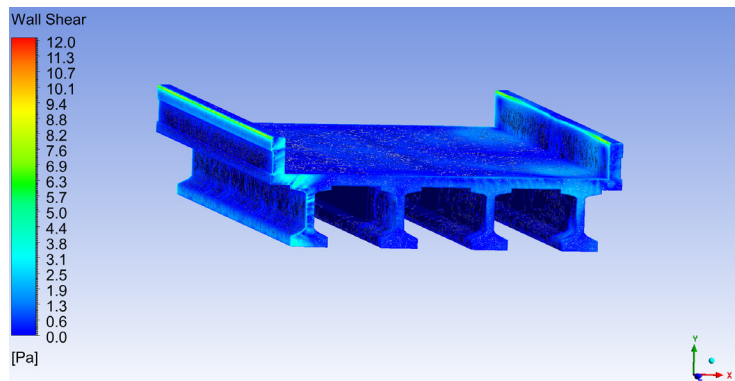
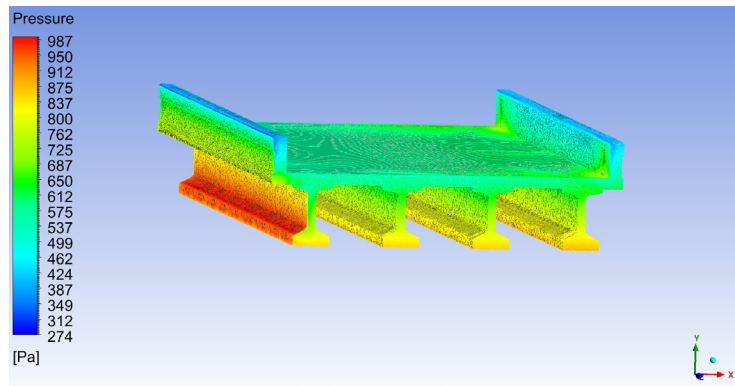
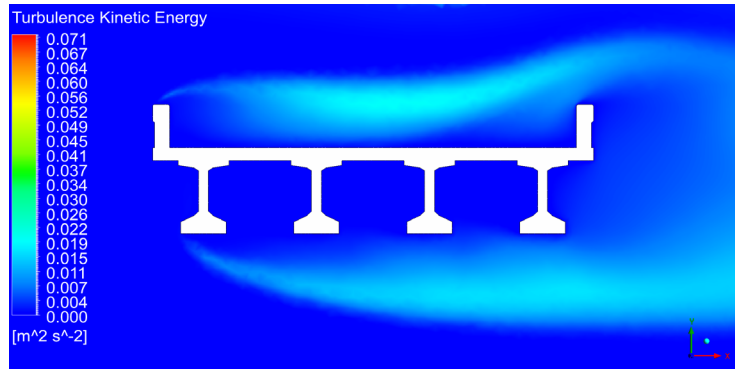
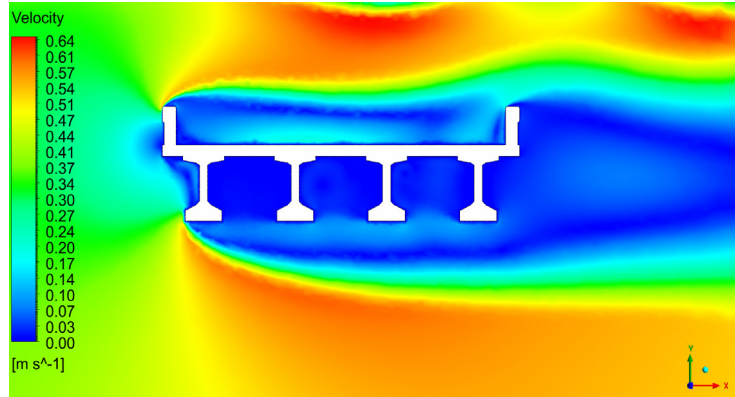


Figure E.3 Bridge Model TX54-26' wide Deck ($h^* = 2$, $Fr = 0.27$)

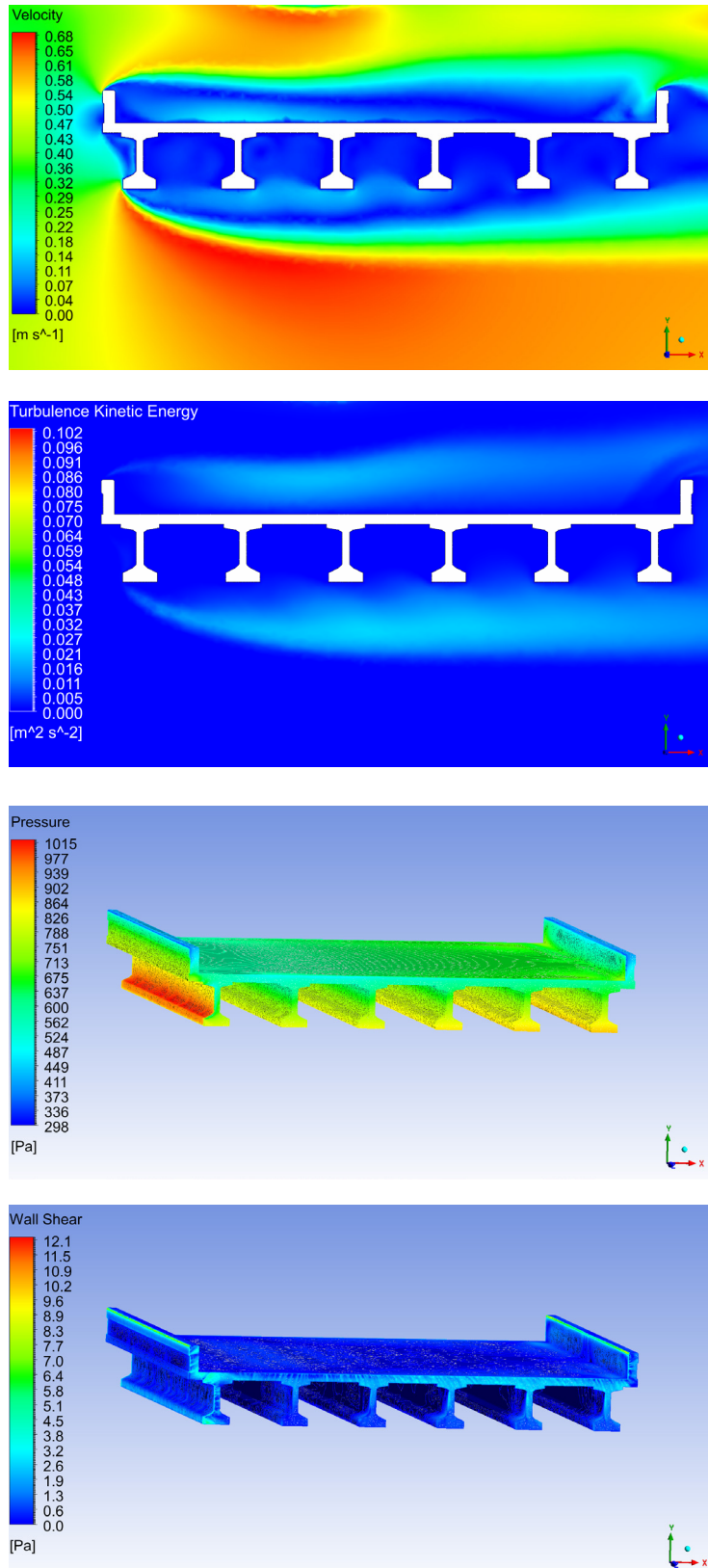


Figure E.4 Bridge Model TX54-46' wide Deck ($h^* = 2$, $Fr = 0.32$)

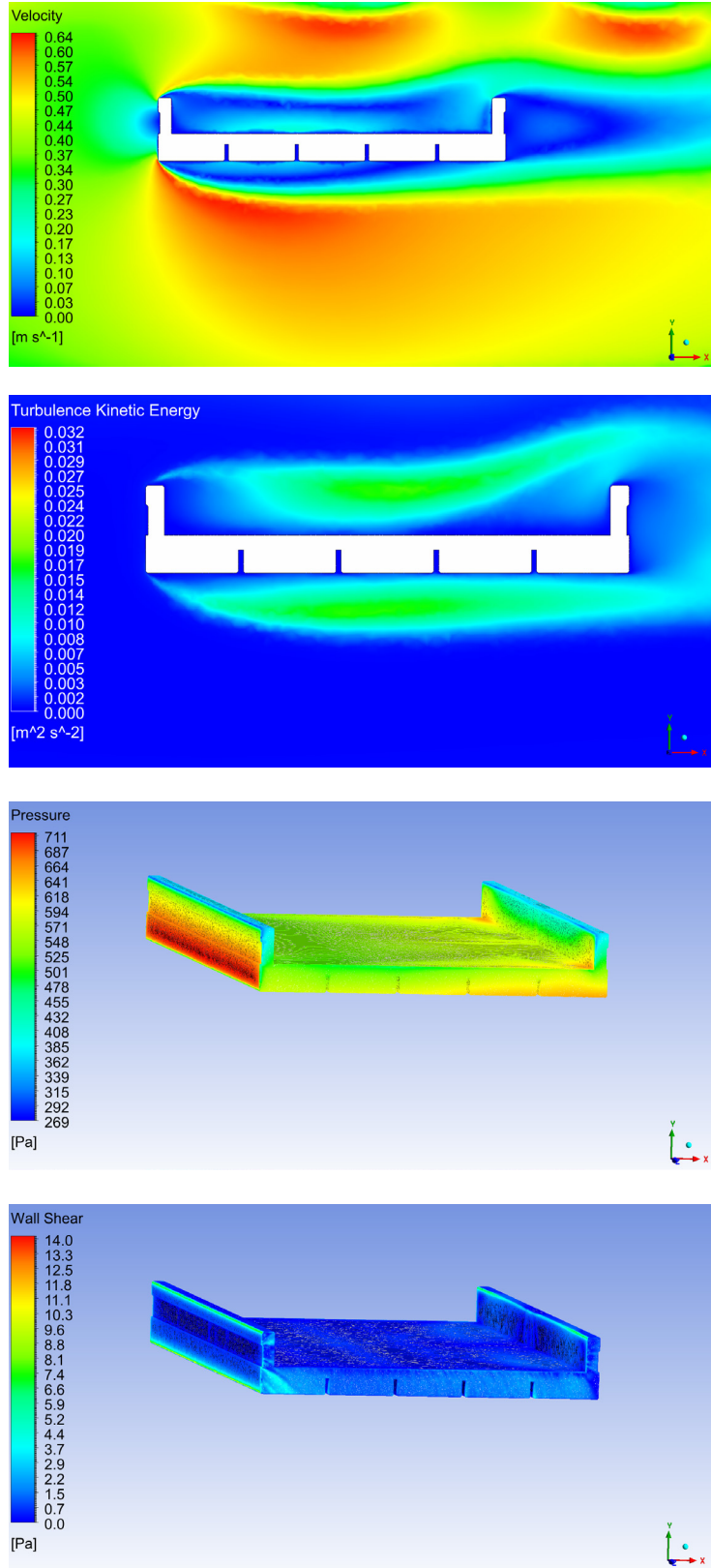


Figure E.5 Bridge Model Slab Beam-26' wide Deck ($h^* = 2.5$, $Fr = 0.34$)

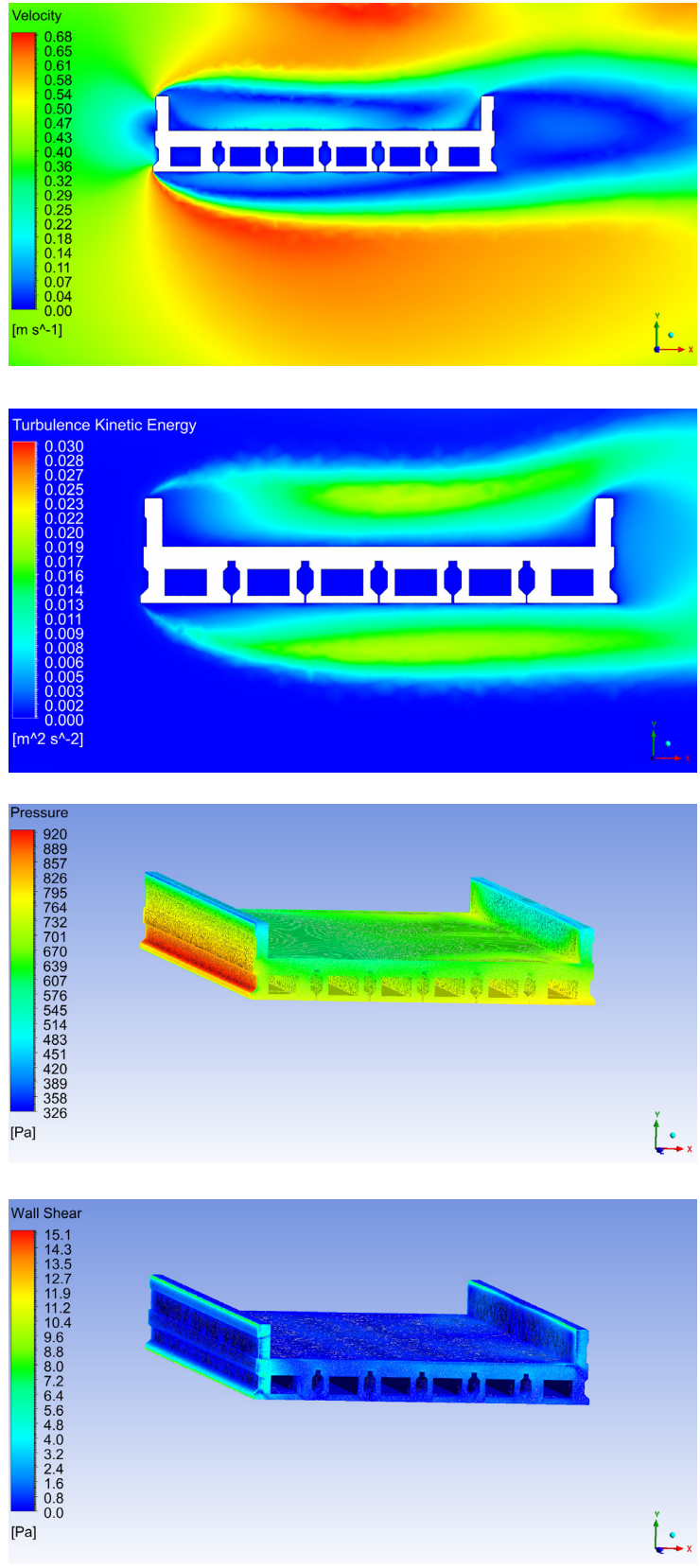


Figure E.6 Bridge Model Box Beam-26' wide Deck ($h^* = 2.5$, $Fr = 0.34$)

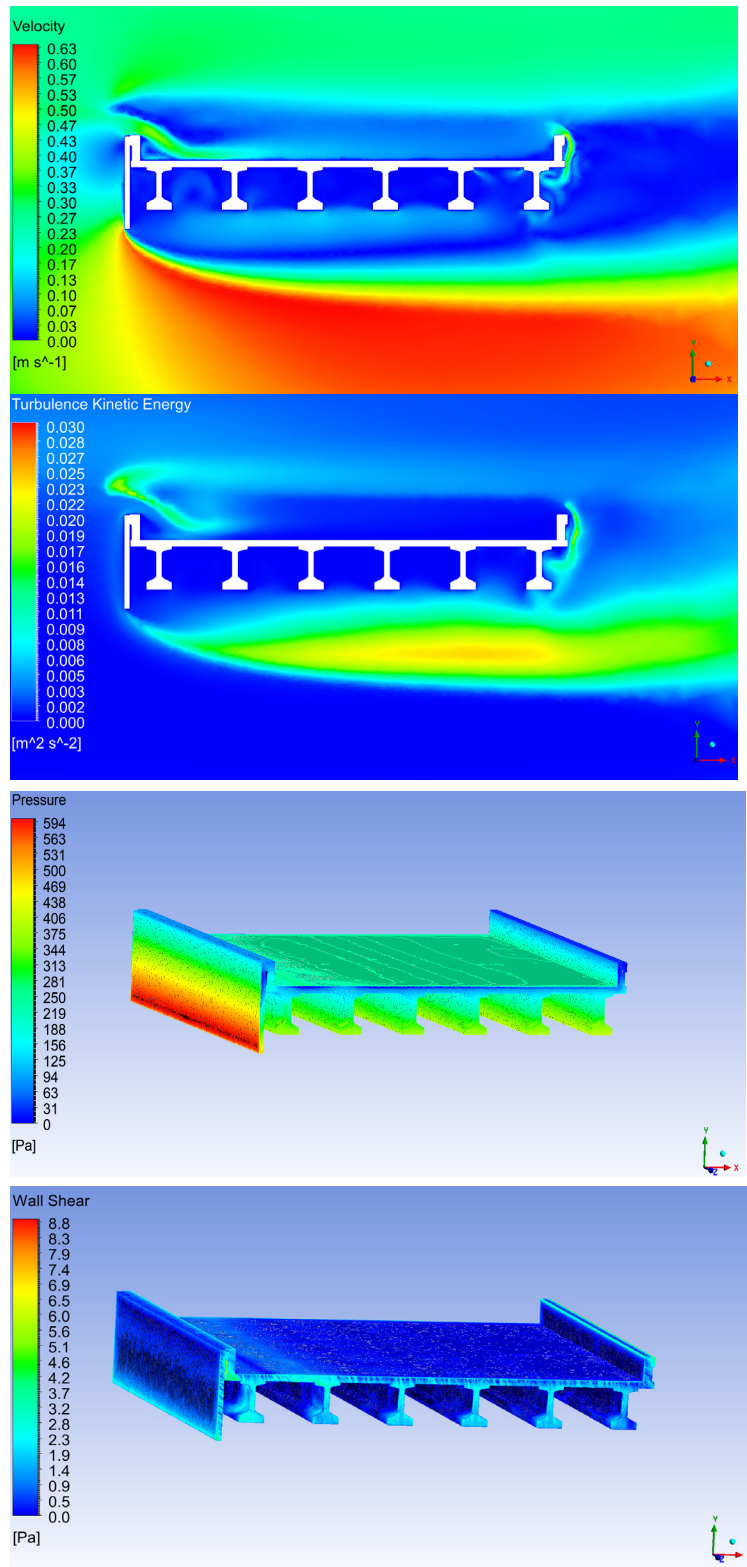


Figure E.7 Bridge Model TX54-46' wide Deck with Flat Plate Debris ($h^* = 1$, $Fr = 0.34$)

II. Contour Plots of Air Volume Fraction for waves

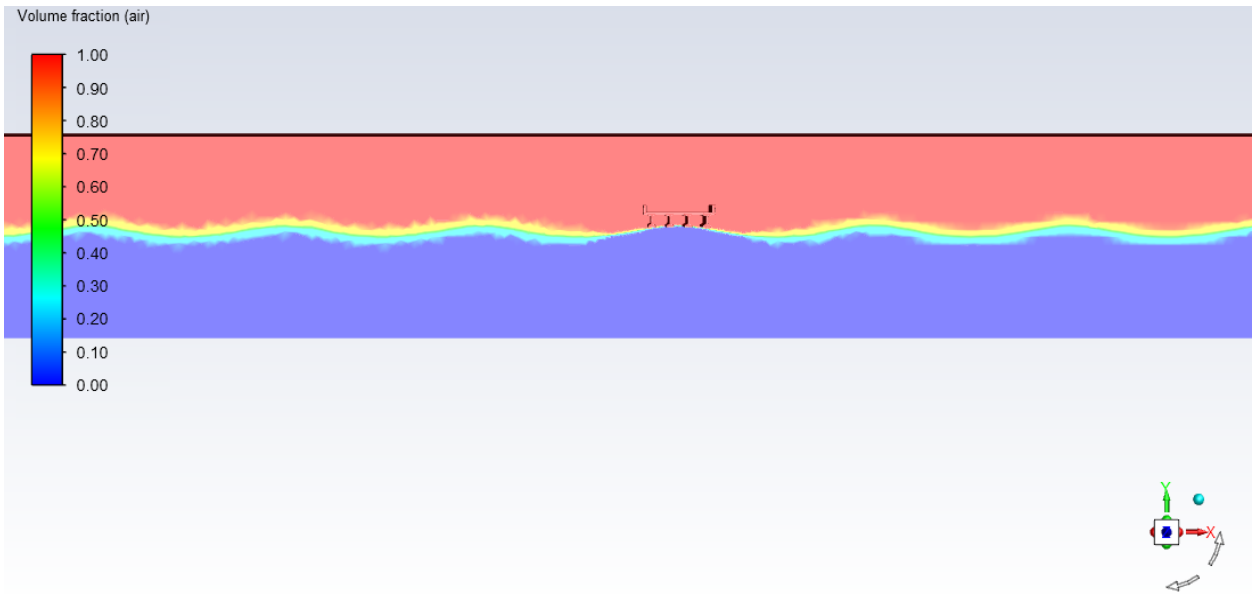


Figure E.8 Wave height = 1" Bridge Model TX54-26' wide Deck ($h^* = 0.26$)

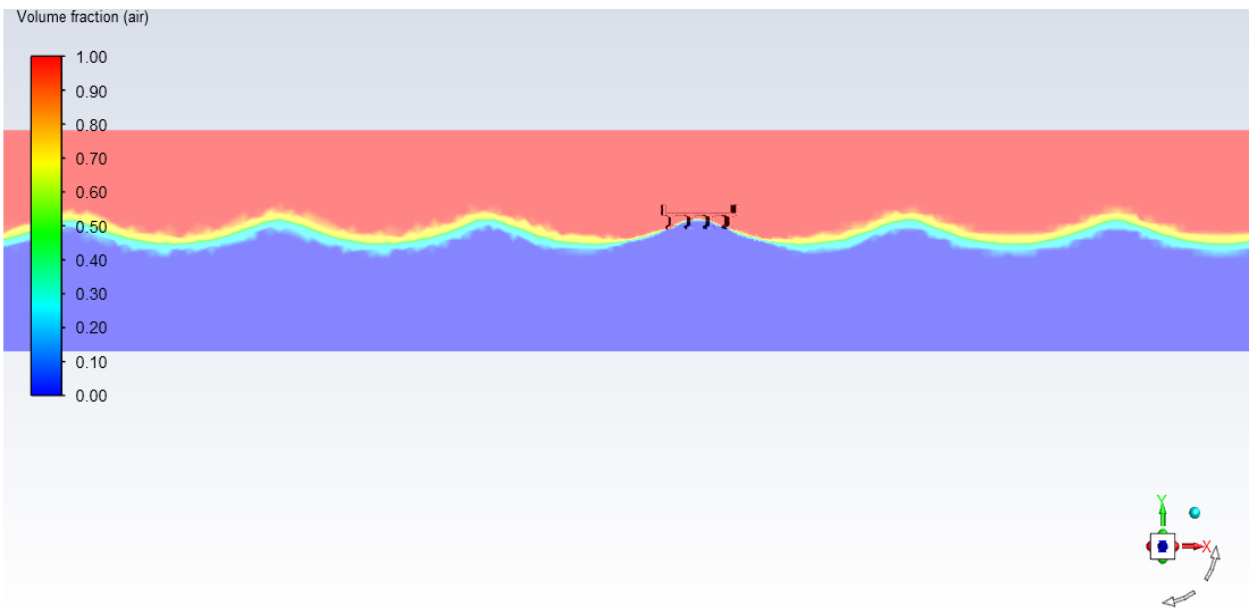


Figure E.9 Wave height = 2" Bridge Model TX54-26' wide Deck ($h^* = 0.26$)

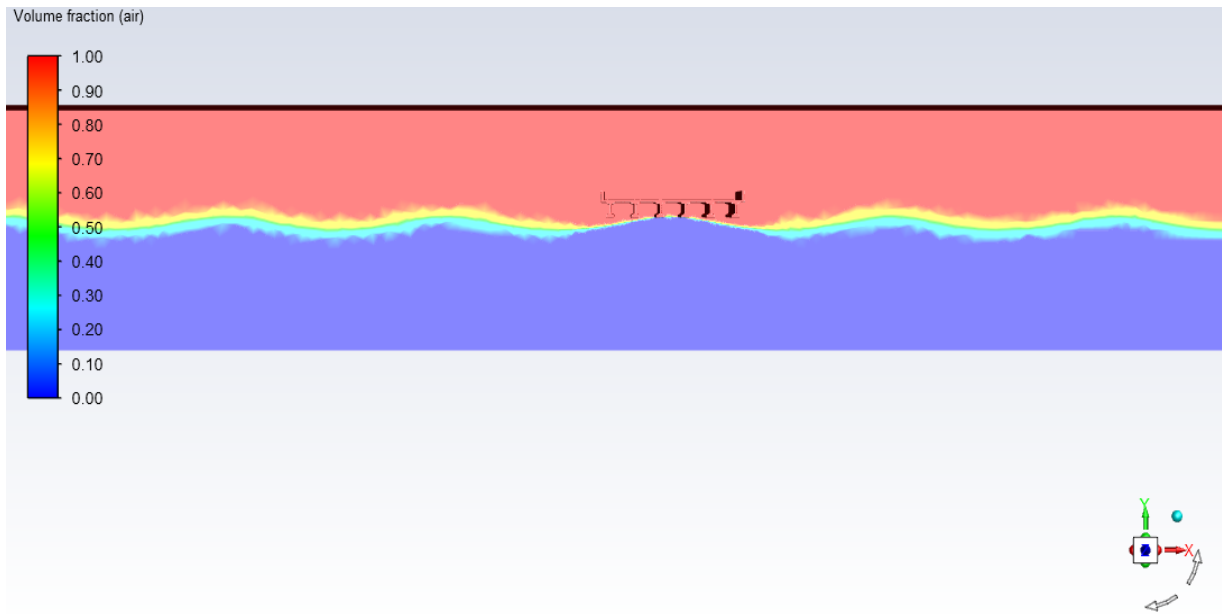


Figure E.10 Wave height = 1” Bridge Model TX54-46’ wide Deck ($h^* = 0.26$)

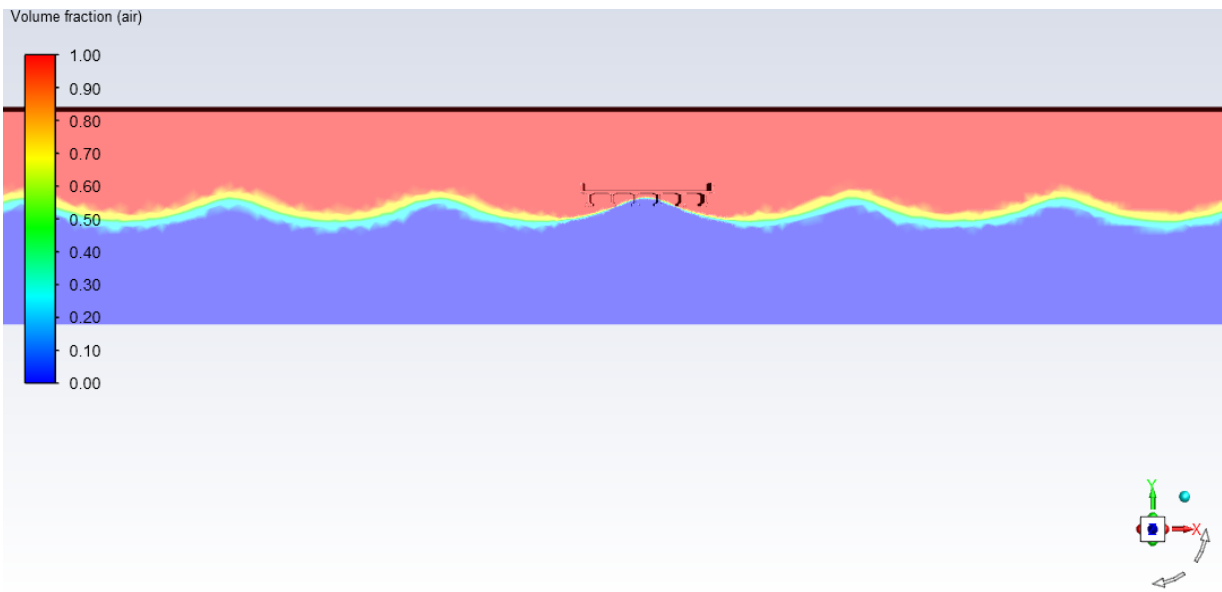


Figure E.11 Wave height = 2” Bridge Model TX54-46’ wide Deck ($h^* = 0.26$)

III. Contour Plots for Variables around Full-Scale Bridge Decks

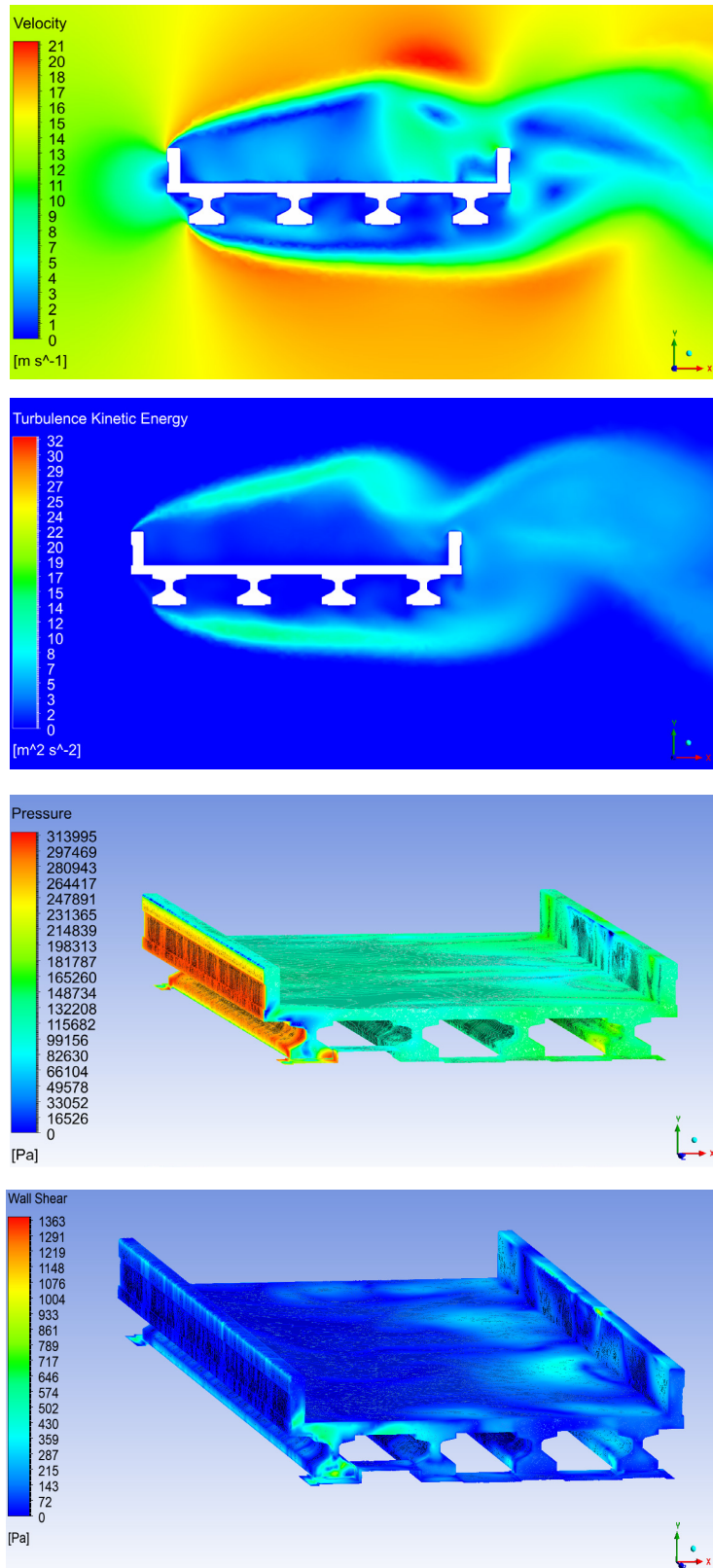


Figure E.12 Bridge Model TX28-26' wide Deck ($h^* = 2.5$, $Fr = 0.9$)

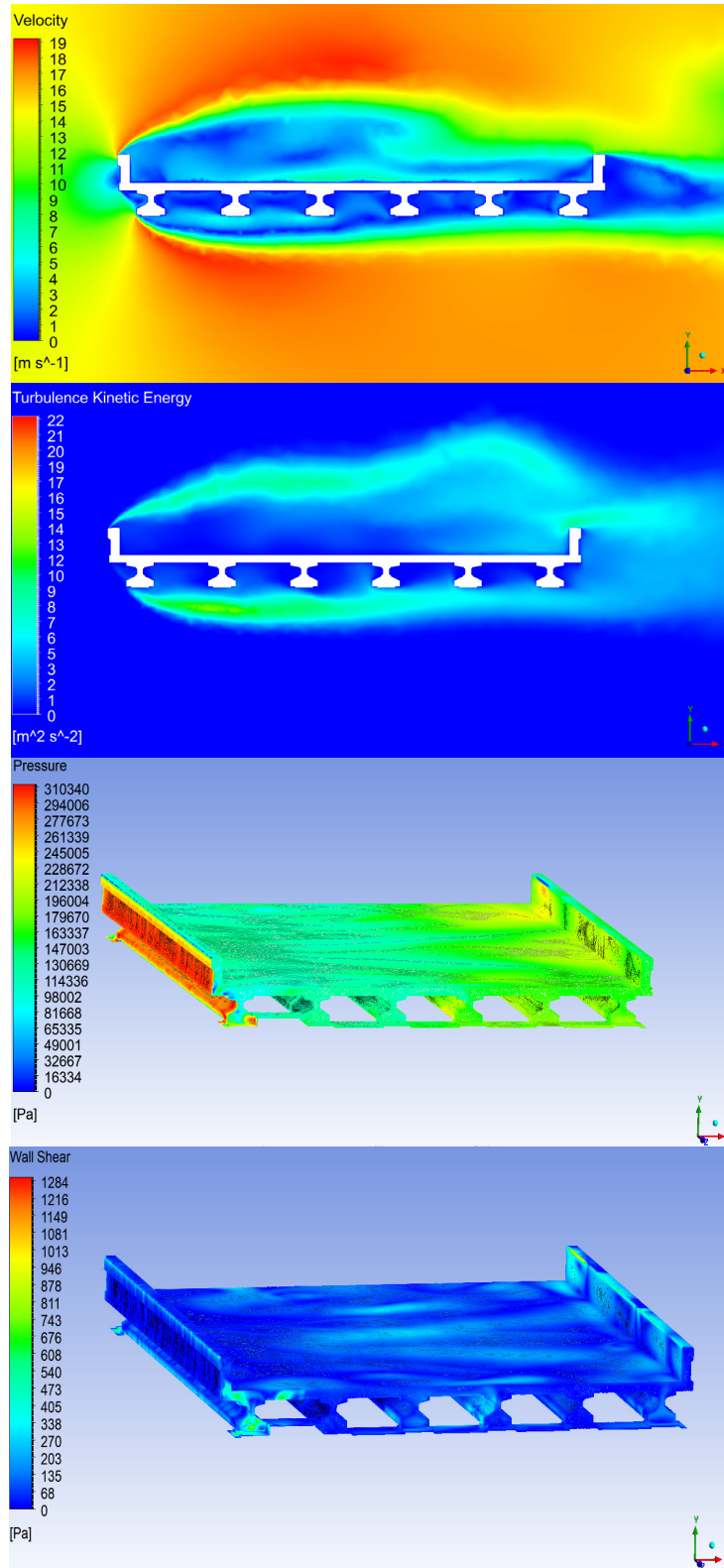


Figure E.13 Bridge Model TX28-46' wide Deck ($h^* = 2.5$, $Fr = 0.9$)

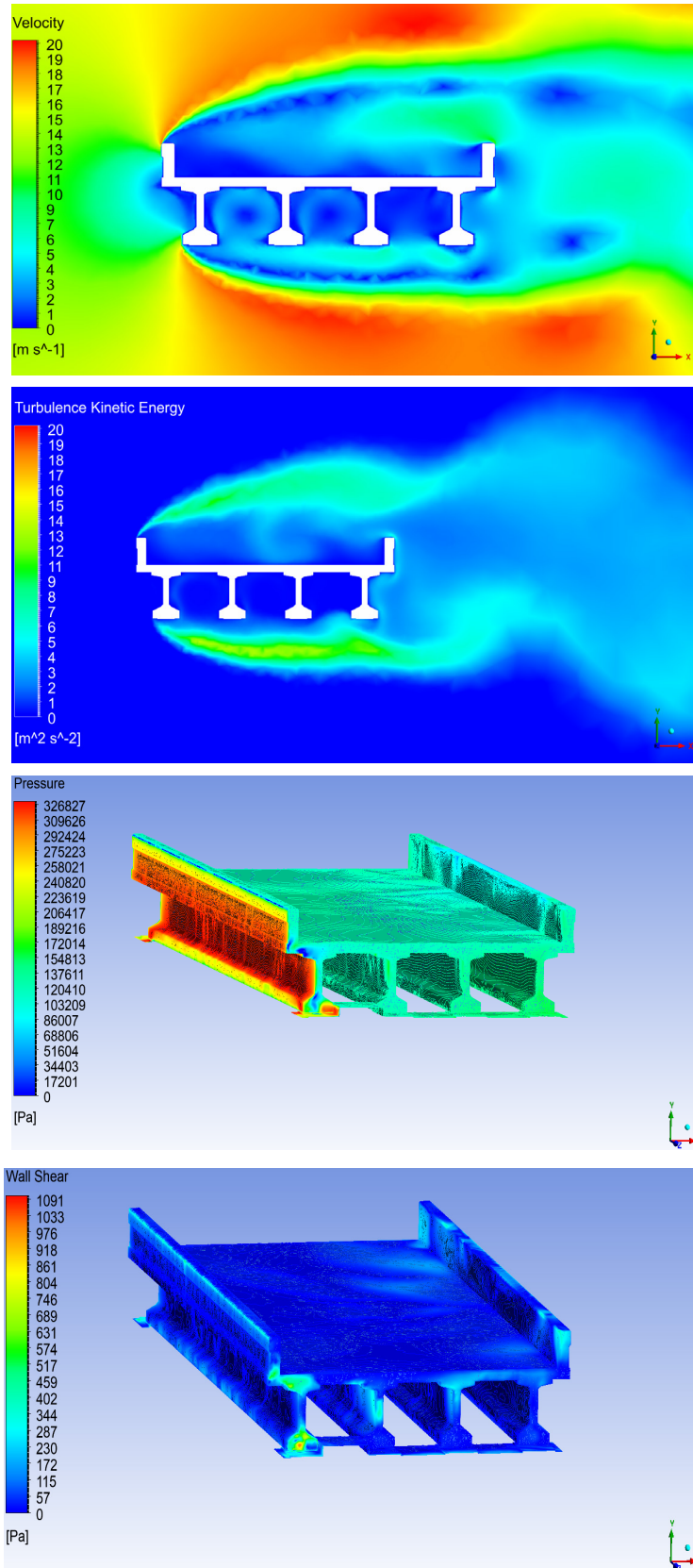


Figure E.14 Bridge Model TX54-26' wide Deck ($h^* = 2.5$, $Fr = 0.9$)

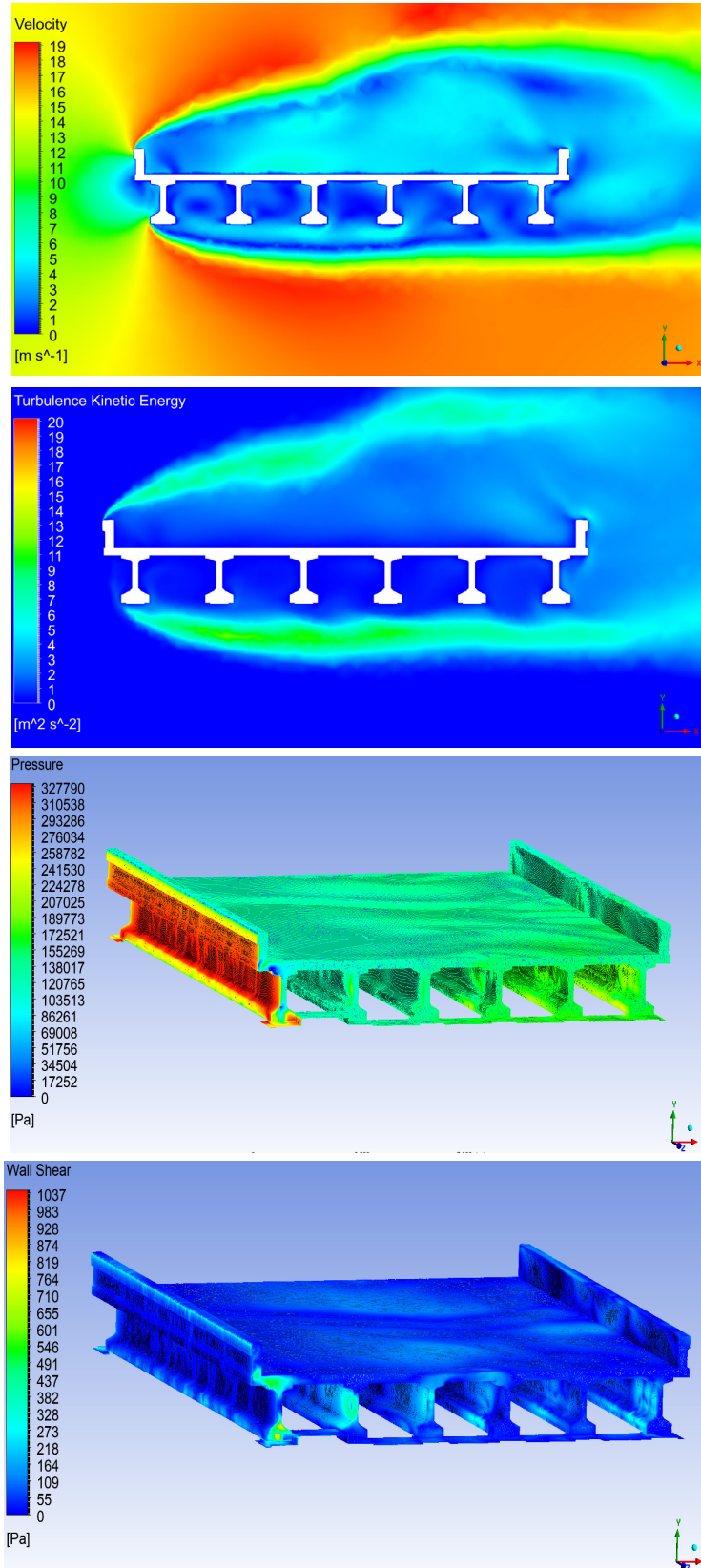


Figure E.15 Bridge Model TX54-46' wide Deck ($h^* = 2.5$, $Fr = 0.9$)

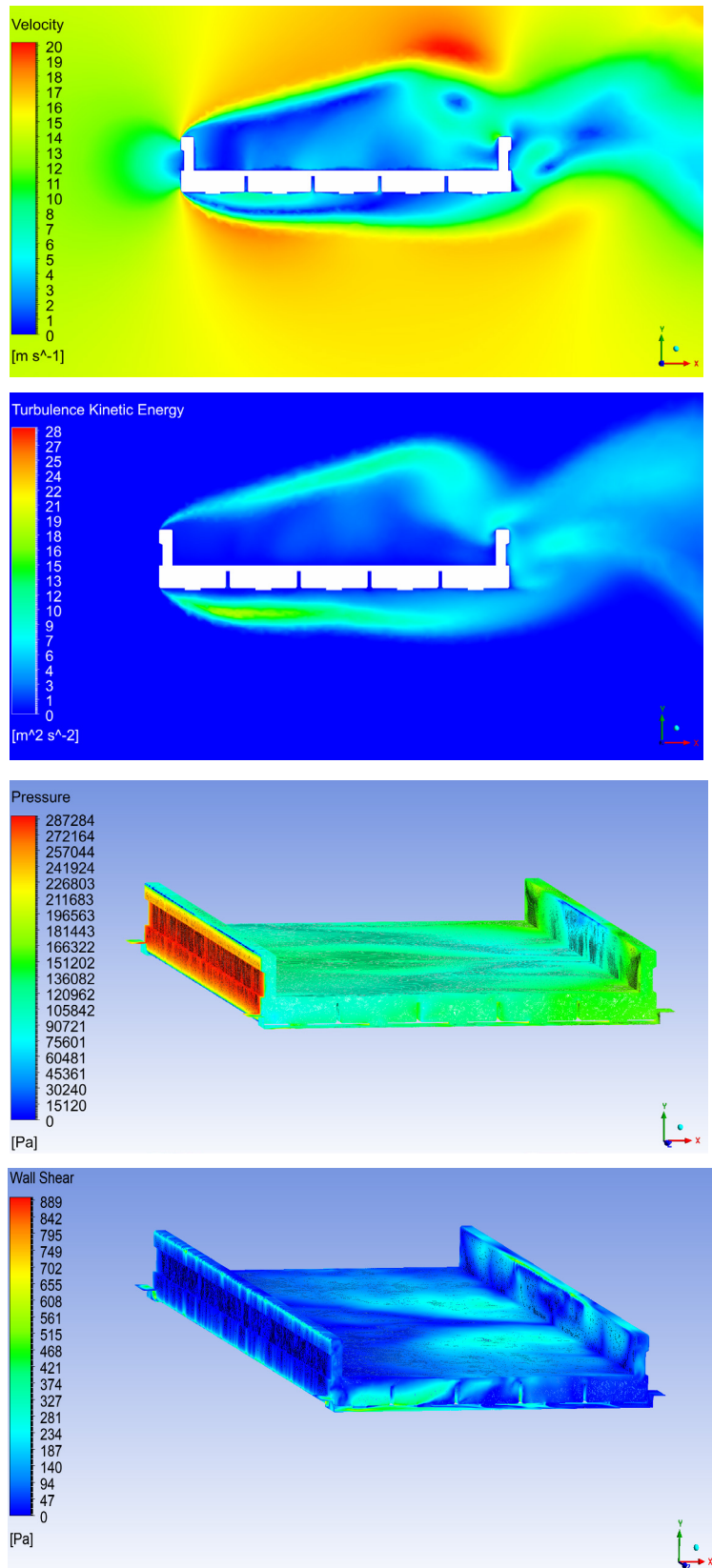


Figure E.16 Bridge Model Slab Beam-26' wide Deck ($h^* = 2.5$, $Fr = 0.9$)

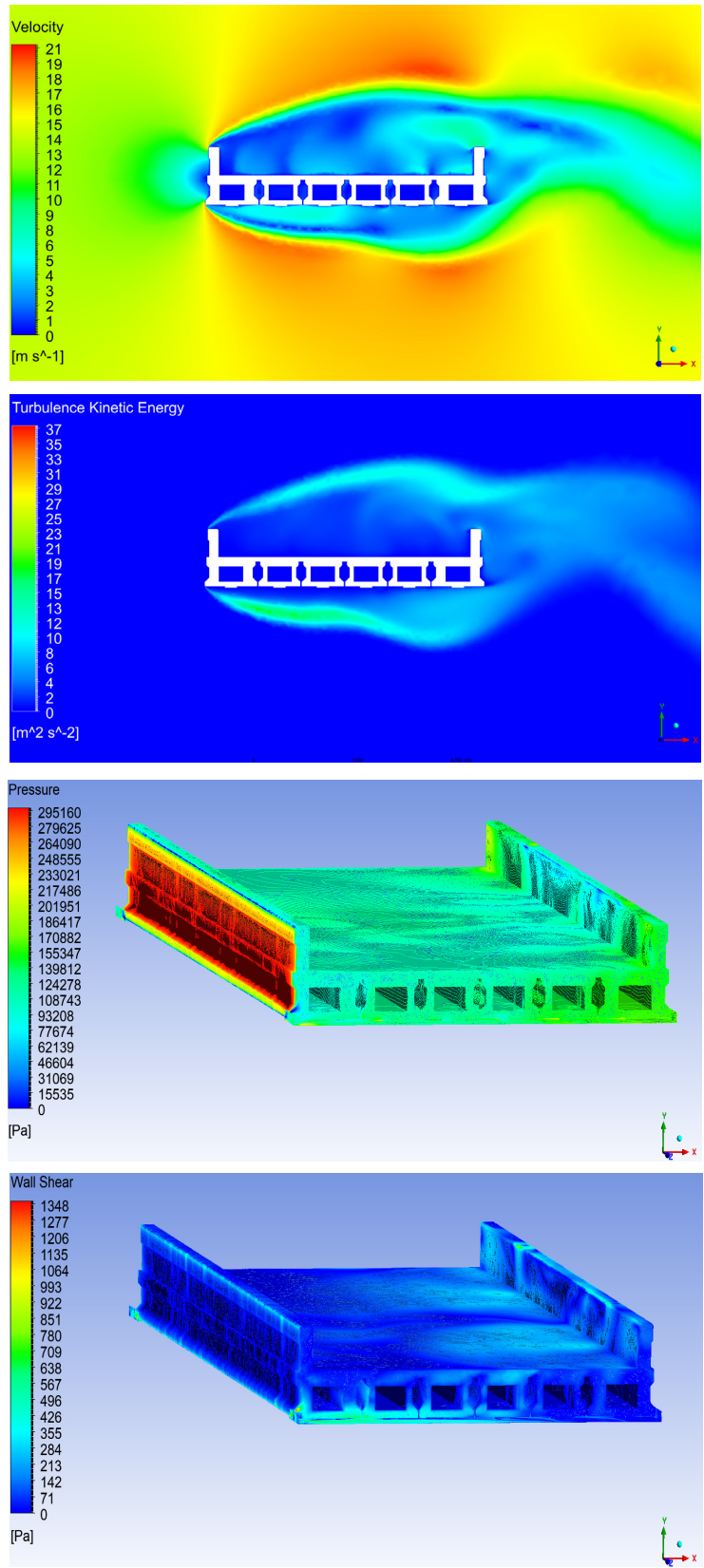


Figure E.17 Bridge Model Box Beam-26' wide Deck ($h^* = 2.5$, $Fr = 0.9$)

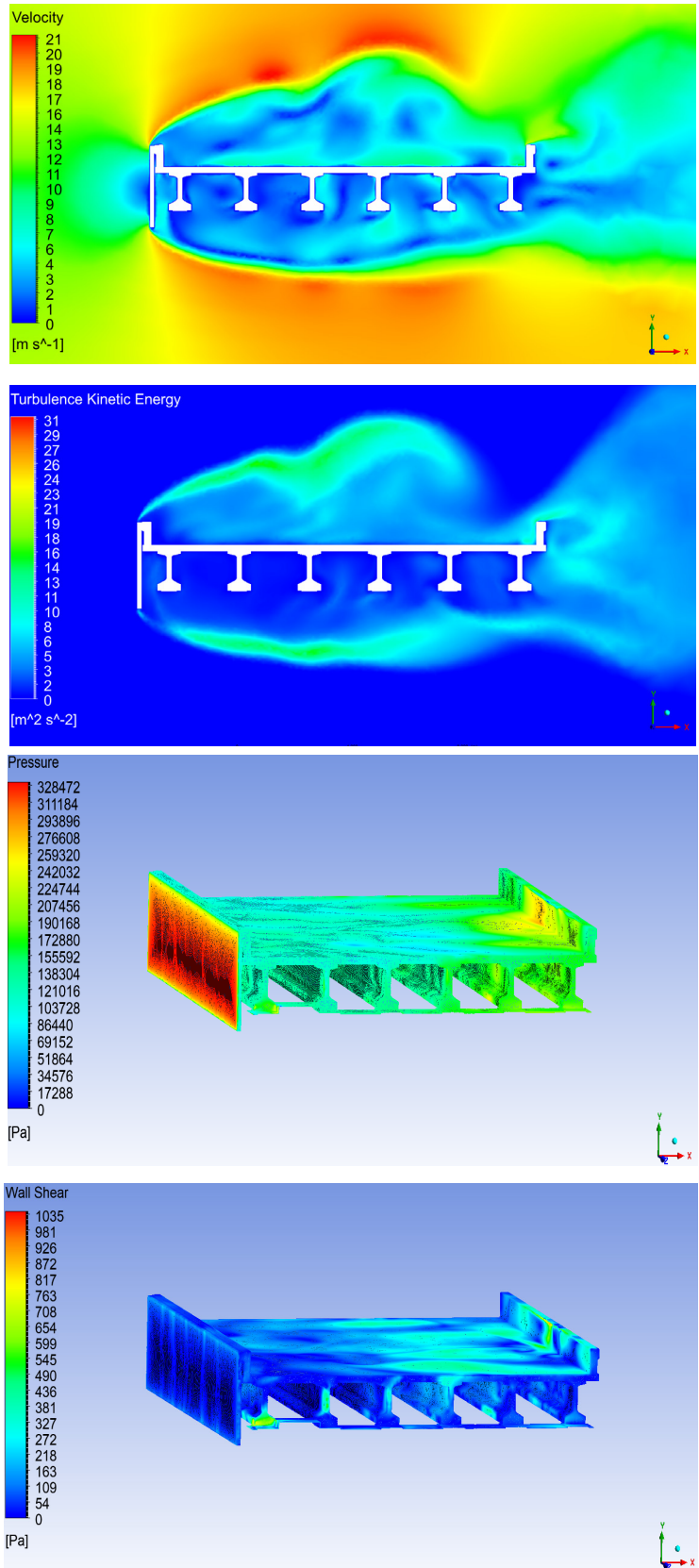


Figure E.18 Bridge Model TX54-46' wide Deck with Flat Plate Debris ($h^* = 2.5$, $Fr = 0.9$)

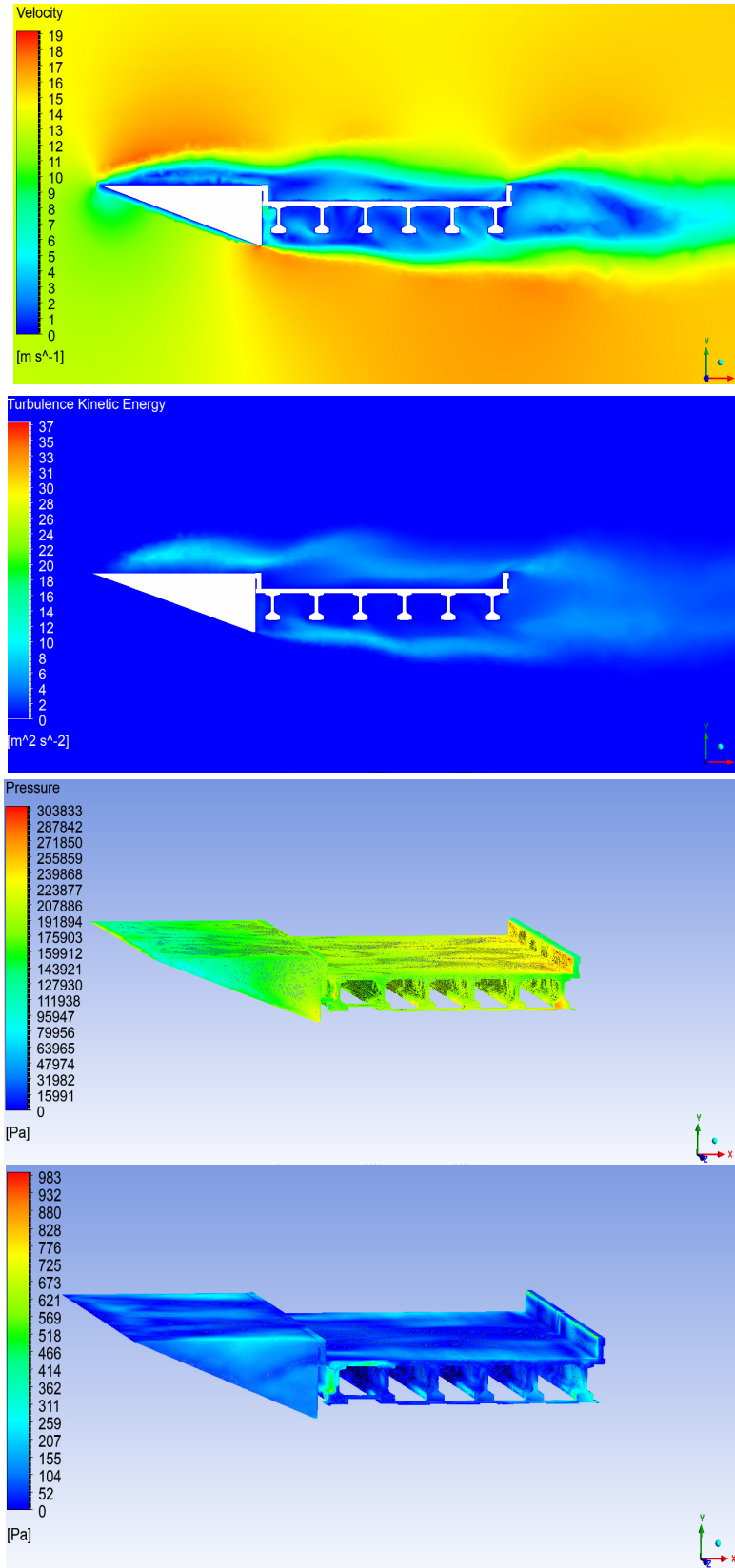


Figure E.19 Bridge Model TX54-46' wide Deck with Wedge Shape Debris ($h^* = 2.5$, $Fr = 0.9$)

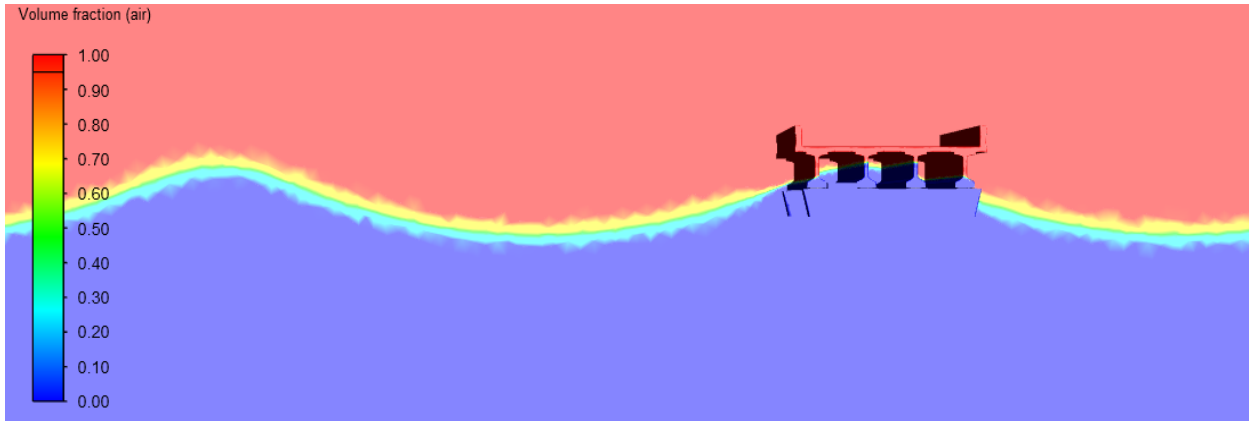


Figure E.20 Contour Plots of Air Volume Fraction for Waves modeling

